Dielectrophoretic nanotweezers for single-particle force spectroscopy

Dimitrios Soulias

Submitted in accordance with the requirements for the degree of

Doctor of Philosophy

The University of Leeds

School of Electronic and Electrical Engineering

January 2023

The candidate confirms that the work submitted is his own, except where work which has formed part of jointly authored publications has been included. The contribution of the candidate and the other authors to this work has been explicitly indicated below. The candidate confirms that appropriate credit has been given within the thesis where reference has been made to the work of others.

Publication (Journal Article): F. Marcuccio *et al.*, “Mechanistic Study of the Conductance and Enhanced Single-Molecule Detection in a Polymer–Electrolyte Nanopore,” *ACS Nanoscience Au*, **2023** *3* (2), 172-181. DOI: 10.1021/acsnanoscienceau.2c00050.

> Appendix A was reproduced from published material of the above cited publication. All simulations, data analysis and writing were equally contributed by the candidate, Dimitrios Soulias, and Fabio Marcuccio (School of Electronic and Electrical Engineering, University of Leeds).

To my life partner, Panagiota

who was constantly by my side.

“*When you set out on your journey to Ithaca,*

pray that the road is long, full of adventure, full of knowledge”

- C. P. Cavafy -

Acknowledgements

I would like to sincerely thank my supervisors Prof Christoph Wälti and Dr Paolo Actis for giving me the opportunity to pursue my academic dreams and for their continuous guidance and support throughout my PhD journey. Over my time in the Bioelectronics group, they helped me evolve not only as a scientist but also as an individual.

I would like to extend my appreciation to Dr Martin A. Edwards for his supervision on our published work titled “Mechanistic Study of the Conductance and Enhanced Single-Molecule Detection in a Polymer–Electrolyte Nanopore”. It was a unique long-distance learning experience and collaboration that, besides improving my skills in finite element modelling, taught me to think more critically and structured.

My special thanks to my PhD companions, Dr Fabio Marcuccio, Dr Samuel Confederat and Dr Chalmers Chau, for all the moments we shared together inside and outside the lab and for sticking together, even after all the difficulties we faced during these years. My kindest regards also to all the rest of my colleagues in Bioelectronics for being lovely to work and hang out with. I will most certainly miss our daily lunch breaks and our Friday pub nights.

My warmest gratitude extends to my mentor, Prof Stamatis Vokos, for all the life inspiring discussions we exchanged at Roussos over the previous ten summers. Of course, I would like to thank my family for always believing in me.

Last but not least, I would like to thank my life partner, Panagiota Gidopoulou. Words are not enough to express my gratitude for her continuous and unconditional support. Having her by my side since the first day of my undergraduate studies, through both good and tough moments, helped me achieve my goals.

Abstract

Studying the structural and functional properties of biological molecules using single-molecule techniques has been fundamental in establishing a comprehensive understanding of the mechanisms that govern complex living systems. The aim of this thesis was to develop a dielectrophoretic nanotweezers setup to provide a new approach for applying and measuring dielectrophoretic forces on individual particles in aqueous solution. To achieve this goal, dual-barrel quartz nanopipettes were filled with pyrolytic carbon, forming a pair of nanoelectrodes at their tip. Their size and shape were characterised both through SEM imaging and electrochemical cyclic voltammetry. By applying low AC voltages (< 1 V) between these nanoelectrodes, very strong and highly inhomogeneous electric fields were generated at the nanopipette's tip to form dielectrophoretic nanotweezers. The frequency of the electric field was tuned so that individual entities were either attracted or repelled depending on their dielectric properties. In this work, experimental measurements of the dielectrophoretic force acting on single polystyrene beads (2 μm) were acquired by single particle tracking on an inverted fluorescence microscope. The spatial coordinates of individual beads were extracted from their trajectories as a function of time under trapping conditions. The force magnitude, measured from their velocity over distance from the nanotweezers tip, was found in the femtonewtons range for a set of applied voltages and frequencies. In addition, the electric field distribution was simulated close to the nanotweezers tip by a finite element model developed for this system. Estimations of the dielectrophoretic force magnitude for different nanotweezers geometries were also performed. Overall, the simple operational mechanism and design of these dielectrophoretic nanotweezers combined with their ability to be controlled in three-dimensions, make them a versatile and promising platform for single-particle manipulation and force probing.

Table of contents

List of figures

List of tables

Abbreviations

1D	one-dimensional
2D	two-dimensional
3D	three-dimensional
AC	alternating current
ACEO	alternating current electroosmosis
ACET	alternating current electrothermal flow
AFM	atomic force microscopy
ATP	adenosine triphosphate
CAD	computer-aided design
CCD	charged-coupled device
CVD	chemical vapour deposition
DC	direct current
DEP	dielectrophoresis
DI	de-ionised
DNA	deoxyribonucleic acid
dsDNA	double-stranded deoxyribonucleic acid
EIS	electrochemical impedance spectroscopy
eDEP	electrode-based dielectrophoresis
EDL	electrical double layer
ELS	electrophoretic light scattering
EMCCD	electron-multiplying charged-coupled device
FEM	finite element method
FIB	focused ion beam
GUV	giant unilamellar vesicle
ICEO	induced charge electroosmosis

IDEs	interdigitated electrodes
kbp	kilo-base pair
NA	numerical aperture
PBS	phosphate-buffered saline
PCR	polymer chain reaction
PDMS	polydimethylsiloxane
PSF	point spread function
RNA	ribonucleic acid
ROI	region of interest
sCMOS	scientific complementary metal oxide semiconductor
SECM	scanning electrochemical microscopy
SEM	scanning electron microscopy
SERS	surface-enhanced Raman spectroscopy
SMFM	single-molecule fluorescence microscopy
SMFS	single-molecule force spectroscopy
SPT	single particle tracking
ssDNA	single-stranded deoxyribonucleic acid
TEM	transmission electron microscopy
TIRF	total-internal reflection

Chapter 1
Introduction

1.1 Motivation

Biological molecules are the building blocks of living systems. Unravelling their structural and functional properties could lead to a comprehensive description of the mechanisms that govern cellular arrangements and even entire organisms. Conformational changes to a biomolecule or its interaction with other entities increase the temporal and spatial heterogeneity within a system [1]. The dynamics of such interactions, from cellular cargo transportation to muscle contraction, are principally regulated by forces. Over the past decades, our ability to investigate these fundamental processes has been transformed by the development of techniques based on single-molecule force spectroscopy (SMFS). These techniques allow force probing of individual molecules and cells with sub-piconewton resolution [2].

Although ensemble measurement methods in biophysics have provided important information about the average state of a system, any differences within seemingly identical organisations (i.e., cells), such as in viscosity or concentration of molecules in aqueous solution, cannot be detected. In contrast, single-molecule studies permit researchers to acquire data in real-time and with nanometre resolution for individual entities. This information can then enable the understanding of key mechanisms at larger length scales and eventually build a picture of a whole organism's heterogeneity [3]. The difference between ensemble and single-molecule measurements can be explained with the use of an analogy based on the emission spectrum of electromagnetic radiation. Imagine two closely spaced (few nanometres) molecules that carry a fluorescent label, one emitting at a wavelength equal to blue and the other to yellow. If both get excited at the same time and are imaged from a long distance, the observer will report the presence of a single fluorescent molecule emitting green colour, instead of two separate ones emitting at different wavelengths [4].

The most established and widely used single-molecule force spectroscopy tools are the optical tweezers, magnetic tweezers and atomic force microscopy (AFM). Their differences exist not only in the experimental configuration but in the applied forces range as well as in spatial and temporal resolution [1], [2]. In brief, optical tweezers operate by

focusing a laser beam through a high numerical aperture microscope objective lens to trap, manipulate, apply and probe calibrated forces to refractive objects. When the dimensions of the sample of interest fall below the sub-micrometre range, interactions with the trapping light become weak and integration of artificial handles (i.e., micron-sized polystyrene or silica beads) is required. Magnetic tweezers resemble the optical ones with the key difference that they utilise a magnetic field generated by a pair of magnets to apply forces or torques on handles which are mainly micron-sized super-paramagnetic beads. Lastly, atomic force microscopy relies on a silicon-based tip attached to a metal cantilever which moves vertically towards the specimen's surface and interacts with it through Van der Waals attraction or Coulomb repulsion. It is known for its ability to perform both imaging and force measurements with high precision which depends on the cantilever material and geometry [3], [4].

In more recent years, acoustophoresis and dielectrophoresis (DEP), two well-established techniques for manipulating and sorting cells in aqueous solutions, have attracted interest as emerging single-molecule force spectroscopy tools. On one hand, acoustic tweezers operate with sound waves which generate air pressure gradients to trap individual biological particles across a wide range of sizes (from nanometres to millimetres). The acoustic force relies on the relative speed of sound between the entity and the medium. In the case of small molecules, it is expected to be dominated by other forces so the use of handles would also be required here [5]. On the other hand, dielectrophoretic tweezers could be considered the electrokinetic equivalent of magnetic tweezers, as they rely on the generation of inhomogeneous electric fields through the application of an electric potential, mainly alternating current (AC) voltages, between two or more electrodes [6].

Depending on the dielectric properties of polarisable biological molecules and their surrounding medium, the gradient of these non-uniform electric fields can implement an attractive or repulsive force on such entities by tuning the frequency of the applied signal. Significant attributes of dielectrophoretic manipulation include the instrumentation simplicity, electrodes' design flexibility and its ability to trap a wide range of particle sizes from few nanometres to several millimetres without the need of tethering on handles [7]. Moreover, biomolecules are found in a variety of shapes, either spherical or ellipsoidal with or without additional layers surrounding their cores. This complexity and heterogeneity are beneficial for trapping only the analyte of interest from a mixed population via dielectrophoresis. However, at the same time, their sophisticated dielectric properties in combination with the intricate cell environment are not easily predictable with theoretical models which makes describing dielectrophoresis phenomena hard [6].

Currently, an important challenge for single-molecule force spectroscopy tools is the transition from *in vitro* to *in vivo* studies. As mentioned above, the dynamics of biomolecular interactions have been extensively investigated so far in vitro, where the impact of a parameter of the system can be isolated. Nevertheless, it is of great importance for the functional force probing to be performed in the molecules' natural environment, even though such experiments are challenging due to the delicate structure of cells [4]. For example, intracellular manipulation or force sensing with an AFM tip requires the penetration of cell wall which can be highly invasive. Additionally, for optical and magnetic and acoustic tweezers, artificial handles would need to be inserted inside living cells which could have bio-incompatibility or cytotoxic effects.

An additional tool for single-molecule manipulation and sensing, offering single-cell penetration and performing in vivo measurements is nanopipettes [8]. They are typically made of glass and possess a geometry similar to a truncated cone (needle-like), with a tip diameter that can vary from tens of micrometres to a few nanometres and a total length of several centimetres. This small sharp tip, which is fabricated easily and reproducibly, diminishes damage to the cell wall upon penetration, as well as intracellular entities in proximity, and can be spatially controlled in three dimensions (3D). Nanopipettes can also be functionalised by conductive materials, such as carbon or platinum, to comprise a nanoelectrode [9].

The combination of dual nanoelectrodes separated by a thin glass septum, when immersed into an aqueous medium, offers an alternative type of dielectrophoretic tweezers. A great demonstration of such a configuration reflects on the work performed by Nadappuram et al. (2019) [10] where minimally invasive dielectrophoretic tweezers were developed and utilised for capturing and extracting individual biological molecules (proteins, nucleic acids), as well as single organelles (mitochondrion), from living cells. This type of tweezers was based on a dual-barrel nanopipette (fabricated from theta-shaped capillaries) that was filled with pyrolytic carbon and acted as two electrodes with a separation distance of approximately 20 nm at the nanopipette's tip. The application of AC voltages (~1 V peak) produced significantly high electric field gradients (10^{28} V^2m^{-3}) close to the electrodes which led to the attraction of the entities under investigation for particular frequencies.

Inspired by this work, this project aims in developing this configuration of dielectrophoretic tweezers further and validating it as a new approach to apply and probe sub-piconewton forces on single particles. Firstly, a device was developed to fabricate dual-carbon nanoelectrodes starting from dual-barrel quartz nanopipettes. By applying AC voltages smaller than 1 V between these nanoelectrodes, very strong and highly inhomogeneous electric fields can be generated at the nanopipette's tip to form

dielectrophoretic nanotweezers. The frequency of the electric field can be tuned so that individual entities are either attracted or repelled depending on their dielectric properties. Overall, the simple operational mechanism and design of these dielectrophoretic nanotweezers combined with their ability to be manipulated in three dimensions, make them a versatile and promising platform for single-molecule manipulation and force probing for a wide variety of entities.

Here, data are presented on the measurement of the dielectrophoretic forces acting on individual polystyrene latex beads that are 2 μm in diameter by optically tracking their displacement during a manipulation timeframe. In addition, using finite element simulations, the electric field distribution was also simulated close to the nanotweezers and the force magnitude applied on a single particle under manipulation was estimated, along its simulated trajectory. Subsequently, this thesis is expected to add an additional dimension for single-particle force spectroscopy that has the potential to further our understanding on the dynamics of biomolecular and particular interactions. The following section provides a brief outline of my PhD thesis, listing the contents of each chapter.

1.2 Thesis outline

In this section, the structure and contents of each chapter and section of my Ph.D. thesis are briefly outlined. To start with, Chapter 2 provides an extensive literature review covering the key aspects of this project, as follows:

- *Section 2.2* mentions the currently established single-molecule force spectroscopy techniques, such as optical, magnetic, acoustic and electrical tweezers, as well as atomic force microscopy.
- *Section 2.3* summarises recent advances in single molecule fluorescence microscopy and single particle tracking.
- *Section 2.4* explains the theoretical background behind the phenomenon of dielectrophoresis, the current models that describe entities of different shape, as well as other electrokinetic phenomena that occur due to the application of electric potentials in aqueous solutions and discusses the dielectrophoretic impedance spectroscopy of biomolecules and nanoparticles.
- *Section 2.5* lists fabrication and characterisation techniques for nanoelectrodes, as well as a range of applications on single-molecule manipulation.

Chapter 3 focuses on the fabrication and characterisation of dielectrophoretic nanotweezers which are based on dual-barrel nanopipettes coated and filled internally with carbon via a pyrolytic deposition instrument I constructed. In more detail:

- *Section 3.2* describes the fabrication of single- and dual-barrel nanopipettes, as well as their characterisation. The dimensions of their tip (pore opening diameter, glass wall thickness) are measured by electrochemical and imaging techniques.
- *Section 3.3* introduces a new instrumentation for fabricating the dielectrophoretic nanotweezers by coating such nanopipettes internally with carbon and turning them into nanoelectrodes.
- *Section 3.4* analyses the characterisation of these nanoelectrodes based on electrochemical and imaging techniques again. In addition, focused-ion beam (FIB) and scanning electron microscopy (SEM) are used to turn their tip into a significantly smoother planar surface.
- *Section 3.5* mentions all the methods and materials used to fabricate and characterise nanopipettes and carbon-based nanoelectrodes.

Chapter 4 concentrates on simulating the electric field distribution generated between two closely-spaced carbon nanoelectrodes when immersed in aqueous solution by finite element method modelling. Specifically:

- *Section 4.2* explains the three-dimensional design of the finite element model for the carbon nanoelectrodes in water, the boundary conditions and physics implemented, as well as the material properties allocated to each domain.
- *Section 4.3* illustrates the two- and three-dimensional distribution of the electrical potential and electric field modulus between these two nanoelectrodes.
- *Section 4.4* provides estimations for the dielectrophoretic force magnitude 1 μm away the nanotweezers tip. The effect of changes in the gap separating the two nanoelectrodes on the dielectrophoretic force is also studied. Additionally, the effect of carbon recession inside the nanopipette pore opening on the dielectrophoretic force distribution at the nanotweezers tip is investigated.
- *Section 4.5* presents a revised version of the model introduced in the previous sections which simulated the electrical impedance across the dielectrophoretic nanotweezers when they were left in air, immersed in water and trapped a 2 μm spherical particle at their tip while immersed in water.

Here, it is important to clarify that due to the COVID-19 pandemic, and labs not being accessible for several months, my PhD work was adjusted accordingly during that period and the main focus was shifted to finite element modelling with COMSOL. Part of the work conducted then was directly relevant to the main aim of my PhD thesis, as listed in the bullet points above for Chapter 4, and another very large part was related to a side project, done in collaboration with Fabio Marcuccio [11], which was recently published in a peer-reviewed journal. The content of this published work was not directly related to the work presented in this thesis and was not included. However, the main text of the published work can be found in Appendix A. Links for the supporting information file and model report are provided there as well.

Then, Chapter 5 focuses on developing and validating a protocol to measure femtonewton dielectrophoretic forces acting on individual latex beads in water with the nanotweezers described in Chapter 3. To be more precise:

- *Section 5.2* explains how the electric conductivity of beads in aqueous medium can be calculated based on their zeta potential which is obtained by electrophoretic light scattering measurements.
- *Section 5.3* describes a statistical analysis on measuring the diffusion coefficient of the beads in water as accurately as possible, when the system has reached its equilibrium state, based on single particle tracking and wide-field fluorescence microscopy.
- *Section 5.4* assesses whether the two-dimensional (2D) motion of freely diffusing beads on top of the microscope slide is hindered due to the distance between

these two charged surfaces which could lead to changes in the surrounding medium viscosity.

- *Section 5.5* shows how the effective measured viscosity of the medium surrounding the beads is used to estimate the distance between their outer surface and the top surface of the microscope cover glass.
- *Section 5.6* analyses the dielectric properties of the polarisable beads-water system under the presence of AC electric fields. The real part of the Clausius-Mossotti factor is calculated from the electric permittivity and conductivity of the beads, measured in Section 5.2, and water. Then, the crossover frequency of this system is calculated to define the frequencies range where beads get attracted to or repelled away from the nanotweezers tip.
- *Section 5.7* establishes a new protocol for measuring and analysing the dielectrophoretic forces applied on individual latex beads by single particle tracking and wide-field fluorescence microscopy. A data smoothing algorithm is presented as well.
- *Section 5.8* analyses how the dielectrophoretic force generated by the nanotweezers on individual beads is affected by changes in two parameters, the applied voltage and frequency of an AC signal.

Finally, Chapter 6 summarises the project objectives achieved in the previous chapters, discusses the key findings, concludes whether the dielectrophoretic nanotweezers can be considered as a valid additional platform in single-molecule force spectroscopy, and shows preliminary data on the trapping of individual lipid vesicles as well as using them for single-molecule detection based on impedance spectroscopy techniques.

Chapter 2

Literature review

2.1 Introduction

In comparison with the traditional ensemble experiments, where large groups of molecules are studied simultaneously, single-molecule techniques offer the advantages of observing rare events, collecting information for non-uniform systems and understanding their structural and functional properties in real-time [1]. At first, the basic principles and applications of some single-molecule force spectroscopy techniques are presented. The techniques reviewed include optical, magnetic, acoustic, electrical tweezers and atomic force microscopy (AFM). Then, fluorescence imaging microscopy, which has been a central component of single-molecule force spectroscopy since its inception, is explained with key focus on single-particle tracking techniques.

The chapter then describes the fundamental theory on dielectrophoresis (DEP) for a homogeneous spherical particle, including mentions of multi-shell spherical and non-spherical particles. Recently, dielectrophoretic-based platforms have been applied for manipulating, trapping, sorting, separating or characterising single entities [6]. Dielectrophoresis has also been combined with electrochemical impedance spectroscopy for single particle/molecule detection which could allow label-free sensing. In an electrokinetic system based on dielectrophoretic forces, however, two more phenomena are frequently observed, the electroosmosis and electrothermal flow which are also discussed in this chapter. Lately, DEP devices based on nanopipettes have shown great potential in manipulating single molecules inside living samples without affecting their viability. Therefore, the final section is concentrated on analysing the fabrication and characterisation processes of such platforms, along with recent applications.

2.2 Single-molecule force spectroscopy techniques

2.2.1 Optical tweezers

Light carries linear and angular momentum so when a photon collides with a polarisable spherical particle, the particle experiences gradient $(\vec{F}_{grad})$ and scattering $(\vec{F}_{scat})$ forces by the photon. If the wavelength of light is larger than the particle (Rayleigh scatterer), the gradient force depends on the object's polarisability [1]. For a laser beam given by a Gaussian function, the generated electric field is non-uniform, so the formed dipole across the particle is attracted to or repelled away from the beam's region of maximum intensity. In addition, the object also absorbs and scatters (reflects or refracts) part of the beam which leads to $\vec{F}_{scat}$ acting along the direction of the light propagation. Figure 2.1a illustrates this scenario, with $\vec{F}_{grad}$ (black arrow) attracting the particle towards the focus of the beam at its axis of symmetry against $\vec{F}_{scat}$ (red arrow) which tends to move it along the direction of the light [12].

However, when the wavelength of light is smaller than the particle, the applied forces on the body can be described by ray optics. Based on energy conservation within a system and the fact that absorption, reflection or refraction of the beam by the object change light's momentum, an equal change in the momentum of the particle is expected to take place [1]. As shown in Figure 2.1b, reflected light loses momentum which is transferred to the sphere leading to $\vec{F}_{reflection}$ (red arrow) applied in the same direction as the propagation of light. Moreover, refracted light gains momentum from the particle resulting in $\vec{F}_{refraction}$ (black arrow) which acts in the opposite direction of $\vec{F}_{reflection}$. Controlled trapping and manipulation for a spherical object is achieved when these two forces become equal in magnitude [12].

In their simplest configuration, optical tweezers utilise a continuous laser beam focused through a high numerical aperture microscope objective lens, so that micrometre or nanometre-sized entities get trapped near the centre of the focal area [1]. By altering the beam's focal point, the captured body can be manipulated in three dimensions. Optical tweezers can also enable the measurement of forces and displacements of the sample in real-time [4]. In most experiments, biological molecules under investigation need to be tethered onto micron-sized beads (usually from 0.2 – 5 μm in diameter). The force exerted on the molecule has equal magnitude but opposite direction to the force

experienced by the trapped bead. Any displacement caused by this force on the bead leads to changes in the momentum of the laser beam which can be detected via photodetectors. This is the basic principle of single-molecule force probing on optical tweezers for nanometre sized entities [12].

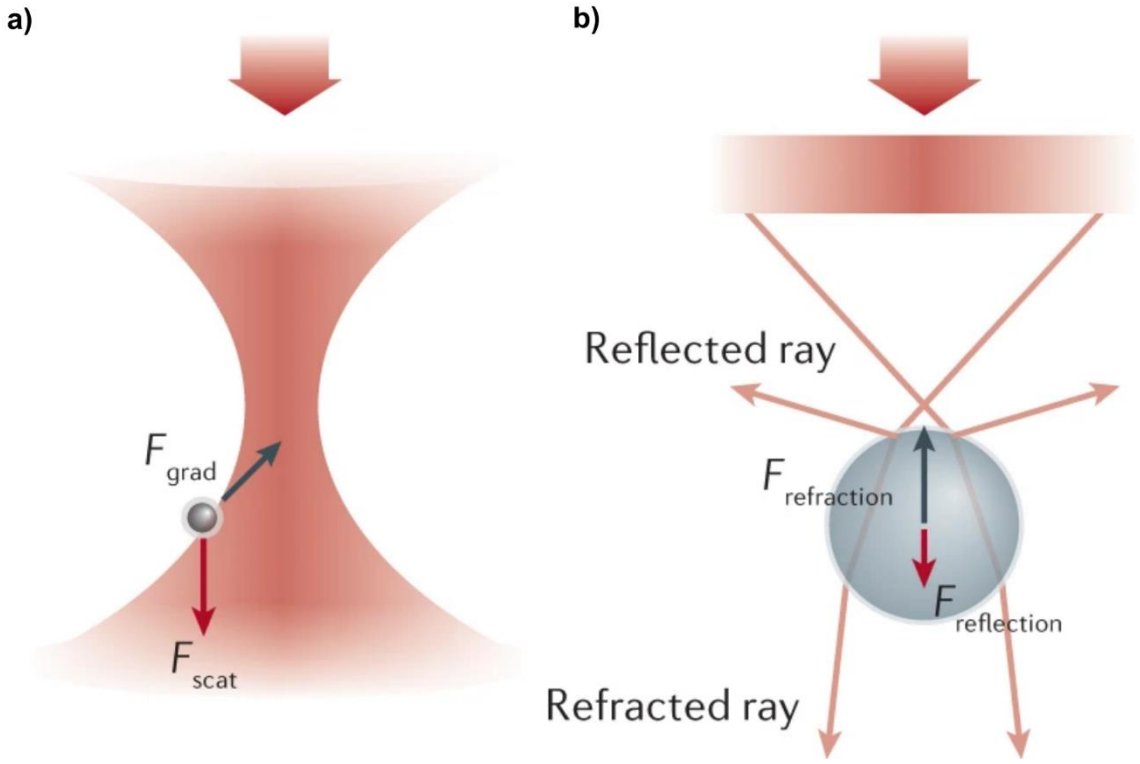

Figure 2.1 Schematic illustration of the basic principles behind the operation of optical tweezers. **a)** When the wavelength of light is larger than the particle (Rayleigh scatterer), the gradient force depends on the object's polarisability. For a bead with greater polarisability than its surrounding medium, $\vec{F}_{grad}$ (black arrow) attracts the particle towards the focus of the beam at its axis of symmetry against $\vec{F}_{scat}$ (red arrow) which tends to move it along the direction of the light. **b)** When the wavelength of light is smaller than the particle, reflected rays by the bead lose momentum which is transferred to the sphere leading to $\vec{F}_{reflection}$ (red arrow) in the same direction with the propagation of light. Refracted rays through the bead gain momentum form the particle resulting in $\vec{F}_{refraction}$ (black arrow) which acts in the opposite direction of $\vec{F}_{reflection}$. Controlled trapping and manipulation of the bead is achieved when these two forces become equal in magnitude. Reproduced from [12].

Arthur Ashkin introduced the first optical trap by managing to trap and transport micron-sized latex spheres immersed in water with radiation pressure forces generated by laser beams [13]. In 1986, Ashkin and his colleagues [14] published another pioneering study where they presented the first optical tweezers system. This was based on a single tightly focused laser beam that could trap in all three dimensions dielectric particles of different

sizes, from 25 nanometres to 10 micrometres, in aqueous solution. A year later [15], Ashkin et al. achieved in vivo manipulation of living bacteria and viruses by utilising an improved laser system emitting infrared light. For this work, Ashkin was awarded the 2018 Nobel Prize in Physics. As discussed in the following paragraphs, optical tweezers have become one of the most established tools for manipulating and probing forces from biological specimens both in vitro and in vivo, from single molecules to single cells [12].

One of the most widely explored proteins with optical tweezers has been kinesin, a cytoskeleton motor protein that carries molecules along microtubules in eukaryotic cells. In 1993, Svoboda et al. proved that each step of kinesin's motion is 8 nm long [16] when a maximum trapping of ~1.5 pN was applied on silica beads attached to individual molecules. Ten years later, another study from Block's group [17] focused on whether the hand-over-hand (different head is leading per step) or inchworm (same head is leading per step) model described best the kinesin's movement. By attaching such single molecules on 500 nm beads while trapping them with optical tweezers, they found that kinesin's motion on microtubules is best described by an asymmetric hand-over-hand pattern. More recently, Ramaiya et al. (2017) [18] demonstrated that this motion mechanism also includes rotation which could induce spinning of its cargo. The authors adjusted the common optical trap configuration by adding a rotation detector based on liquid crystalline microspheres (Figure 2.2a).

Single-molecule force spectroscopy with optical tweezers then quickly expanded towards applications related to nucleic acids (deoxyribonucleic acid (DNA) and ribonucleic acid (RNA) molecules) [19], [20]. The classic configuration is based on a single trap, where a molecule's end is attached to a dielectric bead held by the light beam while the other end is tethered either to a glass slide or attached to another bead held by a glass nanopipette (Figures 2.2b and 2.2c, respectively) [19], [20]. Although the addition of a micropipette into the configuration increases complexity, additional information about the biological sample can be obtained by its capability for rotation and extension. Another common configuration for optical tweezers is the dual-trap. As Figure 2.2d displays, and when compared to the previous case (Figure 2.2c), instead of the glass micropipette a second laser beam is used to trap another dielectric microsphere and the molecule attached between them can be manipulated by moving the two beads [20].

Depending on the optical tweezers' setup and the applied forces to the tethered molecule, there are three different modes for recording data [19]. The pulling or force-extension mode, which can be used for both single- and dual-traps, is based on recording the responses of a tethered molecule to either a force or an extension ramp. Then, the constant force or force-clamp mode relies on a constant force applied on the tethered

molecule throughout the measurement. This can be achieved by changing the position of the passivated glass slide or micropipette or bead held by the optical trap. Lastly, during the passive or extension clamp mode which is also the simplest one, the optical traps position is fixed and any tensions acting on the entity are monitored in real-time under constant extension [19].

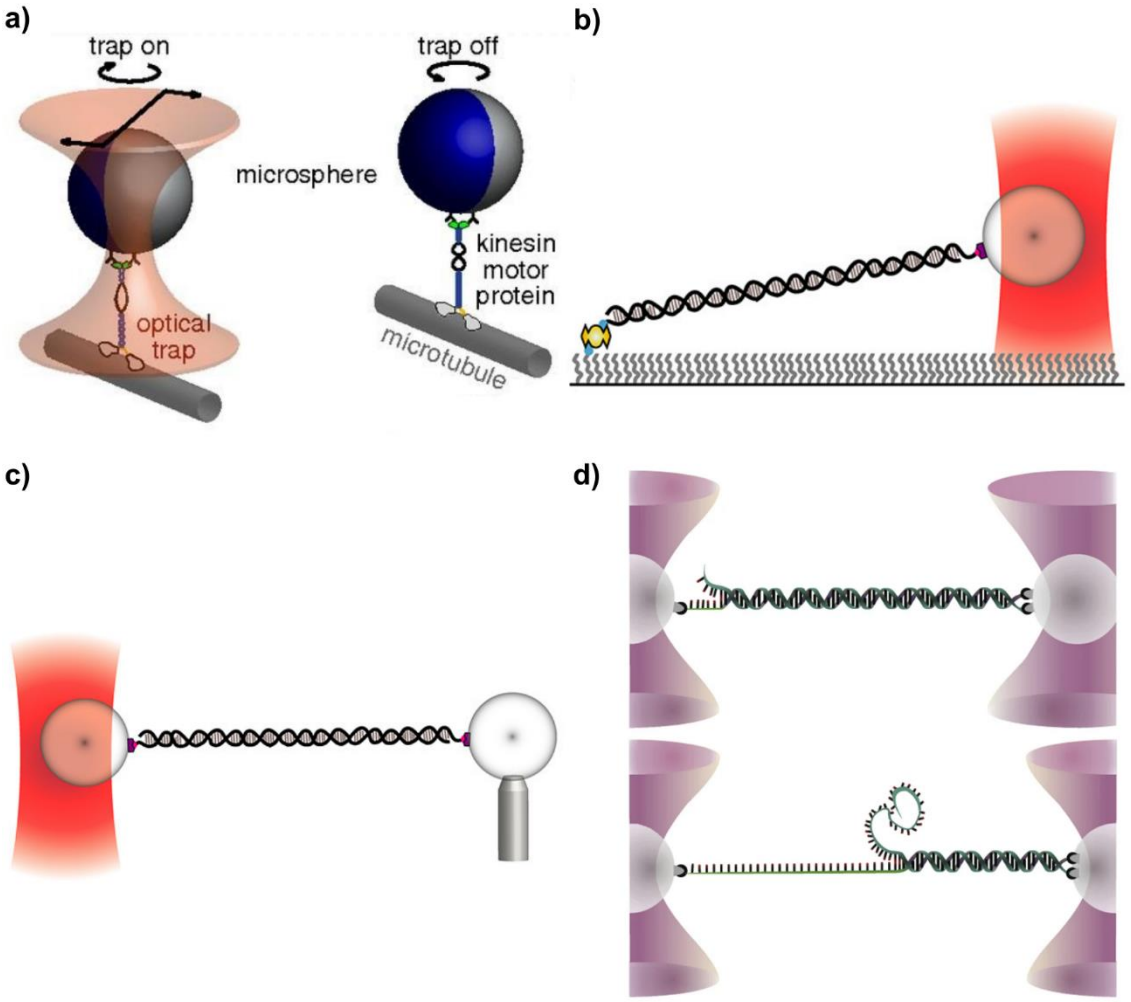

Figure 2.2 Schematic illustrations of standard optical tweezers configurations for single-molecule force spectroscopy measurements. **a)** Liquid crystalline microspheres with kinesin motor proteins attached to their surface from one end and to a microtubule from the other. The torsional stiffness of the molecule was observed by controlling the rotation of the bead through the laser beam. Adapted from [18]. Single trap configuration where a molecule's end is attached to a dielectric bead held by the light beam and its other is bound **b)** either on a passivated microscope glass slide or **c)** attached to another bead held by a glass micropipette. Reproduced from [20]. **d)** Dual trap configuration where two separate dielectric beads are held by two laser beams, respectively, and a molecule is attached between them. Reproduced from [22].

Starting with the elastic properties of DNA, the extension of individual single- or double-stranded DNA molecules (ssDNA, dsDNA respectively) has led to the recording of force-extension curves which provide information about the nucleic acid's mechanical dynamics. Smith et al. (1996) [21] stretched ssDNA and dsDNA molecules with a force magnitude of 800 pN and 65 pN, respectively, and measured their lengths at their maximum extension. In 2011, Gross et al. [22] attempted to explain in greater detail how a DNA molecule responds to mechanical stress. By using a dual-trap configuration and attaching three ends of a dsDNA molecule between two dielectric beads, they found that the molecule started unpeeling upon extension as shown in Figure 2.2d. Recently, researchers from the same group [23] managed to generate negatively supercoiled DNA molecules with the standard dual-trap optical tweezers. This assay offered rapid and controllable measurements and coupled force spectroscopy with fluorescence imaging, as well as quick buffer exchange.

An additional deeply investigated molecule is RNA polymerase, an enzyme that takes part in the transcription of DNA by unbinding its double-strand to synthesise RNA. The dual-trap optical tweezers configuration has been widely employed for studying DNA-RNA interactions. Shaevitz et al. (2003) [24] investigated transcriptional elongation by attaching a DNA and RNA molecule to separate beads which were optically manipulated. The entire bead-molecules-bead complex was suspended in solution which reduced noise and drift originated from the instruments. Following the same dual-trap system, Hodges et al. (2009) [25] monitored individual RNA polymerase molecules during DNA transcription and proved that RNA is continuously rectifying nucleosomal fluctuations. In another study based on the same optical trapping configuration, Fazal et al. (2015) [26] observed the initiation stages of RNA polymerase II transcription along a DNA molecule in real-time.

Besides the applications mentioned so far, different configurations for single-molecule optical trapping have been suggested over the past decade. It is worth clarifying that the following methods have not been utilised for force spectroscopy measurements yet but could succeed in the near future. For instance, Roxworthy et al. (2012) [27] developed an alternative single-molecule optical trapping technique based on plasmonic bowtie-shaped nano-antenna arrays. These nanostructures operate with low power input offering 20 times higher efficiency than the optical tweezers configurations shown in Figure 2.2 and achieved trapping, sorting and manipulation of individual sub-micrometre particles (polystyrene beads). Moreover, Pang and Gordon (2012) [28] demonstrated optical trapping of individual bovine serum albumin (BSA) molecules with a hydrodynamic radius of 3.4 nm by using a dual-nanohole in a gold (Au) film. The strong applied forces achieved stable trapping and led such individual proteins to unfolding, but

without offering specificity. Lastly, Lin et al. (2018) [29] presented opto-thermoelectric nanotweezers which benefited from requiring low power to operate and had simple implementation. This type of tweezers relied on optically heating thermo-plasmonic substrates for trapping and manipulating metal nanoparticles.

All the studies discussed in this section have provided significant breakthroughs in single-molecule force spectroscopy but, at the same time, they have been conducted in highly controlled environments. It still remains a challenge to bridge the gap between in vitro and in vivo measurements with a few exceptions. Blehm et al. (2013) [30] managed to trap cytoskeletal cargos after calibrating the optical trap in the cytoplasm, while Goldman et al. (2015) [31] demonstrated unblocking of a clogged channel by optically pulling the immobile protein chain. However, the main obstacle is the inability to selectively trap individual entities inside living cells, even when beads are in the intracellular environment, because most organelles have slightly higher refractive index than the cytoplasm. Other limitations for the optical tweezers are their low throughput, temporal and spatial resolution as well as the manipulation speed. Instrumental noise, slow response of the stage compared to changes in the measured signal or beads position due to hydrodynamic drag flow are some of the factors that could be optimised [12].

2.2.2 Magnetic tweezers

Another well-established tool for single-molecule force spectroscopy are the magnetic tweezers. This type of tweezers benefits from its low cost, simple instrumentation and operation, as well as their ability to manipulate a broad range of biological molecules [1]. Their basic working principle relies on a magnetic field produced between a pair of magnets which induces magnetic momentum and hence a force on individual magnetic beads. As illustrated in Figure 2.3, the most common instrumentation consists of two permanent magnets (or electromagnets) located on top of the sample under investigation which is bound between a magnetic bead, usually paramagnetic or superparamagnetic, and a flow chamber fixed on top of an inverted microscope [32]. The beads, which can be trapped even outside the flow chamber, are usually in the micrometre scale and the forces applied to them can vary from tens of femtonewtons to hundreds piconewtons.

The magnetic field gradient changes over relatively large distances (~1 mm) so the applied force on the tethered bead is considered constant relative to its movement along much shorter length scales. This allows magnetic tweezers to operate without complicated active force feedback as in the case of optical tweezers. Furthermore, by

adjusting the position of the external magnets or by rotating them, the magnetic bead responds to such changes accordingly and as a result, the attached molecule can either be stretched or coiled [2], [4]. In 1950, Crick and Hughes [33] were the first ever to move magnetic particles inside the cytoplasm of cells by using externally applied magnetic fields. Four decades later, Smith et al. (1992) [34] demonstrated stretching of individual DNA molecules with magnetic tweezers. The sample was bound between a magnetic microbead and the surface of a microscope glass slide. Following this technique, Strick et al. (1996) [35] managed to coil single DNA molecules by rotating the magnetic beads, as schematically displayed in Figure 2.4a.

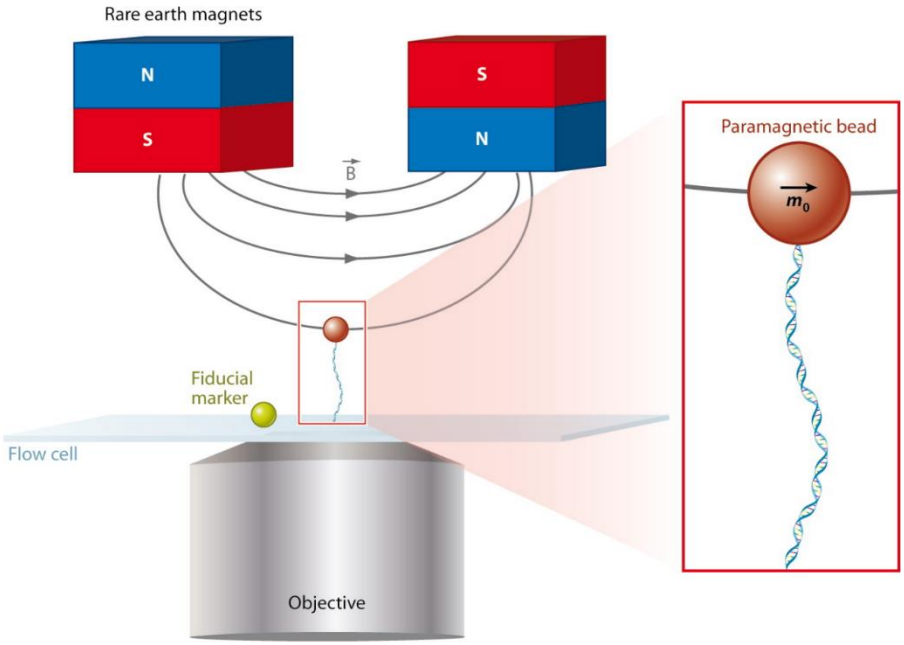

Figure 2.3 Schematic illustration of most widely used magnetic tweezers configuration for single-molecule force spectroscopy. A pair of permanent magnets located on top of the sample under investigation which is bound between a magnetic bead, usually paramagnetic or superparamagnetic, and a flow chamber fixed on top of an inverted microscope. The field $\vec{B}$ produced between the magnets induces a moment $\vec{m}_0$ and hence a force on the bead, analogous to its gradient. A fluorescent marker is attached on the flow chamber for calibrating vertical displacements of the bead. Note that N and S are abbreviations for magnetic north and south pole, respectively. Reproduced from [32].

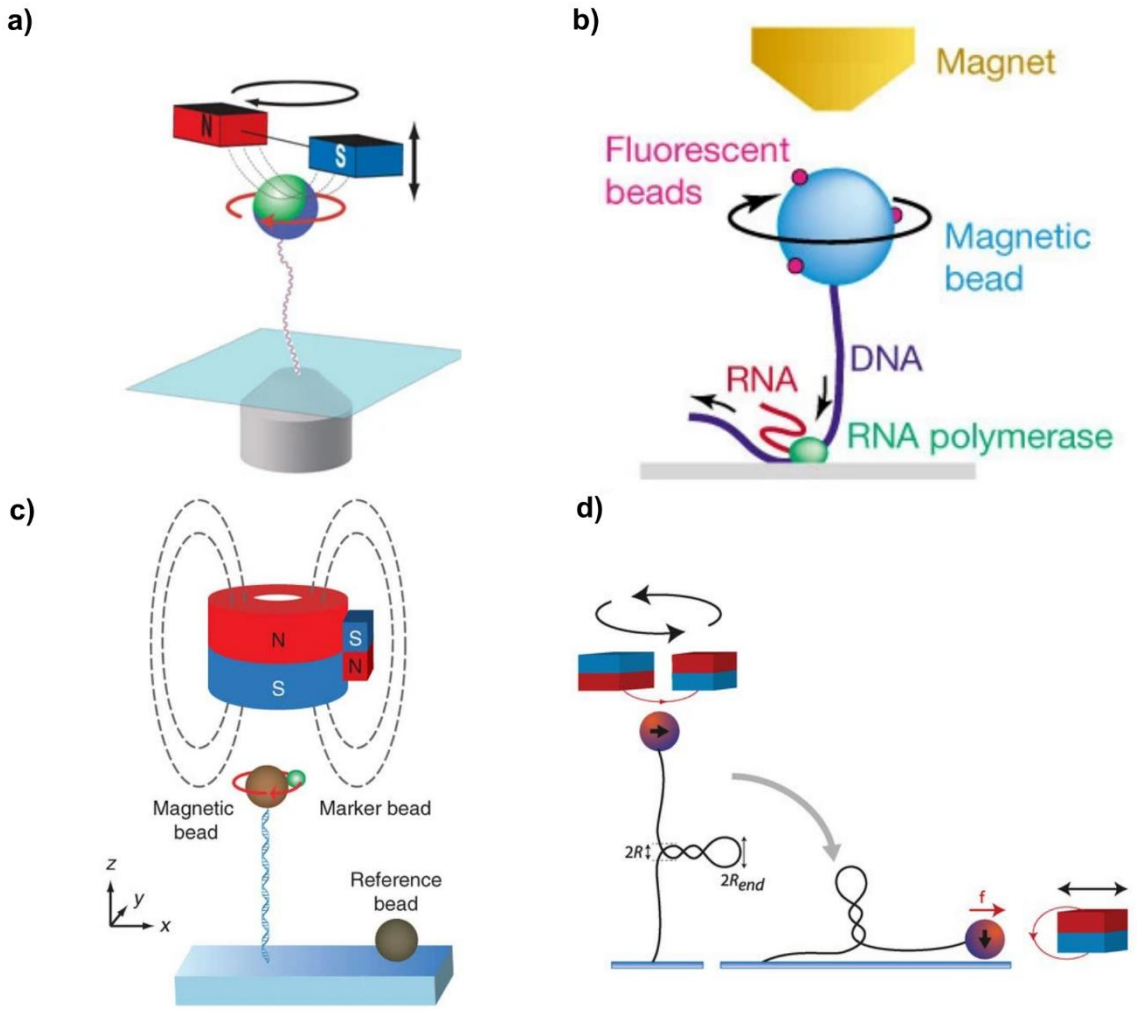

Figure 2.4 Schematic illustration of magnetic tweezers configurations for single-molecule torque measurements. **a)** A pair of permanent magnets located on top of the sample under investigation which is bound between a magnetic bead and a flow chamber fixed on top of an inverted microscope. By adjusting the position of the magnets or by rotating them, the magnetic bead responds to such changes accordingly and as a result, the attached molecule can either be stretched or rotated. Reproduced by [2]. **b)** Single magnet aligned with the bead-molecule system to investigate its torque during transcription by an RNA polymerase molecule which was fixed on the glass coverslip. Reproduced by [36]. **c)** Cylindrical permanent magnet for applying forces, together with a much smaller magnet bound on its side at opposite orientation giving rise to desired torques on a tethered molecule between a magnetic bead and the surface of a glass slide. Reproduced by [38]. **d)** Supercoiled individual DNA molecules by rotating a pair of magnets which were then attracted towards the focal plane, parallel to the microscope glass cover, by an additional magnet positioned on the side. Reproduced by [39].

Forces causing rotation act as regulators in cellular processes like transcription, replication, recombination, and supercoiling of DNA [1]. As reported in the previous paragraph, magnetic tweezers are able to apply and probe torques to individual molecules (Figure 2.4a). However, direct torque measurement is limited with their

traditional design since the strong field gradient experienced by the bead dominates any torque originated by the tethered molecule [32]. Multiple approaches have been reported to tackle this limitation. For instance, Harada et al. (2001) [36], used a single magnet that was aligned with the bead-molecule system to investigate its torque during transcription by an RNA polymerase molecule which was fixed on the glass coverslip. This configuration, presented in Figure 2.4b, generates magnetic fields that induce extremely low rotation to the bead, lower than the expected torque magnitude caused by the molecule.

Moreover, Gore et al. (2006) [37] attached a non-magnetic fluorescent bead at the side of a DNA molecule which was tethered between a magnetic bead and the coverslip surface. Then, by stretching the molecule along the vertical axis, they tracked optically the fluorescent bead and observed maximum twist of the double helix at ~30 pN. Lipfert et al. (2010) [38] employed a cylindrical permanent magnet for applying forces, coupled with a much smaller magnet bound on its side at opposite orientation which gave rise to desired torques (Figure 2.4c). This approach enabled the generation and measurement of both forces and torques directly from single biomolecules. Lastly, in an attempt to visualise the dynamics of twisted loops along the DNA double helix, the so-called plectonemes, van Loenhout et al. (2012) [39] supercoiled individual DNA molecules by rotating a pair of magnets which were then attracted towards the focal plane, parallel to the microscope glass cover, by an additional magnet positioned on the side (Figure 2.4d).

Single-molecule force spectroscopy methods mainly lack high experimental throughput but advances in the imaging tools have led to magnetic tweezers being used to study in parallel a population of single molecules, under the same conditions [32]. As previously mentioned, magnetic tweezers generate fields that can be considered uniform for approximately 1 mm and thus they can trap numerous biological molecules, such as ATP synthases (~ 10 nm) or DNA molecules (long axis ~ 15 μm) [1]. A novel method of high throughput magnetic traps was introduced by De Vlaminck et al. [32] who managed to track systematically 450 targeted beads each bound to single DNA molecules and acquired data for the dynamics of almost 80% of the samples.

Nevertheless, high-throughput magnetic tweezers usually lack an accurate force calibration and the acquired quantitative data is limited to small forces mainly due to the camera open shutter time. Ostrofet et al. [40] demonstrated that by reducing this time to 25%, the position of the bead was recorded accurately (relative error ~10%) at low image acquisition frequency, and the force was calibrated with no need for corrections. Furthermore, optical and magnetic tweezers have been combined in an attempt to decouple the generation of force from its measurement [1]. In 2013, van Loenhout et al.

[41] created this type of trap to define the position of proteins bound on DNA molecules. Lastly, Zhou et al. (2015) [42] demonstrated a magneto-optical tweezer which improved temporal resolution for monitoring molecules undergoing rotation for different applied frequencies and noted that their design could be improved by tuning the amount of heat the magnetised beads absorb.

Further design alterations of the magnetic tweezers standard configurations have allowed three-dimensional control of the molecules under investigation. In 2002, Gosse and Croquette [43] introduced a system of six electromagnets with their poles on top of a bead which was rotated across the 3D plane. The forces experienced by the tethered molecule ranged from 50 fN to 20 pN. Following a similar approach, Chiou et al. [44] fabricated lithographic magnetic nanotweezers on a flow cell. Six micro-electromagnets were embedded hexagonally on the same plane allowing linear and angular manipulation of individual DNA molecules. The bead's vertical displacement was controlled by a circular ring at the centre. This combination generated large field gradients when compared to traditional designs due to the proximity of the poles. Later, Schuerle et al. (2013) [45] presented the "MiniMag", a system of 8 electromagnets capable of generating oscillating magnetic fields and controlling the position of entities in 3D for both upright and inverted microscopy with zero restrictions in the rotational plane.

Nanofabricated magnetic tweezers use small coils which have lower inductance and lead to faster experiments [1]. This design handled very smartly the generation of Joule heating. From one hand, the coil was attached to the flow cell where a big part of resistive heating was deposited without affecting the magnetic field. From the other hand though, this smaller coil and the proximity of the magnets produced a significant amount of Joule heating which could be controlled only by setting a maximum value for the applied currents so that they would not affect the magnetic field. Gonzalez et al. (2015) [46] showed how custom-designed magnetic tweezers composed of Helmholtz coils and lithographically nanofabricated "islands" provided accurate control for the positioning and alignment of magnetic particles and bacteria. A common drawback of all these designs is their fixed position regarding the studied molecules, hence the movement of the flow cell in relation to the microscope stage is impossible because the magnetic field lines need to be focused on the centre of the objective focal point [1].

In general, single-molecule force spectroscopy with magnetic tweezers is a versatile and powerful technique but with several limitations. To start with, entities interacting with magnetic fields are difficult to manipulate. Although there are not many magnetic biomolecules, a small number of proteins with such properties that also can associate with metal clusters has been reported [1], [2], [4]. In addition, the large geometry of the magnetic poles and the fact that they need to be positioned near the sample makes their

integration with microscopes rather complicated. This was one of the reasons magnetic and optical tweezers were combined. As for most techniques, little progress has been reported on selective single-molecule manipulation inside living cells, even when beads are in the intracellular environment. Finally, three-dimensional translation of individual entities under trapping conditions still remains a great challenge and has been achieved only with highly sophisticated configurations [2], [4].

2.2.3 Atomic force microscopy (AFM)

Atomic force microscopy (AFM) is a powerful tool which has also been extensively used for single-molecule force spectroscopy [4]. Its mechanism is based on a cantilever with a very sharp tip that approaches, and then binds to the target molecule which is immobilised on a surface [47]. The sample platform is fixed on a piezoelectric mechanism which can be controlled with sub-Angstrom precision in all three dimensions (Figure 2.5a). Once this stage moves and the separation distance between the surface and the cantilever tip increases, the tethered molecule between them stretches under tension leading to the displacement of the cantilever [1], [47]. Consequently, the reflected laser beam off the cantilever's backside is displaced while a photodetector senses this spatial shift and eventually quantifies both the extension and the force applied on the tethered molecule. It is worth mentioning that this nanometre-sized tip can either attract or repel individual molecules through Van der Waals and Coulombic forces, respectively [1], [2].

AFM offers the ability to perform single-molecule force measurements with piconewton resolution under physiological conditions [47]. However, placing the tip (stage III, Figure 2.5b) into crowded systems can sometimes lead to random binding or to the adsorption of unwanted contaminants. As a result, it can be hard to distinguish whether the AFM tip has attached to the targeted molecule, the desired location or to multiple sites on that entity. To eliminate non-specific interactions, chemical modification or attachment of synthetic handles (i.e., micrometre-sized beads) to the cantilever's tip is required. The target molecule is tethered between the handle and stage, as previously reported for optical and magnetic tweezers [4].

In general, cantilevers are manufactured in different shapes and coatings which affect their stiffness and hence spring constants [2]. To acquire precise force measurements by AFM, its cantilever needs to be properly calibrated before the start of an experiment. The most widely used calibration techniques are based on comparing it with a reference cantilever of a fixed stiffness value, using thermal vibrations, adding known particle masses or measuring its resonant frequency [1], [2]. Nevertheless, for single-molecule

force spectroscopy experiments the cantilever stiffness needs to be relatively low in order to probe piconewton forces. When its spring constant is reduced though, the sensitivity is limited because the tip becomes more susceptible to thermal noise and hydrodynamic drag. However, appropriate changes in the cantilever's shape and dimensions diminish such effects [48].

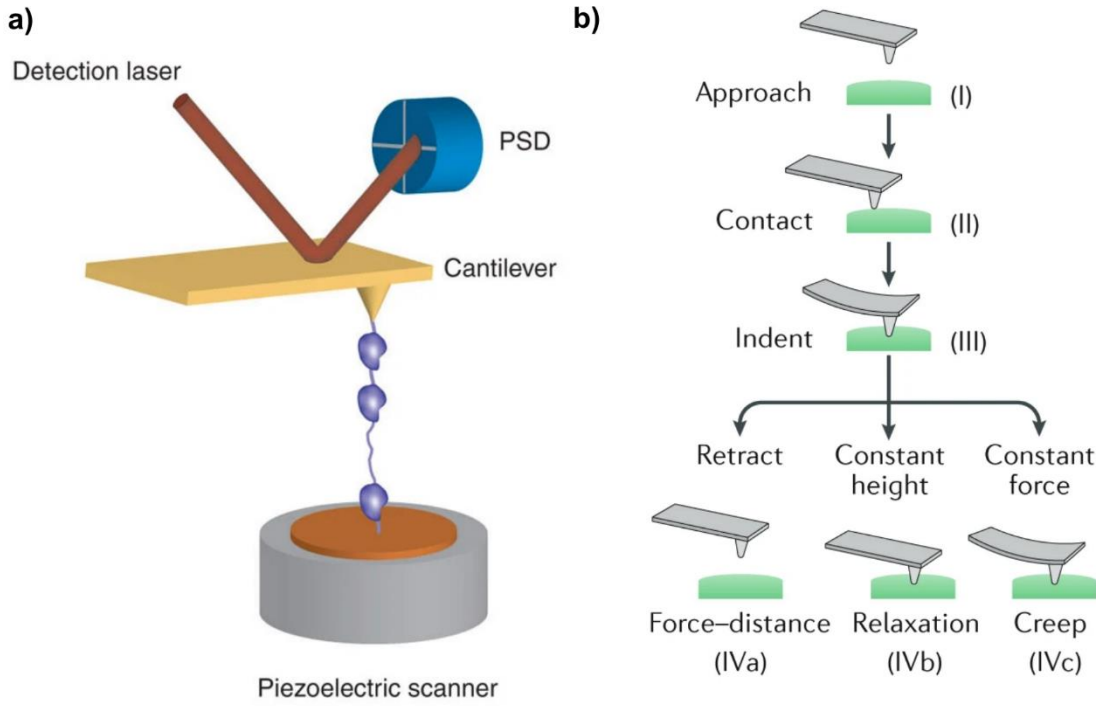

Figure 2.5 Single-molecule force spectroscopy with AFM. **a)** Schematic illustrations of the atomic force microscope which is composed of a cantilever and a nanometre-sized sharp tip (yellow) positioned above a piezoelectric scanning stage (grey). A molecule (purple) is attached between the cantilever's tip and the stage surface (bronze). Displacement of the latter induces a force on the molecule which deflects the cantilever and shifts the position of the laser beam (red), reflected off the cantilever's back, on a photodetector (PSD). Reproduced from [2]. **b)** Schematic representation of the indentation stages of an atomic microscope probe (cantilever-tip) to a biological system. The cantilever approaches the sample surface (I), creates contact (II) and indents (III) to probe mechanical responses. Then, single-molecule force probing can be achieved by retracting it (IVa), keeping it a constant height (IVb) or applying a constant force (IVc) to the trapped entity. Reproduced from [47].

Initial single-molecule studies with AFM were based on applying different force magnitudes to observe their dynamics at sub-nanometre resolution [47]. For example, Rief et al. (1997) [49] performed vertical stretching of dextran filaments under different loads to understand the mechanical properties and conformational changes of these polymers with Angstrom precision. In 2003, Marshall et al. [50] explored the influence of applied tensile forces on the lifetime of the bond between a selectin and ligand molecule. These entities mediate the interaction of leukocytes with vascular membranes after the

occurrence of an infection or tissue injury. By using AFM, the authors showed that an increase in shear stress by the cellular wall led to an initial increase and then decrease in the selectin-ligand bond lifetime. Fernandez and Li (2004) [51] then distinguished several folding stages of a small protein after maximum extension where they measured its entire length.

More recent approaches probe the mechanical properties of individual biomolecules in highly sophisticated ways [47]. For instance, changes in the cantilever geometry, as well as in its flexural and torsional properties allowed the monitoring of protein flexibility by applying extensions across its domain with a microsecond temporal resolution under physiologically relevant conditions [52]. Rico et al. (2011) [53] optimised the indentation mode of AFM to study the degree of deformation on individual membrane proteins in their native folded state and concluded that their crystal structure contributed significantly to the mechanical stability of the molecule. Bimodal AFM is an alternative method to monitor the dynamics of water-soluble or membrane proteins. By exciting two separate modes of the cantilever and modulating the applied frequency the structural topography and flexibility of single proteins can be mapped simultaneously [54]. This mode allows measurements under very low applied loads, for the standards of AFM (30 – 40 pN).

Other types of biomolecules that have been investigated by AFM are microtubules, DNA origami and lipid vesicles [47]. In 2003, de Pablo et al. [55] proved that the elasticity of microtubules has a linear response at small loads and a non-linear response at higher tension which can lead to structural collapse. Moreover, the axial compressibility of individual DNA tetrahedra with nanometre dimensions, a type of DNA origami, was assessed under high forces applied by the AFM cantilever with permanent deformation occurring between 70 and 200 pN [56]. Lastly, Vorselen et al. (2017) [57] defined the degree of lamellarity for individual small multilamellar lipid vesicles by penetrating up to 5 lipid bilayers with AFM nanoindentations. They also found that these vesicles have a higher stiffness constant compared to small unilamellar vesicles.

The studies mentioned above are a small fraction of the application of AFM to probe the mechanical properties of individual molecules, such as proteins, nucleic acids, lipid membranes and cells [47]. However, further developments in single-molecule force spectroscopy with AFM need to be introduced to overcome some of its current limitations. Measuring forces in the sub-piconewton range, acquiring measurements at smaller timescales and conducting in vivo experiments are three main examples. Changes in the cantilever geometry and material properties have already contributed towards this direction but its combination with multimethodological approaches, such as integration with optical or magnetic tweezers, are expected to promote force measurements inside living cells [4].

2.2.4 Acoustic tweezers

So far, this review has focused on the most widely established single-molecule force spectroscopy methods which are based on optical, magnetic and mechanical forces. Another platform that has found application in studying the physical properties of single biological entities are the acoustic tweezers. Their working principle relies on acoustic waves that generate pressure gradients to trap individual molecules [5]. These acoustic or sound waves propagate in parallel to the travelling direction of bioparticles and oscillate between their pressure nodes, peak amplitudes at maximum pressure regions, and pressure antinodes, lowest amplitudes at minimum pressure regions. So, the molecules will be forced to move towards either nodes or antinodes based on their physical properties [1].

Although they are classified into three major categories, the standing-wave, travelling-wave and acoustic streaming tweezers, in this subsection only standing-wave acoustic tweezers are discussed [5]. To form such a wave, two interdigital transducers (IDTs), positioned opposite to each other, each generate a travelling wave which end up being superimposed. The nodes and antinodes positions can be controlled by adjusting the wavelength and phase of these two oscillations. To achieve three-dimensional manipulation with acoustic tweezers, two pairs of such sound wave transducers are required (Figure 2.6a). Trapping individual molecules along the vertical axis results from the generation of fluid flow at nodes/antinodes which counteracts gravitational, buoyancy or viscous drag forces [1]. Guo et al. (2016) [58] demonstrated 3D trapping of microparticles and cells with this instrumentation. By tuning the phase and amplitude of acoustic waves they managed to lift, translate and position single cells and cellular assemblies in a precise and non-invasive way. Figure 2.6b displays their numerical simulation for modelling the acoustic field near a trapped particle created by superimposing two orthogonal standing waves.

Acoustic waves can be generated by kilohertz to megahertz frequencies which makes acoustic tweezers versatile, as they can trap particles within a size range from 100 nm to 1 cm [5]. In 2016, Baresch et al. [59] utilised a single acoustical beam to trap elastic particles in three dimensions. The forces experienced by beads, with a diameter smaller than 1 mm, were higher than 1 μN. The ability to move manually the beam focus in combination with the translation of the stage allowed precise manipulation of particles in damage free conditions, as the power used was ~50 W/cm^2. Chen et al. (2017) [60] fabricated single-beam acoustic tweezers based on an ultrasonic transducer that could be tuned selectively to manipulate individual microparticles. Acoustic tweezers based on single beam transducer have also been used to study calcium signalling inside living

cells [61]. Hwang et al. (2015) [61] monitored the propagation of calcium inside breast cancer cells by manipulating fibronectin-coated microbeads.

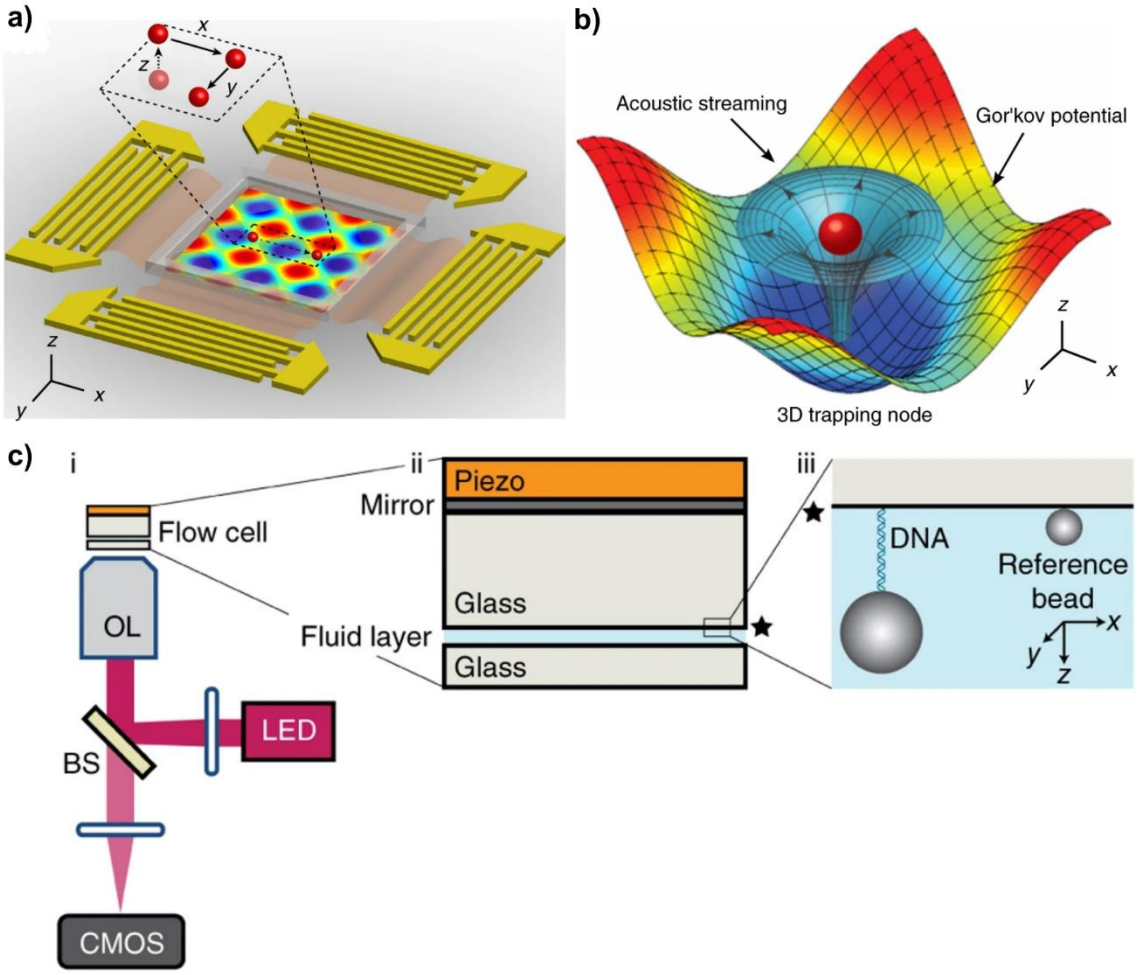

Figure 2.6 Single-molecule force spectroscopy with acoustic tweezers. **a)** Schematic illustration of two pairs of interdigital transducers (IDTs), positioned opposite to each other, generating planar acoustic standing waves. The nodes (blue) and antinodes (red) spots can be controlled by adjusting the wavelength and phase of these two oscillations. The inset shows a path across the xyz plane for a trapped particle. Reproduced from [58]. **b)** Numerical 3D simulation showing a model of the acoustic field distribution around a single trapped particle for the waves generated in a). Reproduced from [58]. **c, i)** Schematic of the acoustic tweezers integrated in a flow chamber on top of an inverted microscope. **c, ii)** The flow chamber is fixed between two glass slides and on top of the thicker one an acoustic piezo stage, sputtered with aluminium, is generating acoustic waves. **c, iii)** A single DNA molecule tethered between the upper glass surface and a micrometre-sized polystyrene bead is extended or compressed due to the presence of acoustic waves. The reference bead is attached to the upper glass for calibrating the z-displacement of the tethered bead. Reproduced from [62].

In general, acoustic trapping, handling, and sorting of single cells have proved to be a well-founded technique [4]. It has not been too long ago though since acoustic tweezers were utilised for single-molecule manipulation [5]. In 2015, Sitters et al. [62] developed

an acoustic force spectroscopy device capable of measuring and applying forces, from sub- to hundreds piconewtons, on multiple individual molecules at the same time with a temporal resolution lower than a millisecond. The right inset (iii) of Figure 2.6c illustrates a DNA molecule tethered between a polystyrene microsphere and the glass coverslip. An acoustic standing wave was formed inside the fluidic chamber and pushed the bead towards the nodes/antinodes which led to stretching of the bound entity. Then, by comparing the bead's displacement with the applied force magnitude, information regarding structural and functional properties of the tethered DNA were obtained. Due to multiple nodes and antinodes in the chamber, high throughput was also achieved while generated heat was maintained in much lower rates compared to the case of optical tweezers [62].

A year later, further reconfigurations of this acoustic tweezers design allowed better imaging resolution for optical tracking of beads and the application of forces up to 350 pN. The acoustic field gradient was also optimised by using different frequencies simultaneously [63]. More recent developments seem to promise higher control and flexibility in trapping single particles. In 2019, Marzo and Drinkwater [64] introduced holographic acoustic tweezers where a system of multiple sound emitters achieved high throughput single-particle manipulation in air medium. Up to 25 millimetre-sized spherical particles were lifted and translated in 2D and 3D at the same time. The authors developed an algorithm which could form different trap configurations by rearranging the transducers. Bogatyr et al. (2022) [65] presented an acoustophoresis-based technique to quantify the size, compressibility and density of multiple individual entities in a non-uniform population. The acoustic force exerted on single cells and giant unilamellar vesicles (GUVs) was measured by tracking their orbits in relation to Stokes drag and buoyant forces.

In conclusion, acoustic tweezers are an additional versatile technique in the single-molecule force spectroscopy toolbox which addresses efficiently some of the limitations of other methods. Individual particles can be manipulated with a spatial resolution ranging from hundreds of nanometres to centimetres because acoustic waves with kHz to MHz frequencies can easily be applied [5]. They are considered a biocompatible option since their power is similar to the one used for ultrasonic imaging and are capable of handling both synthetic and living cells. Moreover, acoustic single-molecule manipulation does not depend on the optical, magnetic or electrical properties of an entity and does not require specific media as they can be used in air or liquid. They can also manipulate both fluids and particles in fluids or select both individual molecules and larger populations [1], [4].

Despite all these advantages, acoustic tweezers are several steps behind the level of the most established single-molecule force spectroscopy tools (optical, magnetic tweezers and AFM). Their main disadvantage is limited spatial resolution. Acoustic tweezers do not offer the same precision with optical tweezers as the former operate at much lower frequencies [5]. Besides their contribution on cell manipulation and sorting, the vast majority of studies is restricted only to in vitro experiments [4]. However, their non-invasive deep penetration attribute makes them a strong candidate for intracellular force probing once technological developments are in place.

2.2.5 Electrical tweezers

There are a broad range of biophysical techniques that rely on electrical forces for single-molecule manipulation either in the form of electrostatic traps or electrokinetic tweezers [1]. The first type is based on Coulombic attraction or repulsion between two charged surfaces while the second one depends on the generation of electric fields, between at least two electrodes to trap and manipulate individual entities with a size that can range from few nanometres up to millimetres [5]. An extensive analysis on the differences between electrophoresis and dielectrophoresis is provided in Section 2.4. Key parameters in this single-molecule force spectroscopy method are the electrical properties of the entities, such as their surface charge or polarisability, as well as the surrounding medium's. Since this project is focused on dielectrophoretic tweezers, this subsection is mainly focused on reporting studies based on this technique with a few noteworthy exceptions.

Dielectrophoretic tweezers are based on the generation of inhomogeneous electric fields through the application of an electric potential, mainly alternating current (AC) voltages, between two or more electrodes [6]. Depending on the dielectric properties of polarisable biological molecules and their surrounding medium, the gradient of these non-uniform electric fields can deliver an attractive or repulsive force on such entities by tuning the frequency of the applied voltage. Significant attributes of dielectrophoretic manipulation include the instrumentation simplicity, electrodes' design flexibility and its ability to trap a wide range of particle sizes without the need of tethering on handles [7]. Moreover, biomolecules are found in a variety of shapes, either spherical or ellipsoidal with or without additional layers surrounding their cores. This complexity and heterogeneity are beneficial for trapping only the analyte of interest from a mixed population. However, at the same time, their sophisticated dielectric properties in combination with the intricate

cell environment are not easily described with theoretical models which makes the elucidation of dielectrophoresis phenomena particularly complex [6].

Most recent advancements have achieved highly controllable manipulation of individual biomolecules with electrical forces but without the capability of determining the force magnitude experienced by each molecule. In 2005, Hölzel et al. [66] trapped and released single proteins on demand between the sharp tips of two gold electrodes on a silicon substrate. The electric field gradient, hence, the forces applied on the molecules, were tuned by changing the electrode separation (tens to hundreds nanometres) and exceeded thermal diffusion which was expected in the sub-femtonewton range. Brownian motion of diffusing molecules in solution has been harnessed by electrokinetic traps of similar design which managed to hold and manipulate single proteins, viral particles and lipid vesicles without the need for tethering [67]. Moreover, Giraud et al. (2011) [68] were the first ones to demonstrate attraction and repulsion of individual RNA molecules via interdigitated microelectrodes (IDEs) and total internal reflection fluorescence microscopy (TIRF) without knowing their dielectric properties in advance.

Barik et al. (2016) [69] pushed the design specifications of IDEs to the nanometre scale, as they fabricated gold electrodes with smaller than 10 nm gap between them. The configuration shown in Figure 2.7a allowed trapping of polystyrene nanoparticles, quantum dots and nanodiamond particles across a millimetre-sized zone by applying extremely low voltages (~200 mV) which generated DEP forces of approximately 200 fN. This diminishes the presence of unwanted heat or bubble formation caused by electrochemical reactions. In the past, the challenges linked with application of high potentials in solution were major concerns for dielectrophoretic single-molecule manipulation. A year later, Barik et al. (2017) [70] optimised further their device by integrating a graphene layer and used its edges as trapping areas for nanoparticles and biological molecules. In more detail, an 8 nm insulating gap separated palladium electrodes with the graphene monolayer where gold electrodes were making contact to complete the circuit (Figure 2.7b). By applying a bias of approximately 400 mV, four trapping locations were created with forces recorded 10 times higher than the one generated using conventional metal electrodes. Eventually, the combination of such high forces and low voltages could overcome a major limitation for graphene sensors which is the diffusion-limited transport of biomolecules.

An additional well-established platform for single-molecule detection and manipulation is solid-state nanopores and especially glass nanopipettes. Over the past two decades, this tool has improved molecular throughput, sensitivity and detection resolution, as well as contributed to measuring single-molecule kinetics and achieving single-cell manipulation [71]. Its most common configuration consists of an elongated glass

truncated cone, with a pore opening at its tip that can vary from a few nanometres to several micrometres, filled with and immersed in an aqueous electrolyte including the molecules of interest. Single-molecule manipulation is achieved by applying a bias between one electrode in the bath solution and another in the back of the nanopipette. Depending on the voltage polarity, molecules will translocate either from the bath solution towards inside the pore, or the other way around. From a collaborative study between Ivanov's and Dekker's groups [72], an innovative method of controlling single-molecule transportation between a dual pore nanopipette was reported. The two nanopores were separated by a 20 nm glass septum and individual DNA molecules were either bridged or translocated between them with almost complete efficiency, improved temporal resolution and non-compromised signal quality.

An interesting way to utilise single-molecule dielectrophoretic trapping and detection was suggested by Freedman et al. (2016) [73], [74] who used gold-coated nanopipettes immersed in an aqueous electrolyte. In the first citation [73], as illustrated in Figure 2.7c, an AC voltage was applied to the outer gold-coated surface (5 nm thickness) at the nanopipette tip (25 nm diameter) for capturing 10 kbp dsDNA molecules in electrolyte solution while a 10 V DC voltage between the electrodes inside the nanopipette pore and external solution was used for the detection of molecules passing through the tip opening. Single molecules were detected at a concentration of 5 fM with a rate of 52.5 events per second which improved the detection limit of existing platforms at that time by 1000 times while preserved its productive output. However, it was observed that DNA molecules were subjected to two forces at higher voltages, the dielectrophoretic force and the electrothermal flow which was generated due to temperature non-uniformity of the medium around the nanopipette.

Furthermore, Freedman et al. (2013) [74] used these gold-coated nanopipettes to dielectrophoretically form surface-enhanced Raman spectroscopy (SERS) substrates. Gold nanoparticles in the external solution were attracted and concentrated around the tip aperture where they got self-assembled and then were detected through SERS. The dielectrophoretic force acting on the nanoparticles was measured by recording their trajectories through fluorescent imaging and was ranging from approximately 50 to 300 fN, depending on the applied frequency of the AC signal. In 2019, Nadappuram et al. [10] reported single-molecule trapping and extraction from living cells with dielectrophoretic nanoscale tweezers and without affecting the cells' functional integrity. These nanotweezers were composed of dual-barrel quartz glass nanopipettes filled internally with pyrolytic carbon, forming two closely spaced nanoelectrodes separated by 10 – 20 nm glass at the tip of the nanopipette. These nanoelectrodes enabled the accurate manipulation, trapping, releasing and extracting of nucleic acids and organelles

from solutions with a concentration as low as 100 fM driven by one of the strongest dielectrophoretic forces ever reported, based on the currently available literature, which arose at the tip from the application of ~3 V.

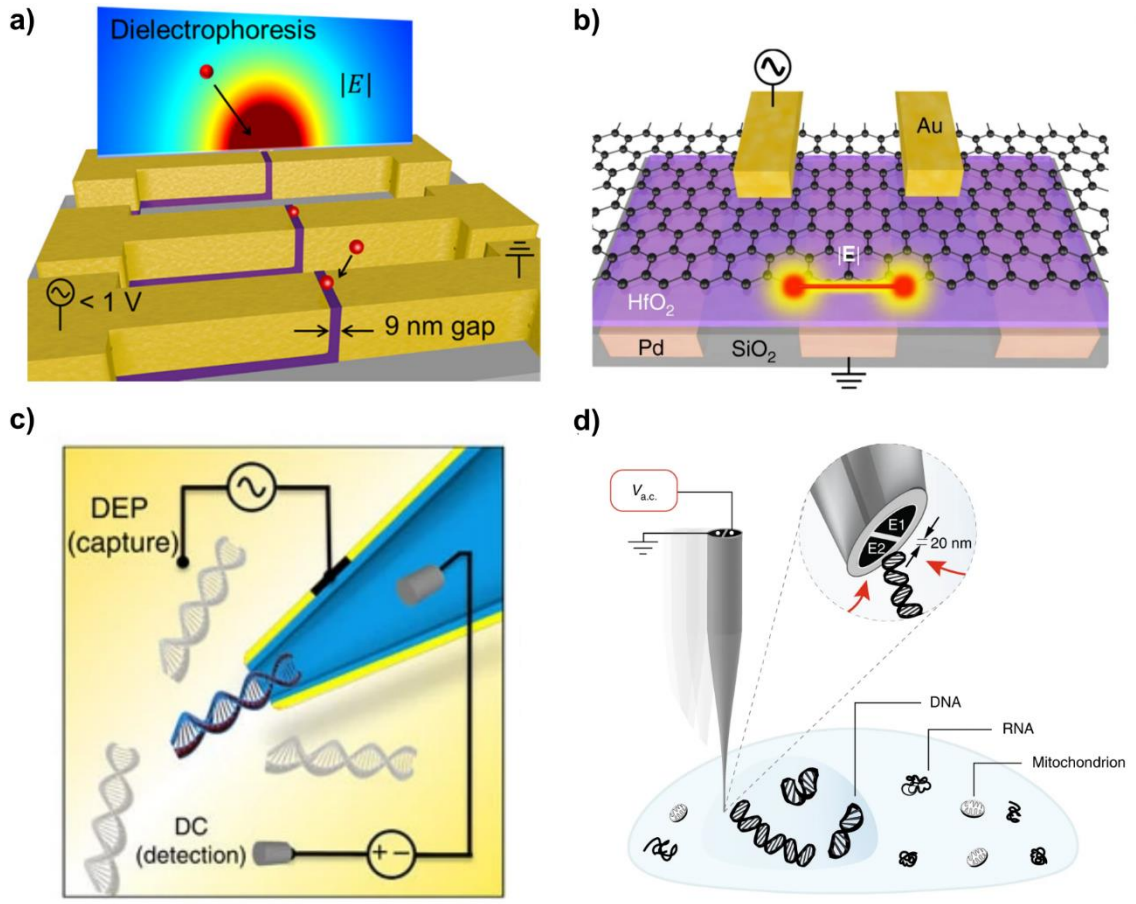

Figure 2.7 Schematic illustrations of dielectrophoretic platforms for single-molecule manipulation. **a)** Interdigitated gold microelectrodes (IDEs) with a 9 nm insulating separation gap where individual nanoparticles (red spheres) were trapped upon application of low peak amplitude AC voltages (~200 mV, 100 kHz – 10 MHz) between each pair (yellow). The colour map shows the electric field distribution away from these gaps. Reproduced from [69]. **b)** Palladium electrodes (beige) were separated by an 8 nm insulating layer of HfO_2 from a graphene monolayer (black mesh), onto which gold electrodes (yellow) were formed to complete the circuit. Single entities were trapped at the 4 edges of this layer by applying low voltages (~400 mV) and achieving very strong forces. Reproduced from [70]. **c)** DNA molecules are first attracted towards the tip of a nanopipette immersed in aqueous medium and then translocated through its aperture and towards inside the pore. Molecules were attracted by applying AC voltages at the gold-coated surfaces outside the nanopipette tip while translocations were driven by a 10 V DC voltage between an electrode inside and outside the nanopipette. Reproduced from [73]. **d)** A pair of semi-elliptical closely-spaced (10 – 20 nm) carbon nanoelectrodes pyrolytically formed at the tip of a dual-barrel nanopipette traps individual molecules (DNA, RNA) and organelles (mitochondrion) in solution or inside a living cell by applying low peak amplitude AC voltages. Reproduced from [10].

It is worth highlighting the achievements of the experiments from this [10] and its contribution to a more comprehensive understanding of the cellular environment by bringing the single-molecule/organelle manipulation and cell biology closer. For instance, single-stranded DNA (22 bases) was removed from the cell nucleus, while RNA molecules were extracted from the cytoplasm of live human cells for single-cell DNA and gene expression analyses. The carbon nanopipette tweezers were also capable of handling single organelles, as the authors demonstrated the removal of single mitochondria from mice neuron cells. Overall, they suggested that modifications could be easily applied to this type of nanotweezers to be combined with numerous electrochemical scanning techniques for the measurement of single-cell gene expression [10]. In a further optimisation of this design, Tang et al. (2021) [75] demonstrated trapping and sub-millisecond detection of individual mononucleotides and proteins of numerous sizes by quantum mechanical tunnelling probes. These probes were fabricated by electrodepositing gold controllably at the previously mentioned nanotweezers tip and the distance between the two electrodes could be tuned with high precision. Single-molecule dielectrophoretic trapping was achieved by applying an AC voltage between them in combination with a DC bias that gave rise to quantum tunnelling.

Electric traps have also been developed with the standard design of solid-state nanopores, where an insulating plane with a nanometre-sized pore connects two reservoirs that contain the analyte under investigation in electrolyte solution. Schmid et al. (2021) [76] recently presented the NEO-trap, a relatively simple but powerful nanopore-based electroosmotic trap that achieved trapping and detection of individual proteins with sub-millisecond resolution while each measurement could be hours long. The NEO-trap consists of a spherical DNA-origami attached on a lipid passivated silicon-nitride nanopore which blocks its opening only from one side (Figure 2.8a). Particles close to the formed nano-cavity get trapped due to local electroosmotic flow and depending on their shape and size, different electrical signals are recorded. Finally, fluidic slits have also been used for field-free single-molecule trapping [77], [78]. By tuning the design of these slits or the ionic strength of the electrolyte solution, individual particles (Au particle, latex beads, lipid vesicles) were electrostatically captured and optically monitored for several hours [77]. Ruggeri et al. (2017) [78] proved that this configuration provided significantly accurate measurements of the electric charge of single trapped molecules in real time and with high throughput. This technique, which was named “single-molecule electrometry”, demonstrated precise detection of changes in the 3D conformation of nucleic acids or proteins that are directly linked to the charge distribution along a macromolecule.

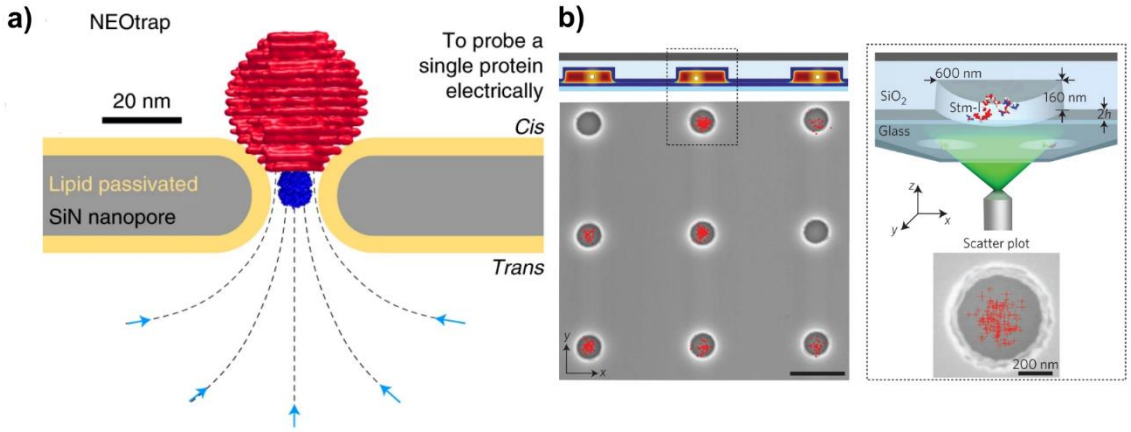

Figure 2.8 Schematic illustrations of non-dielectrophoretic platforms for single-molecule manipulation. **a)** A spherical DNA-origami (red) attached on a lipid passivated (yellow) silicon-nitride nanopore (grey) which blocks its opening only from one side. Particles (purple) close to the formed nano-cavity get trapped due to local electroosmotic flow (dotted lines) depending on their shape and size. Reproduced from [76]. **b)** 2D projection of an array of electrostatic fluidic traps. (Top left) Simulated electric potential distribution inside three slits. (Right) 3D zoomed representation of a fluorescent protein trapped in one slit with key dimensions of the trap shown. Scatter plot indicates the position of tracked molecules. Reproduced from [78].

2.2.6 Summary of single-molecule force spectroscopy techniques

To summarise, single molecule force spectroscopy techniques are valuable tools for studying the mechanical properties and interactions of individual molecules. The techniques reviewed in Section 2.2 include optical, magnetic, acoustic, electrical tweezers and atomic force microscopy. As discussed, each technology come with its advantages and disadvantages depending on the experimental conditions. One of the most established techniques, the optical tweezers, use focused laser beams to trap and manipulate micro- and nanoscale particles, including biomolecules. The force on the trapped object is determined by the laser's intensity gradient. Optical tweezers can measure forces with piconewton precision but they are limited within this range. There is no physical contact between the trapping laser beam and the sample, minimizing mechanical perturbations, although high-powered lasers and high numerical aperture lens are usually required. As a consequence, their maintenance can be expensive and technically challenging. They can also quickly measure multiple molecules, with a size range approximately between 100 nm and 1 mm, in parallel but their effectiveness can be influenced by the sample’s optical properties and size.

Another single molecule force probing technique are the magnetic tweezers which use magnetic beads attached to molecules of interest. An external magnetic field is applied to manipulate the beads and, indirectly, the attached molecules. The force is determined by the strength of the magnetic field. Magnetic tweezers can exert forces spanning from piconewtons to tens of nanonewtons. Multiple molecules can be manipulated simultaneously allowing for high-throughput experiments, they can be used in various environments and are suitable for studying DNA, proteins, and other biomolecules. Magnetic tweezers typically have lower spatial resolution compared to AFM and optical tweezers while they are primarily suited for stretching experiments and may not be ideal for other applications. The force applied to the molecule is inferred from the motion of the magnetic beads, which can introduce uncertainties.

Another well-established technique is AFM which uses a sharp tip attached to a cantilever to measure forces between the tip and the sample surface. It measures the deflection of the cantilever caused by these forces, allowing for precise force measurements. AFM can achieve sub-nanometre resolution in force measurements, it can be used in various environments, including liquid and air, and can measure a wide range of forces. However, it is not suitable for very high forces due to the potential for tip-sample damage, it can be time-consuming to collect data on multiple molecules and requires skilled users and careful calibration. Next, acoustic tweezers represent a unique and emerging technology which harnesses the mechanical forces generated by acoustic waves to control and manipulate microparticles or biological molecules in a non-contact and label-free manner. Single particle manipulation is achieved without physical contact with the sample, avoiding potential damage or interference caused by probes or surfaces which is particularly useful for delicate biological samples. They offer high throughput and can trap a variety of particles, including cells, bacteria and microbeads. The acoustic forces are generally gentle and can be used to manipulate sensitive biological specimens without altering their viability or functionality but high spatial resolution can be challenging. Moreover, their effectiveness can vary based on the size, density, and compressibility of the particles being manipulated.

Finally, there are a broad range of biophysical techniques that rely on electrical forces for single-molecule manipulation either in the form of electrostatic traps or electrokinetic tweezers. Lately, an increasing interest has emerged for dielectrophoretic force probing nanotweezers which use non-uniform electric fields to manipulate and probe biological molecules or particles. This method is particularly useful for studying the electrical and mechanical properties of particles, or their interactions with other molecules and surfaces mainly in microfluidic systems or other controlled environments. Like the acoustic tweezers, DEP nanotweezers are non-destructive and do not require physical contact

with the molecules, making them suitable for studying delicate biological samples. They offer label-free force probing, avoiding the need for fluorescent markers that may interfere with the biological properties being studied.

DEP nanotweezers also allow precise control of the forces acting on particles sized between 1 nm and 1 mm, enabling detailed investigations of the particles' physical properties. Since they are based on pair of electrodes, they offer high flexibility in their design and instrumentation but at the same time the application of electric fields can generate heat, which may affect biological samples, so careful control of the conditions is required to mitigate this. One of their main disadvantage is that DEP primarily works with dielectric particles. Some of the key benefits of the nanopipette-based dielectrophoretic nanotweezers, which are presented and discussed in the next chapters, are their spatial resolution, as they can be precisely controlled in three dimensions and the ability to probe very gentle forces (in the range of tens of femtonewtons) compared to the previously mentioned techniques. Most importantly, they are minimally invasive when penetrating a cell and could potentially allow intracellular force probing measurements without the need of handles.

2.3 Single-molecule fluorescence microscopy (SMFM)

Fluorescence imaging microscopy has been a central component of single-molecule force spectroscopy since its inception [79]. The general concept is based on fluorescently labelled or auto-fluorescent entities becoming bright when they absorb light against a dark background in a way that does not affect their structural or functional properties providing useful information on their geometry, dynamics and interactions. Compared to previous spectroscopy methods based on ensemble average measurements, optical parameters such as brightness, duration, emission wavelength and polarisation can now be defined for individual particles with a significantly improved spatial and temporal resolution [79]. This allows the direct observation of properties that reveal the heterogeneity within a system (i.e., cells, polymers) or intermediate states of molecular kinetic transitions which would not be detectable by ensemble measurements.

This section mainly focuses on one application of single-molecule fluorescence microscopy (SMFM), called single-particle tracking (SPT) [80], which is heavily used in Chapter 5 for monitoring the two-dimensional trajectory of individual molecules and measuring any applied dielectrophoretic forces on them. Further microscopy-based modifications have allowed three-dimensional single-molecule localisation but will not be covered here as it is not linked to the work presented in the next chapters. Analysing the recorded orbits of single-molecules unravels important information on the status of their motion which can either diffuse, be spatially confined, interact with other molecules in proximity or even move due to a combination of these [80]. To achieve single-molecule concentration for in vitro experiments, diluting the fluorescent probe is the most typical method while for in vivo experiments other techniques need to be followed, such as quenching or photobleaching many emitters or activating specific molecules at a time [79]. Although in vitro single-molecule imaging is much more straightforward than in vivo, where intracellular crowding and interactions with other structures or organelles affect the trajectory of the molecule under observation, it provides a realistic representation of the entity's behaviour in its native biological environment.

Single-particle tracking relies on single-molecule localisation (Figure 2.10a), where single fluorescent entities are imaged while their two-dimensional spatial trajectories (x and y coordinates) are recorded at sequential time points, as displayed in Figure 2.10b, by an array detector (i.e., sensitive camera) [79]. So far, multiple types of microscopes have been used for single-molecule imaging with the most common being wide-field, confocal, total-internal reflection (TIRF) and two-photon microscopes [81]. Each

configuration can achieve different precision on localising the position of individual molecules depending on the experimental conditions required and the system under investigation. Epifluorescence or inverted microscopes for 2D single-molecule wide-field imaging usually produce a Gaussian illumination spot, which can range from few to tens of micrometres, on the plane where the molecules of interest diffuse. As a result, all fluorescent molecules that are excited with the wavelength of the beam are detected simultaneously without the need of scanning across the plane [79]. To achieve this the light source (i.e., laser beam) is focused on the back side of the microscope objective, as illustrated in Figure 2.9.

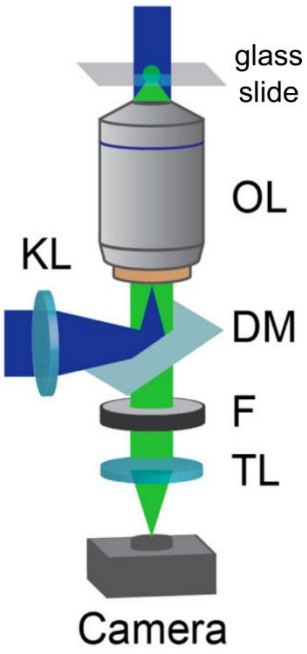

Figure 2.9 Schematic of imaging geometry used in epifluorescence (inverted) configuration for wide-field microscopy. The beam emitted from the light source (blue) is focused on the back side of a microscope objective lens (OL) through a Köhler lens (KL) and dichroic mirror (DM). Once the wavelength is absorbed by a fluorescent molecule, the latter gets excited and emits a different wavelength (green) which passes through an OL, DM, filter(s) and is focused on the camera sensor via a tube lens (TL). Reproduced from [79].

The microscope objective lens is the most important optical component of such systems with its numerical aperture (NA), which depends on the refractive index between the sample and the lens, determining the resolution of the obtained image. However, light diffraction limits the capability of single-molecule localisation from its emission distribution [79]. The numerical aperture of the most advanced infinity-corrected microscope objectives can reach up to 1.3 – 1.5, which means that for a light of 500 nm

wavelength the minimum spot of a single entity that can be observed would not be smaller than ~200 nm. It is worth noting that NA of greater than 0.95 can only be achieved with immersion lenses, using either oil or water. Moreover, even when the optimum optical configurations and brightest fluorophores are used, background signal can severely affect the image acquisition. Filtering background light is required for single-molecule imaging with integrated filters on microscopes also reducing auto-fluorescence and scattering. As illumination by the excited molecules passes again through the objective, photons are collected by the camera sensor. Improving the efficiency at which photons are converted to photoelectrons has contributed significantly to single-molecule imaging [79].

Thermal noise is usually generated by the electronics inside cameras which leads to noise when photoelectrons are converted to a signal voltage. Charge-coupled device (CCD) cameras are much more prone to such noise compared to electron-multiplying CCD (EMCCD) and scientific complementary metal oxide semiconductor (sCMOS) ones. Both camera types have demonstrated quantum efficiencies close to 95% each with their own technology, either via charge multiplication before readout for EMCCD or engineering low read noise in the first place for sCMOS [79]. In summary, before conducting a single-molecule imaging experiment, the signal-to-background ratio (SBR) or contrast and intensity of light source have to be carefully considered. Even if SBR is kept at a constant value though, the signal-to-noise ratio is increased by amplifying the intensity of the beam which depends on the maximum intensity a fluorophore can emit. Actually, the latter illumination saturates when the fluorophore reaches its maximum number of photons before photobleaching which adds additional noise to the system. This and background light are noise sources that highly affect modern detectors [82].

With all these types of noise involved in single-molecule imaging, post-acquisition techniques have been developed to estimate accurately and precisely the position of molecules under investigation. These techniques are based on algorithms that can extract valuable information from noisy images [79]. The point spread function (PSF) is the three-dimensional diffraction pattern from the illumination emitted by an individual molecule and transmitted through the high numerical objective. The average intensity produced by a molecule is proportional to a cross-section of this function scaled by the total amount of photons in the signal and the constant background noise (left image in Figure 2.10a). Within a region of interest (ROI), where one molecule is present and emitting, the image produced by the camera is subject to noise and binned into pixels, producing a specific signal at each pixel.

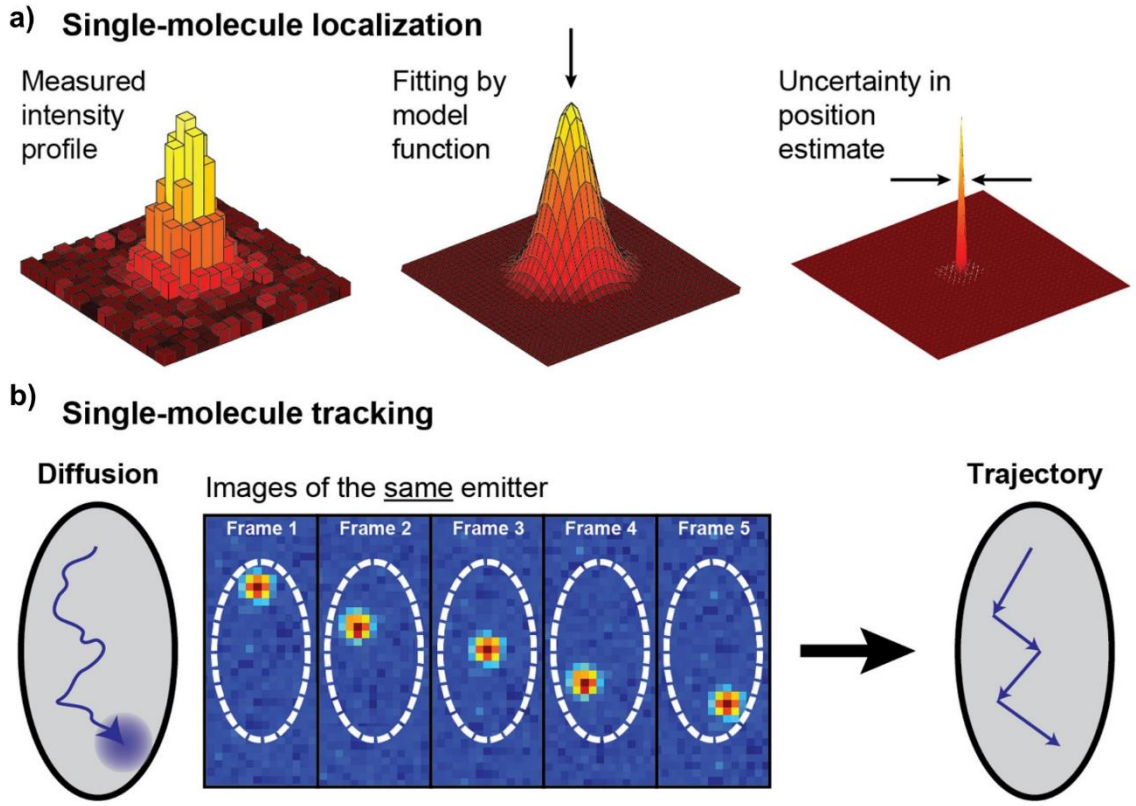

Figure 2.10 Basic concepts for single-molecule localisation and single-particle tracking. **a)** (Left) Measured intensity profile on a camera sensor, emitted by a fluorescent molecule and blurred due to light diffraction. (Middle) Intensity profile fitted by a model function to estimate the two-dimensional position of the molecule. (Right) Uncertainty in the position estimate from the model function fitting. **b)** The two-dimensional position of a diffusing fluorescent molecule is recorded over a sequence of time intervals. By applying single-molecule localisation, the spatial trajectory of this molecule can be extracted. Reproduced from [79].

For two-dimensional localisation, the PSF is brightest close to the molecule's position and darker further from it so an algorithm could allocate the maximum brightness to the centre of the molecule and predict its position profile based on the surrounding distribution (middle image in Figure 2.10a) [79]. These estimators are computationally efficient but limited as the maximum value is sensitive to noise and pixel size leading eventually to low precision (right image in Figure 2.10a). Least-squares fitting and maximum likelihood estimation are two methods that can improve these limitations by fitting the image data to respective functions. Recently, several open access single-particle tracking software packages have been released and found wide application in the single-molecule imaging field. One of the most commonly known platforms is TrackMate [83], a Fiji (ImageJ) plugin with three classes of algorithms that offer automated, semi-automated and manual particle-tracking depending on the molecule's

motion in the recording. It can also be easily customised based on the user's needs by importing additional scripts to improve data analysis and is operatable for 1D, 2D and 3D image acquisitions. Other honourable mentions for single-molecule tracking, each with its own implementation and advantages, have been published by Rösch et al. (2018) [84], Granik et al. (2019) [85], Hou et al. (2020) [86] and Kuhn et al. (2021) [87].

2.4 Dielectrophoresis (DEP)

After a short description of single-molecule fluorescence microscopy and its contribution to the field of single-molecule force spectroscopy, the focus of this review is shifted again to electrical trapping and in particular to dielectrophoresis. This section begins by explaining its key concepts and defining the dielectrophoretic force acting on a polarisable spherical particle when immersed in a dielectric medium. In addition, I comment on how the frequency of applied AC signals determines the polarity of the force or how more complex shapes of the manipulated entity affect this equation, from multiple shells around the core of a spherical particle to prolate and oblate geometries, or the slightly more delicate properties of biological macromolecules (i.e., DNA, RNA, proteins). Lastly, two electrohydrodynamic phenomena that usually take place in combination to dielectrophoresis, the so-called electroosmosis and electrothermal flow, are presented before summarising prospects of this technique in the single-molecule field.

2.4.1 Dielectrophoretic force on spherical homogeneous particles

In 1951, Pohl [88] established a novel physical concept, named “dielectrophoresis (DEP)” which was defined as the resulting motion of polarisable particles or liquids due to the application of a non-uniform electric field. The following two decades, Pohl and colleagues started to utilise dielectrophoresis as a tool to separate living from dead cells [89] and accumulate cell populations at specific locations within a circuit, such as the tip of an electrode [90]. Their research inspired the global scientific community to consider dielectrophoresis as an effective option for handling and sorting particles, especially biological ones [91]. Several recent applications on single-molecule manipulation with dielectrophoretic tweezers based on IDEs or nanopipette-based electrodes were mentioned in great detail in Section 2.2.5 (Figure 2.7).

The application of an electric field between two or more electrodes to an entity with a defined polarisability (a) leads to temporal redistribution of its surface charges, resulting in the formation of a dipole or multipoles [92]. When the field lines are uniform, as shown in Figure 2.11a, the Coulomb forces between the particle’s poles are equal and opposite (red and green arrows), so the net force becomes zero and there is no movement of the induced polarised particle. However, when the field is non-uniform and the particle’s surface charges are unevenly distributed at its poles, the overall force obtains a finite

value which as a result induces particle motion (Figure 2.11b) [7]. It is worth clarifying that this net force is responsible for polarisable charged biological entities, such DNA, RNA and protein molecules, but also neutral ones, like single cells [93]. This phenomenon should not be confused with electrophoretic motion which depends on the polarity of the fixed electric charge (positive or negative) a particle carries in combination to the polarity of the applied electric field (left particle in Figure 2.11a).

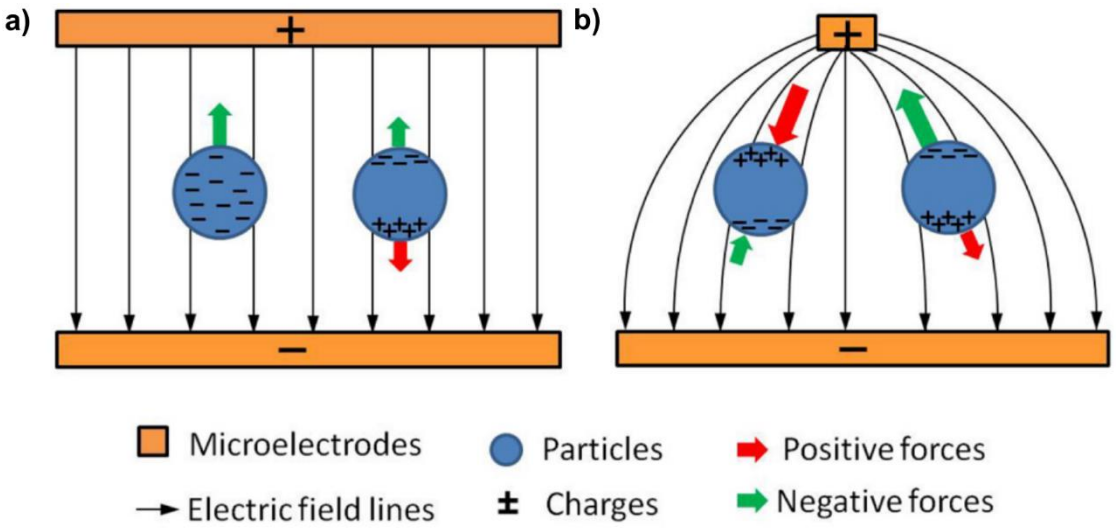

Figure 2.11 Basic principles of electrophoresis and dielectrophoresis. **a)** A uniform electric field is formed between two parallel microelectrodes. A spherical particle with a fixed negative charge moves towards the electrode of opposite polarity (+), while another polarisable spherical particle remains static as its surface charge distribution is opposite and equal between its poles. **b)** A non-uniform electric field is generated between two microelectrodes of different geometry where polarisable spherical particles are either attracted or repelled from the bottom electrode based on their intrinsic dielectric properties. Reproduced from [94].

The dielectrophoretic force that acts on an induced polarised particle $(\vec{F}_{DEP})$ with a dipole moment $(\vec{p})$, polarisability (a) and a finite electric field gradient $(\nabla\vec{E})$ is described by the following equation [94]:

$$\vec{F}_{DEP} = (\vec{p} \cdot \nabla) \cdot \vec{E} \quad (2.1),$$

where

$$\vec{p} = a \cdot \vec{E} \quad (2.2).$$

Consequently, when the electric field is uniform its gradient equals to zero $(\nabla \cdot \vec{E} = 0)$, hence there is no dielectrophoretic force acting on the particle (right particle in Figure 2.11a). It should be noted that this equation is valid only under the dipole approximation,

which states that the dipole length needs to be smaller than the estimated dimension of the inhomogeneity of the electric field. In other words, its magnitude must not change considerably across the dimensions of this dipole, otherwise, multipole force terms need to be added to the expression [95].

The time-averaged dielectrophoretic force experienced by a homogeneous sphere of radius r_p, relative electrical permittivity ε_p and conductivity σ_p when immersed in a medium of ε_m and σ_m is described by Equation 2.3 [94]. This is considered the most basic model and is illustrated in Figure 2.12a. Here, it is worth clarifying that dielectrophoresis can be used with both direct (DC) and alternating (AC) current fields. By using the time-averaged relation, any force components arising from DC fields, such as electrophoretic, will average to zero and be eventually eliminated [95]. This equation is as follows:

$$\langle \vec{F}_{DEP} \rangle = 2\pi\varepsilon_0\varepsilon_m r_p^3 * Re\left[\frac{\varepsilon_p^* - \varepsilon_m^*}{\varepsilon_p^* + 2\varepsilon_m^*}\right] * \nabla\left|\vec{E}_{rms}\right|^2 \quad (2.3),$$

where $\nabla\left|\vec{E}_{rms}\right|^2$ is the gradient of the squared non-uniform root mean square value of the electric field, ε_0 is the vacuum permittivity (F/m), $\varepsilon_{p,m}^* = \varepsilon_{p,m} - j\sigma_{p,m}/\omega$ are the relative complex electrical permittivity of the particle and medium respectively with $j = \sqrt{-1}$ and ω the angular frequency of the applied AC signal. The ratio of these complex permittivity terms is called the Clausius-Mossotti (or Maxwell-Wagner) factor and describes the polarisability of the particle as a function of ω [91]:

$$f_{CM}(\omega) = \frac{\varepsilon_p^* - \varepsilon_m^*}{\varepsilon_p^* + 2\varepsilon_m^*} \quad (2.4).$$

The two equations above suggest that the magnitude of the dielectrophoretic force is directly linked to the particle's volume $\left(r_p^3\right)$, $Re[f_{CM}(\omega)]$ and gradient of the electric field squared. Therefore, it is dependent on the angular frequency (ω) of the applied field, the relative electric permittivity and the conductivity of the polarised particle $\left(\varepsilon_p, \sigma_p\right)$ and medium $(\varepsilon_m, \sigma_m)$. As a consequence, the real part of the Clausius-Mossotti factor plays a crucial role in the direction of the dielectrophoretic force acting on the particle [92]. When $Re[f_{CM}(\omega)] > 0$, the particle moves towards regions where the electric field magnitude is maximum. This phenomenon is called positive dielectrophoresis (pDEP) (right particle in Figure 2.11b). However, when this becomes negative $Re[f_{CM}(\omega)] < 0$, the particle is repelled away from regions of maximum electric field magnitude and it is called negative dielectrophoresis (nDEP) (left particle in Figure 2.11b) [95].

From the definition of the complex relative electrical permittivity and Equation 2.4, it can be derived that at high frequencies ($\omega \to \infty$), the particle functions as a capacitor

because the dielectric displacement is leading the applied field by $\pi/2$ and hence the DEP force is influenced only by the permittivity of the particle and the medium $(\varepsilon_p, \varepsilon_m)$ [96]. At low frequencies $(\omega \to 0)$, the displacement current has less influence than the conduction of free charges of the Clausius-Mossotti factor, and thus the dielectrophoretic force is governed by the conductivity of both the particle and medium (σ_p, σ_m). The graph in the middle of Figure 2.12a displays how the real part of this factor changes as a function of the angular frequency (ω) for a polystyrene latex bead in the case of $\varepsilon_p < \varepsilon_m$ and $\sigma_p < \sigma_m$. Positive dielectrophoresis is expected at higher frequencies while nDEP at low. The frequency value at which $Re[f_{CM}(\omega)] = 0$ is the crossover frequency $(f_{CM,0})$ and that is where no DEP force is applied on the particle [96].

2.4.2 Dielectrophoretic force on particles of different shapes

Although the homogeneous spherical model has been extensively applied for manipulating biological micro- and nanoparticles, more comprehensive models are required for describing the effect of DEP for structurally complex biomolecules, like DNA, and cells [6]. A bioanalyte, such as a cell membrane or other aqueous cellular compartments with varying bio-functionality, is comprised of various types of charged chemical groups or polarisable molecules with non-identical dielectric properties. More frequently, the structure of biological particles consists of a core surrounded by one or more different layers which could all affect the polarisation between their interfaces. Therefore, the homogeneous spherical model cannot properly describe their dielectric properties and that is why single-, double- or even multi-shell models are required [6]. For instance, Figure 2.12c provides a schematic illustration of a cell with an inner core (cytoplasm), surrounded by two shells (a cell membrane and wall) of radii r_1, r_2, r_3 and effective complex permittivity terms $\varepsilon_p^*, \varepsilon_{s1}^*, \varepsilon_{s2}^*$, respectively. This representation is called the double-shell model and it describes the dielectrophoretic characteristics of bioparticles of such structures.

Nevertheless, biological particles are diverse in size, shape and structure with most of them being non-spherical and expressing varying electrophysiological characteristics [97]. In comparison to spherical particles, ellipsoidal ones are not polarised symmetrically across the axes of the applied electric field and thus its frequency determines the orientation of the particle [98]. Due to the alternating orientation of these particles to the electric field, a polarisation factor that depends on the direction of the DEP field was introduced, the so-called depolarisation factor (A_a). Two of the most frequently used ellipsoidal shapes in dielectrophoretic models are the oblate and prolate ellipsoids, as

illustrated in Figure 2.13a and 2.13b, respectively. Moreover, an elongated version of the prolate ellipsoid model is utilised to describe the majority of rod-shaped entities [99], where a slightly different expression for the applied dielectrophoretic force was adopted (Figure 2.13c).

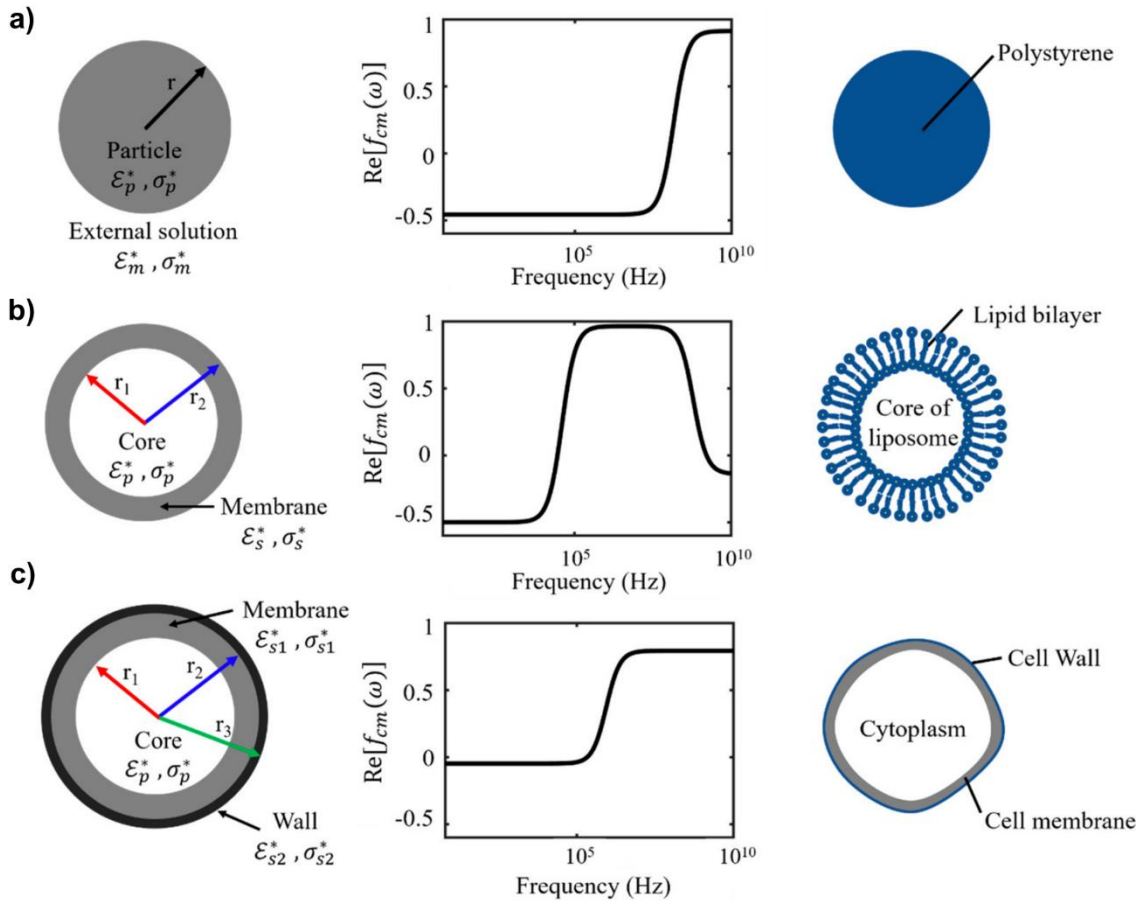

Figure 2.12 Schematic representation of three spherical DEP models (left), graphs for $Re[f_{CM}(\omega)]$ over a frequency range from 0 to 10^{10} Hz (middle) and one example of spherical model molecules (right). **a)** Homogeneous spherical particle model for a polystyrene bead $(\varepsilon_p^*, \sigma_p^*)$ immersed in aqueous solution $(\varepsilon_m^*, \sigma_m^*)$. Positive DEP occurs at high frequencies while nDEP at low. **b)** Single-shell spherical particle model for the core $(\varepsilon_p^*, \sigma_p^*)$ and lipid bilayer $(\varepsilon_s^*, \sigma_s^*)$ of a liposome. Negative DEP takes place at very low and high frequencies, with pDEP dominating in between. **c)** Double-shell spherical particle model for the cytoplasm $(\varepsilon_p^*, \sigma_p^*)$, membrane $(\varepsilon_{s1}^*, \sigma_{s1}^*)$ and wall of a cell. Strong pDEP occurs at high frequencies and very weak nDEP at low. Reproduced from [6].

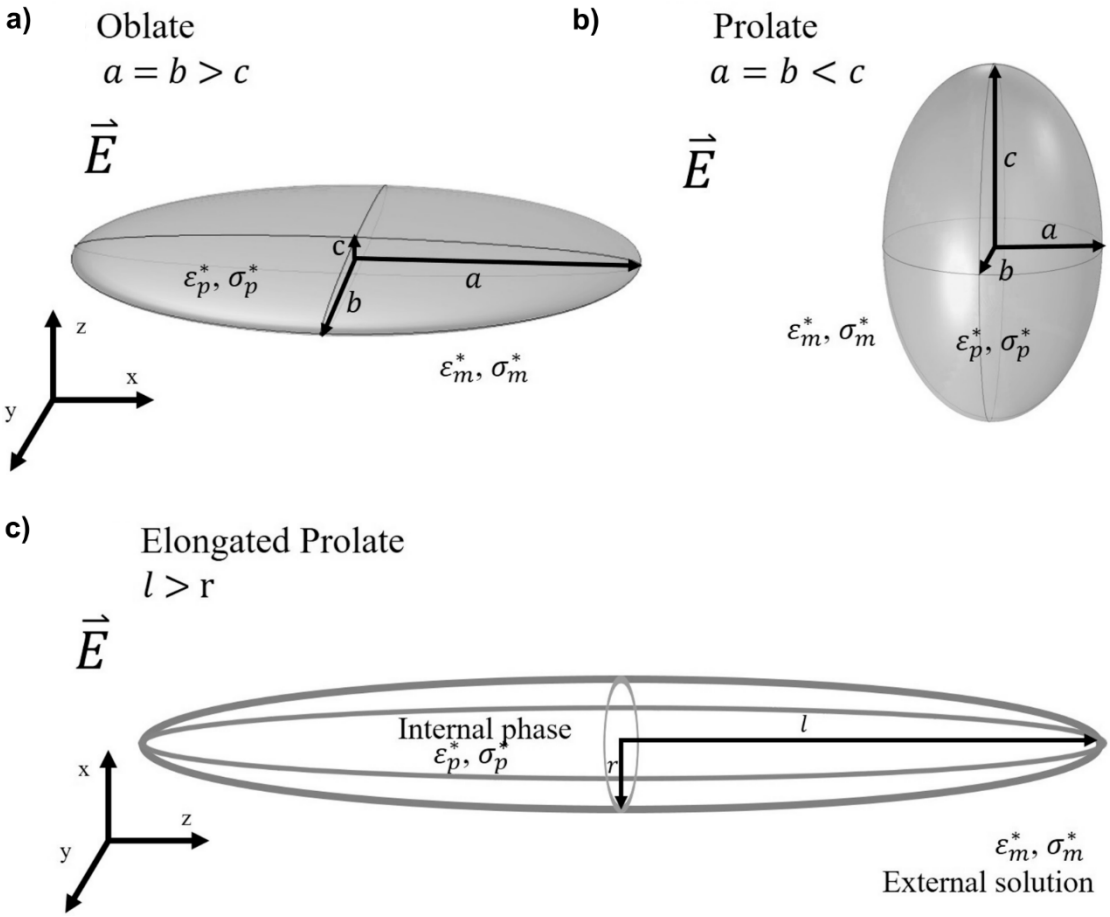

Figure 2.13 Schematic representation of three ellipsoidal models. **a)** Homogeneous oblate model with semi-axes $a = b > c$. **b)** Homogeneous prolate model with semi-axes $a = b < c$. **c)** Elongated prolate model of radius r and length l. Reproduced from [6].

2.4.3 Dielectrophoresis on biological macromolecules

Proteins and nucleic acids, such as DNA and RNA, are responsible for the function of a cell, from its structural integrity to regulation and communication with other cells [6]. Throughout the past decades, the scientific community has been trying to understand their principal mechanisms by manipulating such molecules through dielectrophoretic platforms. So far, numerous biomolecules with different structure, shape, size and chemical composition have successfully been sorted, trapped and separated due to their electrodynamic characteristics. Therefore, understanding the theoretical principles of how DEP acts on biological molecules is crucial for the development of more advanced applications in the future [100].

The dielectrophoretic force applied on biomolecules is strongly dependant on the ion cloud that surrounds them [6]. Almost all of them, especially DNA and proteins, have a

finite surface charge when they are immersed in an aqueous environment which results in a formation of electric double shells due to the attraction of counterions from the medium (left column, Figure 2.14) [7]. Figure 2.14b shows a DNA strand as a negatively charged coil-like configuration enveloped by positive counterions. When an electric field is applied to this DNA bundle, the surrounding counterions distribution shifts opposite to the negative surface charge of the macromolecule resulting in an effective dipole. This polarisation happens only if it is quicker than the relaxation of the counterions cloud, otherwise, the dipole moment does not exist due to the neutralisation of the counterions layer.

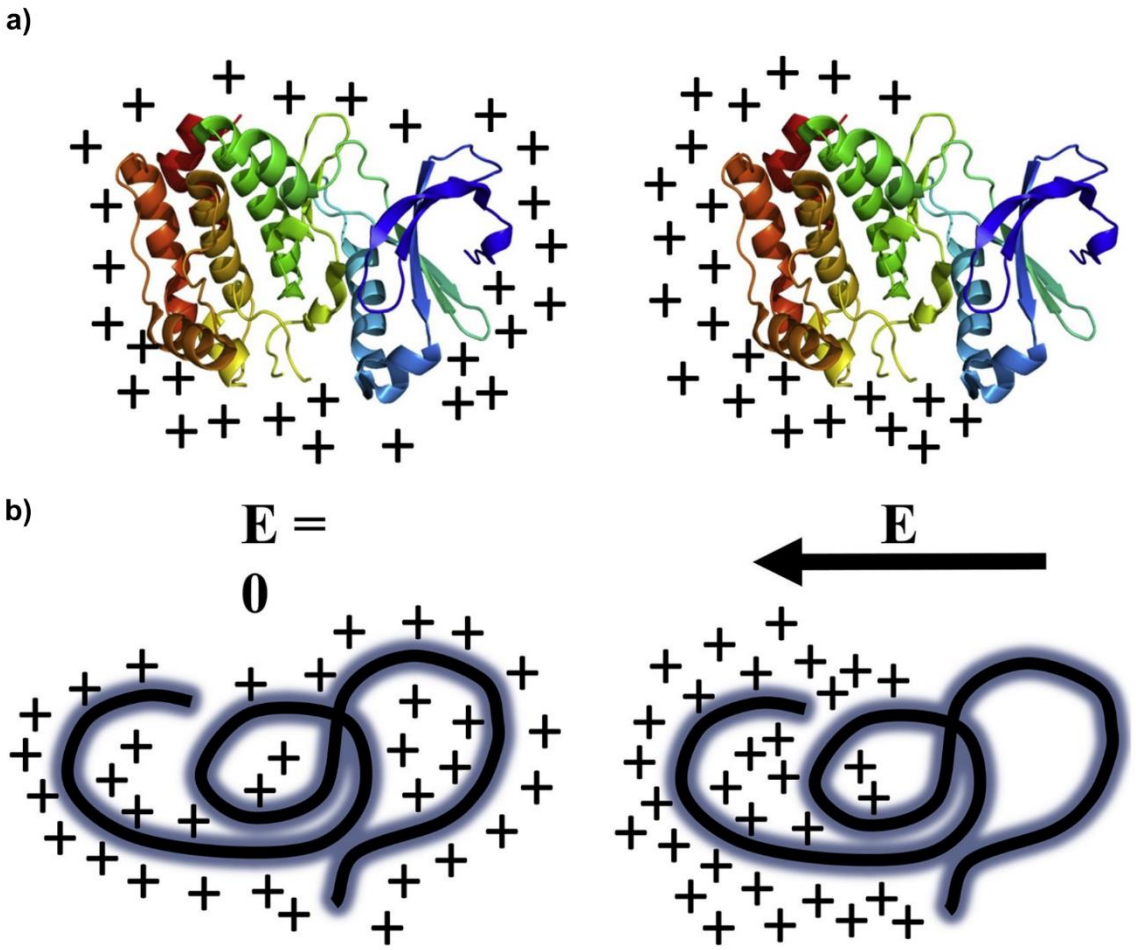

Figure 2.14 Schematic illustration of counterion cloud distribution (positive charges) around a negatively charged **a)** protein and **b)** DNA molecule when an electric field is absent (left column) and present (right column). The negative charges on the biomolecules are not shown. Reproduced from [7].

Proteins with their intricate structural conformations exhibit dynamic behaviour in various media that are very complex to explain [6]. This is one of the reasons, their dielectric response and mechanisms regarding DEP phenomena are still not fully understood or expressed via a model. Currently, the commonly accepted theory is the classical one

which states that DEP events can occur on a protein only if ultra-high electric field gradients (> 10^{16} V^2/m^3) are achieved and significantly exceed other forces, like Brownian motion [101]. On the other hand, experiments have also indicated that a further mechanistic understanding should be included in the theoretical explanation for the DEP of proteins to account for interactions with the counterions atmosphere or intrinsic polarisation effects [6]. A recent study by Seyedi and Mathyushov [102] stated that the calculated DEP forces on proteins based on the classical theory model were underestimated, but further validations of their model on different proteins are required for reliability.

In a recent publication, Pethig [103] argued that the currently accepted theory regarding the Clausius – Mossotti factor for DEP experiments which involve proteins and other macromolecules with fixed dipole moments needs to be replaced due to its inaccuracy. He also claimed that the standard theory regarding the dielectrophoresis of non-polar and extremely charged macromolecules, like DNA, requires revision since it lacks a valid explanation for the rise of interfacial charges by molecular interactions in the counterions atmosphere. Furthermore, the author suggests that for a specific frequency range the positive dielectrophoretic force applied on proteins should depend on the electric field gradient and not on its gradient squared, which would be only exhibited by the negative DEP. Finally, the current theory does not take into consideration the effects that arise from particles with non-symmetric surface charge distribution and further investigation needs to be undertaken [103].

2.4.4 Electroosmosis and electrothermal flow

The phenomenon of the bulk movement of a fluid that surrounds a charged surface after the application of an electric field is called electroosmosis (Figure 2.15a) [7], [104]. This surface charge attracts counterions from the aqueous electrolyte which form an electric double layer. The counterions that have bonded strongly with the charged surface are considered as the Stern layer, while the rest create a diffuse layer that reaches the electroneutral part of the fluid [95]. The advantages of electroosmotic flow, like its uniform profile, straightforward fluidic interface and no requirement for pumping mechanism, have led to its application in microfluidic designs [105]. However, its strong dependence to the electrochemical properties of the medium, need for high applied voltages (kV range) that could lead to undesired products (bubble formation) and heat production can limit the electroosmosis function in devices.

The effect described in the previous paragraph is a result of direct-current (DC) applied voltages. Hence, some of the factors which regulate the electroosmotic flow are the electric field, pH, ionic strength of the solution and temperature [106]. When the electric field increases, electroosmosis increases proportionally with very high values leading to Joule heating. Additionally, higher pH, larger temperature and lower ionic strength of the medium increase electroosmotic flow too [95]. Nevertheless, the application of AC voltages on the electrodes give rise to induced charge electroosmosis (ICEO) or AC electroosmosis (ACEO). During the first half-cycle of the wave, the same mechanism as described for DC electroosmosis occurs. In the second half-cycle though, the polarity of both the electrodes surface and double layer change so the force magnitude and direction remain stable [7].

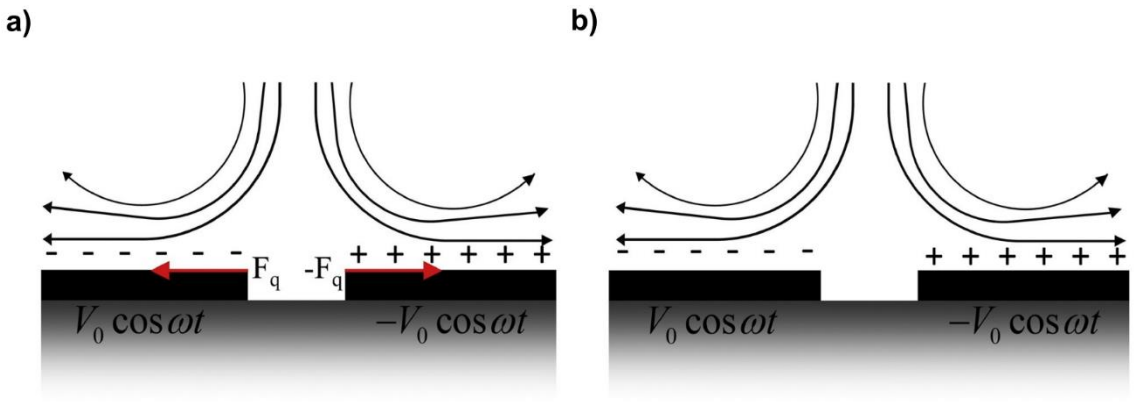

Figure 2.15 Schematic illustration of AC **a)** electroosmosis flow $(\pm F_q)$ and **b)** electrothermal flow close to the surface of two electrodes of opposite polarity $(\pm V_0 cos\omega t)$. This direction for electrothermal flow occurs at frequencies (ω) below the crossover frequency $(f_{CM,0})$ while for higher ones the flow reverses to the opposite direction, which means upwards from the electrode gap. Reproduced from [7].

However, two important factors need to be accounted for the manufacture of AC electroosmotic devices. The first one is related to the reversal of ACEO flow which occurs when high voltages are applied in combination with a frequency range of 10 – 100 kHz. At low frequencies, Faradaic charging takes place between the electrolyte and the electrode, while at high frequencies, the double layer is over-filled by ions. The second factor is associated with the concentration of the bulk in salt, which above a certain limit (~10 mM), leads to rapid decay or even diminishes the ACEO flow [7]. Another crucial electrohydrodynamic phenomenon arises from inhomogeneities in the electric permittivity and conductivity of the medium, and it is called electrothermal flow (Figure 2.15b). In AC systems, high applied voltages often lead to Joule heating which generates temperature gradients that increase the conductivity of the fluid, decrease its permittivity and eventually induce electrothermal flow [105].

Subsequently, the electric field is also reduced to achieve charge conservation, finally resulting in a local charge density that varies with the electrostatic force [7]. Since the AC electrothermal flow of the medium is largely affected by its conductivity, especially for electrolytes that are more conductive than 0.1 S/m, the design of dielectrophoretic systems must keep it within a specific range. It has been shown that ACET flow almost vanished in experiments that involved proteins or DNA molecules with buffers of a few mS/m, while it became significant for conductivities above the S/m threshold [7]. Sridharan et al. (2011) [106] were the first ever to investigate the influence of Joule heating on electrothermal flow in an insulator-based dielectrophoretic device.

After experimental and finite element method studies, the authors concluded that under DC-biased AC voltages, the electric field interacts with the emerging fluid flow due to localised non-uniformities in the materials' properties. Two years later, the same group [107] upgraded the simulation model that described these events by predicting the locations of electrothermal flow circulations in a three-dimensional design. Lastly, dielectrophoretic experiments always need to consider these two electrohydrodynamic phenomena. Freedman et al. [73] studied both experimentally and theoretically (simulations) temperature gradients in the electrolyte of a nanopipette system due to Joule heating. All their results showed that for a voltage range between -400 mV and -700 mV, no significant change in temperature occurred since the ionic current remained stable and did not increase the conductance of the fluid.

2.4.5 Dielectrophoresis-based platforms

As mentioned in Section 2.2, numerous platforms have been developed for single-molecule manipulation and force spectroscopy by implementing optical, magnetic, acoustic and atomic force microscopy configurations. In addition, dielectrophoresis has attracted significant interest from the research community due to its advantageous properties. However, it has been acknowledged that metal-based devices have also disadvantages [108]. One restriction for metal electrodes in aqueous solution is the application of signals with frequencies below ~5 kHz where the formation of unwanted electrochemical species, electrolysis effects as well as electroosmotic fluid flow may arise. A potential solution has been suggested by not creating a direct contact between the charged surface of the electrodes and the solution (contactless DEP) [108]. Another limitation for electrode-based DEP (eDEP) is the operation in an electrolyte solution with a conductivity below ~1 S/m which may be inappropriate when mimicking the physiological conditions of a biomolecule. This issue was also addressed by changing the design and using insulator-based dielectrophoretic platforms (iDEP) [108].

To summarise, a plethora of geometries and implementations of electrodes have been reported over the past years for assessing the manipulation of particles [6]. Nevertheless, an optimal design or fabrication technique have not been achieved yet because different platforms have proved to be more suitable for a range of dielectrophoretic applications [108]. For instance, electrode-based dielectrophoresis produces high magnitude electric fields with just a few volts, but at the same time, fouling effects or electrolysis may arise. In contrast, insulator-based dielectrophoresis may involve a cheaper and quicker fabrication method, but higher potentials are required for achieving the desired forces which could lead to unwanted effects. Due to the applications immediately linked to this project, the next section is focused exclusively on the fabrication and characterisation of nanopipette-based electrodes.

2.4.6 DEP impedance spectroscopy on biomolecules and nanoparticles

Besides single-molecule manipulation and force probing, dielectrophoresis-based platforms have also been used for single-particle detection. Dielectrophoretic impedance spectroscopy is an emerging and promising analytical technique that combines the principles of dielectrophoresis (DEP) and electrochemical impedance spectroscopy (EIS) for the manipulation, detection and characterization of biomolecules and nanoparticles. EIS is a technique that provides information about the electrical properties of a particle by recording changes in resistance and capacitance of a circuit at the surface of an electrode [109]. It can detect subtle changes in the impedance spectra caused by the presence, concentration, size, and surface properties of particles. Unlike other analytical techniques (i.e., fluorescence microscopy) that require the labelling or modification of samples, DEP-EIS allows for their label-free detection without altering their intrinsic characteristics. A few examples of dielectrophoretic impedance spectroscopy for single particle detection are discussed below.

In 2006, Mureau et al. [110] presented a fast and accurate method based on dielectrophoresis in combination with impedance spectroscopy to detect and study the dielectric properties of single-walled carbon nanotubes. They accurately distinguished metallic from semiconducting proportions of single-walled carbon nanotubes in the same solution. Their results outperformed Raman spectroscopy for the specific conditions used and agreed with data collected by optical absorption. A frequency range between 1 and 15 MHz was chosen to dielectrophoretically collect only the metallic ones within 60 s while full characterisation of the dielectric properties of both species was achieved

between 250 kHz and 13 MHz. Later, Hamada et al. (2013) [111] developed a 2-microelectrode configuration to manipulate and detect bacteria. An electrode close to the inlet of the microfluidic channel was used to repel bacteria by negative dielectrophoresis (nDEP) away from this region. Another electrode close to the outlet of the channel was utilised instead to detect the repelled bacteria from the inlet with positive dielectrophoresis (pDEP). Since bacteria possess intrinsic electrical impedance, upon their arrival on the second electrode, a change in the electrical impedance of the electrode was monitored.

As discussed above, the electrode design and configuration are important factors for dielectrophoretic impedance spectroscopy. Koklu et al. (2017) [112] studied the differences between fractal and planar gold nanoelectrodes and investigated which geometry generated higher electric field gradients. The magnitude of the dielectrophoretic forces experienced by both yeast cells and colloidal gold microparticles increased (both for pDEP and nDEP) when fractal electrodes were used compared to planar. The dielectrophoretic force was calculated from the particle's velocity under trapping conditions based on single-particle tracking. The different DEP responses were investigated by measuring the microfluidic device impedance and the potential drop across the electrolyte. Recently, Bhatt et al. (2019) [113] combined dielectrophoresis and impedance spectroscopy to study DNA molecules for the first time. Polymer reaction chain products (labelled/non-labelled PCR) were labelled by gold nanoparticles and were concentrated at the centre of two electrodes due to the presence of an electric field gradient between them. The double layer capacitance, and hence the impedance, across the pair of electrodes was measured for an extended range of frequencies (10 Hz – 10 MHz) towards the end of the dielectrophoretic trapping. Results from this study provided an increased detection signal to noise ratio and specificity of PCR products just by introducing fluorescent gold nanoparticles.

Overall, dielectrophoresis-impedance spectroscopy has emerged as one of the most promising single-particle detection methods mainly due to their accurate, rapid and easy nature of measurement with micro- or nanoelectrodes. Its ability to manipulate, trap on demand and characterise particles or biomolecules based on their dielectric properties makes it a valuable tool for researchers seeking to advance their understanding of biological and physical systems at the micro- and nanoscale. Its main advantage over other techniques, such as fluorescent microscopy, is label-free trapping and detection which allows studying the properties of individual biomolecules without the need for modification. However, it also presents challenges at this stage (i.e., sensitivity) that must be addressed for wider adoption and more robust applications in the future.

2.5 Nanoelectrodes

Nanoelectrodes can be considered as conductive surfaces with dimensions ranging from few to hundreds nanometres [114]. At this scale, mass transport dominates diffusion at the nanoelectrodes surface making them a significantly capable platform to study electrochemical processes. Over the past decades, this tool has found broad applications as electrochemical probes for single-molecule detection, manipulation, single-cell analysis and high-resolution electrochemical imaging [115]. In this section, I will first focus on reporting the most widely applied fabrication techniques for different nanoelectrode configurations, especially those based on nanopipettes. Then, I will analyse electrochemical methods to characterise in real time key parameters of their geometry and response to external stimuli. Finally, I will discuss examples of using nanoelectrodes in single-molecule manipulation and detection, as well as single-cell probing and analysis.

2.5.1 Fabrication of nanoelectrodes

In the currently available literature, a wide range of nanoelectrode types have been presented based on numerous geometries such as disk-shaped, hemispherical, ring-shaped, band-shaped, cylindrical and interdigitated (IDEs) [114]. Over the years, several approaches have been developed and adopted to fabricate nanoelectrodes with these geometries. The first one follows bottom-up manufacturing processes including photolithography, electron beam lithography and focused ion beam (FIB) milling where a metal layer is formed either on the top or bottom of a substrate [115]. These techniques are mainly used to fabricate interdigitated or arrays of nanoelectrodes, as shown in Section 2.2.5, for the work of Barik et al. (2016) [69] where they constructed nanogap gold micro-electrodes based on a combination of atomic layer lithography, photolithography and tape peeling. A layer of alumina (Al_2O_3) was deposited on top of a patterned gold (Au) substrate via atomic layer lithography (Figure 2.16a). Then, another layer of Au was deposited on top of the alumina without making a contact with the bottom Au substrate. The excess gold layer was peeled off to form the nanogap between two electrodes. Lastly, lithography and ion milling were used to create an array of such electrodes [69].

The second fabrication method is based on electrochemical or thermal etching of thin cylindrical metal wires, usually platinum (Pt), which results in nanoelectrodes with a conical-shaped tip. Slevin et al. (1999) [116] achieved this by fitting Pt microwires inside

glass needle-like capillaries after laser-pulling them. The protruding wire at the capillary's tip was placed at the centre of a counter ring-shaped Pt electrode inside an electrochemical etching solution where a sharp point was formed after the application of an AC bias (Figure 2.16b). The resulting microwire was insulated by paint electrodeposition. By slightly adjusting this procedure, Sun et al. (2001) [117] and Watkins et al. (2003) [118] managed to fabricate nanometre-sized Pt electrodes while, much earlier, Strein and Ewing (1992) [119] had already achieved sub-micron electrodes fabrication by using carbon fibres instead of metal wire inside a glass capillary.

Another widespread fabrication technique for nanoelectrodes has been reported by laser pulling metal wires, mainly Pt again, inside glass capillaries [115]. A commercial laser-based micropipette puller heats and seals the glass and wire surfaces inside, as illustrated in Figure 2.16c. Further heating is applied to pull the capillary and wire apart at their two ends, resulting in two almost identical conical-shaped nanoelectrodes which are insulated along their circumference by glass [115]. Small amounts of glass that might have remained on the metal tip of the nanoelectrode could be removed by either polishing or chemical etching procedures. In 2002, Katemann and Schuhmann [120] demonstrated fabrication of Pt nanoelectrodes with a diameter as small as 10 nm after polishing them via rotation on a polishing plate inside a drop of water.

The last nanoelectrodes fabrication method mentioned in this short review depends on the pyrolytic deposition of carbon inside quartz glass capillaries [115]. In this procedure, an organic gas (methane, butane, acetylene or mixture) is injected into quartz glass capillaries, heated up to high temperatures (~1000 °C) at which it gets thermally decomposed, and fills the capillary with deposited graphitic carbon. In 1978, Blaedel and Mabbott [121] presented pyrolytic carbon film electrodes inside glass rods after filling them with natural gas that did not contain oxygen and heating in with a torch. Wong and Xu (1995) [122] used methane, instead, for their gas source and managed to construct carbon electrodes with diameter close to 100 nm under 4 minutes, whereas McNally and Wong (2001) [123] achieved it with acetylene. Moreover, glass nanopipettes have been filled reproducibly with carbon via chemical vapour deposition (CVD) where the capillary is placed in a furnace that reaches the required temperature under a gaseous mixture which contains Argon (Ar) and methane [93], [124]–[129]. The formed disk-shaped or cavity-like carbon nanoelectrodes at their tip can be optimised either by chemical etching, to remove glass and expose carbon further [124], [125], or focused ion beam (FIB) milling, to make the tip surface smoother and more homogeneous [126].

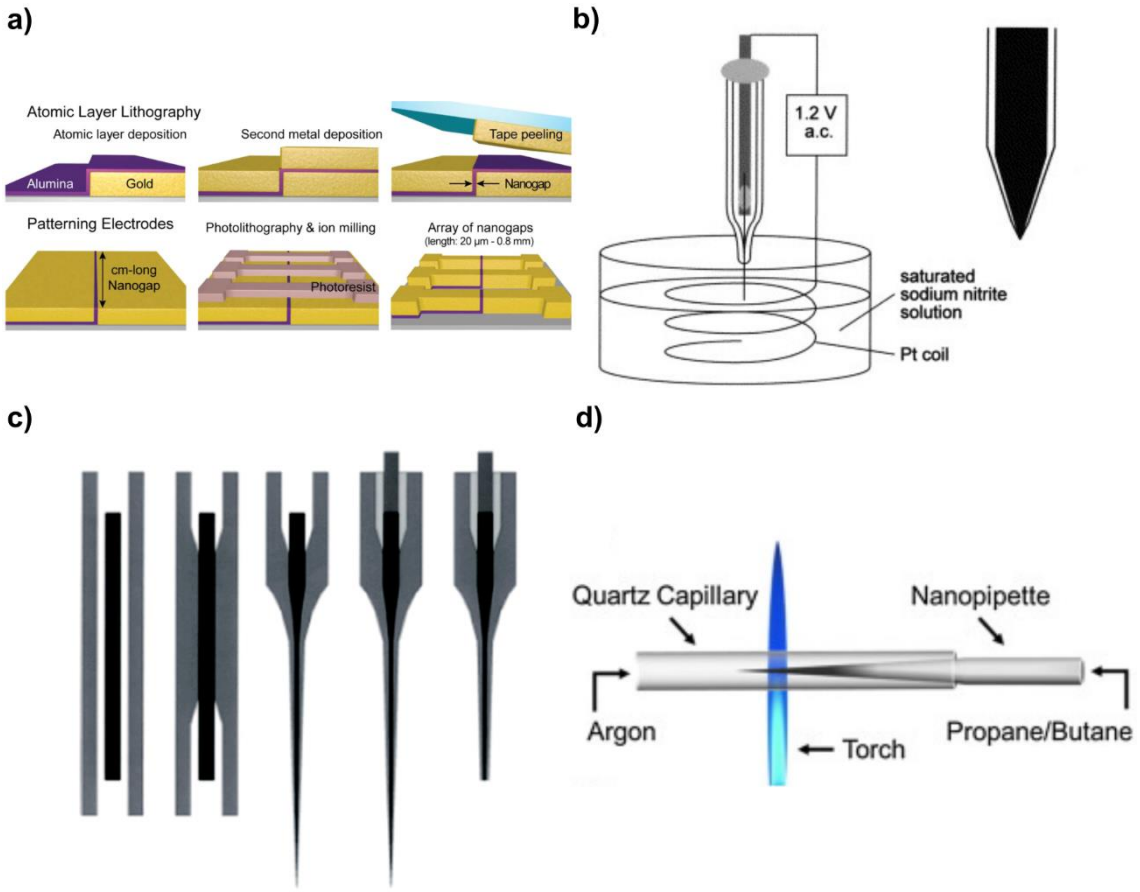

Figure 2.16 Schematic illustrations for most common fabrication techniques of nanoelectrodes. **a)** Nanogap gold micro-electrodes based on a combination of atomic layer lithography, photolithography and tape peeling. A layer of alumina was deposited on top of a patterned gold substrate via atomic layer lithography. Then, another layer of Au was deposited on top of the alumina without making a contact with the bottom Au substrate. The excess gold layer was peeled off to form the nanogap between two electrodes. Lastly, lithography and ion milling were used to create an array of such electrodes. Reproduced from [69]. **b)** Platinum nanoelectrode with a conical tip surrounded by insulating glass. A Pt microwire was placed inside a glass needle-like capillary after laser-pulling it. The protruding wire at the capillary's tip was placed at the centre of a counter ring-shaped Pt electrode inside an electrochemical etching solution where a sharp point was formed after the application of an AC bias. The resulting microwire was insulated by paint electrodeposition. Reproduced from [116]. **c)** A glass capillary is heated at the middle of its longest dimension to initially bring in contact and seal the glass and metal wire surfaces inside. Further heating is applied to pull the capillary and wire apart at their two ends, resulting in two almost identical conical-shaped nanoelectrodes which are insulated along their circumference by glass. Reproduced from [120]. **d)** Butane gas was injected inside a quartz glass nanopipette and maintained at higher than the atmospheric pressure values. Then, the nanopipette tip was inserted into a glass capillary where Argon gas was flowing from the opposite direction to prevent oxidation of the tip during heating. Lastly, a Bunsen burner was used to heat the butane gas up to ~900 °C for a few seconds until it thermally decomposed and filled the nanopipette barrel with pyrolytic carbon. Reproduced from [132].

However, chemical vapour deposition is an expensive, time-consuming and not easily accessible technique for fabricating pyrolytic carbon nanoelectrodes. For this reason, a cost-effective and time-efficient benchtop alternative was introduced by Takahashi et al. (2011) [130] (Figure 2.16d). Initially, quartz theta glass capillaries (which have a similar cross-sectional geometry to the Greek letter θ) were laser pulled to form dual-barrel nanopipettes. Butane gas was injected to one of the two barrels, as the other one was blocked with an adhesive sealing, and maintained at higher than the atmospheric pressure values. Then, the nanopipette tip was inserted into a glass capillary where Argon gas was flowing from the opposite direction to prevent oxidation of the tip during heating. Lastly, a Bunsen burner was used to heat the butane gas up to ~900 °C for a few seconds until it thermally decomposed and filled the nanopipette barrel with pyrolytic carbon. McKelvey et al. (2013) [131] adopted the same technique to deposit pyrolytic carbon inside both barrels of theta capillaries and produced carbon nanoelectrodes with a nanometre-sized gap between them. Pyrolytic carbon was also deposited in single-barrel nanopipettes which could be further optimised by chemically etching their tip to expose larger surface of carbon [132].

Nevertheless, this benchtop method proved to be not as reproducible as chemical vapour deposition. To tackle this limitation, Wilde et al. (2018) [133] developed an automated configuration based on a moving heating coil for the fabrication of carbon nanoelectrodes. The basic principles follow the method mentioned in the previous paragraph with the main difference that, instead of a Bunsen burner, a heating coil was mounted on a moving stage around the nanopipette. The heat generated from this coil was controlled by a power supply and the temperature on the nanopipette tip was adjusted by moving the position of the coil which the authors programmed to achieve controlled values at specific time intervals. Although they managed to improve the reproducibility rate, further modification of the carbon nanoelectrodes tip was suggested by either chemical etching or focused ion beam (FIB) milling. Recently, an additional polishing strategy was introduced by Gao et al. (2022) [134] where paraffin coating protection was used to avoid breaking the surrounding glass material. The process was monitored in real time with an impedance meter to form homogeneous and smooth carbon nanodisk electrodes, removing any existing irregularities on their surface. Finally, nanopipettes can be turned into electrodes by electrophoretic deposition of different metals, such as gold, platinum, silver and copper, on their tips [135].

2.5.2 Characterisation of nanoelectrodes

Small differences or inconsistencies in the geometry of a nanoelectrode could lead to changes in their electrochemical properties [136]. Consequently, characterising their shape and size are of significant importance for undertaking sensitive measurements. Nanoelectrodes are usually characterised by electron-based microscopy, either scanning electron microscopy (SEM) or transmission electron microscopy (TEM), as well as numerous electrochemical techniques. Although electron microscopy provides detailed characterisation for the geometry of a nanoelectrode, with SEM mapping mainly its outer and TEM its inner size and shape, the presence of insulating materials (i.e., glass) causes charging effects under imaging conditions which could limit the spatial resolution of each instrument [115]. In contrast, electrochemical techniques have the advantage of achieving a quick estimate of the nanoelectrode size if its geometry is known or predicted in advance. Nevertheless, any results obtained from such methods require verification with electron microscopy.

Scanning electron microscopy has demonstrated the ability to characterise the three-dimensional geometry of nanoelectrodes with a spatial resolution on the order of 1 to 2 nm which depends though on the instrumentation, the skills of the operator and the conductance of the nanoelectrode [136]. Figure 2.17a displays an SEM image of a Pt disk-shaped nanoelectrode with a radius of approximately 200 nm encapsulated in quartz glass. Transmission electron microscopy can achieve higher spatial resolution than SEM, but specific configurations and mounting stages for nanoelectrodes are required to obtain clear images [115]. Figure 2.17b shows a TEM image of a Pt disk-shaped nanoelectrode of 3 nm radius sealed in quartz glass. Here, the high-energy electrons used in TEM, penetrated the thin insulating glass domain and provided a two-dimensional representation of the Pt nanoelectrode at the centre due to the contrast between the nanowire and surrounding quartz. In general, as the insulating domain becomes thicker, the more difficult gets to acquire a clear TEM image of the nanoelectrode [136].

Traditional electrochemical techniques, such as voltammetry, have also been implemented for the characterisation of nanoelectrodes [114]. Usually the reduction and oxidation (phenomena related to exchange of electrons) processes of reactive molecules in electrolyte solution are examined by measuring the generated current between the nanoelectrode and a counter macroelectrode (diameter > 20 μm) after the application of DC bias. While for macroelectrodes in solution mass transport occurs perpendicular to the surface of the electrode (left schematic in Figure 2.17c), once its dimensions reach the sub-micrometre regime radial diffusion emerges as well with its field distribution

depending always on the size and shape of the electrode (right schematic in Figure 2.17c) [114]. Due to the small size of nanoelectrodes, a stationary diffusion layer is rapidly established adjacent to its interface with the aqueous solution leading to relatively high mass transport locally. This phenomenon is called steady-state mass transport and once established, the cathodic and anodic curves in a cyclic voltammogram (CV) overlap each other in a sigmoid-like (“S”) trend [136] (Figure 2.17d).

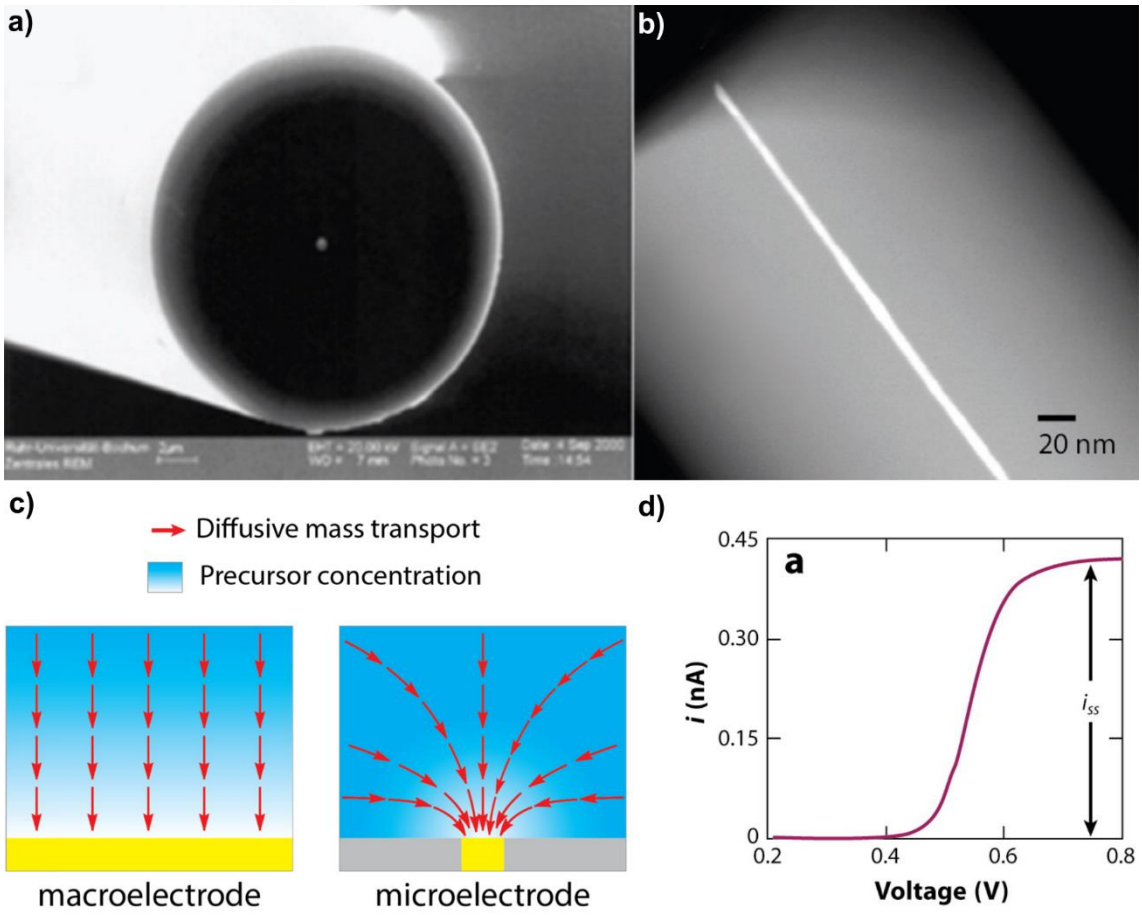

Figure 2.17 Nanoelectrode characterisation techniques. **a)** A scanning electron microscope (SEM) image of a 220 nm Pt disk-shaped nanoelectrode encapsulated in quartz glass. Reproduced from [136]. **b)** A transmission electron microscope (TEM) image of a 6 nm Pt disk-shaped nanoelectrode encapsulated in quartz glass. Reproduced from [136]. **c)** Schematic illustration for diffusive mass transport field distribution on a macroelectrode and microelectrode surface. Reproduced from [114]. **d)** The steady-state voltametric (current-voltage) response of a 172 nm Pt disk-shaped nanoelectrode in an electrolyte solution containing a redox mediator. The electrode radius is estimated from the magnitude of the steady-state limiting current (i_{ss}), the concentration (c_r) and diffusion coefficient (D_r) of the dissolved electroactive mediator. Reproduced from [136].

In chronoamperometry, the generated diffusion-limited steady-state current (i_{ss}) between a disk-shaped nanoelectrode and a counter macroelectrode when immersed in an electrolyte solution with dissolved electroactive mediator can be described by Oldham's equation, a modified version of Cottrell's general equation (not described here), as follows [137]:

$$i_{ss} = 4n_e F D_r c_r r_e \quad (2.5),$$

where n_e is the number of electrons exchanged between the redox molecule and the electrode's surface, F is Faraday's constant, r_e is the radius of the disk-shaped nanoelectrode surface, D_r and c_r is the diffusion coefficient and bulk concentration of the redox mediator dissolved in the electrolyte solution, respectively. The value of i_{ss} is obtained from the sigmoidal steady-state voltammogram, similar curve to the one presented in Figure 2.17d, by subtracting its magnitude at the plateau region (at ~0.8 V) with the intercept at 0 V [114]. Alternative modified forms of the Cottrell equation describe various shapes of nanoelectrodes. A more detailed explanation and analysis is provided in Chapter 3 where cyclic voltammetry was applied to characterise nanopipette-based carbon electrodes in a solution that contains hexaammineruthenium chloride and potassium chloride.

Despite the various electrochemical techniques developed to assess the geometry of nanoelectrodes, almost none has demonstrated a comprehensive and real time analysis [115]. If the properties of the redox species are known in advance, the diffusion-limited steady-state current is used only to estimate the size of a nanoelectrode. For instance, potential absorbance of contaminants on the electrode's surface during the electrochemical measurements could significantly affect the current magnitude leading to underestimation of its surface diameter. Consequently, electron microscopy imaging (SEM or TEM) of nanoelectrodes is suggested to verify any estimation of their size or shape obtained by electrochemical analysis. Ideally, a combination of both methods should be undertaken to characterise with as high resolution as possible the geometry of a nanoelectrode [115].

2.5.3 Applications of nanoelectrodes

In Section 2.2.5, where a few examples of single-molecule manipulation were presented, trapping and detection with different configurations of nanoelectrodes [10], [69], [70], [73]–[75]. Here, some additional applications are mentioned to highlight their high sensitivity and spatial resolution. To start with, the size, shape, concentration and diffusion coefficients of nanoparticles were determined accurately after observing

electrochemically individual collision events on a carbon nanoelectrode's surface [132]. In addition, the same electrode type was utilised to attach individual nanoparticles on its surface and study their intrinsic electrocatalytic behaviour [138]. Yang et al. (2019) [129] fabricated cavity carbon nanopipette electrodes and used this open-tube geometry to perform fast-scan cyclic voltammetry to detect neurotransmitters, such as dopamine molecules. Moreover, stochastic detection of individual freely diffusing in solution redox molecules was achieved upon repeated oxidation and reduction processes between two closely spaced (70 nm) electrodes in a microfabricated nanofluidic device [139].

Nanoelectrodes have also been used as imaging probes. In 2011, Takahashi et al. [130] introduced dual-barrel carbon nanoelectrodes for probing chemical and topographical properties of a solution or substrate, respectively. These techniques are called scanning electrochemical microscopy (SECM) and scanning ion conductance microscopy (SICM) [131]. Finally, nanoelectrodes have proved a promising tool for conducting experiments inside living cells due to their minimally-invasive and spatially controllable properties. Actis et al. (2014) [140] functionalised carbon nanopipette-based electrodes with Pt to penetrate tissue (brain slices) or isolated living cells and perform electrochemical measurements without affecting their function. In the same year, Li et al. (2014) [94] claimed successful amperometric observation of individual exocytotic events inside single synapses. A similar configuration and technique were utilised by Marquitan et al. (2016) [141] to quantify intracellular hydrogen peroxide molecules in a single-cell level.

Chapter 3
Nanotweezers fabrication and characterisation

3.1 Introduction

As discussed in the previous chapter, the combination of two nanopipette-based electrodes, when immersed into an aqueous medium, offers an alternative type of dielectrophoretic tweezers. Such a configuration was demonstrated by Nadappuram et al. (2019) [10] where minimally invasive dielectrophoretic nanotweezers were developed and utilised for capturing and extracting individual biological molecules (proteins, nucleic acids), as well as single organelles (mitochondria), from living cells. These nanotweezers were based on a double-barrel nanopipette where both nanopores at its tip were filled with pyrolytic carbon and acted as two nanoelectrodes with a separation distance of approximately 20 nm. The application of AC voltages produced high electric field gradients close to the electrodes which led to the trapping of single entities.

In this chapter, I will discuss how quartz glass single- and double-barrel nanopipettes are fabricated via laser pulling, how scanning electron microscopy and electrochemical measurements can be used to characterise the dimensions and geometry of these nanopipettes. Moreover, I will present an alternative method for fabricating nanopipette-based carbon electrodes based on an Arduino controller. Then, SEM and cyclic voltammetry are utilised to geometrically characterise these nanoelectrodes. Finally, additional modification of the nanopipette tip by focused ion beam (FIB) milling will be demonstrated to create well-defined surfaces at the nanopipette tip.

3.2 Fabrication and characterisation of quartz glass nanopipettes

In this section, I explain the procedure of fabricating single-barrel and double-barrel quartz glass nanopipettes on a commercially available laser puller. Nanopipettes are a category of solid-state nanopores, shaped like truncated hollow cones with a tip orifice in the nanometre range [142]. Once fabricated, it is crucial to define their pore opening(s) size and insulating wall thickness at the tip. As described in the previous chapter, and in particular in Section 2.4.2, these properties of a glass nanopipette can be characterised by both scanning electron microscopy (SEM) and electrochemically. For simplicity, I performed these two techniques first for single-barrel nanopipettes for which the tip aperture is considered disk-shaped and then for the double-barrel ones that have two semi-elliptical pore openings with an insulating septum separating them at the tip. SEM measurements were undertaken first to verify with high accuracy the nanopipette's dimensions and to correlate them with the selected parameters on the laser puller. Then, their electrochemical resistance was quantified upon application of a bias between two electrodes in solution (one immersed inside the nanopipette and the other in an external bath solution). This measurement can be used to estimate the size of the nanopipette tip aperture and compare it with values obtained from SEM imaging.

3.2.1 Fabrication of quartz glass nanopipettes

At first, single-barrel capillaries with filament (QF120-90-10) were selected for tuning the parameters of the laser puller to obtain nanopipettes with a tip aperture in the hundreds of nanometres range (~100 – 400 nm). Their outer and inner diameters are equal to 1.2 mm and 0.9 mm (see Figure 3.7b, Section 3.6.1), respectively, and match the dimensions of the double-barrel quartz glass capillaries (see Figure 3.7c, Section 3.6.1) that will be eventually used for fabricating the desired nanopipettes. Consequently, any set of parameters selected for the former is expected to provide similar results for the latter. The glass filament inside the single-barrel capillaries helps the wetting process. An in-depth analysis of this technique is presented in Section 3.2.3.

Table 3.1 Laser-puller parameters programme (Programme 1) for fabrication of nanopipettes with long taper and ~120 nm tip aperture.

Line	Heat	Filament	Velocity	Delay	Pull
1	770	4	30	125	95
2	770	3	40	130	150

Table 3.2 Laser-puller parameters programme (Programme 2) for fabrication of nanopipettes with short taper and ~400 nm tip aperture.

Line	Heat	Filament	Velocity	Delay	Pull
1	750	4	30	150	80
2	625	3	40	135	150

Table 3.3 Typical laser pulling times for the fabrication of single- and double-barrel nanopipettes after the application of Programmes 1 and 2.

Quartz glass capillary	Laser puller programme	Pulling time (s)
QF120-90-10	1	6.46
QF120-90-10	2	9.92
QT120-90-7.5	1	11.92
QT120-90-7.5	2	16.37

After multiple adjustments in the “Heat”, “Filament”, “Velocity”, “Delay” and “Pull” values of the laser puller (for more information refer to Section 3.6), two types of single-barrel nanopipettes were achieved. The first one had a longer taper and tip aperture approximately equal to 120 nm, while the second one had a shorter taper and tip aperture approximately equal to 400 nm. Besides the difference in the nanopipette pore opening, the taper length is expected to be an important factor in the nanopipette’s structural integrity during the pyrolytic carbon deposition. The two-line laser puller programmes, Programmes 1 and 2, are shown in Table 3.1 and Table 3.2 above. Here, it is worth noting that the laser puller parameters are instrument specific and may vary from pull to pull [10], [73], [143]. Furthermore, the same set of parameters was used to fabricate double-barrel nanopipettes. As mentioned in Section 3.6.2, when the time required to complete the laser pulling of a specific type of capillaries (pulling time) does not exceed the average value by more than 10%, it can be assumed that the shape and size of the nanopipette is reproducible. However, it is expected that the pulling time of double-barrel capillaries will be significantly larger than the one for single-barrel because of the additional glass domain at their centre instead of just a filament. A few examples of these pulling times are listed in Table 3.3.

3.2.2 SEM imaging characterisation of quartz glass nanopipettes

Scanning electron microscope (SEM) imaging was performed on fabricated quartz glass nanopipettes to obtain an accurate understanding of their shape as well as measure the dimensions of their tip aperture and surrounding insulating wall thickness. Figure 3.1 presents a representative SEM micrograph for every nanopipette type fabricated throughout this project. The side view of a single-barrel nanopipette with filament fabricated with Programme 1 verifies the approximately conical-shaped geometry of its taper which is hundreds of micrometres long, as shown in Figure 3.1a. The external non-linear shape variations along its vertical length agree with the findings from Perry et al. (2016) [144] who characterised with high precision the geometry of such nanopipettes by transmission electron microscopy (TEM) imaging. At higher magnification, the pore opening and insulating wall thickness at the sample's tip (Figure 3.1b) were found equal to 130 ± 10 nm and 32 ± 2 nm, respectively.

The glass filament forms a small cylindrical domain inside the nanopipette's pore which aids in filling the nanopipette with aqueous solution until the end of the tip when its diameter is small (< 100 nm). Mean and standard error of the mean values were acquired after 5 repetitions for each length. Moreover, a single-barrel nanopipette without filament, fabricated with Programme 1, had a tip aperture diameter equal to 136 ± 10 nm and wall thickness equal to 27 ± 6 nm (Figure 3.1c). These dimensions are in close agreement with the ones stated above for a nanopipette with filament. However, when Programme 2 was selected for the fabrication of single-barrel nanopipettes without filament, its tip aperture increased to a 522 ± 27 nm diameter, as displayed in Figure 3.1d.

Interestingly, the same effect was observed for double-barrel (theta) nanopipettes, although their tip geometry is considered elliptical rather than circular. Following the schematic in Figure 3.5b of Section 3.6, a rectangle of width w splits the ellipse at the centre into two semi-ellipses (pore apertures) surrounded by a concentric elliptical shell of thickness t. These semi-ellipses have a common minor axis h and a major semi-axis a which would be equivalent to half of the major axis of an ellipse. In fact, Programme 1 provided two slightly different semi-elliptical pore openings at the tip $(a_1 \neq a_2)$. For the top opening in Figure 3.1e, a_1 = 47 ± 3 nm, while for the bottom one a_2 = 31 ± 1. The minor axis, separating glass septum width and surrounding wall thickness were h = 87 ± 3 nm, w = 12 ± 2 nm and t = 13 ± 2 nm, respectively.

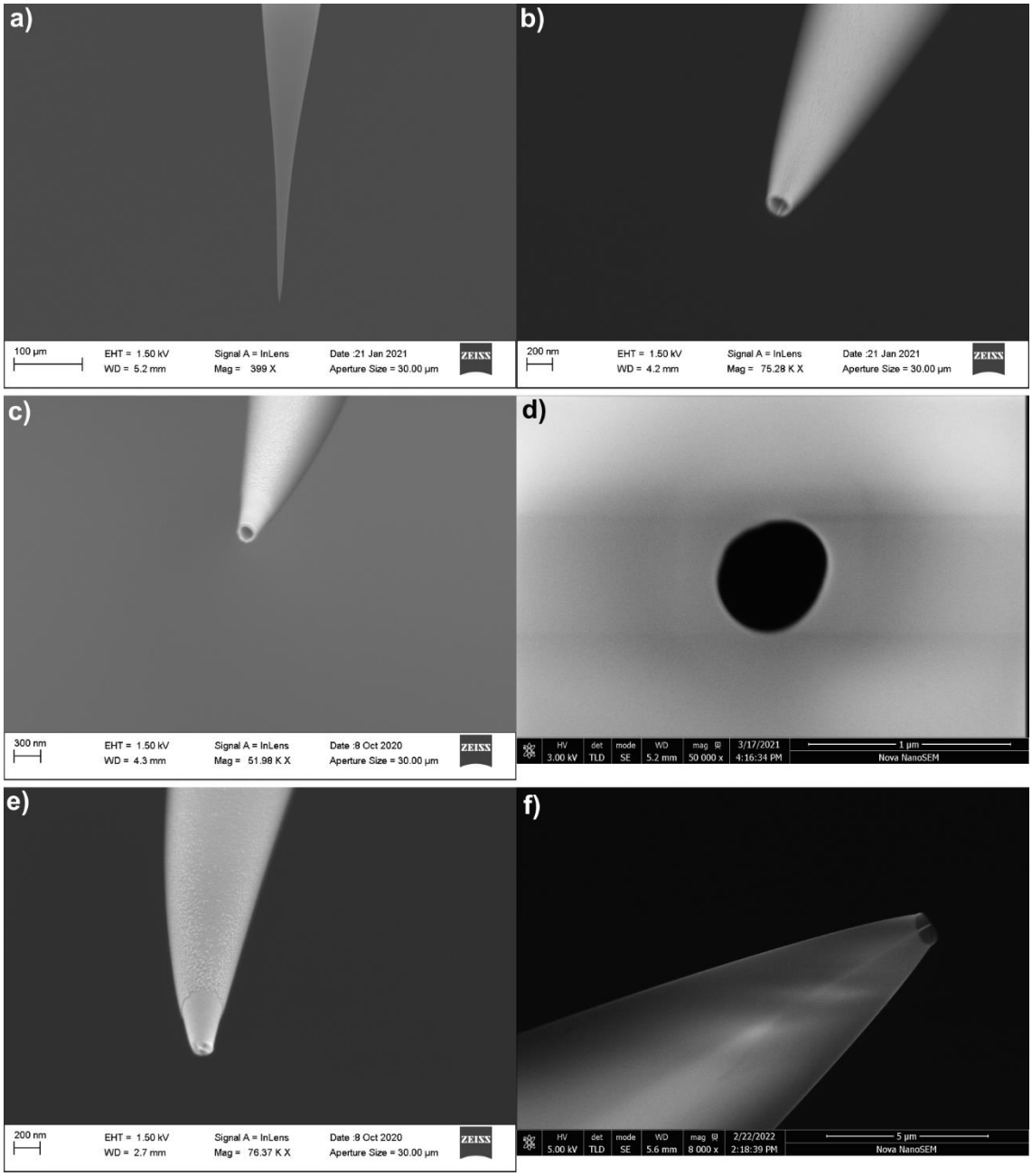

Figure 3.1 SEM images for quartz glass nanopipettes. **a)** Side view of a single-barrel nanopipette taper demonstrating its approximately conical-shaped geometry. **b)** Tilted view (~30°) of a single-barrel nanopipette with filament focusing on its 130 nm tip aperture. **c)** Tilted view (~30°) of a single-barrel nanopipette focusing on its 136 nm tip aperture. **d)** Bottom view of a single-barrel nanopipette focusing on its 522 nm tip aperture. **e)** Tilted view (~30°) of a double-barrel nanopipette focusing on its semi-elliptical tip apertures (a_1 = 47 ± 3 nm, a_2 = 31 ± 1 nm). **f)** Tilted view (~30°) of a double-barrel nanopipette focusing on its semi-elliptical tip apertures (a_1 = 545 nm, a_2 = 437 nm). Note that images in panels a), b), c) and e) were acquired by myself in the cleanroom facilities of the University of Leeds. All nanopipettes were fabricated with Programme 1 and sputtered externally with a ~5 nm iridium layer to aid with imaging. Images in panels d) and f) were acquired with the help of Dr Alexander Kulak (School of Chemistry, University of Leeds). These nanopipettes were fabricated with Programme 2 and imaged without any modification.

In addition, the application of Programme 2 resulted also in two not completely symmetrical semi-elliptical pore openings at the tip ($a_1 \neq a_2$, Figure 3.1f). For the top opening, a_1 = 545 ± 1 nm and for the bottom one a_2 = 437 ± 2 nm. The minor axis, separating glass septum width and surrounding wall thickness were h = 599 ± 1 nm, w = 33 ± 6 nm and t = 18 ± 3 nm, respectively. The mean and standard error of the mean values were obtained after 5 measurements for each dimension. Overall, this slight asymmetry in the tip geometry is attributed to the laser beam heating first one side of the glass.

3.2.3 Electrochemical characterisation of quartz glass nanopipettes

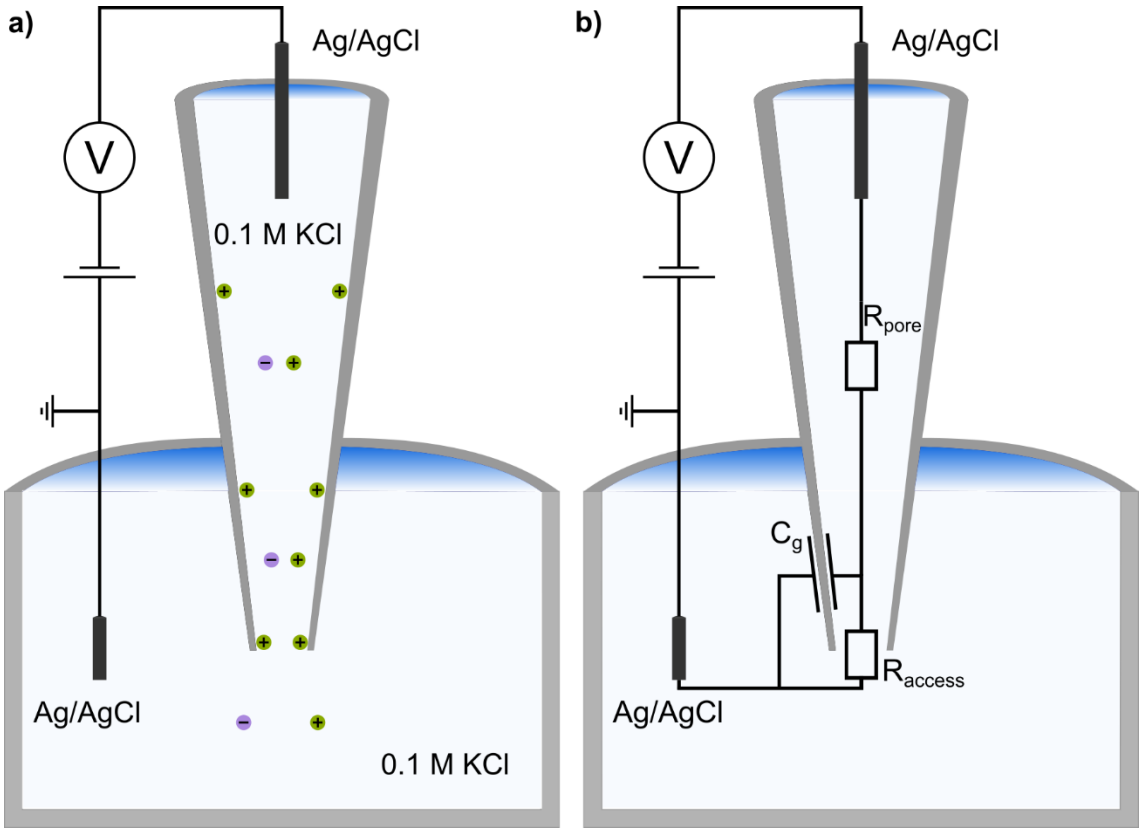

Figure 3.2 a) Schematic illustration of the experimental configuration for the electrochemical characterisation of a nanopipette filled with and immersed in 0.1 M KCl. **b)** The equivalent electrochemical circuit of the nanopipette system. The resistance inside the nanopipette pore (R_{pore}) together with the resistance between the tip opening and the surface of the external bath walls (R_{access}) compose the total resistance of the circuit which can be analytically estimated by Equation 3.1.

The experimental setup for the electrochemical characterisation of quartz glass nanopipettes is illustrated in Figure 3.2a. A nanopipette with filament was filled with 0.1 M KCl electrolyte solution and immersed into an external bath containing 0.1 M KCl solution. A complete electrochemical circuit was established when an Ag/AgCl quasi-reference electrode was immersed in this external bath and a second Ag/AgCl electrode (0.25 mm in diameter, GoodFellow, Huntingdon, UK), which acted as the working electrode, was inserted in the nanopipette. When a DC potential bias is applied between these two electrodes, anodic or cathodic electron exchange, depending on its polarity, is described by $Ag + Cl^- \rightarrow AgCl + e^-$ or $AgCl + e^- \rightarrow Ag + Cl^-$, respectively [145]. Consequently, for a negative bias K^+ ions are attracted towards the electrode inside the nanopipette and simultaneously Cl^- ions are transferred towards the electrode in the external solution.

However, the surface of glass nanopipettes is negatively charged and when immersed in an aqueous solution an electric double layer of mainly opposite charges is formed at this interface. A detailed explanation of this phenomenon is included in Chapter 5 where the conductivity of a spherical particle is measured in solution. Due to this layer of positive charges, the recorded current at negative biases will be larger than the one at positive bias. This phenomenon is called ion current rectification and has been analysed extensively for glass nanopipettes [145]. If the nanopipette is assumed as a shortened truncated hollow cone, then the electrochemical resistance of this circuit can be analytically calculated. As Figure 3.2b displays, the total resistance (R) is a combination of the resistance inside the conical pore (R_{pore}) with the resistance (R_{access}) between the pore opening at the tip and any substrate in close proximity (external bath walls) [144]. The nanopipette glass walls are considered as capacitors (C_g).

Following this hypothesis, the resistance of a single-barrel quartz glass nanopipette filled with and immersed in the same electrolyte solution depends on its tip aperture radius (r_{tip}), length of the pore (L_{pore}), electrical conductivity of solution (σ_m), inner half-cone angle (θ_{pore}) and is described by the following equation [146]:

$$R = R_{pore} + R_{access} = \frac{L_{pore}}{\pi \sigma_m r_{tip}\left(r_{tip} + L_{pore}\tan\left(\theta_{pore}\right)\right)} + \frac{1}{4\sigma_m r_{tip}} \qquad (3.1),$$

which for $L_{pore}\tan\left(\theta_{pore}\right) \gg r_{tip}$ [144] simplifies to:

$$R = \frac{1}{\sigma_m r_{tip}} * \left(\frac{1}{\pi \tan\left(\theta_{pore}\right)} + \frac{1}{4}\right) \qquad (3.2).$$

The condition $L_{pore}\tan\left(\theta_{pore}\right) \gg r_{tip}$ is assumed valid for nanopipettes, so Equation 3.2 will be applied for the analysis below. Nevertheless, it is worth clarifying that this

approach relies heavily on the rough estimation that the inner-half cone angle of the nanopipette is constant throughout its entire length. Perry et al. (2016) [144] proved that accurate nanopipette characterisation is achieved by combining different methods, such as TEM and optical microscopy. This study demonstrated that the nanopipette's geometry is not described by an ideal truncated cone because its inner and outer half-cone angles change gradually along its length. Despite their findings, this electrochemical technique is still applied extensively for rough estimations of a nanopipette's tip size and shape [147]. When combined with SEM images of the tip, the electrochemical resistance provides a time-efficient alternative to verify the reproducibility of its geometry.

Based on the conclusions above, the electrochemical resistance of a quartz glass nanopipette was recorded with a patch-clamp amplifier (MultiClamp 700B, Molecular Devices, San Jose, CA, USA) in voltage-clamp mode. In this configuration, one electrode was used to measure the voltage and the other one to provide the current required to keep the recorded voltage constant in the cell. At a gain of 1, the amplitude of the current output pulse, which usually is in the millivolts range but depends on the nanopipette geometry, corresponded to 1 nA. Therefore, the nanopipette resistance obtained from the amplifier's software is calculated from Ohm's law $(R = V/I)$. Table 3.4 lists some of the measured resistance values for single-barrel quartz glass nanopipettes with or without filament, fabricated with either Programme 1 or 2.

Table 3.4 Typical resistance values for single-barrel quartz glass nanopipettes with or without filament fabricated with Programme 1 or 2. The measured tip radius of nanopipettes fabricated with the same programmes are included as well as the estimate values for θ_{pore}.

Sample	Capillary	Programme	R (MΩ)	$r_{tip}^{SEM} \pm \delta r_{tip}^{SEM}$ (nm)	θ_{pore} (°)
1	Q120-90-7.5	2	7.6	261 ± 14	7.79
2	Q120-90-7.5	2	7.7	261 ± 14	7.68
3	QF120-90-10	1	26.2	68 ± 5	8.77
4	QF120-90-10	1	27.6	68 ± 5	8.28
5	QF120-90-10	2	7.2	261 ± 14	8.27
6	QF120-90-10	2	7.4	261 ± 14	8.02

Single-barrel nanopipettes fabricated with Programme 1 had an electrochemical resistance of approximately 7.5 MΩ, while the resistance for ones fabricated with Programme 2 was between 26.2 MΩ and 27.6 MΩ. Based on Equation 3.2, the tip radii obtained from SEM imaging (Section 3.2.2) and a solution conductivity of 1.299 S/m (for

more information see Section 3.6.4), the inner half-cone angle for each sample was estimated. The mean and standard of the mean error for the values in the last column of Table 3.4 were equal to 8.1 ± 0.2°. By considering this value constant for every fabricated nanopipette in this work, their tip aperture can be evaluated based on Equation 3.2 and compared with the respective values obtained with SEM imaging. Each time the resistance changed significantly from the values above, the laser puller parameters were optimised to compensate this effect and produce again the expected results.

3.3 Fabrication of carbon nanopipette-based electrodes

As mentioned in Section 2.5.1, carbon nanopipette-based electrodes are commonly fabricated by pyrolytic carbon deposition which is based on thermal decomposition of a hydrocarbon gas. Usually, a mixture of butane and propane is heated to high temperatures (~1000 ℃) leading to deposition of graphitic carbon (porous material) on the surface of the inner pore(s) of the nanopipette until it completely fills the nanopipette opening [148]. So far, fabrication of carbon nanopipette-based electrodes has been achieved mainly by two configurations. The first one was reported by Takahashi et al. (2011) [130] (refer to Section 2.5.1), where a quartz glass nanopipette was filled with an organic gas, its tip was sealed inside another quartz capillary from where Argon gas was flowing towards the tip to create inert conditions and prevent oxidation. Then, a gas blow torch heated the tip of the nanopipette until carbon was fully deposited inside its pore.

The limiting factor of this technique is the gas blow torch. Heating is the most crucial aspect for the reproducibility of the process, and the blow gas torch output fluctuates during every run due to the consumption of its fuel source. Additionally, the distance between the flame and the nanopipette tip could not be accurately controlled which adds further variability. My first attempts for fabricating carbon nanopipette-based electrodes following this technique provided a ~10% successful yield. This percentage was deemed insufficient for the number of nanoelectrodes required for the purposes of this project, as well as cost-ineffective due to wasting many glass capillaries. Here, it is worth clarifying that only quartz capillaries are suitable for this procedure as its material properties are maintained intact at the high temperatures applied during carbon deposition. Other commercially available capillaries, such as borosilicate glass, have not been used so far due to their intolerance to such high temperatures [10], [75], [130]–[134].

To tackle this issue, in 2018, Wilde et al. [133] developed an automated configuration based on the key aspects of the previous instrumentation but replacing the blow gas torch with a conductive coil-shaped wire. This heating coil was connected to a power supply, which provided the required current to achieve high temperatures around it, and it was also mounted on a moving stage to increase or decrease the produced temperature by bringing it closer or away from the area of interest. At first, a sensor that mimicked the nanopipette tip probed the temperature in real time and was used to create a heating profile that would achieve carbon pyrolysis. Then, the nanopipette was placed at the centre of this coil instead and was heated following this profile. The automated procedure reached a significantly higher fabrication yield compared to the one previously

mentioned but increased considerably the complexity and cost of the fabrication process. Nevertheless, when compared to other pyrolytic deposition techniques, the instrumentation by Wilde et al. (2018) [133] is considered easier to use and more cost-efficient.

Inspired by the last configuration, a slightly different version from the setup reported by Wilde et al. (2018) [133] was constructed which achieved also an improved fabrication rate of disk-shaped nanoelectrodes compared to the one based on Takahashi et al. (2011) [130]. In this configuration, shown in Figures 3.3a and 3.10, the moving stage was replaced with an Arduino system connected to a DC power supply and a K-type temperature probe (Omega) mounted inside the counter-flow ceramic capillary. The Arduino was programmed to read the temperature in real time (1 count/sec) and control the output from the power supply, hence the heat generated by the coil, to achieve specific temperature values at selected time points. Probing the temperature experienced by the nanopipette tip in real time, allowed any variation in the heat produced by the coil to be compensated through the PID-controller and power supply system so that the desired values were reached.

This configuration allows complete control of the most important parameter in the pyrolysis process and offers good reproducibility. The overall process takes less than 10 minutes, is compatible with both single- and double-barrel nanopipettes, while the successful fabrication of disk-shaped nanoelectrodes increases to approximately 33%. A detailed operational protocol is provided in Section 3.6.6. In brief, the fabricated quartz nanopipette is mounted under the coil with its tip sealed and protected inside another ceramic capillary, as shown in Figure 3.3a, where Argon gas is constantly flowing at low rates to create an inert environment for the nanopipette tip and aid with its cooling after the maximum temperature is reached. The thermometer sensor is also fixed inside this capillary. At this point, the nanopipette is injected with a butane/propane gas until maximum pressure is achieved (usually ~3 bar) and then, Argon gas is used to reach a pressure of 4.2 bar which remains constant throughout the entire process. The heating coil delivers the designed temperature profile inputted in the Arduino controller (Figure 3.3b) which is run twice. During the first cycle, a thin layer of carbon is deposited on the inner nanopipette walls, while during the second one, carbon fills entirely the nanopipette pore forming a disk-shaped electrode at its tip. A macroscopic picture of a carbon nanopipette-based electrode is depicted in Figure 3.3c (black) next to a bare nanopipette (transparent). The black part of the nanopipette is where carbon has been deposited.

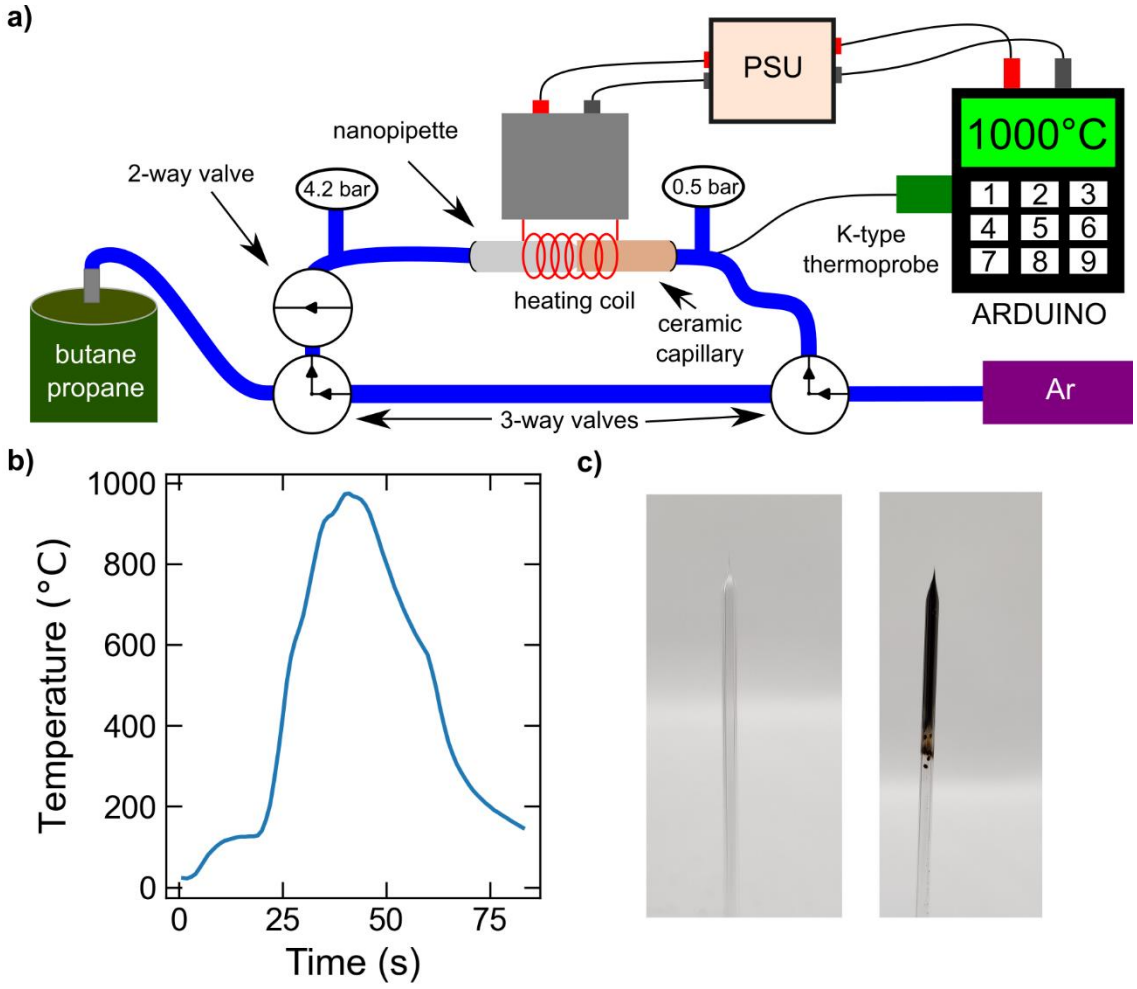

Figure 3.3 a) Schematic illustration of the Arduino-based pyrolytic carbon deposition configuration for the fabrication of carbon nanopipette-based electrodes. **b)** Temperature profile generated at the centre of the heating coil and experienced by the nanopipette tip. **c)** Pictures of a quartz glass nanopipette (transparent) and a carbon-filled nanopipette (black) fabricated by the Arduino-based setup.

Despite the increased success rate of this configuration, a significant number of nanopipettes (around 67%) could not be used as disk-shaped nanoelectrodes after the pyrolytic carbon deposition. Two observed phenomena responsible for this inefficiency were the glass wall melting at the tip, which resulted in either partial or complete occlusion of the deposited carbon surface (Figures B.1a and B.1d in Appendix Section B.1); and the formation of a “cavity” at the tip where a thin layer of carbon was formed inside the walls close to the orifice with a bulkier domain further inside connecting them (U-shaped geometry, Figures B.1b and B.1c in Appendix Section B.1). The former prevented electrical connection between the deposited carbon and electrolyte solution (open circuit), while the latter had a much longer active surface, equivalent to a macroelectrode, thereby losing the advantages a nanoelectrode offers. However, further

modification of the tip into a smooth, flat surface is possible with several techniques such as focused ion beam (FIB) milling [126], [133], chemical etching [75] or mechanical polishing [134]. In some cases, the electrode diameter at the tip aperture remains in the nanometre range and is fully functional.

FIB offers the most precise, time-efficient but also expensive milling compared to the other two techniques for both single- and double-barrel carbon nanoelectrodes. It is part of a dual-beam instrument that performs SEM imaging in parallel, offering real time feedback for accurate sample material etching. As already explained, SEM relies on an electron beam while FIB on an ion beam. In particular, a reservoir of gallium (Ga) is in contact with a conical tungsten tip (10 – 20 nm diameter) and upon the application of a high electric field, it flows towards the end of this tip [149]. Once Ga^+ ions are accelerated down the FIB column and towards the surface of the sample, they enter its bulk and remove particles causing material etching. Chen et al. (2016) [126] proved with TEM imaging that the focused Ga^+ beam is described by a Gaussian distribution with ~10 nm broadening at FWHM leading to a perfectly smooth tip of a nanopipette-based carbon electrode that is rounded at the edges.

It can also be conducted without sputtering conductive material on to the sample's surface, although this process is generally recommended for higher quality images. Furthermore, most carbon nanoelectrodes fabricated via pyrolytic deposition have a recessed tip (carbon does not reach the outer walls) and by applying FIB milling the hollow part of the tip is removed, exposing the formed disk-shaped surface. To achieve this with chemical etching, hazardous chemicals (i.e., potassium hydroxide) are required and further SEM imaging to verify the extent of glass etching. Mechanical polishing is probably the least accurate technique for nanometre-sized tips as it is polished against a hard surface which could cause uncontrolled breaking of the glass wall at the edges or unequal material removal for double-barrel nanoelectrodes. For the purposes of this work FIB milling was the only technique conducted for smoothing the carbon electrodes surface at the nanopipette tip and an extensive analysis is included in the following section.

3.4 Characterisation of nanopipette-based carbon electrodes

The fabricated nanoelectrodes, described in Section 3.3, were characterised both by SEM imaging and electrochemical voltametric measurements to investigate the dimensions of their tip orifice, glass wall thickness and separation gap between the two semi-elliptical electrodes for double-barrel nanopipettes. SEM imaging was performed in the same way as described in Section 3.2.2 for quartz glass nanopipettes with the difference that FIB milling was also performed for a small number of samples. Electrochemical characterisation was conducted by cyclic voltammetry. The tip size of disk-shaped carbon nanoelectrodes was determined analytically through the recorded current magnitude, the number of exchanged electrons, the concentration and diffusion coefficient of the redox mediator.

3.4.1 SEM imaging characterisation of nanopipette-based carbon electrodes

Disk-shaped carbon nanoelectrodes are expected to be obtained upon pyrolytic deposition. To assess this hypothesis, define their shape and measure their size at the tip region, scanning electron microscope (SEM) imaging was performed, as previously described in Section 3.2.2 and also in Section 3.6.3 for quartz glass nanopipettes. The samples were not sputtered externally with any metal layer to allow reusing them for electrochemical characterisation and force probe measurements. The potential addition of a conductive layer at the outer walls would give rise to unwanted electrochemical responses, affecting the characterisation of the carbon surface. Figure 3.4 shows typical SEM micrographs for two double-barrel semi-elliptical carbon nanoelectrodes (4 electrodes in total). In all images the external insulating domain of the nanopipette seems to remain intact following the heating procedure, isolating the deposited carbon inside and exposing only the surface formed close to the tip aperture. This finding proves that the pyrolysis setup developed for this project is capable of delivering the desired outcome. It should be noted that any geometries protruding from the outer glass wall are related to contamination after the fabrication procedure or during sample loading on the SEM instrument.

Nevertheless, as expected due to its small thickness (<100 nm), the glass wall at the tip orifice exhibited signs of melting leading to changes in its initial semi-elliptical shape (see

Figure 3.1f). For the double-barrel nanopipettes, the glass septum between the two nanoelectrodes acts as a supporting domain preventing complete collapse of the glass wall towards the centre which could potentially cause full sealing of the carbon surfaces. This phenomenon was observed more frequently for single-barrel carbon nanoelectrodes. A few examples of severe glass wall damage are included in Section B.1 (Figure B.1, Appendix B). In addition, recessed carbon deposition was observed at most nanoelectrodes tips. As depicted in the left channel of Figure 3.4d, carbon material does not extend until the end of the tip orifice. Instead, the image suggests that pyrolytic deposition occurred only inside the nanopipette pore. Since SEM imaging does not provide information for material properties inside the nanopipette, the actual dimensions of the formed carbon surface cannot be accurately determined. Instead, the pore opening and glass wall thickness at the tip are the only quantifiable parameters by assuming semi-elliptical geometries.

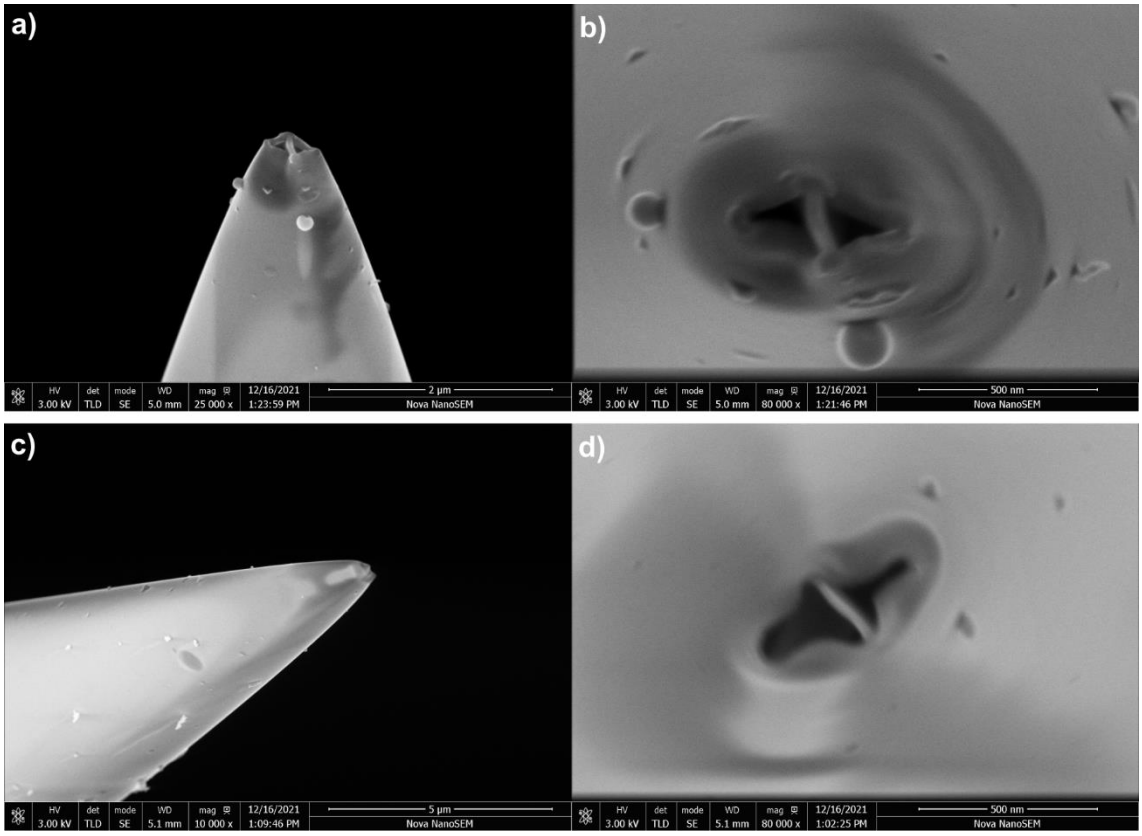

Figure 3.4 Scanning electron microscope (SEM) images for quartz glass double-barrel nanopipette-based carbon electrodes fabricated via the pyrolytic deposition procedure described in Section 3.3. These pair of nanoelectrodes were utilised as dielectrophoretic nanotweezers for single-molecule manipulation and force probing in Chapter 5. **a), c)** Side views of conically-shaped nanopipettes with two semi-elliptical openings at the tip. **b)** Top zoomed in view of the nanopipette tip shown in a). **d)** Top zoomed in view of the nanopipette tip shown in c). All SEM micrographs were acquired by Dr Alexander Kulak, as described in Section 3.6.3.

Based on the top view images in Figures 3.4b and 3.4d, both small and large variability between the two barrels were identified, respectively. The left barrel in Figure 3.4b had a major semi-axis (a_1) equal to 161 ± 2 nm and a minor semi-axis ($h/2$) equal to 81 ± 2 nm, while its right barrel had a 154 ± 2 nm major semi-axis (a_2). The glass septum separating the two barrels (w) was 62 ± 2 nm wide and the thickness of the glass surrounding wall (t) was equal to 59 ± 5 nm. Moreover, the left barrel in Figure 3.4d had a_1 = 234.4 ± 0.7 nm, a_2 = to 102 ± 5 nm and $h/2$ = 115.0 ± 3 nm, while w = 36 ± 2 nm and t = 75 ± 10 nm. The mean and standard error of the mean values were obtained after 5 measurements for each length in ImageJ.

These two examples demonstrated the level of variability in the dimensions of the fabricated carbon nanoelectrodes. While the geometry of the tip in Figure 3.4b is described by two almost symmetrical pore openings, the one in Figure 3.9d shows a slight difference between the major semi-axes ($a_1 \neq a_2$). Besides this, the pore openings (a_1, a_2, h), glass septum (w) and surrounding wall thickness (t) at the tip between the two carbon nanoelectrodes were all different. Although both quartz glass capillaries were initially laser pulled with Programme 2, which as explained in the previous section it was supposed to provide semi-elliptical openings with $a_1 \approx a_2 \approx$ 500 nm, the size of the tip orifices observed in Figure 3.4 were significantly smaller. This can be attributed to two factors: the pulling time during nanopipette fabrication and the degree of glass wall melting at the tip during pyrolysis. The former was diminished by keeping nanopipettes with similar laser pulling times, while the latter was largely uncontrollable.

This finding combined with carbon being recessed at the tip raised the need for further optimisation of the double-barrel carbon nanoelectrodes tip to increase reproducibility and control over their sizes and shape. The width of the glass septum (w) that separates the two nanoelectrodes at the tip is considered the most important parameter in this geometry. This distance determines the magnitude of the electric field gradient that can be generated upon the application of an electric potential between them, and hence the magnitude of the dielectrophoretic force applied on dielectric particles diffusing close to the nanopipette tip. Bringing the two nanoelectrodes' surfaces on the same plane significantly increases the control over the formed non-uniform electric fields between them which is highly desirable for the application of the nanotweezers in this work (Chapter 5). Such modification of the nanopipette tip was performed with focused ion beam (FIB) milling in parallel to SEM imaging. Further details about its operation and image analysis are included in Section 3.3 and 3.6.7.

In brief, Dr Stuart Micklethwaite (Leeds Electron Microscopy and Spectroscopy Centre, University of Leeds) milled both the insulating quartz glass and deposited carbon at the tip by accelerating Ga^+ ions perpendicular to the tip with a step as small as 10 nm until

a smooth surface was obtained. SEM imaging was performed at the same time to monitor the milling process. Based on the conical geometry that nanopipettes possess, it was expected that as material was being removed from the tip the size of the disk-shaped nanoelectrodes would increase proportionally. For this reason, it was crucial to mill as little material as possible so that nanometre-sized electrodes were not turned into microelectrodes. An in-depth analysis of the effect such changes in the nanopipette tip geometry would have on the generated electric field is provided in Chapter 4 via finite element simulations.

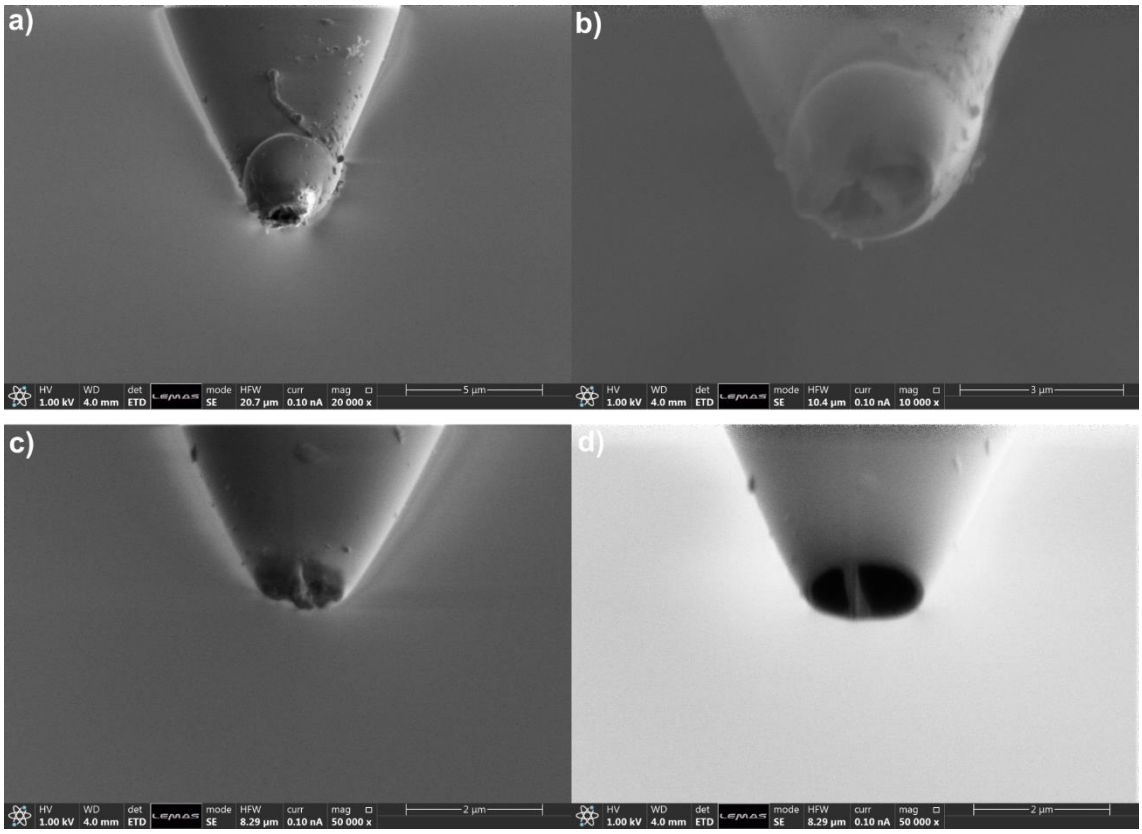

Figure 3.5 SEM images of quartz glass double-barrel nanopipette-based carbon electrodes **a)**, **c)** before and **b)**, **d)** after the application of focused ion beam (FIB) milling at the tip surface. Pipettes in the left column show carbon recession inside the semi-elliptical pores while the geometry at the tip orifice was rough due to the applied heating during pyrolysis. The same pipettes are shown in the right column following removal of excessive glass wall material by a focused beam of accelerated Ga^+ ions perpendicular to the tip surface, resulting in a smooth and flat surface where semi-elliptical carbon nanoelectrodes (black domain) are considered co-planar. Note that quartz glass theta capillaries were laser pulled with Programme 2 and the nanopipettes external wall was not sputtered with a conductive layer so that the carbon nanoelectrodes could be used as dielectrophoretic nanotweezers. Any protrusions in the geometry of the outer glass walls were due to salt contamination during electrochemical measurements that was not removed after cleaning. Dr Stuart Micklethwaite (LEMAS, University of Leeds) acquired the SEM micrographs and performed FIB milling at the regions of interest I selected.

Figure 3.5 depicts the difference in the tip geometry of double-barrel nanopipette-based carbon electrodes before and after the application of FIB milling. Focusing on the left column of Figure 3.5 (panels a, c), the roughness at the tip surface is evident as well as carbon being recessed inside the nanopipette pores, especially in panel c where the glass septum and surrounding wall were at different planes. Nevertheless, FIB milling allows the creation of a smooth and flat surface, turning the carbon nanoelectrodes into disk-shaped surfaces aligned in the same plane. Following the analysis included in Section 3.6.7 on measuring accurately lengths from SEM/FIB images (Figure 3.11b), the left barrel in Figure 3.5b had a_1 = 992 nm while for its right barrel a_2 = 928 nm. The minor semi-axis was found to be equal for the two barrels, h = 613 nm. The glass septum separating them was w = 541 nm and the thickness of the glass surrounding wall (t) was 398 nm.

In contrast to the high degree of symmetry between the two nanoelectrodes in Figure 3.5b, the tip geometry in Figure 3.5d had a_1 = 710 nm, a_2 = 887 nm, $h/2$ = 284 nm, w = 180 nm and t = 74 nm. This asymmetry originates from the way quartz glass capillaries are manufactured industrially and could not be optimised. The large differences between the septum width (w) and wall thickness (t) were due to larger portion of glass and carbon material being milled out of the nanopipette in panel b compared to the one in panel d. Two additional SEM images of FIB milled nanopipette-based carbon nanoelectrode are presented in Figure A.2 (Appendix A.1). Here, it is worth clarifying that in cases where perfectly flat and co-planar nanoelectrodes are not needed, imaging every one of them by SEM is time consuming and could affect its structural integrity (i.e., electrostatic charging, damage during sample handling). This technique to assess the size and shape of the nanoelectrodes tip should be used less frequently, and once the desired geometry has been achieved reproducibly, other quicker bench-top techniques should be applied, such as electrochemical characterisation by cyclic voltammetry which is explained in the next section.

3.4.2 Electrochemical characterisation of nanopipette-based carbon electrodes

Electrochemical characterisation of double-barrel nanopipette-based carbon electrodes based on voltametric techniques has been extensively applied in the past to estimate the nanoelectrode radius, as discussed in Section 2.5.2. In this work, cyclic voltammetry, which relies on oxidation (loss of e^-) and reduction (gain of e^-) processes of molecules in solution, was performed. The electrochemical circuit consisted of three electrodes: a

working (carbon nanoelectrode, WE), counter (Pt wire, CE) and reference (Ag/AgCl/3M KCl, RE) electrode (Figure 3.9). All three were connected to a potentiostat (VSP, BioLogic) from one end and immersed in a 0.1 M KCl supporting electrolyte including 10 mM RuHex (hexaammineruthenium (III) chloride) which acted as the redox mediator, from their other end. Section 3.6.5 includes a schematic illustration and picture of the setup (Figure 3.9) as well as further information on each component. Upon the application of a potential, the generated current passes between the WE and CE while the potential is controlled between the RE and WE [150].

Electrochemical phenomena associated with nanoelectrodes originate from changes in the transport of ions in solution [137]. For disk-shaped electrodes, which are the main focus of this work, as the electrode size decreases, diffusion of redox species onto the electrode becomes hemispherical. This time-dependent change leads to an increase in the surface occupied by the diffuse layer (angle relative to electrode increases), and eventually becomes greater than the electrode. Consequently, a significantly larger number of RuHex molecules over time and area arrive at the electrode's surface compared to planar diffusion [137]. In contrast to conventional macroelectrodes (> 50 µm in diameter), the generated current does not rely on the electrode's surface area but its disk radius (Equation 2.5) [151]. The cyclic voltammograms obtained with nanoelectrodes are characterised by sigmoidal trends with oxidation and reduction being overlapped, while conventional ones by the common peak-shaped curves (Figure B.3, Appendix B.2).

Cyclic voltammograms were performed to calculate the current generated by the one-electron exchange between the $[Ru(NH_3)_6]Cl_3$ molecules and the carbon surface of the semi-elliptical nanoelectrodes. The required potential to initiate this process was approximately -200 mV versus the reference point of Ag/AgCl/3M KCl [133]. Following this, three cycles of a potential sweep were applied from 0 mV to -400 mV and with a scan rate between 20 – 500 mV/s. This range was selected to verify that current was independent from the scan rate value, as expected from Equation 2.5, $i_{ss} = 4n_eFD_rc_rr_e$. By considering a diffusion coefficient of 9.1 x 10^{-10} m^2/s for 10 mM $[Ru(NH_3)_6]Cl_3$ [10], [75], [152], the radius of the carbon nanoelectrodes was estimated by the recorded current (i_{ss}). It is worth clarifying that this estimation assumes that disk-shaped electrodes instead of semi-elliptical were formed at the nanopipette tip, hence differences in the sizes obtained with SEM imaging and cyclic voltammetry were expected [10], [75].

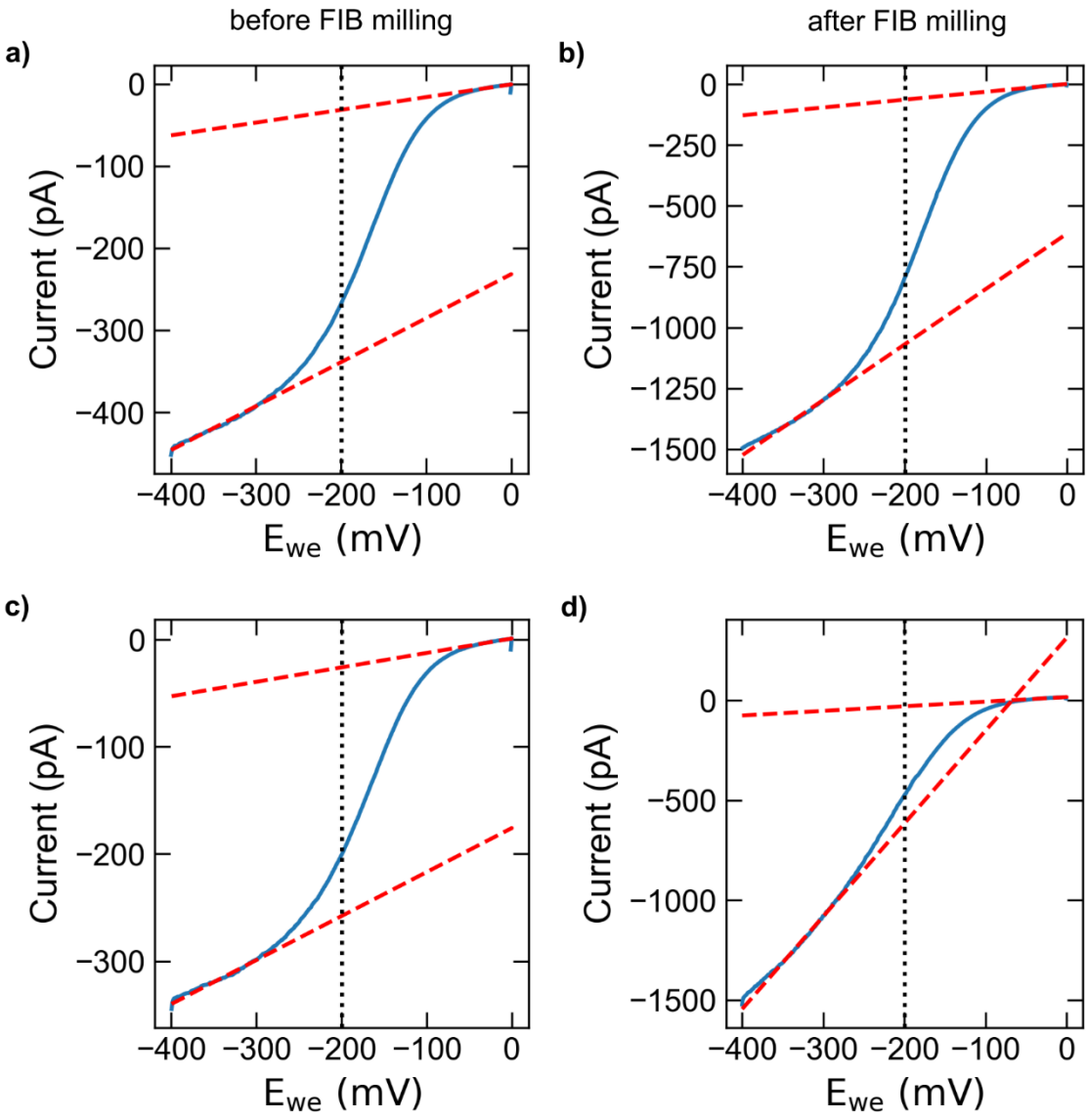

Figure 3.6 Sigmoid cyclic voltammograms (cyan curve) for a pair of semi-elliptical carbon nanoelectrodes **a), c)** before and **b), d)** after FIB milling of the quartz glass double-barrel nanopipette tip. The carbon nanoelectrodes are presented in Figure 3.5b. A potential sweep from 0 to -400 mV was repeated 3 times with a 50 mV/s scan rate. The curves represent the last reduction process. A three-electrode system, where the carbon nanoelectrode acted as the working electrode, was used for these measurements. Linear fitting (red dashed lines) between two points at the baseline and plateau was applied to estimate the mass transport limiting current (i_{ss}) at the standard redox potential (black dotted line at -200 mV). The presence of capacitive currents in the system is responsible for the plateau region not being stationary.

Figure 3.6 displays sigmoid cyclic voltammograms for the one electron reduction of 10 mM RuHex in 0.1M KCl before (left column) and after (right column) FIB milling of the nanopipette tip for the pair of carbon nanoelectrodes shown in Figure 3.5. Based on the experimental conditions mentioned above, the radius of the nanoelectrodes was

estimated by rearranging Equation 2.5 into $r_e = i_{ss}/4n_eFD_rc_r$, where the only unknown parameter is the steady-state current. It has to be noted that the trend of the obtained voltammograms showed a linear increase for voltages between -300 mV and -400 mV instead of reaching a plateau. This is due to the presence of a capacitive current in addition to the one flowing between the working and counter electrodes [137]. Quartz glass has a negative surface charge and when immersed in solution, an electric double layer is established which creates current flow along the glass wall. If we assume the electrolyte solution as a resistor, then the electric double layer is a capacitor connected in series.

This phenomenon is commonly observed in nanoelectrodes when performing cyclic voltammetry and commercially available software packages have been developed to extract the mass transport limiting current. Inspired by the software package "Aftermath" developed by Pine Research Instrumentation (Durham, NC, USA), I prepared a Python script (https://github.com/dsoulias/depNanotweezers) that performs the following analysis. Since the applied voltage was constantly swept from 0 to -400 mV, linear fitting (red dashed lines in Figure 3.6) was applied between two points on the baseline of the current (-10 mV and -30 mV) and another two points on the plateau (-300 mV and -350 mV) region. Then, the difference in current between the fitted red lines at the standard redox potential (dotted vertical black line in Figure 3.6), which was always at the midpoint of this range (-200 mV), was considered equal to the steady-state current $\left(i_{ss} = i_{fit,plateau}(-200) - i_{fit,baseline}(-200)\right)$. The mean value and standard error of the mean obtained from three reduction and oxidation repetitions (six in total) provided a good estimation for the current magnitude.

From the voltammogram in Figure 3.6b, the steady-state current was measured equal to -1071 ± 24 pA with an estimated disk-shaped radius of 305 ± 16 nm. Revisiting the dimensions for the same nanoelectrode obtained from SEM imaging in the previous section (Figure 3.5b), there is only a small difference between them. The minor semi-axis (h/2 in Figure 3.11b) was found equal to 284 nm while half of the major semi-axis (a_1/2 in Figure 3.11b) had a length of 443.5 nm. Considering the assumption of the electrode shape being disk-shaped instead of semi-elliptical, the electrochemical characterisation provided a fair estimation. In addition, the steady-state current from the voltammogram in Figure 3.6a, which represented the same electrode before its tip was milled, had a mean value of -313 ± 5 pA with an estimated radius of 89 ± 1 nm. As expected, etching the nanopipette tip to make it smoother and flat resulted in increasing the electrode radius by approximately 216 nm.

Similar results were observed for the second nanoelectrode of this double-barrel nanopipette (Figure 3.5d). From the voltammogram in Figure 3.6d, the mean value of i_{ss}

was found equal to -700 ± 99 pA with an average radius of 199 ± 28 nm. The respective dimensions from SEM imaging were 284 nm for the minor semi-axis and 355 nm for half of the major semi-axis. The same nanoelectrode prior to FIB milling (Figure 3.6c), provided a -237 ± 3 pA steady-state current and a 68 ± 1 nm radius. This nanoelectrode was also smaller before modified, as the previous one. Both before and after FIB milling, the two closely-spaced nanoelectrodes had similar sizes which agree with the image in Figure 3.5d. Additional examples of double-barrel nanopipette-based carbon nanoelectrode can be found in Appendix B.2.

Overall, these findings proved that electrochemical characterisation of carbon nanoelectrodes is useful when assessing their type. Acquiring sigmoid cyclic voltammograms demonstrated electrical connection between the carbon surface at the tip and the electrolyte solution. In addition, it verified the formation of disk-shaped, or at least disk-like-shaped, geometry at the nanopipette tip. Their size was usually underestimated due to the assumption of being disk-shaped instead of semi-elliptical with estimated dimensions not diverging significantly from the actual values. However, the technique lacks the ability to determine the width of the glass septum separating the two nanoelectrodes or the thickness of the glass wall that surrounds them. To measure these dimensions and assess the reproducibility of voltametric responses, SEM imaging is recommended at some point in this process, but not frequently as it would affect its surface properties. In general, the combination of the two techniques offers an accurate characterisation of the fabricated nanoelectrodes size and shape which is important before conducting single-molecule force probing experiments.

3.5 Conclusions

To summarise, in this chapter, I have initially explained in detail the fabrication of quartz glass single- and double-barrel nanopipettes via laser pulling. Two different programmes were created to form tip openings either with a ~120 nm or ~400 nm diameter. The size and shape of the nanopipette tip aperture were characterised by scanning electron microscopy imaging as well as electrochemical measurements of the nanopore resistance. The combination of these two techniques allowed the estimation of the inner half-cone angle of nanopipettes made of quartz glass capillaries with an outer and inner diameter equal to 1.2 mm and 0.9 mm, respectively, and was found approximately equal to 8°. Then, I developed a new configuration for fabricating carbon nanopipette-based electrode via pyrolytic carbon deposition. Although previous techniques have reported successful formation of disk-shaped carbon nanoelectrodes at the tip of nanopipettes, they either lacked reproducibility [130] or optimised the setup to such an extent in order to obtain better results that increased the complexity of building the setup and operating it [133].

Inspired by the latter approach, an Arduino PID-controller was introduced to probe the temperature produced by a heating coil in real-time and adjust the output of the power supply so that it precisely followed the desired temperature profile. This technique achieved greater fabrication yield compared to the first setup, reduced operation and construction complexity, while offered benchtop access at a much lower cost. Furthermore, the fabricated carbon nanoelectrodes at the tip of double-barrel nanopipettes were characterised with SEM imaging. In most cases, the glass wall was not affected by the extreme heating applied during pyrolysis which further strengthens the efficiency of the developed fabrication technique. Interestingly, I observed that carbon was not deposited until the tip openings and was instead recessed. This prevented quantification of the actual dimensions of the nanoelectrodes with SEM, as only the tip size and shape could be studied. As a result, additional modification (FIB milling) was performed to obtain smooth and co-planar disk-shaped nanoelectrodes. At this stage it was demonstrated that the two barrels were not completely identical but this resulted from inconsistencies during the manufacturing process of the capillaries.

Additionally, electrochemical characterisation of both modified and non-modified nanopipette tips was conducted by cyclic voltammetry. The difference between the estimated radius and the one obtained by SEM was not in agreement. However, it was concluded that a combination of these two techniques provided a more accurate characterisation of the carbon nanoelectrodes size. In conclusion, there are several

techniques that can be applied for the fabrication and characterisation of disk-shaped carbon nanoelectrodes, each with its own advantages and disadvantages. Here, I would like to suggest that to improve the fabrication of carbon nanoelectrodes a different approach should be adopted. As mentioned in Section 3.3, the setup I developed throughout this work has the capability of depositing a thin layer of carbon inside the nanopipette walls. This was achieved only during the first run of the heating profile. If instead of performing the pyrolysis after the fabrication of nanopipettes, quartz glass capillaries were coated internally with a thin layer of carbon first and then were laser pulled into nanopipettes, a perfectly smooth and flat pair of carbon nanoelectrodes would form at the tip. Attention is needed though as this process might affect the optics on the laser puller.

3.6 Materials, experimental methods and setups

This section contains information related to the materials used for fabricating and characterising pyrolytic carbon nanopipette-based electrodes, as well as the experimental methods and configurations developed for data acquisition and analysis.

3.6.1 Quartz glass capillaries

Single-barrel quartz capillaries with (QF120-90-10, World Precision Instruments Ltd) and without (Q120-90-7.5, World Precision Instruments Ltd) filament were used for initial nanopipette characterisation and pyrolytic carbon deposition experiments. Double-barrel, also called theta (θ), quartz capillaries (QT120-90-7.5, World Precision Instruments Ltd) were selected for the fabrication of pyrolytic carbon nanopipette-based electrodes which were then implemented as dielectrophoretic nanotweezers for single-molecule force spectroscopy measurements. As illustrated in Figure 3.7, the outer diameter of all these capillaries is equal to 1.2 mm while their inner is equal to 0.9 mm. A tolerance of 0.03 mm and 0.02 mm is expected based on the manufacturer specifications for the outer and inner diameter of the capillaries, respectively.

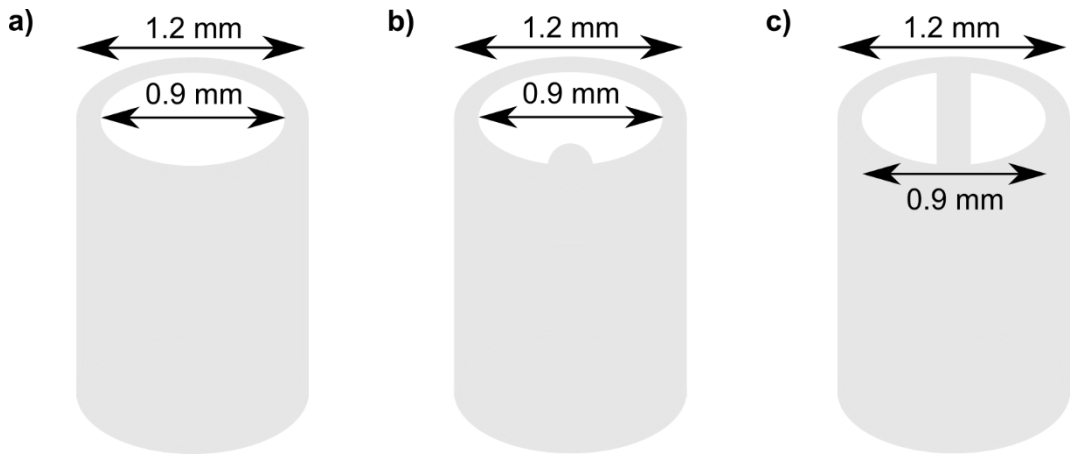

Figure 3.7 Schematic illustration of quartz glass capillaries geometries. **a)** Single-barrel capillary with an outer and inner diameter equal to 1.2 mm and 0.9 mm, respectively. **b)** Single-barrel capillary with glass filament at the side of the inner hollow domain. This type has the same dimensions as the one in a). **c)** Double-barrel (theta, θ) capillary with a glass septum dividing the inner hollow domain into two identical semi-elliptical open channels. The inner and outer diameter are again the same as in a).

3.6.2 Laser-based nanopipette pulling

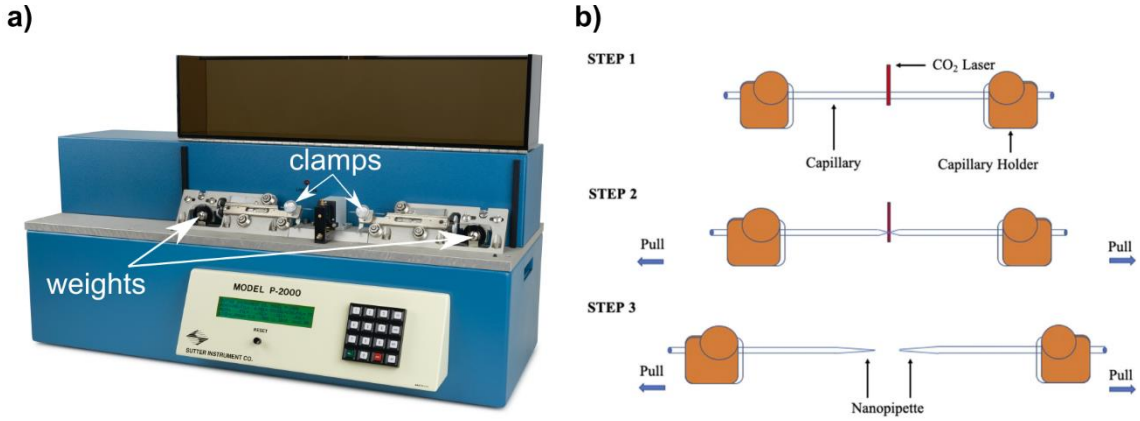

Figure 3.8 a) Picture of the P-2000 (Sutter Instrument) laser-based micropipette pulling instrument. The top two white arrows indicate the location of the metal screw-fixed clamps where the glass capillary is mounted, while the bottom ones highlight the location of the mechanical weights connected to the clamps. **b)** Schematic illustration of the three steps for nanopipette fabrication. In STEP 1, a CO_2 laser heats the glass capillary at its centre. In STEP 2, two mechanical weights pull the pliable now capillary ends towards opposite directions upon further heating. In STEP 3, further pulling results in the division of the capillary into two almost identical sharp nanopipettes. Reproduced from [147].

A P-2000 (Sutter Instrument) laser-based micropipette pulling instrument (Figure 3.8a) was used to fabricate nanopipettes. At first, a glass capillary was mounted between two metal screw-fixed clamps so that its centre was situated inside a protective box where a carbon dioxide (CO_2) laser beam was focused. Once the laser beam was activated, the capillary was heated and became pliable locally (STEP 1, Figure 3.8b). At that moment, mechanical weights connected to either side of the clamps pulled the capillary in opposite directions leading to the formation of an hourglass-like geometry (STEP 2, Figure 3.8b). Further heating and pulling caused the division of the capillary into two almost identical sharp nanopipettes (STEP 3, Figure 3.8b). Considerable deviations in the overall pulling time value (> 10%) for otherwise fixed parameters indicate changes in its size or shape. Furthermore, the size of the resulting nanopipette tip aperture can be tuned by adjusting the laser puller's parameters which are displayed in arbitrary units. In addition, multiple sets of these parameters, called lines, can be selected in a single run for achieving the desired dimensions. There are five parameters, as follows:

- "Heat" sets the laser output power and hence the energy supplied to the glass capillary.
- "Filament" controls the width of this laser beam emitted on the capillary surface.
- "Velocity" adjusts the pulling speed under constant load by the weights on the sides of the clamped capillary.

- “Delay” is the time between the moment heat switches off and hard pull gets activated.
- “Pull” controls the force applied by these weights.

3.6.3 Scanning electron microscope (SEM) imaging of quartz glass nanopipettes and carbon nanoelectrodes

Initial imaging of quartz glass nanopipettes was performed on a Zeiss LEO 1530 scanning electron microscope at the cleanroom facilities in the School of Electronic and Electrical Engineering of the University of Leeds. Sample preparation consisted of sputtering its external surface with a ~5 nm Iridium layer, mounting the nanopipette on the microscope holder with double-sided tape and placing it inside the SEM chamber under vacuum. Note that images with curved glass surfaces were due to electrostatic charging that caused the sample to drift during imaging. Further imaging of quartz glass nanopipettes and carbon nanoelectrodes were conducted with the help of Dr Alexander Kulak (School of Chemistry, University of Leeds) on a Nova NanoSEM450 scanning electron microscope (3 kV, ~5.0 mm working distance). Dr Alexander Kulak mounted the sample, operated the instrument and acquired images while I guided him to the regions of interest for each sample. This instrument was equipped with a circular backscatter detector which made imaging non-conductive samples without coating possible. As a result, glass nanopipettes and carbon nanoelectrodes were not sputtered with a conductive layer. The difference in image resolution can be seen in Figure 3.11 between panels a, b, c, d and panels e, f. All lengths from SEM micrographs were measured via ImageJ, an open access image processing programme developed by Schneider et al. (2012) [153].

3.6.4 Electrolyte solutions

<u>0.1 M KCl</u>

7.455 g of potassium chloride (KCl, 7447-40-7, Sigma-Aldrich) were diluted in 1 L of Milli-Q type 1 water (18.2 MΩ*cm at 25 °C, Milli-Q EQ7000, Merck, Darmstadt, Germany) to form 0.1 M KCl solution. Conductivity measurements were carried out using Fisherbrand™ Traceable™ Conductivity Meter Pen (Cat. No. 15-078-200).

10 mM $[Ru(NH_3)_6]Cl_3$ in 0.1 M KCl

0.31 g of hexaammineruthenium trichloride ($[Ru(NH_3)_6]Cl_3$, 14282-91-8, Sigma-Aldrich) were diluted in 100 mL of 0.1 M KCl by magnetically stirring the mixture for 10 minutes, to form 10 mM $[Ru(NH_3)_6]Cl_3$ solution.

3.6.5 Electrodes configurations for electrochemical measurements

Two-electrode configuration

Silver wires with a 0.25 mm diameter (Ag, GoodFellow, Huntingdon, UK) were immersed in sodium hypochlorite for 2 hours to form Ag/AgCl electrodes. After washing them with Milli-Q type 1 water, they were used in a two-electrode system as working and quasi-reference electrodes, respectively. Since very low currents flew between them, the reference electrode worked as counter electrode at the same time. One end of each electrode was connected to a patch-clamp (MultiClamp 700B, Molecular Devices, San Jose, CA, USA) while the other end was immersed in electrolyte solution. All measurements were performed inside a Faraday cage to reduce external electrical noise.

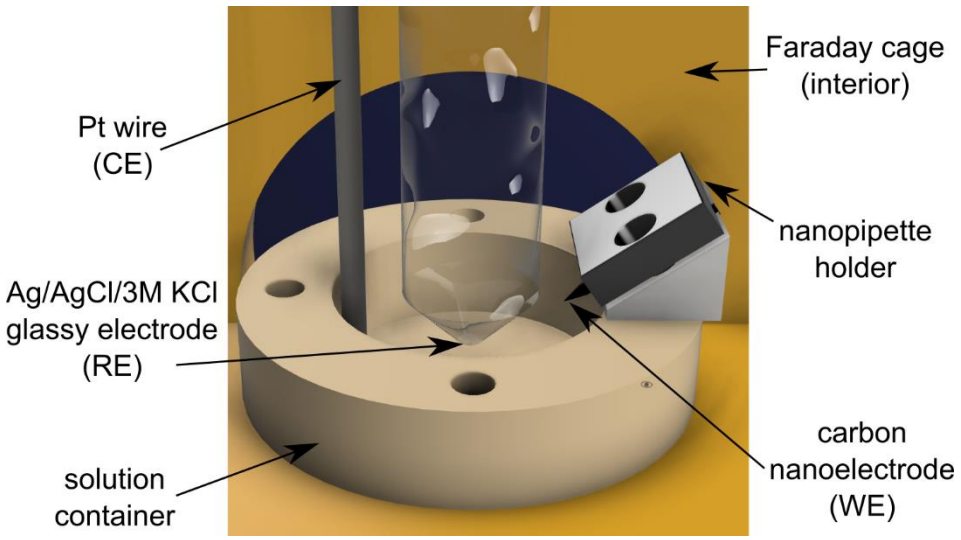

Figure 3.9 Computer-aided design (CAD) of the three-electrode configuration used in electrochemical characterisation of carbon nanoelectrodes. The carbon nanoelectrode (WE), Pt wire (CE) and Ag/AgCl/3M KCl glassy electrode were mounted on a holder so that their tips were immersed in the electrolyte solution including the redox active species. The yellow surface represents the Faraday cage inside which all measurements took place to reduce electrical noise from the surrounding environment.

Three-electrode configuration

In the three-electrode system, the carbon nanoelectrode acted as the working electrode, a 3M Ag/AgCl glassy electrode acted as the reference electrode and a Pt wire with 0.5 mm in diameter acted as the counter electrode (Figure 3.9). All three electrodes were connected to 5-channel potentiostat (VSP, BioLogic Science Instruments, Seyssinet-Pariset, France). The Ag/AgCl/3M KCl (saturated) option was selected as the reference electrode in the settings for the reference point when probing voltages. All measurements were performed inside a Faraday cage to reduce external electrical noise.

3.6.6 Arduino-based pyrolytic carbon deposition operation procedure

There are four main steps for the pyrolytic deposition of carbon inside a nanopipette's tip which are illustrated in Figure 10. Firstly, the backside of a nanopipette (grey conical structure, Figure 3.10a) is connected to a Tygon tube (blue tube in Figure 5.10a, Tygon S3 E-3603, Saint Gobain) with a 2.38 mm and 0.79 mm outer and inner diameter, respectively. The left three-way valve in Figure 3.10a is set to allow butane/propane gas in the nanopipette until ~3 bar pressure is achieved. In parallel, the ceramic counter-flow capillary (beige cylinder) is placed under the heating coil (black coil) while the right three-way valve is set to allow Argon gas of ~0.5 bar pressure to create an inert environment for the nanopipette tip and minimise the chances of oxidation. The ARDUINO keeps the temperature inside the ceramic capillary, where the K-type thermocouple probe is fixed, at 25 °C by controlling the current generated by the PSU.

Secondly, the nanopipette is moved to the right until its tip reaches the centre of the heating coil (CrFeAl allow wire or Kanthal-A1 wire). Then, the ceramic counter capillary (outer diameter 1.2, inner diameter 0.8 mm, Al-23 insulating tube, Y24G061, Alfa Aesar) is moved to the left until it touches the nanopipette's outer walls under the heating coil (Figure 3.10b). At this point, the right and left three-way valves are set to let Ar (Argon 99.998%, ISO 14175-I1-Ar, BOC) flow into the nanopipette until ~4.2 bar pressure is achieved. The pressure inside the ceramic capillary falls to 0 bar. Thirdly, the two-way valve just before the nanopipette is turned by 90° to isolate the gas mixture inside the nanopipette (Figure 3.10c). The right 3-way valve is fixed to provide again ~0.5 bar Ar gas pressure in the ceramic capillary.

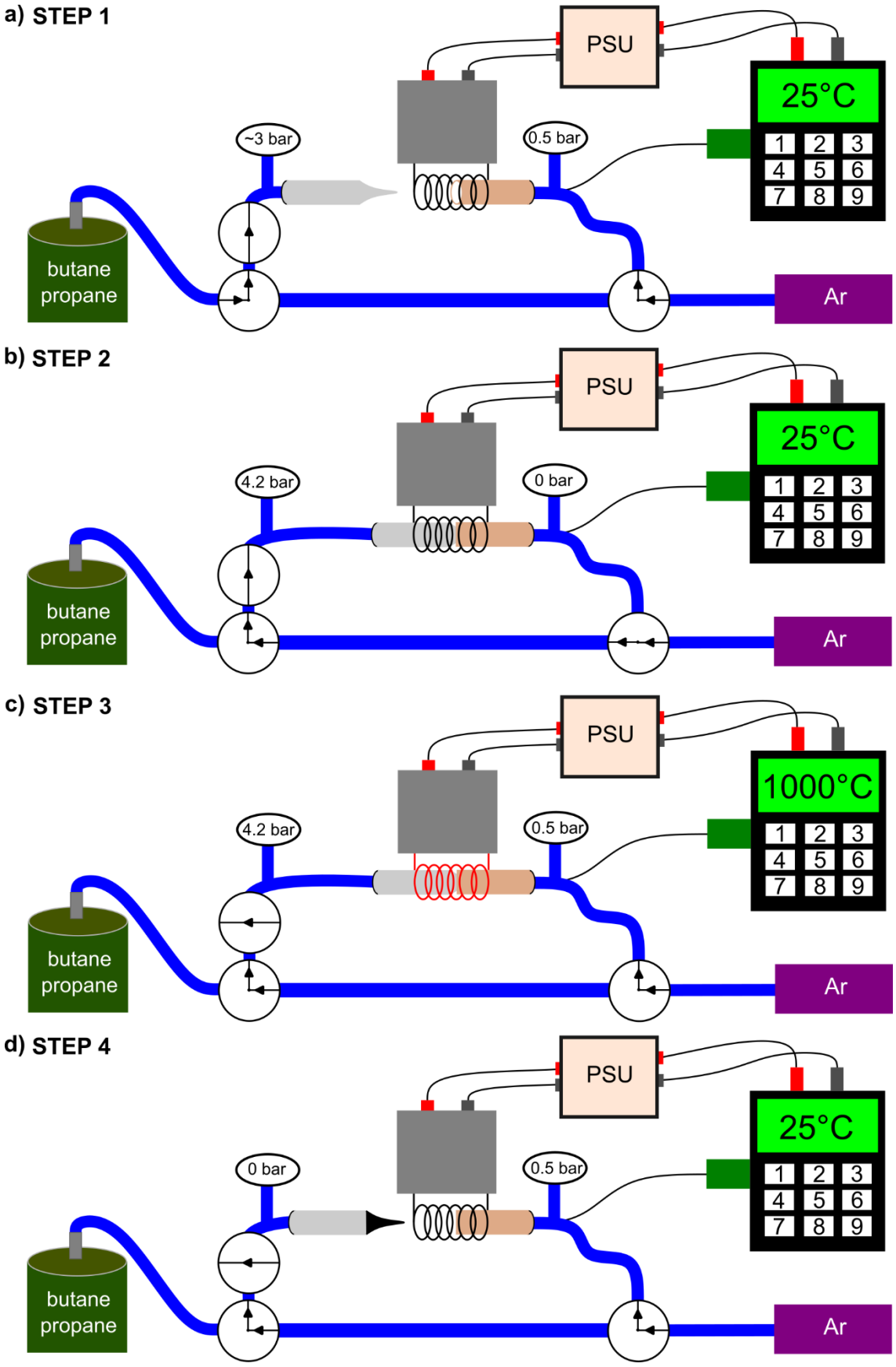

Figure 3.10 2D schematic illustrations of the pyrolytic carbon deposition steps for the fabrication of carbon nanopipette-based electrodes.

Then, the heating programme was selected on the Arduino PID-controller (Arduino Uno) which tuned the output of the DC power supply (SPS 1560 PFC, Voltcraft) to generate 1000° inside the heating coil, as measured by the K-type thermocouple probe in the ceramic capillary (Figure 3.10c). This programme is run twice to fill the nanopipette tip with deposited pyrolytic carbon. Finally (STEP 4, Figure 3.10d), once the system has cooled down to 25 °C, the carbon-filled nanopipette is detached from the tube and all gas sources are switched off.

3.6.7 SEM/FIB imaging/milling of double-barrel nanopipette-based carbon nanoelectrodes

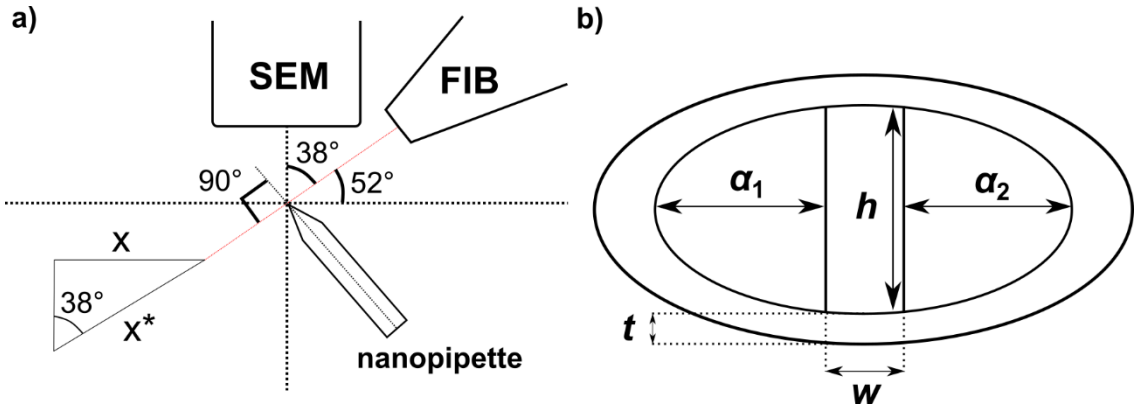

Figure 3.11 a) Schematic diagram of SEM imaging and FIB milling configuration. **b)** The measured dimensions (a_1, a_2, w, h and t) on ImageJ of semi-elliptical nanoelectrodes at the nanopipette tip were corrected by the geometrical analysis shown in a).

A Helios™ G4 PFIB UXe DualBeam™ FIB/SEM instrument was operated by Dr Stuart Micklethwaite (LEMAS, School of Chemical and Process Engineering, University of Leeds). Each dual-barrel quartz glass nanopipette was attached to a stage holder with carbon paste, without sputtering any metal conductive layer at the outer surface of the nanopipette and mounted on the SEM stage under vacuum conditions. FIB milling was performed one nanopipette tip at a time, with each having different amount of material being removed. Figure 3.11a shows a diagram of how the exact dimensions of the carbon nanoelectrodes were extracted from the SEM micrographs upon analysis on ImageJ. The nanopipette tip plane had a 38° angle with the SEM detector, while the focused ion beam targeted it at a 90° angle.

Based on the imaging configuration shown in Figure 3.11a, the dimensions of the semi-elliptical nanoelectrodes (a_1, a_2, h, w and t) were calculated by applying corrections to

measurements on ImageJ from the two-dimensional SEM images. Lengths measured along the horizontal axis (x-axis) of the image were compensated based on $x^* = \frac{x}{\sin(38°)}$ (Figure 3.11a). Lengths along the vertical axis (y-axis) needed no compensation as they were equal in the projected and actual image of the nanopipette tip. So, to calculate any of the dimensions illustrated in Figure 3.11b, the following equation was used $w = \sqrt{w_y^2 + w_x^{*2}}$, where w_y was the measured length along the vertical axis (y-axis) of the image and w_x^* the compensated measured length along the horizontal axis (x-axis) of the image. The same technique was also applied for a_1, a_2, h and t.

Chapter 4
Simulations of the electric field distribution at the nanotweezers

4.1 Introduction

A spatial gradient in an electric field is generated between two electrodes when they differ in size or shape. This electric field gradient gives rise to dielectrophoretic forces that act on polarisable entities within the field's range. To trap and manipulate nano- or microscale molecules with such forces, their magnitude needs to be at least in the femtonewtons regime to overcome others produced by Brownian motion, electroosmosis or electrothermal flow [10]. In fact, the dielectrophoretic force is proportional to the gradient of the square of the electric field $\left(\nabla\left|\vec{E}\right|^2\right)$ which relies on the applied voltage squared $\left(V_{pk}^2\right)$. Hence, larger forces can be achieved by increasing the applied voltage. However, high voltages usually lead to unwanted electrothermal, electrochemical or electroosmotic effects, so bringing the electrodes closer has proved to be a more efficient option. Nadappuram et al. (2019) [10] managed to achieve a gradient for the electric field squared as high as 10^{28} V^2/m^3 by reducing this gap to 10 – 20 nm. For example, a minimum value of $10^{16.4}$ V^2/m^3 was required to overcome Brownian motion of a 10 kbp (kilo-base pair) dsDNA molecule in solution [73].

Since the electric gradient depends critically on the geometry and arrangement of the electrodes, it was of great importance to understand it for the nanopipette-based carbon nanoelectrodes configuration. As a consequence, this chapter presents a finite element method simulation that aims to calculate the magnitude of dielectrophoretic forces experienced by individual dielectric entities, generated by dual-channel nanopipette-based tweezers. The model geometry was based on a truncated cone consisting of two semi-elliptical channels filled with carbon, immersed in H_2O. A potential bias was applied between the top boundaries of the carbon domain to mimic the experimental conditions. This was expected to lead to the formation of a highly non-uniform electric field around the nanotweezers tip region that could be used for trapping individual particles via dielectrophoresis. The aim of the work presented here was to get a better understanding of the operation of these dielectrophoretic nanotweezers and find the optimal conditions

to apply in the experimental measurements. The effect of parameters related to both the geometry of the nanotweezers configuration and the applied signal were investigated.

4.2 Design of finite element model for nanotweezers in water

Every physical phenomenon depends on the geometry, material properties and boundary conditions of a system, each having their unique level of complexity. Solving analytically differential equations of such systems is often not possible, and as a result, numerical methods which provide approximated solutions to problems have to be employed, with the finite element method (FEM) being one of the most widely used [154]. FEM is based on dividing the geometry of the problem into a larger number of small shapes, the so-called elements, and applying the physical principles directly to each one of them (varying degrees of linearisation may be applied within elements). In general, building computational models by using finite element methods requires four steps [155]. Firstly, designing the geometry of the model as accurately as possible but without leading to extremely long computational time intervals. Secondly, the meshing which is the division of the geometry into elements leading to the simplification of the solution with the most common shapes being the triangles and quadrilaterals for 2D studies, and the tetrahedrons and hexahedrons for 3D studies [154]. Then, material properties allocation to domains, boundaries or points of the geometry, and finally, setting the boundary and initial conditions of the system.

Here, a three-dimensional finite element model (FEM) was developed to simulate the distribution of generated inhomogeneous AC electric field between a pair of semi-elliptical nanopipette-based carbon electrodes when immersed in water (H_2O). FEM simulations were performed by using the commercial finite element solver COMSOL Multiphysics 5.6 with the “Electric Currents” physics package from the “AC/DC Module”. Moreover, by investigating the electric field gradient $\left(\nabla|\vec{E}|^2\right)$, the dielectrophoretic force magnitude around the nanotweezers tip could be estimated for a selection of parameters. These involved the applied electrical potential between the nanoelectrodes, their separation distance and the presence of carbon recessions at their tip. The nanotweezers configuration did not offer any significant form of symmetry in terms of boundary conditions. Although mirror symmetry existed, different initial conditions were applied between these boundaries. As a result, a three-dimensional model was chosen to solve the current conservation equation based on Ohm’s law (Equation 4.1) by using the scalar electric potential V (Equation 4.2) as the dependent value.

$$\vec{J} = \sigma\vec{E} + \vec{J}_e \qquad (4.1),$$

and

$$\vec{E} = -\nabla V \quad (4.2),$$

where $\vec{J}$ is the current density (A/m^2), $\vec{J}_e$ the externally generated current (A/m^2), $\vec{E}$ the electric field (V/m), V the electrical potential (V) and σ the electrical conductivity of the domain (S/m). Stationary studies, which are used when field variables are in steady-state conditions and do not change over time like time-dependent ones, were selected to simulate the voltage, electric field magnitude and gradient distributions along the x-, y- and z-axes. In this section, I explain the reasoning behind the simplified geometry designed in this model, as well as the allocation of initial boundary conditions and meshing of the geometry.

4.2.1 Model geometry design and material properties

So far, in most studies involving glass nanopipettes [10], [11], [73], [144], [145] (refer to Appendix A for more information), a more simplified approach has been adopted when designing their geometry compared to the actual one [144]. Following these models, I designed the nanotweezers 3D geometry when immersed in aqueous solution with the COMSOL CAD software as shown in Figure 4.1a (inset). The nanotweezers consisted of a 5 μm long truncated conical double-barrel nanopipette with two semi-elliptical domains representing pyrolytically deposited carbon (grey semi-elliptical cones at the middle). This length was considered sufficient for the needs of this model as explained in the next section. An 8° inner-half cone angle was applied to extrude the tip geometry in Figure 4.1b. The glass domain, surrounding the two carbon domains, was considered as an ideal insulator (no current passes through) at this point and was deducted from the design to aid with model convergence (lower computational power required). In Section 4.5, a revised version of the model included the glass domains to simulate the total impedance of the nanotweezers circuit. The aqueous solution was designed as a cubical domain of 30 μm width, 30 μm depth and 3 μm height.

Figure 4.1a presents a 2D view (xz-plane) of the designed geometry highlighting its truncated conical shape. It is worth noting that the tip surface was designed on the same plane with the top surface of the aqueous medium to achieve contact between them. Immersing the nanopipette tip deeper into the solution, as in an actual experiment, would not change the simulation results significantly but would increase greatly the computational effort required. In Section 4.4, where the effect of recessed carbon deposition at the nanopipette tip is investigated, a slight change in the design was applied. The carbon surface closer to the tip was set at the plane mentioned above while the deducted glass domain protruded the bath solution. Furthermore, Figure 4.1b

illustrates a 2D view (xy-plane) of the nanotweezers tip size and shape. Each semi-elliptical barrel had a major semi-axis of a_1 = 160 nm and a_2 = 150 nm, respectively, and a minor semi-axis $h/2$ = 75 nm. A 55 nm gap (w) separated the two nanoelectrodes, while the wall thickness across the x-axis (t) was equal to 60 nm. These tip dimensions were obtained from the double-barrel nanopipette-based carbon electrodes shown in Figure 3.4b and represented the most common dimensions for the nanotweezers used for experimental measurements in Chapter 5.

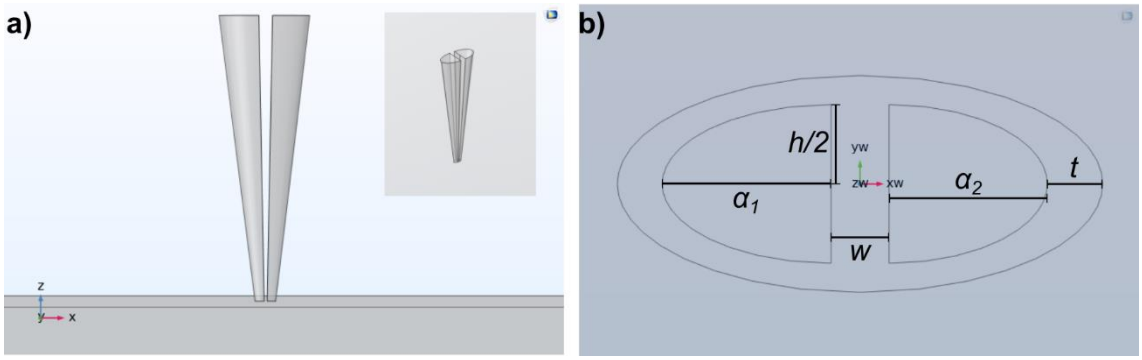

Figure 4.1 a) 2D view (xy-plane) of COMSOL CAD geometry of nanotweezers immersed in aqueous solution. The nanotweezers were designed as a 5 µm long truncated conical double-barrel nanopipette with two semi-elliptical domains representing pyrolytically deposited carbon (grey semi-elliptical cones at the middle). An 8° inner-half cone angle was applied to extrude the tip geometry shown in b). The glass domain was removed from the design. The aqueous solution was designed as a cube of 30 µm width, depth and 3 µm height. Inset shows a 3D view of the geometry. **b)** Nanopipette tip geometry with a_1 = 160 nm, a_2 = 150 nm and $h/2$ = 75 nm. A 55 nm gap (w) separated the two nanoelectrodes, while the wall thickness along the x-axis (t) was equal to 60 nm. These tip dimensions were obtained from the double-barrel nanopipette-based carbon electrodes shown in Figure 3.4b.

For COMSOL's "Electric Currents" module, two material properties were required. The electrical conductivity and relative permittivity of both the aqueous solution (Milli-Q H_2O) and pyrolytically deposited carbon which are listed in Table 4.1. For Milli-Q H_2O, the electrical conductivity was experimentally measured by the filtering unit while its relative electrical permittivity at T = 25 ℃, has been well characterised [152]. In contrast, no attempts have been reported yet to determine these properties for the carbon material deposited pyrolytically inside quartz glass nanopipettes. However, McEvoy et al. (2012) [148] demonstrated electrical characterisation of thin conducting carbon films formed after applying chemical vapour deposition, a similar but significantly more accurate technique than the one developed in Chapter 3. The authors found an electrical conductivity of approximately 5 x 10^4 S/m for films with a thickness larger than 100 nm and proved that their crystal structure was similar to graphite. Additionally, Dovbeshko et al. (2015) [156] found that the relative electrical permittivity of thin pyrolytic carbon

films was equal to 5. In this simulation, I assumed that the nanotweezers would have a similar electrical conductivity as this was the only available reference value in literature.

Table 4.1 Electrical conductivity (σ) and relative permittivity (ε_r) for the materials allocated to the two domains of nanotweezers geometry in the COMSOL model.

Domain	**Material**	$\boldsymbol{\sigma}$ **(**S/m**)**	$\boldsymbol{\varepsilon_r}$
Bath solution	Milli-Q H_2O	5.5 x 10^{-6}	79
Nanoelectrodes	Pyrolytic Carbon (Graphite)	5 x 10^4	5

4.2.2 Initial boundary conditions

The next step in building this finite element model was the allocation of initial conditions on the domains and boundaries of the designed geometry. To achieve this the "AC/DC Module" was chosen in COMSOL, and in particular the "Electric currents" package. This physics interface relies on solving a current conservation equation based on Ohm's law (Equation 4.1) by using the scalar electric potential (Equation 4.2) as the dependent variable. A reference impedance $\left(Z_{ref}\right)$ of 50 Ω was used by default. Current conservation was applied to all domains and boundaries in the system, while different σ and ε_r values were probed depending on the assigned material in the domain (Table 4.1). Electric insulation $\left(\hat{n} \cdot \vec{J} = 0\right)$ was chosen for all external boundaries of the geometry with no initial voltages applied $(V_0 = 0\ V)$. A positive electrical potential $+V$ was assigned to the top surface boundary of the left semi-elliptical truncated cone in Figure 4.1a and a negative $-V$ to the top surface boundary of the left one.

Since a stationary solver was selected for the simulations in this chapter, time-dependent phenomena that would be present in an experiment, were not considered. In general, DEP occurs for both DC and AC voltages. Additional electric field induced forces acting on dielectric particles, such as electrophoresis, are usually much stronger than dielectrophoresis [95]. The big difference between them and DEP is that the latter depends on the gradient while the former on the electric field. When the oscillation of an AC field is fast enough, its time-averaged force equals to zero. However, the gradient does not change polarity $\left(\vec{F}_{DEP} \sim \nabla\left|\vec{E}\right|^2\right)$ in an AC field, so the force points always in the same direction and is not equal to zero when taking the time-average [95]. The reasoning

behind the application of opposite voltages between the two nanoelectrodes, instead of using a positive terminal and a ground, is related to the sinusoidal AC signal applied during a trapping experiment. In steady-state, these voltages (peak root-mean-square $V_{pk,rms}$ used during the experimental measurements) represented a snapshot of the peak-to-peak potential difference of this AC signal.

4.2.3 Mesh of the geometry

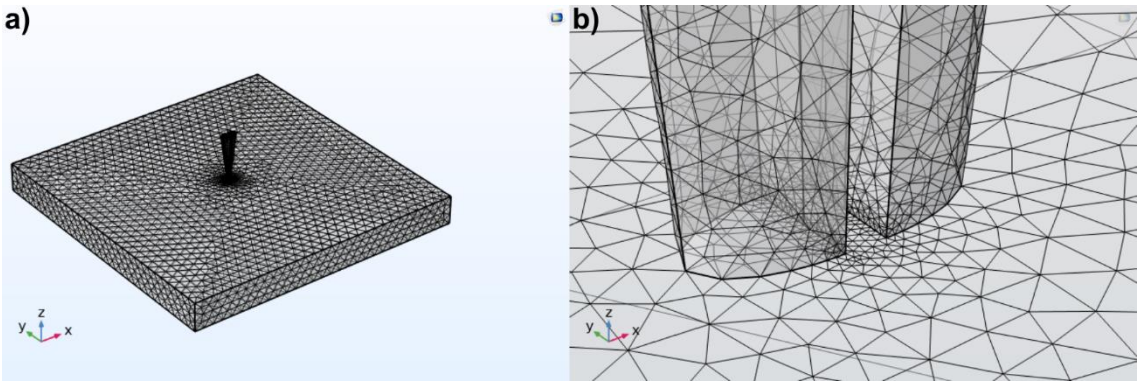

Figure 4.2 3D view of the generated mesh in COMSOL for **a)** the entire geometry of the model and **b)** the nanotweezers tip and bath solution common plane. The mesh was created with free tetrahedral elements after dividing first the parallel edge boundaries at the separation gap between the two nanoelectrodes.

Figure 4.2 depicts the final mesh for the entire geometry of the model and a zoomed-in section of the common plane between the nanotweezers tip and the bath solution. It was created by dividing the parallel edge boundaries that separate the two nanoelectrodes at the tip, into 15 boundaries with a 10 nm length. Then, the “Boundary layers” option was selected for meshing the remaining boundaries and domains. The final mesh contained 61,319 elements with an average mesh element quality of 69.0%. The latter is a dimensionless quantity between 0 and 100%, where 100% represents a perfectly regular element, in the chosen quality measure, and 0 represents a degenerated element. Further details regarding all the steps required to design the geometry of this model, apply the same boundary conditions and mesh are provided in Appendix C in the form of a COMSOL model report.

4.3 Distribution of electrical potential and electric field at the nanotweezers tip region

In this section, I first simulated the electrical potential distribution across all 2D planes (xy, xz and yz) of the model geometry. Colour plots are provided to visualise changes in magnitude. Then, the same technique was used to determine the electric field magnitude and visualise its lines distribution in three dimensions. In the designed geometry, the nanotweezers tip was fixed 3 μm above the bottom surface of the aqueous solution. The reason for doing this was to replicate the trajectory of a potentially trapped 2 μm latex bead when experiencing a dielectrophoretic force by the nanotweezers. As it will be explained in Chapter 5, latex beads suspended in water tend to freely diffuse approximately 700 nm above the top surface of a cover glass. During experiments, a bead's top surface and the nanotweezers tip are assumed to be on the same plane. Based on this, the distance between the tip surface and the bead's centre of mass would be ~1 μm. That is why the magnitude of multiple electric potentials, as well as the electric field's, were probed 1 μm away the nanotweezers tip.

4.3.1 Electrical potential distribution

Figure 4.3a illustrates the electrical potential distribution upon the application of $V_{pk,rms} =$ ±600 mV across the xz- and yz-planes at y = 0 nm and x = 0 nm, respectively. Since the two semi-elliptical domains were filled with conductive carbon, there was no significant drop in the applied voltage. Following the colour scale, where red represented +600 mV and blue -600 mV, the voltage magnitude remained unchanged until the tip boundaries (z = 0 nm, Figure 4.3b). At this point, the nanotweezers tip was in direct contact with H_2O, where the conductivity was almost 10^{10} times lower. This resistive region led to a sharp decrease in voltage for a length of approximately 200 nm below and 400 nm along the interface (z < 0 nm and y = 0 nm, respectively, in Figure 4.3c). In addition, as depicted in Figure 4.3b, the difference in size between the carbon nanoelectrodes at the tip caused an asymmetric voltage distribution in that region. The larger the surface of the nanoelectrode was, the longer distance it took for the electrical potential to reach 0 V.

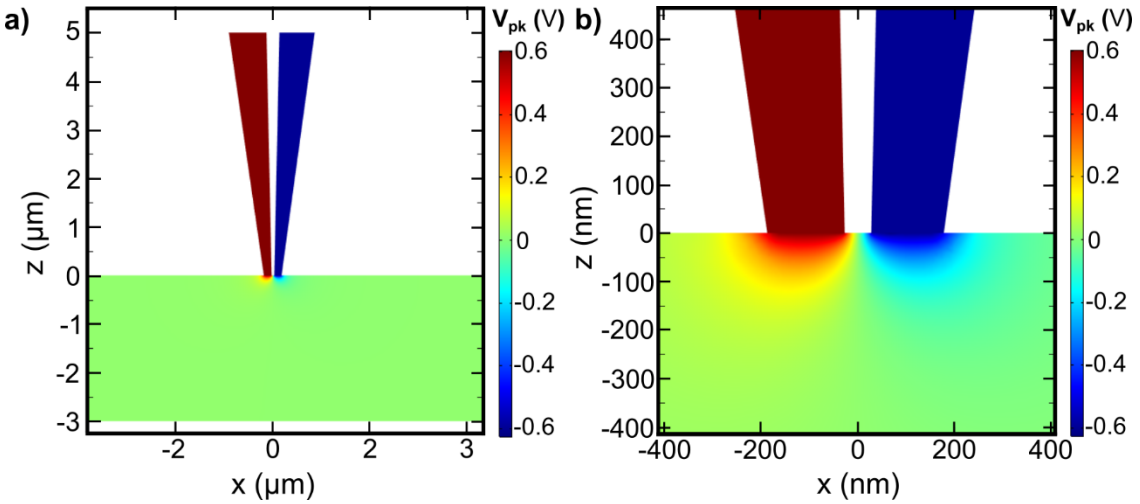

Figure 4.3 a) 2D view (xz-plane at y = 0 nm) of the electrical potential distribution across the entire geometry. A voltage (V_{pk}) of +600 mV (red) and -600 mV (blue) was applied to the top boundary of the left and right semi-elliptical domain, respectively. **b)** Zoomed in 2D view of a) highlighting the significant drop in voltage when transiting from the highly conductive carbon domain to water.

It is commonly known that surfaces such as quartz glass and graphitic carbon carry a finite surface charge [95]. As explained in Chapters 3, when immersed in aqueous solution an electric double layer of mainly counterions is formed at the solid-liquid interface. This layer acts as a capacitor and in an electrical circuit would be connected in series to the resistance of the pyrolytic carbon domain, affecting slightly the distribution of the electrical potential at that region. Nevertheless, neither the surface charge of the nanopipette quartz glass wall nor the pyrolytic carbon could be accurately quantified. At this point, the glass domain was deducted from the rest of the geometry. Since in this work only water was used, this capacitive contribution could be assumed negligible as the number of charged ions in the solution is much smaller than in a typical electrolyte (i.e., KCl, NaCl). However, in Section 4.5 the glass domains are included in a revised version of the model to simulate the total impedance of the nanotweezers circuit.

4.3.2 Electric field distribution

Based on Equation 4.2, the electric field magnitude can be calculated from the gradient of the electrical potential. In the previous section, it was observed that the highest gradient in this system occurred at the interface between carbon and H_2O. Consequently, the largest electric field magnitude was expected to arise at the same region which was verified by the colour plots in Figure 4.4. In Figure 4.4a, the two-dimensional (xz-plane,

y = 0 nm) distribution of the electric field lines (black curves), generated around the nanotweezers tip upon the application of V_{pk} = ±600 mV, is displayed. The colour scale represents the electric field magnitude $\left(\left|\vec{E}\right| = \sqrt{E_x^2 + E_y^2 + E_z^2}\right)$. From these simulations, the formed field was characterised as spatially inhomogeneous, meeting the main requirement for achieving dielectrophoresis. A maximum value (red colour) of ~4.5 x 10^7 V/m was obtained at the tip edges of the separation gap between the two nanoelectrodes. The gradient of this simulated value squared $\left(\nabla\left|\vec{E}\right|^2 \approx 10^{23}\ V^2/m^3\right)$ was in good agreement with the one reported by Freedman et al. (2016) [73] for a similar nanopipette-based configuration modelled in COMSOL.

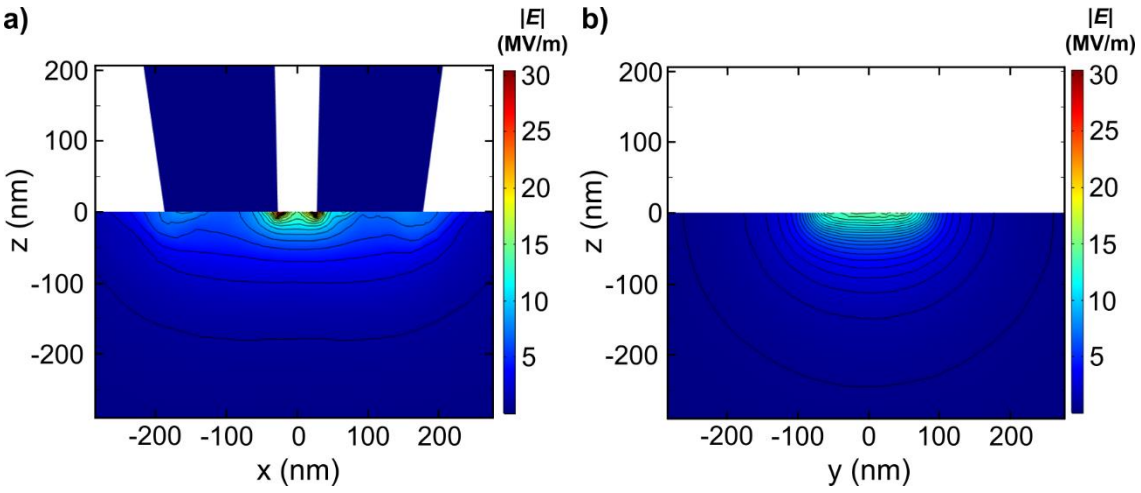

Figure 4.4 a) 2D view (xz-plane at y = 0 nm) of the electric field distribution around the nanotweezers tip region. A voltage of +600 mV (red) and -600 mV (blue) was applied to the top boundary of the left and right semi-elliptical domain, respectively, leading to a maximum value of ~45 MV/m. **b)** 2D view (yz-plane at x = 0 nm) of the electric field distribution around the nanotweezers tip region. Colour plots represent the electric field magnitude $\left(\left|\vec{E}\right| = \sqrt{E_x^2 + E_y^2 + E_z^2}\right)$ across the xz- and yz- planes at y = 0 nm and x = 0 nm, respectively, and contour lines the electric field vector $\vec{E}$.

In contrast, when investigating the yz-plane at x = 0 nm (Figure 4.4b), smaller electric field maximum values were reported (green colour). In fact, the field distribution across this plane appeared to have a more spherical symmetry when compared to the ones across the xz-plane who were highly non-uniform closer to the tip but became more symmetrical as moving away. Based on this, it was of great importance to study the electric field magnitude distribution along z = -1 μm where a latex bead (2 μm in diameter) would move in the case of being dielectrophoretically attracted towards the nanotweezers tip.

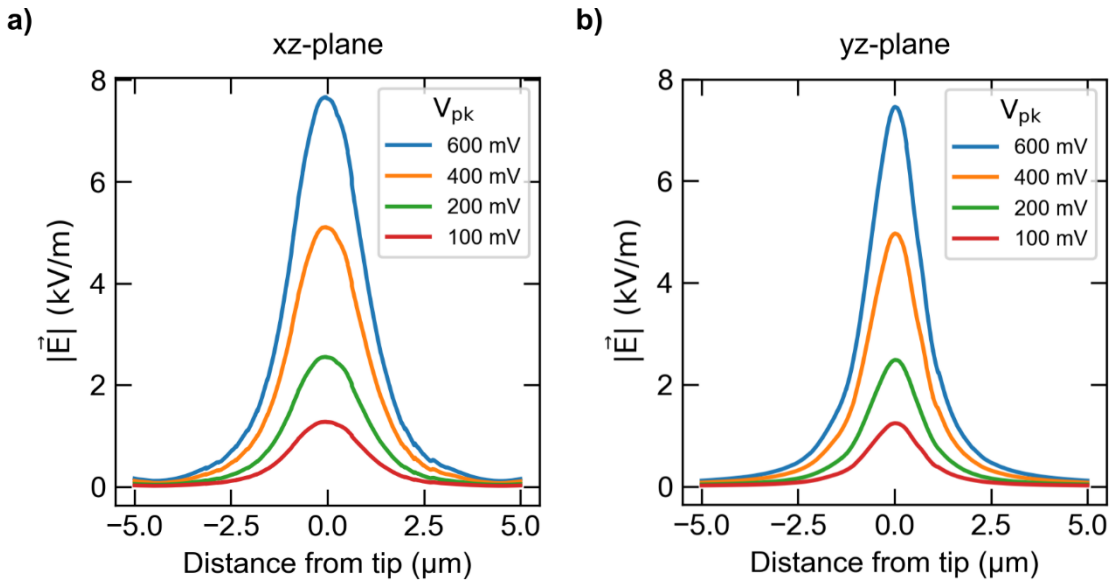

Figure 4.5 Electric field magnitude $|\vec{E}|$ as a function of distance from the nanotweezers tip at z = -1 μm, when a set of voltages $\pm V_{pk}$ were applied to the top boundaries of the semi-elliptical carbon nanoelectrodes. The curves represent $|\vec{E}|$ for -5 μm ≤ y, x ≤ 5 μm across the **a)** xz-plane and **b)** yz-plane, respectively. In both cases, maximum values were reported at the nanotweezers tip centre (x = y = 0 μm), gradually decreasing away from the tip. As V_{pk} became lower, $|\vec{E}|$ decreased accordingly. The full-width at half-maximum (FWHM) of the curves in a) was larger by 600 nm than the curves in b). Small differences (~0.1 kV/m) were observed for the peak values between a) and b).

The electric field magnitude $|\vec{E}|$ as a function of distance from the nanotweezers tip at z = -1 μm, when a set of voltages $\pm V_{pk}$ were applied to the top boundaries of the semi-elliptical carbon nanoelectrodes are presented in Figure 4.5. The curves in Figure 4.5a represent $|\vec{E}|$ across the xz-plane for -5 μm ≤ y ≤ 5 μm, while in Figure 4.5b $|\vec{E}|$ across the yz-plane for -5 μm ≤ x ≤ 5 μm. In both cases, maximum magnitudes were reported at the nanotweezers tip centre (x = y = 0 μm) which gradually decreased as moving away from the tip. For $V_{pk} = \pm 600$ mV, $|\vec{E}|_{xz}^{max} = 7.7$ kV/m and $|\vec{E}|_{yz}^{max} = 7.5$ kV/m. This finding demonstrated a small difference between the peak electric field magnitude of the xz- and yz-planes at the symmetry axis (x = y = 0 nm). In both planes, $|\vec{E}|^{max}$ decreased proportionally to the applied voltage V_{pk} (±400 mV, ±200 mV, ±100 mV). These magnitudes are listed in Table 4.2 together with the full-width at half-maximum (FWHM) values from the curves in Figures 4.5a and 4.5b. For -5 μm ≤ y ≤ 5 μm, Δy_{FWHM} was 600 nm larger than the full-width at half-maximum (Δx_{FWHM}) for -5 μm ≤ x ≤ 5 μm, as already noticed from Figure 4.4. This was a first indication that the trapping area would extend to greater lengths across the xz-plane compared to the yz-plane. Consequently, the

possibility of trapping an individual 2 μm dielectric particle via DEP would be larger in the case shown in Figure 4.5a than the one in Figure 4.5b.

Table 4.2 Electric field magnitude peak and full-width at half-maximum (FWHM) values across the xz- and yz-planes at z = -1 μm, for y = x = 0 μm, respectively, over a range of applied voltages $\pm V_{pk}$.

$\pm V_{pk}$ (mV)	$\left\|\vec{E}\right\|_{xz}^{max}$ (kV/m)	Δy_{FWHM} (μm)	$\left\|\vec{E}\right\|_{yz}^{max}$ (kV/m)	Δx_{FWHM} (μm)
600	7.7	2.2	7.5	1.6
400	5.1	2.2	5.0	1.6
200	2.6	2.2	2.5	1.6
100	1.3	2.2	1.2	1.6

4.4 Estimation of the dielectrophoretic force magnitude close to the nanotweezers tip

Based on Equation 2.3, the dielectrophoretic force magnitude experienced by a homogeneous spherical dielectric particle when suspended in aqueous solution is directly proportional to the gradient of the electric field magnitude squared, $\vec{F}_{DEP} \sim \nabla\left|\vec{E}\right|^2$. In the previous section, $\left|\vec{E}\right|$ was simulated across the entire 3D geometry of the model and its magnitude was determined 1 μm away the nanotweezers tip across the z-axis for a range of 10 μm along the x- and y-axes, separately. By calculating the spatial derivative of the squared variable $\left|\vec{E}\right|$ across the z-axis, the magnitude of $\vec{F}_{DEP}$ was estimated along this x- and y-range. To get a broad understanding of the experimental results in Chapter 5, a 1 μm radius particle and relative electrical permittivity of the medium equal to 79 were assumed. The real part of the Clausius-Mossotti factor, which describes the polarisability of the system, was considered $Re[f_{CM}(\omega)] = 0.5$ for an applied AC signal with a 10 kHz frequency. The selection of these values is explained in Sections 5.7 and 5.8. In this section, I also investigated how the dielectrophoretic force distribution changes at a ±45° angle between the xz- and yz-planes, for different widths separating the two nanoelectrodes at the nanotweezers tip and for carbon being recessed inside the nanopipette glass domain.

4.4.1 Dielectrophoretic force distribution around the nanotweezers tip region

To probe the z-component of the dielectrophoretic force magnitude experienced by a hypothetically present 2 μm particle at z = -1 μm along a 10 μm length on the xz- and yz-planes, the following command was inputted in COMSOL:

$$2\pi\varepsilon_0\varepsilon_m r_p^3 * Re[f_{CM}(\omega)] * d\left|\vec{E}\right|^2/dz,$$

where ε_0 is the vacuum permittivity (F/m), ε_m = 79 the relative electrical permittivity of H_2O, r_p = 1 μm and $Re[f_{CM}(\omega)]$ = 0.5 at 10 kHz. This system mimicked the experimental conditions in Chapter 5 where positive dielectrophoresis was used to attract individual polystyrene beads towards the nanotweezers tip surface. The $d\left|\vec{E}\right|^2/dx$ and $d\left|\vec{E}\right|^2/dy$ components were found to have negligible contribution to $\left|\vec{F}_{DEP}\right|$, hence were not included in the final calculations.

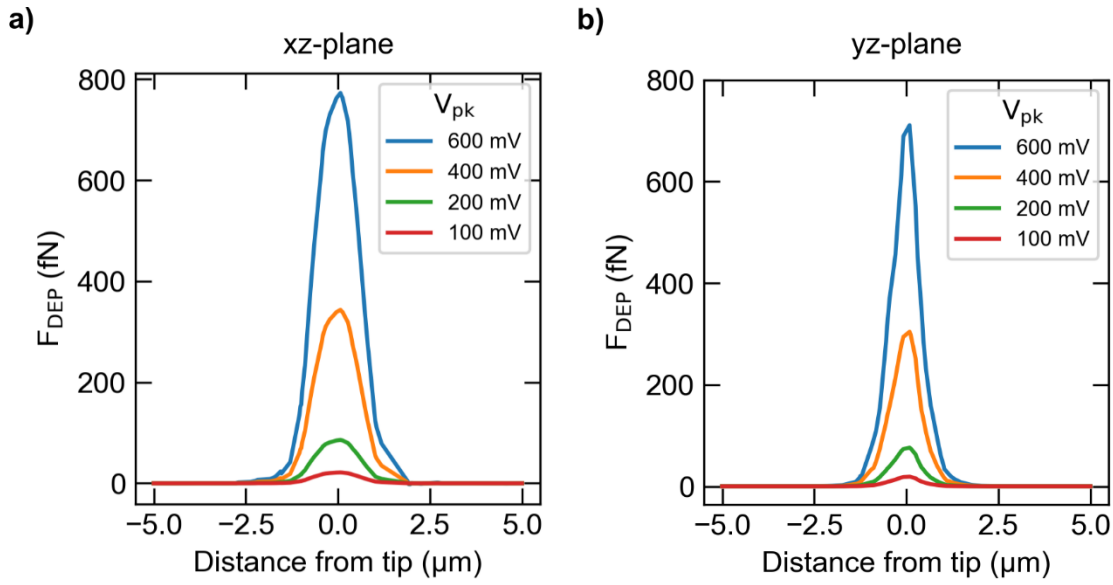

Figure 4.6 Simulated dielectrophoretic force magnitude $|\vec{F}_{DEP}|$ as a function of the distance from the nanotweezers tip at z = -1 μm, when a set of voltages $\pm V_{pk}$ were applied to the top boundaries of the semi-elliptical carbon nanoelectrodes. The curves in **a)** represent $|\vec{F}_{DEP}|$ across the xz-plane for -5 μm ≤ y ≤ 5 μm while in **b)** $|\vec{F}_{DEP}|$ across the yz-plane for -5 μm ≤ x ≤ 5 μm. In both cases, maximum values were reported at the nanotweezers tip centre (x = y = 0 μm) gradually decreasing away from the tip. As V_{pk} became lower, $|\vec{F}_{DEP}|$ decreased accordingly. The full-width at half-maximum (FWHM) of the curves in a) was larger by 600 nm than the curves in b). Small differences were also observed for the peak values between a) and b).

Figure 4.6 shows the simulated dielectrophoretic force magnitude $|\vec{F}_{DEP}|$ as a function of distance from the nanotweezers tip at z = -1 μm, when a set of voltages $\pm V_{pk}$ were applied to the top boundaries of the semi-elliptical carbon nanoelectrodes. The curves in Figure 4.6a represent $|\vec{F}_{DEP}|$ across the xz-plane for -5 μm ≤ y ≤ 5 μm, while in Figure 4.6b $|\vec{F}_{DEP}|$ across the yz-plane for -5 μm ≤ x ≤ 5 μm. In both cases, as for the electric field magnitude, maximum values were reported at the nanotweezers tip centre (x = y = 0 μm) which gradually decreased as moving away from the tip. For $V_{pk} = \pm 600$ mV, $|\vec{F}_{DEP}|_{xz}^{max} = 773$ fN and $|\vec{F}_{DEP}|_{yz}^{max} = 711$ fN. This finding demonstrated a small difference between the peak force magnitudes on the xz- and yz-planes at the axis of symmetry (x = y = 0 nm).

In both planes, $|\vec{F}_{DEP}|^{max}$ decreased proportionally to the applied voltage V_{pk} (±400 mV, ±200 mV, ±100 mV), as expected from $|\vec{F}_{DEP}|^{max} \sim V_{pk}^2$. These magnitudes are listed in Table 4.3 together with the full-width at half-maximum (FWHM) values from the curves

in Figures 4.6a and 4.6b. For -5 μm ≤ y ≤ 5 μm, Δy_{FWHM} was 600 nm larger than the full-width at half-maximum (Δx_{FWHM}) for -5 μm ≤ x ≤ 5 μm. This difference agreed with the one reported in Table 4.2 proving that the force distribution depends on the electric field magnitude. As Barik et al. (2016) [69] suggested, the maximum thermal force on a 2 μm particle is estimated to be ~2 fN (T = 25 °C). Consequently, depending on V_{pk}, the dielectrophoretic force would overcome the one due to thermal energy a few μm away from the nanotweezers tip.

Table 4.3 Simulated dielectrophoretic force peak and full-width at half-maximum (FWHM) values across the xz- and yz-planes at z = -1 μm, for y = x = 0 μm, respectively, over a range of applied voltages $\pm V_{pk}$.

$\pm V_{pk}$ (mV)	$\left\|\vec{F}_{DEP}\right\|_{xz}^{max}$ (fN)	Δy_{FWHM} (μm)	$\left\|\vec{F}_{DEP}\right\|_{yz}^{max}$ (fN)	Δx_{FWHM} (μm)
600	773	1.5	711	0.9
400	344	1.5	304	0.9
200	86	1.5	76	0.9
100	22	1.5	19	0.9

Table 4.4 Simulated dielectrophoretic force peak and full-width at half-maximum (FWHM) values at a ±45° angle across the xy-plane at z = -1 μm, for V_{pk} = ±600 mV.

$\pm V_{pk}$ (mV)	Angle (°)	$\left\|\vec{F}_{DEP}\right\|^{max}$ (fN)	Δy_{FWHM} (μm)
600	0	773	1.5
600	45	664	1.1
600	-45	678	1.2

However, the initial position of a potentially trapped latex bead could be located at any angle in 2D from the centre of the nanotweezers tip surface. To assess this possibility, the dielectrophoretic force was simulated at a ±45° angle between the xz- and yz- planes, for z = -1 μm. Table 4.4 displays the force peak values along 1D lines across the xy-plane for these two angles. The coordinates (x, y) of the first and last point of the line at 45° were (-5 μm, -5 μm) to (5 μm, 5 μm) and at -45° were (5 μm, -5 μm) to (-5 μm, 5 μm). In contrast to what has been found so far, the peak force value decreased by approximately 13% at an angle of ±45°. Moreover, for both cases, the trapping area

became slightly narrower with the full-width at half-maximum shifting from 1.5 μm to ~1.2 μm. This observation is directly related to the non-uniformity of the electric field lines around the nanotweezers tip. As a result, the initial position of a spherical particle located on the same plane (xy-plane) with the tip would affect the dielectrophoretic force magnitude. The particle's trajectory towards the nanotweezers tip would also be impacted leading to different force-distance curves.

4.4.2 Effect of nanoelectrodes gap on dielectrophoretic force

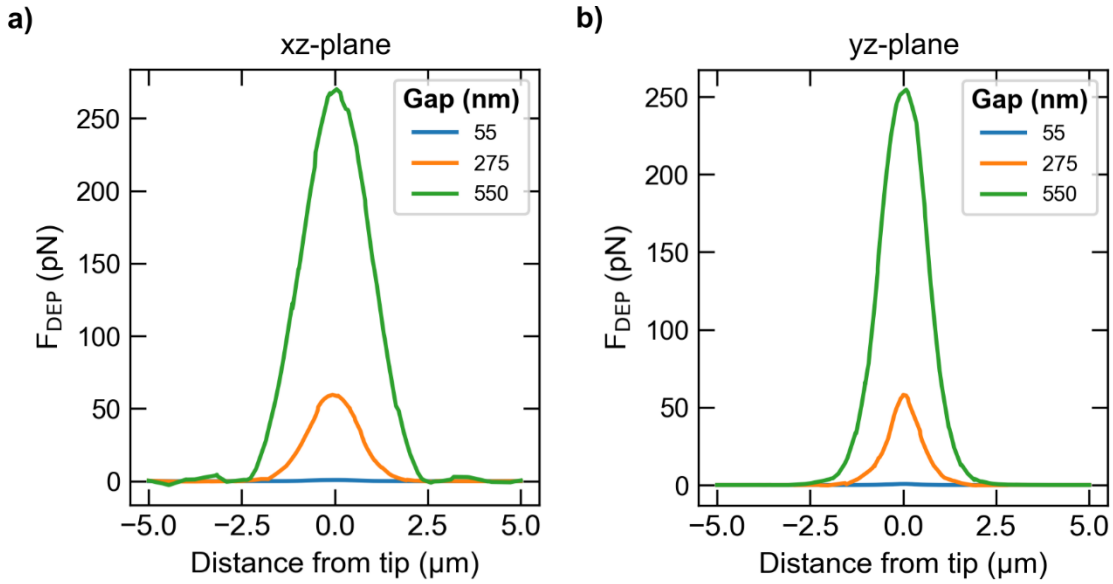

Figure 4.7 Simulated dielectrophoretic force magnitude $|\vec{F}_{DEP}|$ as a function of distance from the nanotweezers tip at z = -1 μm, for a set of separation gaps between the nanoelectrodes when V_{pk} = ±600 mV was applied to their top boundaries. The curves in **a)** represent $|\vec{F}_{DEP}|$ across the xz-plane for -5 μm ≤ y ≤ 5 μm while in **b)** $|\vec{F}_{DEP}|$ across the yz-plane for -5 μm ≤ x ≤ 5 μm. In both cases, maximum values were reported at the nanotweezers tip centre (x = y = 0 μm) gradually decreasing away from the tip. As the separation gaps became larger, $|\vec{F}_{DEP}|$ increased dramatically. The full-width at half-maximum (FWHM) of the curves in a) was larger by 600 nm than the curves in b). Small differences were also observed for the peak values between a) and b).

The highest simulated electric field gradients, and dielectrophoretic force magnitudes, were acquired at the nanoelectrodes edges of the glass domain that separates them at the tip surface. However, all results presented so far were for a separation gap of 55 nm. Based on SEM images provided in Chapter 3, this distance varied between nanotweezers. To evaluate at what extent the separation gap between the two nanoelectrodes at the tip affected the dielectrophoretic force distribution, I redesigned

the geometry of the model. Since 55 nm was the smallest length observed by SEM imaging, two additional gaps were selected to cover all possible cases, 275 nm and 550 nm. The remaining geometry was scaled according to the increase in the separation gap, by a factor of 5 and 10, respectively. Figure 4.7 presents again the z-component of the dielectrophoretic force at z = -1 μm along a 1D line across the xz- and yz-planes when V_{pk} = ±600 mV. Additionally, Table 4.5 includes the peak force and full-width at half-maximum for the three separation gaps across both directions.

Table 4.5 Simulated dielectrophoretic force peak and full-width at half-maximum (FWHM) values across the xz- and yz-planes at z = -1 μm, for y = x = 0 μm, respectively, over a range of nanoelectrodes separation gaps at V_{pk} = ±600 mV.

Gap (nm)	$\left\|\vec{F}_{DEP}\right\|_{xz}^{max}$ (fN)	Δy_{FWHM} (μm)	$\left\|\vec{F}_{DEP}\right\|_{yz}^{max}$ (fN)	Δx_{FWHM} (μm)
55	773	1.5	711	0.9
275	595 x 10^2	1.5	581 x 10^2	1.0
550	270 x 10^3	2.1	255 x 10^3	1.5

From Figure 4.7, it is evident that the increase in the gap separating the nanoelectrodes influenced significantly the dielectrophoretic force peak distribution. In both cases, maximum values were reported at the nanotweezers tip centre (x = y = 0 μm) gradually decreasing away from the tip. As the separation gaps became larger, $\left|\vec{F}_{DEP}\right|$ increased dramatically at z = -1 μm from the nanopipette tip. This force magnitude should not be confused with the one at z = 0 μm where the opposite effect was observed. The smaller the separation gap, the higher $\left|\vec{F}_{DEP}\right|$ was at the nanopipette tip surface but also the more concentrated around it, having decayed considerably to greater than a few hundreds of nanometres away from the tip.

However, a 2 μm bead would never experience the force magnitude at the edges of the nanoelectrodes as its centre of mass would stop moving at z = -1 μm. For a gap of 275 nm, $\left|\vec{F}_{DEP}\right|$ increased by approximately 80 times from the value at 55 nm, while for a gap of 550 nm this increase was ~350 times larger. The difference in full-width at half-maximum (FWHM) between the curves in a) and b) remained constant at 600 nm. Larger differences were observed for the peak values between a) and b). It is important to clarify that increase in the separation gaps means proportional increase in the remaining dimensions of the nanotweezers tip. As the active surface of the nanoelectrodes

becomes bigger (A), and since its electrical resistivity (ρ_e) and length (L) remained constant, the resistance of the carbon domains is expected to decrease $\left(R = \frac{\rho_e L}{A}\right)$ allowing larger current values flowing through the interface between carbon and H_2O. This is the main reason behind the dramatic increase in the simulated dielectrophoretic force.

4.4.3 Effect of recessed carbon at the nanopipette tip on the dielectrophoretic force distribution

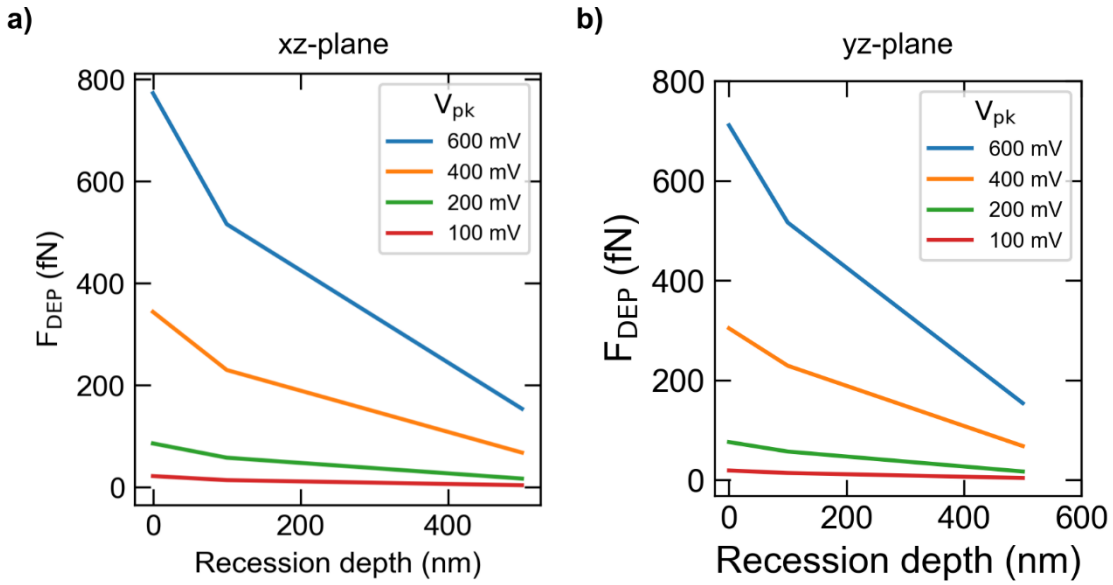

Figure 4.8 Simulated dielectrophoretic force magnitude $\left|\vec{F}_{DEP}\right|$ as a function of carbon recession depth inside the nanopipette tip at z = -1 µm, for a range of V_{pk} and a 55 nm gap between the nanoelectrodes at the tip plane. The curves in **a)** represent $\left|\vec{F}_{DEP}\right|^{max}$ across the xz-plane for -5 µm ≤ y ≤ 5 µm while in **b)** $\left|\vec{F}_{DEP}\right|^{max}$ across the yz-plane for -5 µm ≤ x ≤ 5 µm. In both cases, maximum values were reported for no recession and gradually decreased as carbon was deposited further from the tip. As V_{pk} increased, $\left|\vec{F}_{DEP}\right|^{max}$ ascended as well. Small or even negligible differences were observed for the peak values between a) and b).

Finally, the last study performed with this finite element model was the effect of recessed carbon towards inside the nanopipette tip on the distribution of the dielectrophoretic force experienced by a hypothetical 2 µm latex bead along the z = -1 µm axis. Although the extent of this recession could not be quantified by SEM imaging, its occurrence was visually verified. Actually, when performing FIB milling on nanopipette tips filled with carbon it was noticed that recession did not exceed 500 nm of depth. Based on this, I

conducted a parametric study for two recession depths, one with 100 nm and another with 500 nm. The separation gap between the carbon nanoelectrodes at the nanotweezers tip was 55 nm and a range of electrical potentials was applied to their top boundaries, as in Section 4.4.1. Simulated results are provided in Figure 4.8 and Table 4.6.

Table 4.6 Simulated dielectrophoretic force magnitude across the xz- and yz-planes at z = -1 μm, for y = x = 0 μm, respectively, over a range of V_{pk} and recession depths for a nanoelectrode gap distance of 55 nm.

Depth (nm)	**±100 mV**		**±200 mV**		**±400 mV**		**±600 mV**	
	$\left\|\vec{F}_{DEP}\right\|_{xz}^{max}$ **(fN)**	$\left\|\vec{F}_{DEP}\right\|_{yz}^{max}$ **(fN)**	$\left\|\vec{F}_{DEP}\right\|_{xz}^{max}$ **(fN)**	$\left\|\vec{F}_{DEP}\right\|_{yz}^{max}$ **(fN)**	$\left\|\vec{F}_{DEP}\right\|_{xz}^{max}$ **(fN)**	$\left\|\vec{F}_{DEP}\right\|_{yz}^{max}$ **(fN)**	$\left\|\vec{F}_{DEP}\right\|_{xz}^{max}$ **(fN)**	$\left\|\vec{F}_{DEP}\right\|_{yz}^{max}$ **(fN)**
0	22	19	86	76	344	304	773	711
100	14	14	58	57	230	229	516	516
500	4	4	17	17	68	68	154	154

The simulated dielectrophoretic force peak magnitude as a function of the carbon recession depth inside the nanopipette tip at z = -1 μm is illustrated in Figure 4.8 for a range of V_{pk} and a 55 nm gap between the nanoelectrodes at the tip plane. The curves in Figure 4.8a represent $\left|\vec{F}_{DEP}\right|^{max}$ across the xz-plane for -5 μm ≤ y ≤ 5 μm while in Figure 4.8b $\left|\vec{\mathrm{F}}_{\mathrm{DEP}}\right|^{\max}$ across the yz-plane for -5 μm ≤ x ≤ 5 μm. In both cases, maximum values were reported for no recession and gradually decreased as carbon was deposited further from the tip. As V_{pk} increased, $\left|\vec{F}_{DEP}\right|^{max}$ ascended proportionally. Small to negligible differences were observed for the peak values between the two cases. The descending trends in Figure 4.8, as carbon was deposited further inside the tip openings, had a two-fold explanation. On one hand, the distance across the z-axis between the edges of the nanoelectrodes and a trapped spherical particle increased linearly with recession. The glass walls at the tip would prevent any further attraction towards the carbon surfaces. On the other hand, when the carbon nanoelectrodes where co-planar the electric field gradient at their edges was stronger. When inside the nanopipette, the electric field lines were almost parallel to the glass wall with a direction towards outside the tip opening. This was one of the main reasons FIB milling of the tip was performed on recessed nanotweezers.

4.5 Simulation of the nanotweezers impedance

So far, glass domains separating and surrounding the two carbon domains inside the nanopipette have been excluded from the FEM model to simplify simulations. However, treating this electrical circuit as purely resistive while applying an AC signal is a scenario not expected to take place in an experiment. In fact, when a pair of electrodes is brought in close proximity, such as the nanotweezers, parasitic capacitance could arise between them, affecting the AC signal [112]. To assess this phenomenon, a revised FEM simulation was developed based on the one described in Chapter 4.2. The main differences were the addition of the previously removed glass domains and the use of a frequency dependent solver instead of a stationary. In this section, the nanotweezers impedance magnitude and phase were simulated for three cases. Firstly, for when left in air, secondly when immersed in water and finally when a 2 μm spherical particle (latex bead) was trapped at their tip while immersed in water.

4.5.1 Nanotweezers impedance in air

In the first case, the revised model was used to simulate the total impedance of the nanotweezers system when an AC signal was applied between the two nanoelectrodes and left in air, not immersed in any solution. The electric potential of this signal was V_{pk} = 0.6 V while the frequency ranged from 1 to 10^7 Hz. The model geometry, materials, boundary conditions and mesh were left unchanged from the previous version of the model, except the domain representing air which had a relative electric permittivity (ε_r) of 1 and electric conductivity (σ) of 10^{-14} S/m. Figure 4.9a shows a simplified circuit schematic of this nanotweezers configuration where the two carbon domains are described by two resistors (R_C) connected in series to a capacitor (C_g) which was the glass septum separating them.

For this RC circuit, the total impedance (magnitude and phase) was simulated for three carbon recession depths (0, 100 and 500 nm) as for the estimation of the dielectrophoretic force in Section 4.4.3. The colour plot in Figure 4.9b illustrates the electrical potential distribution close to the nanopipette tip, with red representing the maximum and blue the minimum value, at 100 kHz and 100 nm recession depth. The distribution is similar to the one shown in Figure 4.3, except the voltage drop in the glass septum reaching 0 V at the symmetry axis. The black lines starting from the top left electrode boundary, passing through the separation domain and ending at the top right

electrode boundary represent the x- and y-components of the current density ($\vec{J}_x$,$\vec{J}_y$). This is already an indication of current passing through the capacitor while there is no conductive connection between the two nanoelectrodes.

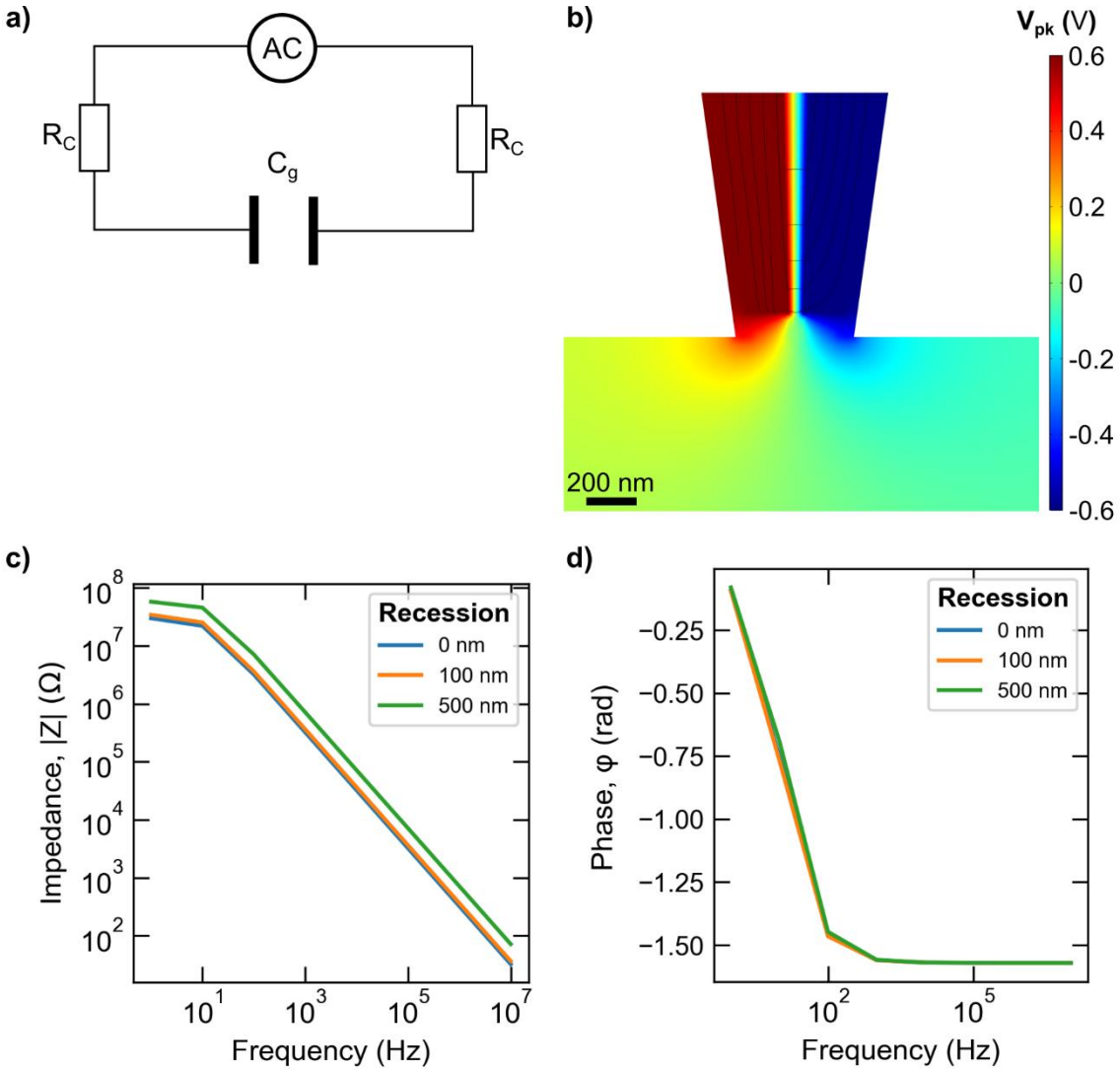

Figure 4.9 Nanotweezers impedance in air. **a)** Simplified circuit diagram where an AC signal (V_{pk}, f_{app}) is applied between a pair of carbon nanopipette electrodes when they are left in air. Carbon domains were considered purely resistive (R_C) while the glass separating and surrounding them capacitive (C_g). **b)** 2D view (xz-plane at y = 0 nm) of the electrical potential distribution near the nanopipette tip (100 nm recession depth). A voltage (V_{pk}) of +600 mV (red) and -600 mV (blue) was applied to the top boundary of the left and right semi-elliptical domain, respectively. The applied frequency was 100 kHz and black lines illustrate the current density ($\vec{J}$). Bode plots of the simulated impedance **c)** magnitude ($|Z|$) and **d)** phase (ϕ) as a function of applied frequency for three different recession depths (0, 100 and 500 nm).

Evaluation of the nanotweezers impedance for each recession depth was performed on the carbon domains. Results always returned complex impedance ($Z = R + jX$), where R is the resistance and X the reactance, hence the impedance magnitude was calculated

from $|Z| = \sqrt{R^2 + X^2}$ and the impedance phase from $\phi = \tan^{-1}(X/R)$. In Figure 4.9c, the impedance magnitude was equal to tens of MΩ at low frequencies (1 – 10 Hz) and gradually decreased at higher frequencies (> 10 Hz) without reaching a plateau in the selected range. Higher magnitudes were achieved when no recession was present, while small differences were noted between 100 and 500 nm recession depths. In contrast, based on Figure 4.9d, the trend of the impedance phase showed a decline up to 100 Hz at -1.50 rad and became flat for frequencies higher than 1 kHz. Since all phase values were negative, the circuit was capacitive with the current leading the voltage. Based on the three curves, carbon recession did not seem to affect the impedance phase.

4.5.2 Nanotweezers impedance when immersed in water

Although results from the previous section already showed the nanotweezers circuit being capacitive when in air, these conditions do not describe the ones during an experiment. As a result, the domain representing air was replaced with water in the model by using the material properties mentioned in Section 4.2, mimicking the nanotweezers being immersed in water. The remaining parameters were kept unchanged. As Figure 4.10a depicts, the nanotweezers circuit has an additional element, the resistance from water (R_{water}), connected in parallel to C_g. By comparing the electric potential distribution illustrated in Figure 4.10b with the one in 4.9b, the voltage seems to reach 0 V (green) much closer to the tip for the latter. The applied voltage was V_{pk} = 0.6 V, applied frequency 100 kHz and recession depth 100 nm. The black lines, representing current density, spread much further into the water domain rather than through the glass septum as in Figure 4.9b.

Evaluation of the nanotweezers impedance was performed in the same way as in Section 4.5.1, with results being in the form of $Z = R + jX$. The impedance magnitude when carbon was deposited up to the nanopipette tip aperture (0 nm) was constant at ~200 kΩ up to 100 Hz but decreased gradually for higher frequencies (Figure 4.10c). As the recession depth increased, the impedance magnitude followed a similar trend but became larger starting at ~600 kΩ for 100 nm depth and at ~1 MΩ for 500 nm depth. These findings suggest that the further inside carbon was formed, the larger was the voltage drop. Based on Figure 4.10d, the impedance phase was close to 0 rad up to 100 Hz, decreased considerably between 100 Hz and 10 kHz where it reached a plateau at approximately -1.5 rad up to 10 MHz. Small differences were observed between the three recession depths with 500 nm noting a drop at lower frequencies compared to 0 nm. The negative values of the impedance phase suggested that this circuit was also capacitive.

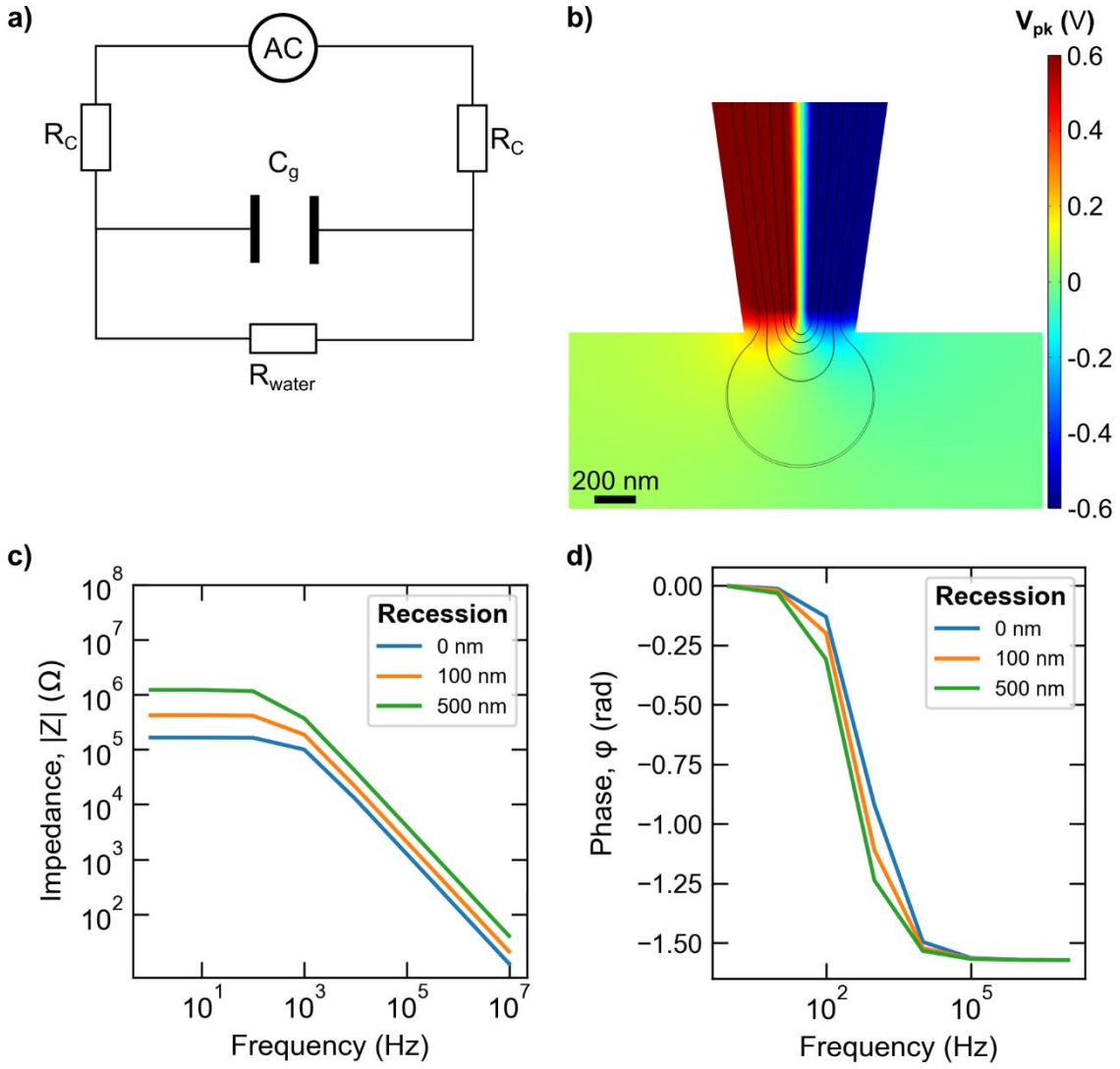

Figure 4.10 Nanotweezers impedance in water. **a)** Simplified circuit diagram where an AC signal (V_{pk}, f_{app}) is applied between a pair of carbon nanopipette electrodes when they are immersed in water. Carbon and water domains were considered purely resistive (R_C, R_{water}) while the glass separating and surrounding them capacitive (C_g). **b)** 2D view (xz-plane at y = 0 nm) of the electrical potential distribution near the nanopipette tip (100 nm recession depth). A voltage (V_{pk}) of +600 mV (red) and -600 mV (blue) was applied to the top boundary of the left and right semi-elliptical domain, respectively. The applied frequency was 100 kHz and black lines illustrate the current density ($\vec{J}$). Bode plots of the simulated impedance **c)** magnitude ($|Z|$) and **d)** phase (ϕ) as a function of applied frequency for three different recession depths (0, 100 and 500 nm).

This conclusion justifies the statements made in Section 3.4.2 for currents not being stationary in the plateau region (sigmoid cyclic voltammograms, Figure 3.6) due to the presence of additional capacitive currents which affected the measured signal. Although the system modelled here is not identical to that for electrochemical characterisation of carbon nanoelectrodes, it contributes to a more comprehensive understanding on the losses within such a circuit. Here, it is worth also clarifying that during electrochemical

characterisation measurements there was no electrical connection between the two carbon nanoelectrodes as in the model, because each nanoelectrode was characterised separately from the other.

4.5.3 Nanotweezers impedance when immersed in water with a trapped spherical bead at the tip

Taking the model in the previous section one step further, a 2 μm in diameter bead was designed with its top edge meeting the nanopipette tip aperture. This system mimicked a latex bead being trapped at the nanotweezers tip during a dielectrophoretic force probing measurement. To assess whether the presence of the trapped bead at the tip would affect the total impedance of the circuit, a relative electric permittivity ε_r = 2.56 and σ = 6 mS/m were allocated to the bead's domain while the remaining model properties and parameters were left unchanged. The final form of the circuit schematic is presented in Figure 4.11a with an additional resistor (R_{bead}) being connected in parallel to R_{water}. By comparing again, the electric potential distribution illustrated in Figure 4.11b with the one in 4.10b, the voltage seems to reach 0 V (green) almost at the tip aperture for the latter. The applied voltage was V_{pk} = 0.6 V, applied frequency 100 kHz and recession depth 100 nm. The black lines, representing current density, spread into the water domain similar to the ones in Figure 4.10b.

Evaluation of the nanotweezers impedance was performed in the same way as in Sections 4.5.1 and 4.5.2, with results being in the form of $Z = R + jX$. The impedance magnitude when carbon was deposited up to the nanopipette tip aperture (0 nm) was constant at ~8 kΩ up to 1 kHz but decreased gradually for higher frequencies (Figure 4.11c). As the recession depth increased, the impedance magnitude followed a similar trend but became larger starting at ~400 kΩ for 100 nm depth and at ~1 MΩ for 500 nm depth. These findings agree with the ones in Section 4.5.2 that the further inside carbon was formed, the larger was the voltage drop but with the first two cases (0 and 100 nm) having lower impedance magnitudes. This could be attributed to the presence of the trapped bead at the nanotweezers tip. Based on Figure 4.11d, the impedance phase was close to 0 rad up to 100 Hz, decreased considerably between 100 Hz and 10 kHz where it reached a plateau at approximately -1.5 rad up to 10 MHz for the two recessed depths (100 and 500 nm). For the 0 nm depth, the curve jumped at -0.5 rad for 100 kHz and started decreasing again towards -1.5 rad at higher frequencies. Small differences were observed between the 100 and 500 nm recession depths with 500 nm noting a drop at

lower frequencies compared to 100 nm. The negative values of the impedance phase suggested that the circuit remained capacitive.

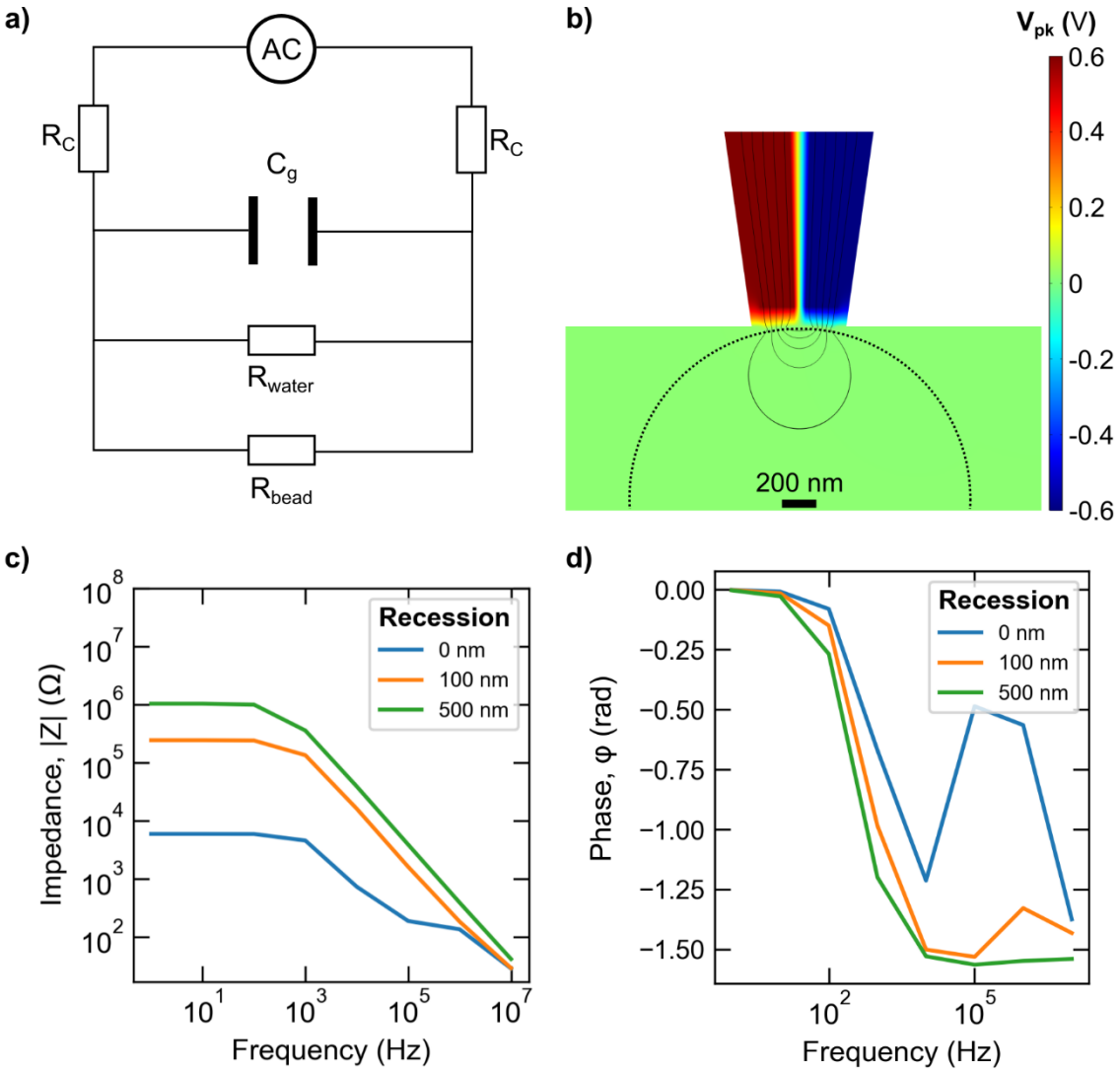

Figure 4.11 Nanotweezers impedance in water with a 2 µm bead trapped at their tip. **a)** Simplified circuit diagram where an AC signal (V_{pk}, f_{app}) is applied between a pair of carbon nanopipette electrodes when they are immersed in water with a 2 µm bead trapped at their tip. Carbon, water and bead domains were considered purely resistive (R_C, R_{water}, R_{bead}) while the glass separating and surrounding them capacitive (C_g). **b)** 2D view (xz-plane at y = 0 nm) of the electrical potential distribution near the nanopipette tip (100 nm recession depth). A voltage (V_{pk}) of +600 mV (red) and -600 mV (blue) was applied to the top boundary of the left and right semi-elliptical domain, respectively. The applied frequency was 100 kHz and black lines illustrate the current density ($\vec{J}$). Dotted black line represents the boundary of the trapped bead. Bode plots of the simulated impedance **c)** magnitude ($|Z|$) and **d)** phase (ϕ) as a function of applied frequency for three different recession depths (0, 100 and 500 nm).

Overall, the impedance magnitude decreased as more components were added in the nanotweezers circuit. The impedance phase had different trends between the case in air

and the ones in water but always being within the same range (0 to -1.5 rad). The case of the nanotweezers being immersed in water with a trapped bead at their tip aperture was interesting at 100 kHz when no carbon recession was present, as the phase increased dramatically to -0.5 rad. This was the only value to deviate significantly from the general trend. Actually, these parameters could potentially be used in an experiment where the detection of an individual bead being trapped at the nanotweezers tip could be monitored by this shift in the impedance phase. Table 4.7 below summarises the impedance magnitude and phase for the three configurations discussed in Section 4.5 when V_{pk} = 0.6 V, f_{app} = 100 kHz and carbon recession was 100 nm inside the nanopipette.

Table 4.7 Simulated total impedance magnitude ($|Z|$) and phase (ϕ) in three different configurations (air, water, water and bead) for V_{pk} = 0.6 V, f_{app} = 100 kHz and 100 nm carbon recession.

Conditions	$\|Z\|$ **(kΩ)**	ϕ **(rad)**
air	3.65	-1.57
water	2.09	-1.57
water + bead	1.62	-1.53

4.6 Conclusions

To summarise, in this chapter, I presented a new three-dimensional finite element model based on a simplified geometry for the nanotweezers configuration when immersed in water. This model can be used as tool to simulate the experimental conditions discussed in the next chapter and get a better understanding of the physical processes involved. The model geometry was based on a truncated cone consisting of two semi-elliptical channels filled with carbon, immersed in a cubical domain that represented H_2O. The simulation was based on the "Electric currents" package of the "AC/DC Module" from COMSOL Multiphysics software. Based on this, the main initial boundary conditions applied to the geometry of the model were a positive and negative electrical potential at the top surface of the carbon nanoelectrodes. The geometry was meshed into smaller 3D elements where the software solved the stationary equations. Further details regarding the geometry of this model, initial boundary conditions and mesh are provided in Appendix C in the form of a COMSOL model report.

Furthermore, I simulated the electrical potential distribution across all 2D planes (xy, xz and yz) of the model geometry, as well as the electric field magnitude and visualised its lines distribution in three dimensions. Both variables were determined as a function of the distance from the nanotweezers tip and for a range of applied voltages. In the designed geometry, the nanotweezers tip was fixed 3 µm above the bottom surface of the aqueous solution. The reason for doing this was to replicate the trajectory of a potentially trapped 2 µm latex bead when experiencing a dielectrophoretic force by the nanotweezers. For $V_{pk} = \pm 600$ mV, the simulated electric field modulus was found $\left|\vec{E}\right|_{xz}^{max} = 7.7$ kV/m and $\left|\vec{E}\right|_{yz}^{max} = 7.5$ kV/m, demonstrating small differences between the xz- and yz-planes when crossing the symmetry axis (x = y = 0 nm). In both planes, $\left|\vec{E}\right|^{max}$ decreased proportionally to the applied voltage V_{pk} (±400 mV, ±200 mV, ±100 mV). For -5 µm ≤ y ≤ 5 µm, Δy_{FWHM} was 600 nm larger than the full-width at half-maximum (Δx_{FWHM}) for -5 µm ≤ x ≤ 5 µm. This was a first indication that the trapping area would extend to greater lengths across the xz-plane compared to the yz-plane.

Based on the findings regarding the electric field distribution, I then estimated the dielectrophoretic force magnitude close to the nanotweezers tip by calculating the spatial derivative of the squared variable $\left|\vec{E}\right|$ across the z-axis. The magnitude of $\vec{F}_{DEP}$ was probed along 1D lines drawn on 2D planes (xz- and yz-planes) for a range of applied voltages and as a function of the distance from the nanotweezers tip. For $V_{pk} = \pm 600$ mV, $\left|\vec{F}_{DEP}\right|_{xz}^{max} = 773$ fN and $\left|\vec{F}_{DEP}\right|_{yz}^{max} = 711$ fN, demonstrating small differences

between the peak force magnitudes on the xz- and yz-planes when crossing the symmetry axis (x = y = 0 nm). In both planes, $\left|\vec{F}_{DEP}\right|^{max}$ decreased proportionally to the applied voltage V_{pk} (±400 mV, ±200 mV, ±100 mV), as expected from $\left|\vec{F}_{DEP}\right|^{max} \sim V_{pk}^2$. As Barik et al. (2016) [69] suggested, the maximum thermal force on a 2 μm particle is estimated to be ~2 fN (T = 25 °C). Consequently, depending on V_{pk}, the dielectrophoretic force would overcome the one due to thermal energy a few μm away from the nanotweezers tip.

I also investigated how the dielectrophoretic force distribution changed at a ±45° angle between the xz- and yz-planes, for z = -1 μm. The initial position of a potentially trapped latex bead could be located at any angle on a 2D plane from the centre of the nanotweezers tip surface. In contrast to what was found before, the peak force value decreased by approximately 13% at an angle of ±45°. Moreover, for both cases, the trapping area became slightly narrower with the full-width at half-maximum shifting from 1.5 μm to ~1.2 μm. This observation was directly related to the non-uniformity of the electric field lines around the nanotweezers tip. In conclusion, the initial position of a spherical particle located on the same plane (xy-plane) with the tip affected the dielectrophoretic force magnitude. The particle's trajectory towards the nanotweezers tip would also be impacted leading to different force-distance curves.

Moreover, the effect of the widths separating the two carbon nanoelectrodes at z = -1 μm away from the nanotweezers tip was studied. It was found that an increase in the gap separating the nanoelectrodes influenced significantly the dielectrophoretic force peak distribution. In both cases, maximum values were reported at the nanotweezers tip centre (x = y = 0 μm) gradually decreasing away from the tip, agreeing with the previous results. As the separation gaps became larger, $\left|\vec{F}_{DEP}\right|$ increased dramatically. For a gap of 275 nm, $\left|\vec{F}_{DEP}\right|$ increased by approximately 80 times from the value at 55 nm, while for a gap of 550 nm this increase was ~350 times larger. However, proportional increase in the remaining dimensions of the nanotweezers tip were expected based on SEM imaging. Finally, the effect of carbon recession, further inside the nanopipette tip, on the dielectrophoretic force magnitude was assessed for a set of recession depths and applied voltages. Maximum values were reported for no recession and gradually decreased as carbon was deposited further from the tip. This was one of the main reasons FIB milling of the tip was performed on recessed nanotweezers. As V_{pk} increased, $\left|\vec{F}_{DEP}\right|^{max}$ ascended proportionally.

Finally, a revised FEM simulation was developed based on the one described in Chapter 4.2 to assess the effect of potential parasitic capacitance between a pair of carbon nanopipette-based electrodes on the AC signal. Previously, glass domains separating

and surrounding the two carbon domains inside the nanopipette had been excluded from the FEM model to simplify simulations. However, treating this electrical circuit as purely resistive while applying an AC signal is a scenario not expected to take place in an experiment. In fact, when a pair of electrodes is brought in close proximity, such as the nanotweezers, parasitic capacitance could arise between them, affecting the AC signal [112]. Based on that, the main differences between the two version of the model were the addition of the previously removed glass domains and the use of a frequency dependent solver instead of a stationary. The nanotweezers impedance magnitude and phase were simulated for three cases. Firstly, for when left in air, secondly when immersed in water and finally when a 2 μm spherical particle (latex bead) was trapped at their tip while immersed in water. All simulations were carried for three recession depths (0, 100 and 500 nm) as in Section 4.4.3. The impedance magnitude decreased as more components were added in the circuit while the phase had different trends between the case in air and the ones in water but always being within the same range (0 to -1.5 rad). The case of the nanotweezers being immersed in water with a trapped bead at their tip aperture was interesting at 100 kHz when no carbon recession was present, as the phase increased dramatically to -0.5 rad. This was the only value to deviate significantly from the general trend. Overall, the negative impedance phase values verified the circuit being capacitive and justified previous statements of capacitive currents in Chapter 3.

In general, the work presented in this chapter could be considered a valuable tool in understanding the physical phenomena involved in dielectrophoretic trapping of individual entities with the nanotweezers. In the next chapter, experimental measurements on single-entity trapping and force probing with the dielectrophoretic nanotweezers are presented and discussed. Direct comparisons to the values for the dielectrophoretic force magnitude obtained in this chapter are made to assess both the accuracy of the simulation and experimental results.

Chapter 5
Probing femtonewton forces with dielectrophoretic nanotweezers

5.1 Introduction

So far, I have discussed the fabrication and characterisation of the nanotweezers (Chapter 3), as well as the simulation of non-uniform electric field generated upon the application of an AC signal between the two carbon nanoelectrodes at the tip region (Chapter 4). The next steps were to use these nanotweezers to trap dielectrophoretically individual polystyrene latex beads in water and probe the forces acting on them across the two-dimensional plane as a function of distance from the nanoelectrodes' tip surface. Before this could be addressed, however, it was necessary to first study the motion and characteristics of beads when immersed in H_2O without any external forces applied. Electrophoretic light scattering measurements were performed to determine their zeta potential, while single particle tracking was applied to measure their diffusion coefficient at equilibrium state. From this value, changes in the bulk viscosity of the solution due to the occurrence of hydrodynamic interactions between a bead and the glass slide were studied.

Following this, the average distance between a bead and the glass surface was estimated to understand where the nanotweezers tip should be positioned for the force probing experiments to assume exclusive 2D motion. To characterise the polarisability of the beads-H_2O suspension when AC fields were generated at the nanotweezers tip, the real part of the Clausius-Mossotti factor was determined as a function of the applied frequency. This predicted at what frequency ranges pDEP and nDEP would take place. Then, a new technique was developed to measure the dielectrophoretic force experienced by individual beads under trapping conditions through single particle tracking. The spatial coordinates were extracted from the trajectory of each bead over time. From these, their velocity was calculated as a function of time. Since the dielectrophoretic force was equal to the Stokes drag force at every time point, the force magnitude was defined by this velocity profile. The effect of the applied voltage and frequency between the nanotweezers on the dielectrophoretic force was investigated by

applying a range of sub-volt voltages and kilohertz to megahertz frequencies. Comparisons to the simulated values obtained in Chapter 4 provided further information about the geometry of the nanotweezers used in the experimental measurements.

The key questions addressed in this chapter are:

1. How could the electrical conductivity of a carboxylate-modified polystyrene latex bead immersed in water be measured?

In Section 5.2, electrophoretic light scattering measurements were performed to determine the zeta potential of carboxylate-modified polystyrene beads in water. A slightly more conductive electrolyte solution was chosen to acquire meaningful measurements for this value. Nevertheless, the obtained zeta potential was then used to estimate the electrical conductivity of the particle which could then be utilised in determining the polarisability of this suspension under the application of an AC signal.

2. How accurately could the diffusion coefficient of an individual bead immersed in H_2O be measured by single particle tracking?

In Section 5.3, the two-dimensional trajectory of individual freely diffusing beads in H_2O on top of a glass slide was recorded on an inverted fluorescence microscope by using single particle tracking. The x- and y-coordinates were used to calculate their time averaged mean squared displacement as a function of lag time for all available displacements. By applying linear fitting between these two variables, the optimum number of fitting points and trajectory length were statistically evaluated. Based on that, the mean diffusion coefficient of individual beads was measured from a trajectory including 1000 data points.

3. How could the effective dynamic viscosity of water surrounding an individual bead be assessed when diffusing close to a glass surface?

In Section 5.4, the analysis for the diffusion coefficient of latex beads in H_2O solution was used to assess whether their diffusion was hindered due to hydrodynamic interactions with the top surface of the cover glass, where most beads were found at equilibrium. From this, a correction factor for the bulk viscosity of the solution was calculated and applied to measure the effective viscosity of H_2O surrounding individual beads when diffusing close to a glass surface. Data sets were collected over 6 consecutive days after applying the same experimental conditions. The effect of temperature in the beads'

diffusion coefficients was also studied by recording their trajectories while in Brownian motion both at the start of sample illumination and 30 minutes afterwards.

4. How could the average distance between the diffusing bead and the top surface of a cover glass be estimated?

In Section 5.5, the measured effective viscosity of H_2O was used to assess the distance between the bottom surface of an individual bead and the top surface of the glass slide. This distance was estimated by applying Faxen's and Brenner's approximations, for particle motion only parallel to the glass wall top surface.

5. How could the polarisability of the beads-H_2O suspension be assessed under the application of an AC signal?

In Section 5.6, the polarisability of the beads-H_2O suspension under the application of an AC signal was analytically obtained. By using the electrical conductivity of latex beads, which was measured in Section 5.2, and the aqueous solution together with their known relative electrical permittivities, the real part of the Clausius-Mossotti factor was analytically measured as a function to the applied frequency. This could predict the frequency ranges at which positive and negative dielectrophoresis would occur.

6. How could the magnitude of the dielectrophoretic force experienced by individual beads close to the nanotweezers tip be determined?

In Section 5.7, I explain the developed technique to measure dielectrophoretic forces experienced by individual latex beads under trapping conditions based on single particle tracking. After integrating the nanotweezers on the inverted fluorescent microscope and placing their tip 1 μm above the 2D plane where most beads diffused, AC signals of sub-volt voltages and tens of kHz frequencies were applied to achieve pDEP. From the individual trajectories of trapped beads, their spatial coordinates were extracted for a range of time frames. By taking their time derivative, their velocity was defined as a function of the distance from the nanotweezers tip. Since, the dielectrophoretic force was equal to the Stokes drag force at every time point, their velocity was used to measure the magnitude of the dielectrophoretic force. A data smoothing algorithm was developed to filter noise created from the time derivatives.

7. How could the electrical potential and frequency of an AC signal affect the dielectrophoretic force magnitude exerted by the nanotweezers?

Finally, in Section 5.8, the effect on the dielectrophoretic force magnitude by the electrical potential and frequency of the applied AC signal between the nanotweezers were investigated. A range of voltages (100 mV, 200 mV, 400 mV and 600 mV) and frequencies (10 kHz, 100 kHz, 250 kHz, 500 kHz, 750 kHz, 1 MHz and 20 MHz) were applied to assess changes in the dielectrophoretic force. This frequency range was selected to verify whether pDEP and nDEP occurred at low and high values, respectively. Comparisons to simulated results from Section 4.4 were performed, to conclude whether the average nanotweezers used throughout these experiments had recessed carbon electrode surface inside the tip opening and whether the separation distance between the two carbon nanoelectrodes was close to 55 nm.

5.2 Measuring the electrical conductivity σ_p of carboxylate-modified polystyrene latex beads in aqueous solution

In general, when a surface carrying a net charge is immersed in an aqueous solution, an electrostatic potential ϕ_0 is generated at the interface between solid and liquid. This leads to attracting counterions (ions of opposite charge to surface) from the solution and repelling co-ions (ions of equal charge to surface) [95]. As a result, a larger number of counterions and a smaller number of co-ions compared to the bulk occupies the region close to this interface which is known as the diffuse region of the electrical double layer (EDL). Eventually, this additional surface charge brought into solution is balanced by the presence of counterions, and on a global scale (bulk), the system is electroneutral. The Poisson – Boltzmann equation for a point charge in a uniform solution below describes the distribution of the electric potential away from this interface (along the z axis), considering surface charge screening by counterions:

$$\nabla^2\phi(z) = -\frac{q}{\varepsilon_0\varepsilon_m} * \sum_i n_{0,i} z_i e^{-\phi(z)*\left(\frac{qz_i}{k_B T}\right)} \quad (5.1),$$

where q is the elementary charge (C), ε_0 the vacuum permittivity (F/m), ε_m the relative electrical permittivity of the medium, $n_{0,i}$ the number density of ions in bulk (m^{-3}), z_i the ion valence, k_B Boltzmann's constant (J/K) and T the solution temperature (K). Although there is no analytical solution for this equation for a spherical particle (i.e., ion, bead), Debye and Hückel provided an approximate solution for the case of low surface potentials [91], [95]. This is known as the thick double layer limit, and the electric potential distribution is described by:

$$\phi(z) = \phi_0 * e^{-\kappa z} \quad (5.2).$$

The potential function (Equation 5.2) shows an exponential decay across the diffuse layer until a particular length, the Debye length (κ^{-1} or λ_D), where electrostatic interactions of charged spherical particles in solution become weak because of ionic screening. For a symmetric electrolyte, where $z = z_+ = z_-$, the Debye length is defined as:

$$\kappa^{-1} = \lambda_D = \sqrt{\frac{\varepsilon_0\varepsilon_m k_B T}{2z^2 q^2 n_0}} = \sqrt{\frac{\varepsilon_0\varepsilon_m RT}{2c_b F^2}} \quad (5.3),$$

where c_b is the bulk solution concentration (mol/m^3), F the Faraday constant (C/mol), R the gas constant (J/[K*mol]) and T the solution temperature (K).

Firstly, it is worth clarifying that between the charged surface and diffuse region there is an additional layer of counterions which are tightly bound on the surface, the so-called Stern layer. In this layer, which is one or two hydrated ions thick (ions surrounded by water molecules due to electrostatic interaction), ϕ_0 drops linearly from the charged surface to the ζ (zeta potential) at the interface between the Stern and diffuse layers. This interface is most commonly defined as the slip plane and represents the boundary between stationary (ions within Stern layer) and moving (ions in diffuse region) fluid. Then, as mentioned above, ϕ drops exponentially for a length equal to κ^{-1}. Secondly, although further refinements of the EDL model exist in literature [91], [95] they will not be covered here, as they fall outside the scope of the work presented in this chapter. Thirdly, an analytical solution for Equation 5.1 was derived by Gouy and Chapman in 1913 [95] for the case of planar surfaces which is equivalent to the thin double layer limit for spherical particles. However, for low surface potential values (ϕ_0 < 50 mV) this solution is equal to the Debye – Hückel approximation, hence the Gouy – Chapman theory is also not included in this chapter.

For the dielectrophoretic trapping system, the charged surfaces immersed in water, which are described extensively in Section 5.10, can be classified into planar and spherical. The surface of the carbon nanoelectrodes, nanopipette quartz glass wall surrounding them, borosilicate microscope cover glass, PDMS ring that keeps the aqueous solution in place and latex beads are all considered planar. The reason for assuming beads being planar and not spherical, was because their diameter (2 μm) is orders of magnitude larger than a typical Debye length in H_2O. The negatively charged surface of the beads prevents aggregation thanks to electrostatic repulsion. Measuring the value of the beads' surface charge density is important for determining their electrical surface conductivity, as well as the bulk polarisability (Clausius-Mossotti factor, Section 5.6), when immersed in water. For low surface charge densities, as expected in this case, the potential at the slip plane (ζ) can be quantified experimentally. Note that such measurements were applied only for latex beads, as the remaining surfaces did not comply with the specifications of the available equipment. To define the zeta potential of such surfaces, an electrokinetic analyser (i.e., SurPASS, Anton Paar) would be needed but access to this type of instrument was not possible. Nevertheless, determining their surface charge would not contribute significantly to understanding the system since all experiments were conducted in H_2O and not in salt solutions.

As explained in Section 5.10.2, the zeta potential of the latex beads was measured by electrophoretic light scattering (ELS) in 1 mL solution composed of 975 μL water (beads

stock solution diluted 10^4 times in Milli-Q H_2O) and 25 μL 10x PBS. Once the sample was pipetted in the capillary cell, a DC voltage was applied between two gold (Au) electrodes which set the beads in motion under the influence of a generated electric field. Although all experiments, described further in this chapter, were undertaken in water, a small volume of PBS was added exclusively for the zeta potential measurements to improve the acquired signal intensity. The minimum volume of 10x PBS required for valid measurement of the beads' ζ value was 25 μL.

Figure 5.1 illustrates the recorded intensity signal over measured zeta potential of the particles for three repetitions, while Table 5.2 lists the mean values of ζ and their standard deviations ($\delta\zeta$). The mean and standard error of the mean from these measurements were found equal to $\bar{\zeta} \pm \sigma_{\bar{\zeta}}$ = -2.4 ± 0.5 mV. For similar systems, no zeta potential values were found in literature so comparisons with reference values were performed for σ_p further below. Although its average relative error is significantly high ($\overline{\delta\zeta}/\bar{\zeta}$ = 2) which minimises the precision of the acquisition, the measurement accuracy falls to ~21%. Eventually, σ_p will be used to estimate the Clausius-Mossotti factor and define the crossover frequency between positive and negative dielectrophoresis. As discussed in Section 5.6, this deviation from the mean value $\bar{\zeta}$ has a negligible effect when determining the crossover frequency.

Table 5.1 Measured mean zeta potential values and standard deviations ($\zeta \pm \delta\zeta$) of 2 μm carboxylate-modified polystyrene latex beads in 1 mL of aqueous solution (975 μL of x10^4 diluted beads stock solution in Milli-Q H_2O mixed with 25 μL of 10x PBS), acquired by ELS. The sample was run 3 times (coloured curves) with 92 recordings per run at 25 °C and $\zeta \pm \delta\zeta$ values represented the peak and half-width at half-maximum, respectively, for each curve in Figure 5.1.

Repetition	***1***	***2***	***3***
ζ (mV)	-2.58	-3.31	-1.25
$\delta\zeta$ (mV)	4.46	4.82	5.04

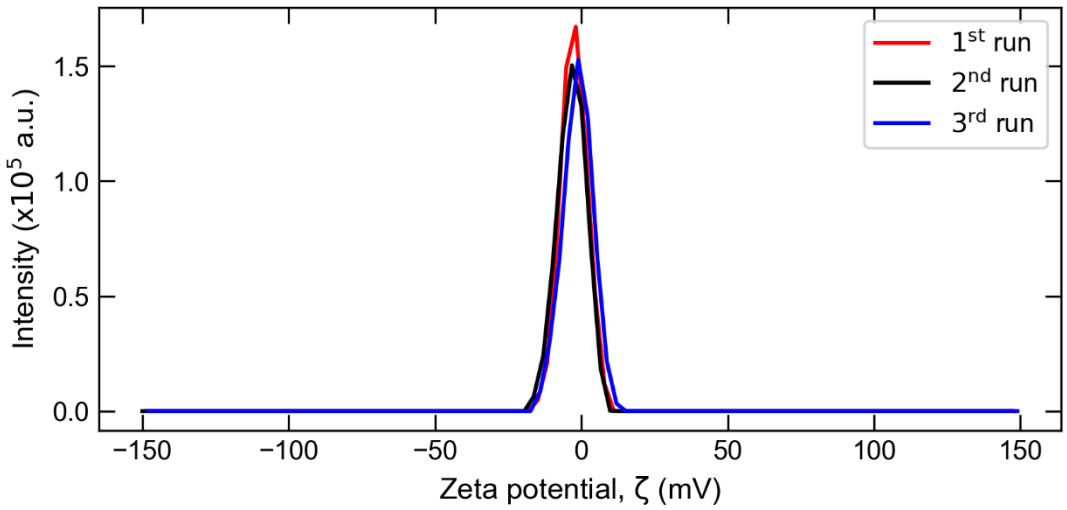

Figure 5.1 Acquired ELS intensity curves for zeta potential measurements of 2 µm carboxylate-modified polystyrene latex beads in 1 mL of aqueous solution (975 µL of x10^4 diluted beads stock solution in type 1 H_2O mixed with 25 µL of 10x PBS). The sample was run 3 times (coloured curves) with 92 recordings per run at 25 °C and the measurements were reported as the mean ± standard deviation ($\zeta \pm \delta\zeta$). These values represented the peak and half-width at half-maximum for each curve. Note that intensity values shown on vertical axis are multiplied by 10^5 and are expressed in arbitrary units.

A spherical particle's conductivity in solution (σ_p) can be described by the sum of its Stern layer conductance (K_S) and the bulk conductivity of its core ($\sigma_{p,bulk}$) [157]:

$$\sigma_p = \sigma_{p,bulk} + \frac{2K_S}{r_p} \quad (5.4),$$

where r_p is the radius of the sphere. For latex beads, it can be assumed that $\sigma_{p,bulk} \approx 0$ [157], [158] which means that their total conductivity mainly depends on K_S. Since the electrical double layer is composed of the Stern and diffuse layers, the Stern layer conductance can also be divided in the same way. If we assume that $K_{S,i}$ and $K_{S,d}$ are the inner Stern and diffuse layer conductance, respectively, then:

$$K_S = K_{S,i} + K_{S,d} \quad (5.5).$$

Overall, the surface conductance can be defined by multiplying the charge density ρ_q within the region of interest and the counterion mobility μ [159], [160]. For the inner Stern layer, when $r_p \gg \kappa^{-1}$, $K_{S,i}$ is equal to:

$$K_{S,i} = \rho_{q,i}\mu_i = -\varepsilon_0\varepsilon_m\zeta\mu_i * \left(\frac{1+\kappa r_p}{r_p}\right) \quad (5.6),$$

where κ is the inverse Debye length, $\rho_{q,i}$ the charge density and μ_i the counterion mobility within the inner Stern layer. In the diffuse layer, under the presence of an electric field, ions interact with the field and move at higher velocities along the charged surface leading to a volume of fluid flowing beyond the slip plane [157]. This phenomenon is called electroosmosis and it takes place in addition to movement of charges due to conduction. Based on that, for a symmetrical electrolyte, the surface conductance $K_{S,d}$ is described by [157]:

$$K_{S,d} = \rho_{q,d}\mu_d = \left(\frac{4F^2 c_b D z^2}{RT\kappa}\right) * \left(1 + \frac{3m}{z^2}\right) * \left(\cosh\left(\frac{zq\zeta}{2k_B T}\right) - 1\right) \quad (5.7),$$

where D is the diffusion coefficient of the counterion and m is a dimensionless parameter which characterises the contribution of electroosmotic ion flux to the surface conductance, as follows:

$$m = \left(\frac{RT}{F}\right)^2 * \frac{2\varepsilon_0 \varepsilon_m}{3\eta_0 D} \quad (5.8),$$

where η_0 is the dynamic viscosity of the suspending bulk medium. The diffusion coefficient for the inner and diffuse Stern layers are assumed equal to the bulk when simple ions are involved (i.e., Na^+, Cl^-) [157], [159], but the diffusion coefficient of the ions in the inner layer is expected smaller than this.

So, the first step in measuring the electrical conductivity of 2 μm carboxylate-modified polystyrene beads was to calculate the Debye length when they were immersed in the sample solution mentioned earlier (97.5% H_2O + 2.5% 10x PBS) that was used for the zeta potential measurements. In the 10x PBS (pH 7.4), the dominant electrolyte is NaCl with an initial ionic strength equal to 1.37 M but since it was diluted further in 975 μL H_2O, its final bulk concentration drops to approximately 34 mM. By assuming c_b ≈ 34 mM at 25 °C, the electrical double layer length was κ^{-1} ≈ 1.7 nm and since this value is significantly smaller compared to the radius of the beads (r_p = 1 μm), the surface conductance for the inner Stern and diffuse layers were evaluated from Equations 5.6 and 5.7, respectively.

As ζ = -2.4 ± 0.5 mV indicates, in this system, latex beads are expected to carry a low negative charge due to their surface modification and attract positively charged ions, Na^+. Based on values found in published literature [152], the diffusion coefficient and mobility of Na^+ ions at infinite dilution is D_{Na^+} = 1.334 x 10^{-9} m^2/s and $\mu_{Na^+} = D_{Na^+}F/RT$ = 5.2 x 10^{-8} $m^2/(V*s)$, respectively. In addition, NaCl is a symmetric electrolyte with a valence of z = 1 and at 34 mM concentration η_0 = 0.99 mPa*s. Inputting all these parameters in Equations 5.6, 5.7 and 5.8, I obtained $K_{S,i}$ = (5 ± 1) x 10^{-11} S and $K_{S,d}$ =

(3.07 ± 0.02) x 10^{-9} S with m = 0.23. Following Equation 5.5, the total surface conductance is equal to the sum of $K_{S,i}$ and $K_{S,d}$, with K_S = 3.12 ± 0.03 nS.

Finally, from Equation 5.4 and the fact that the bulk conductivity of latex particles can be ignored ($\sigma_{p,bulk} \approx 0$ [157]), the conductivity of 2 μm latex beads (σ_p) is estimated at 6.24 ± 0.05 mS/m. Typical conductivities for micron-sized latex beads in distilled (DI) water are in the order of ~1 mS/m [158] and 6.3 mS/m in 1 mM KCl [161]. The calculated value for σ_p is in good agreement (0.95% difference) with the one for 1 mM KCl which could be due to the addition of 25 μL 10x PBS in the solution. Although σ_p is in the same order of magnitude with the value for water, there was no agreement between them. Nevertheless, the measured conductivity σ_p will be revisited in Section 5.6 where the dielectric properties, and in particular the Clausius – Mossotti factor (f_{CM}), of these latex beads will be investigated when immersed in H_2O under the application of an alternating current (AC) electric field.

5.3 Measuring the diffusion coefficient of individual beads by single particle tracking

When inside static water (Section 5.10.1) and on top of a microscope glass surface (Sections 5.10.4 and 5.10.5), latex beads experience different types of forces [95]. Along the vertical z-axis, gravity $\left(\vec{F}_g = \frac{4}{3}\pi r_p^3 \vec{g}\rho_p\right)$ is acting against buoyancy $\left(\vec{F}_B = \frac{4}{3}\pi r_p^3 \vec{g}\rho_m\right)$. Since the beads' density $\left(\rho_p = 1055\ kg/m^3\right)$ [152] is larger than water's $(\rho_m = 1000\ kg/m^3)$ [152], they begin to sediment towards the top surface of the cover glass, as illustrated in Figure 5.2a. At $t = 0\ s$ and for $T = 25\ °C$, the total force acting on a latex bead is $\vec{F}_T = \vec{F}_g + \vec{F}_B = -2.25\ fN$. During its downward motion with a velocity $\vec{v}$ to the bottom of this well, the particle experiences the Stokes' drag force which acts at the opposite direction and is described for small Reynolds' number $\left(Re = \frac{\text{inertial forces}}{\text{viscous forces}} \ll 1\right)$ as follows [162]:

$$\vec{F}_{drag} = 6\pi\eta_0\gamma r_p\vec{v} \qquad (5.9),$$

where γ is a correction factor for the measured dynamic bulk viscosity η_0. For unhindered diffusion $\gamma = 1$, while for hindered $\gamma > 1$. Further analysis on this parameter is included in the following section (Section 5.4). The factor 6 is a constant that represents no-slip boundary conditions at the surface of the bead. In the case of slip boundaries, which it is assumed do not apply here, the value is replaced by 4 [162].

For large distances from the charged glass surface (s_i), the particle in fluid experiences a resistance to its motion which is related to the bulk viscosity of the solution (Figure 5.2a). As it approaches the charged substrate however, pressure gradually builds between the particle and glass surface which results in a change in the local viscosity [162]. In this case, the correction factor in Equation 5.9 becomes greater than 1 and its product with η_0 provides the effective viscosity of the region $\left(\eta_{eff}\right)$. This increased viscosity increases the Stokes' drag force, acting against further sedimentation of the particle. At the same time, since both the glass substrate and bead surfaces are negatively charged, electrostatic repulsion $\left(\vec{F}_e\right)$ takes place between them [162]. Consequently, this electrostatic force is also acting against the bead's hindered sedimentation (Figure 5.2b). Once it is at a distance s_f from the glass surface, the sum of the opposing forces becomes zero and the particle reaches the equilibrium state where does not accelerate further. Due to thermal fluctuations in the region, the particle undergoes Brownian motion, diffusing along the three-dimensional plane (xyz) [162].

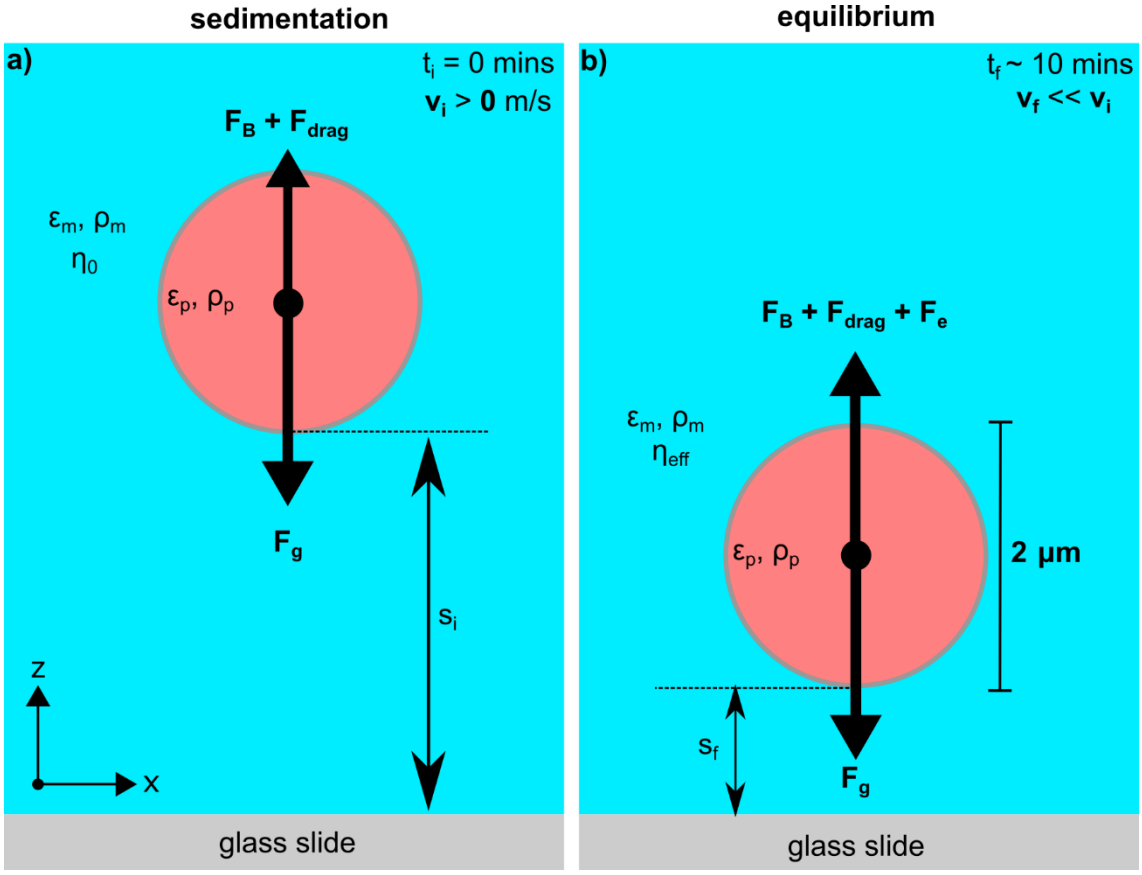

Figure 5.2 Schematic 2D (xz plane) illustrations of the forces acting on a spherical latex bead (ε_p, ρ_p) when inside solution (ε_m, ρ_m). **a)** At $t_i = 0$ and s_i, where the viscosity of the solution is η_0, $\vec{F}_g$ is acting against F_B. Since $\rho_p > \rho_m$, the bead moves towards the glass slide with a velocity $\vec{v}_i$, which gives rise to $\vec{F}_{drag}$ that has the same direction with $\vec{F}_B$. **b)** After approximately 10 mins (t_f), as the bead approaches the glass surface, the viscosity of the solution becomes η_{eff}. At a distance s_f electrostatic repulsion between the surface of the particle and the glass $(\vec{F}_e)$ acts against gravity bringing the latex bead to its equilibrium state $(\vec{v}_f \ll \vec{v}_i)$. At this point, the particle undergoes Brownian motion due to local thermal fluctuations, diffusing in the 3D plane (xyz).

This irregular motion of suspended particles in a liquid due to thermal energy (molecular kinetic theory) is described by their diffusion constant, as follows:

$$D = \mu_p k_B T \tag{5.10},$$

where μ_p is the mobility of the particle in solution and is described as:

$$\mu_p = \frac{\vec{v}}{\vec{F}_{drag}} \tag{5.11},$$

The combination of Equations 5.9 and 5.11 in 5.10 is known as the Stokes-Einstein equation [162]:

$$D = \frac{k_B T}{6\pi r_p \eta_0 \gamma} \quad (5.12),$$

According to Michalet [163], a statistically accurate value for the diffusion coefficient of a single freely diffusing particle can be obtained by linearly fitting its mean squared displacement (MSD) curve as a function of time with an optimum number of data points. Based on Einstein's density equation [164], the 2D coordinates $\vec{r}(t) = [x(t), y(t)]$ of a bead undergoing free diffusion can be described as a Gaussian probability:

$$\rho(r, t) = \rho_0 e^{-\frac{r^2}{4Dt}} \quad (5.13).$$

After a delay τ, the two-dimensional mean squared displacement of the particle is [80]:

$$\rho(\tau) = 4D\tau \quad (5.14).$$

This equation is valid when the available diffusion space L is large enough so that the measurement time interval is shorter than $L^2/4D$ [80]. In another work, Ernst and Köhler [165] demonstrated how the diffusion coefficient of an individual particle can be measured accurately by two-dimensional single particle tracking. After recording a very long trajectory with more than 1.5 x 10^5 time points, they divided it into shorter segments and treated them as individual trajectories. Then, for each segment, they calculated the slope of the mean squared displacement over lag time and by statistically comparing the values between all segmented trajectories, they defined the optimum number of fitting points needed. Their findings proved that this optimum number does not depend on the length of the segments.

In this section, following this technique, I will measure the diffusion coefficient of individual beads, suspended in H_2O on top of a microscope glass cover, from their recorded trajectories. Each trajectory consisted of 1000 data points and was obtained as described in Section 5.10.8. It is worth clarifying that the results shown below represent the trajectory of one latex bead, which was used as an example out of a larger number of recorded trajectories (120 in total) for individual beads. In addition, all data presented below were analysed with a single Python script (https://github.com/dsoulias/depNanotweezers).

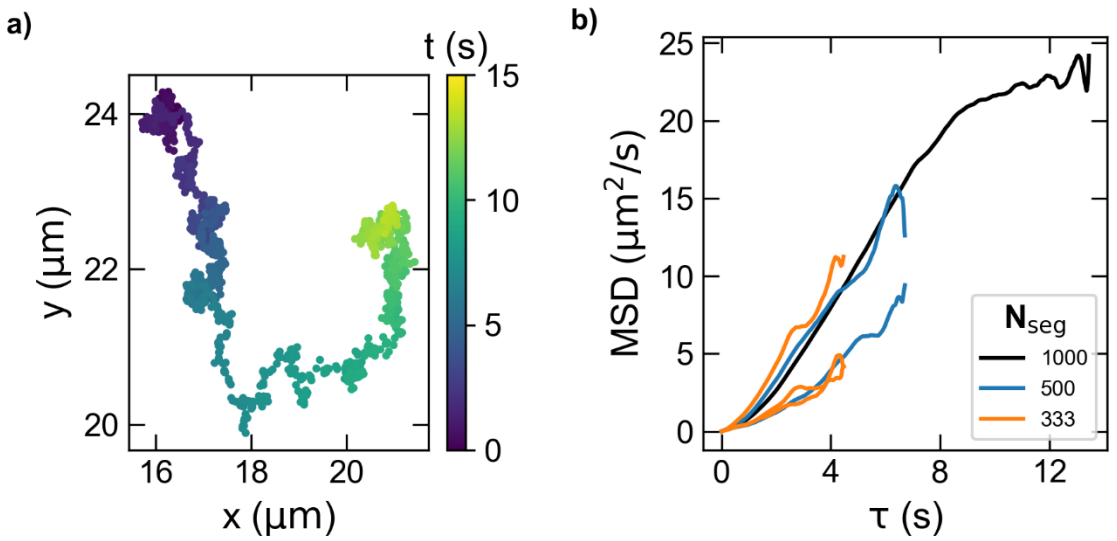

Figure 5.3 a) Example of a 2D trajectory (x, y) of a 2 µm carboxylate-modified polystyrene latex bead in H_2O diffusing on top of a cover glass. The colour bar on the right refers to the elapsed time of 13.4 s (N_T = N_{seg} = 1000 data points) with purple corresponding to the start and yellow to the end of the recorded acquisition. **b)** The mean squared displacement (MSD) as a function of lag time (τ) for the full trajectory (N_{seg} = 1000, black curve) shown in a). The cyan and orange curves represent the MSD vs τ for two (N_{seg} = 500) and three (N_{seg} = 333) segments of the full trajectory, respectively. Note that the last data point from N_T was excluded when splitting it into 3 shorter trajectories. The remaining segments (N_{seg} = 25, 50, 100, 200 and 250) are not displayed to improve data visualisation at short lag times [0, 4 s].

The entire two-dimensional trajectory (N_T) of the 2 µm carboxylate-modified polystyrene latex bead diffusing in H_2O on top of a cover glass that will be analysed in this section is shown in Figure 5.3a. The start of the recorded acquisition that lasted 13.4 s (1000 time points) is displayed in darker colours (purple) while the end is in lighter ones (yellow). The first step towards calculating the bead's diffusion coefficient from its 2D orbit was to divide its trajectory (N_T) into N_{seg}/N_T shorter trajectories which had 25, 50, 100, 200, 250, 333 and 500 data points, respectively. For the case of N_{seg} = 333, the last data point from N_T was excluded when splitting it into 3 shorter trajectories. For every trajectory, segmented or not, the mean squared displacement (MSD) was calculated for all available displacements n (from 1 to N_{seg}) at a given duration ($\tau = n\Delta t$) by inputting the radial (x, y) and temporal (t) coordinates of the bead into an alternative form of Equation 5.13 as follows:

$$\bar{\rho}_n = \frac{1}{(N-n)} * \sum_{i=1}^{N-n} (\vec{r}_{i+n} - \vec{r}_i)^2 \qquad (5.15).$$

Figure 5.3b shows this value as a function of lag time (τ) for N_{seg} = 333, 500 and N_T = 1000. Based on Equation 5.14, since the system is two-dimensional and the bead is undergoing normal diffusion (Brownian motion), its diffusion coefficient can be obtained by the slope of these curves ($D = 4D^*$). When $N_{seg} < N_T$, even for the ones not shown in Figure 5.3b, unweighted linear fitting was applied to each curve for calculating the slope to the first n data points. Consequently, the slope (D^*) was determined as a function of n with N_{seg} values obtained from each curve. As an example, Figure 5.4a presents the linear fitting for the first n = 6 points from one of the orange MSD – τ curves (N_{seg} = 333) in Figure 5.3b.

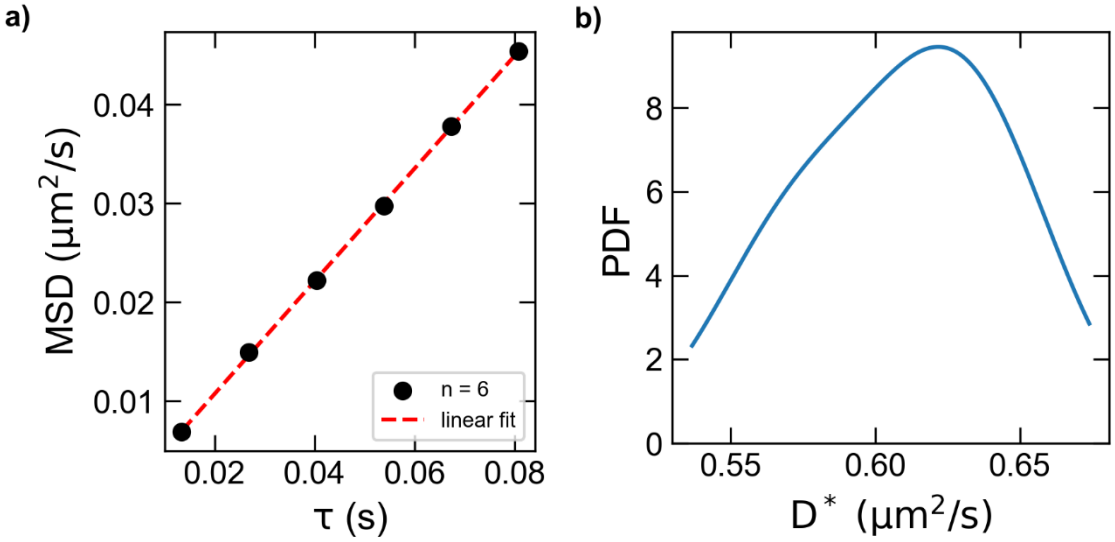

Figure 5.4 a) MSD curve as a function of lag time (τ) for one of the three segmented trajectories with N_{seg} = 333 where only the first 6 points (black data points) were considered for the applied unweighted linear fitting (red dashed line) to obtain the slope D^*. **b)** Probability density function (PDF) of the slopes (D^*) obtained from the three segmented trajectories for n = 6 and N_{seg} = 333. From this distribution, the mean value and standard deviation of the slopes were extracted with $\overline{D^*} \pm s_{D^*}$ = 0.62 ± 0.03 $\mu m^2/s$. Note that $\overline{D^*} \pm s_{D^*}$ were calculated from the slopes of N_{seg}/N_T segmented trajectories for each N_{seg} by fitting the first n points.

To statistically assess D^*, at first, probability density functions (PDF) were utilised to find the mean and standard deviation of the slopes of N_{seg}/N_T segmented trajectories per N_{seg} and n. Figure 5.4b illustrates the PDF of D^* for fitting the first 6 data points of 3 trajectories with N_{seg} = 333, where $\overline{D^*} \pm s_{D^*}$ = 0.62 ± 0.03 $\mu m^2/s$. Once, this process

was repeated for all remaining segments, the relative error of each slope was calculated by dividing its standard deviation over mean value ($s_{D^*}/\overline{D^*}$). The optimum number of fitting points could then be determined by identifying the minimum relative error when plotting it as a function of n for all N_{seg}.

As shown in Figure 5.5, the logarithmic trend of this curve varies between the length of segmented trajectories. For N_{seg}/N_T = 2, 3, 4, 5 and 10, the relative error first increases for a few points, then decreases within a small range and finally increases as n becomes larger. Without considering the first point (n = 1) as minimum, the optimum number of fitting points for the accuracy of the slope is 6 and was obtained for the case of N_{seg} = 333. Although the relative error that was achieved for D^* depends on the segmented trajectories length (~5% for N_{seg} = 333, ~10% for N_{seg} = 200 and ~11% for N_{seg} = 100), it is worth highlighting that the optimum number of fitting points does not, which agrees with Ernst's and Köhler's findings [165]. For most cases, the minimum relative error was acquired very close to the value n = 6, even for the shorter trajectories (N_{seg}/N_T = 20, brown markers).

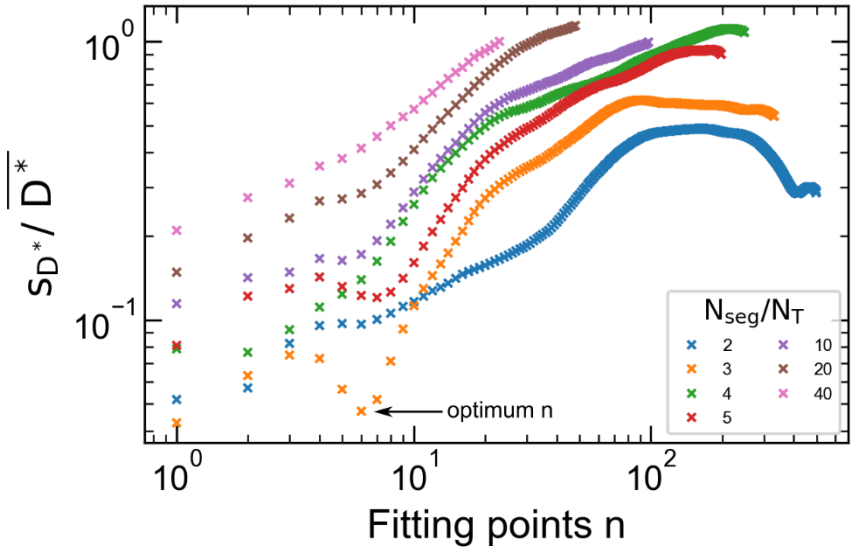

Figure 5.5 Relative error of the slope ($s_{D^*}/\overline{D^*}$) obtained from unweighted linear fitting to the MSD – τ curve as a function of the number of fitting points (n) for N_{seg}/N_T = 2 (cyan), 3 (orange), 4 (green), 5 (red), 10 (pink), 20 (brown) and 40 (pink markers). The black arrow points to the minimum relative error (~ 5%) at n = 6 which is defined as the optimum number of fitting points for the accuracy of the slope. Note that both axes are plotted in logarithmic scale to enhance data visualisation.

Next, I focused on investigating how the length of the segmented trajectories affected the value of the experimentally determined diffusion coefficient ($D = D^*/4$) of the bead. By keeping the slope values (D^*) that were previously obtained only for n = 6 from all N_{seg}/N_T, I plotted the resulting distributions of D in Figure 5.6a. These curves represent probability density functions when measuring a range of values for the diffusion coefficient for a specific length of the segmented trajectory. For lower N_{seg}, the distributions spread over a wide range of values D and diverge from the axis of symmetry (N_{seg}/N_T = 1, dashed grey line) denoting that diffusion coefficients measured from trajectories with fewer data points (N_{seg} = 25, pink curve) cannot be considered accurate enough. As N_{seg} increases, the distributions become narrower, and their peaks approach the axis of symmetry which is equal to the diffusion coefficient of the full trajectory (D_T).

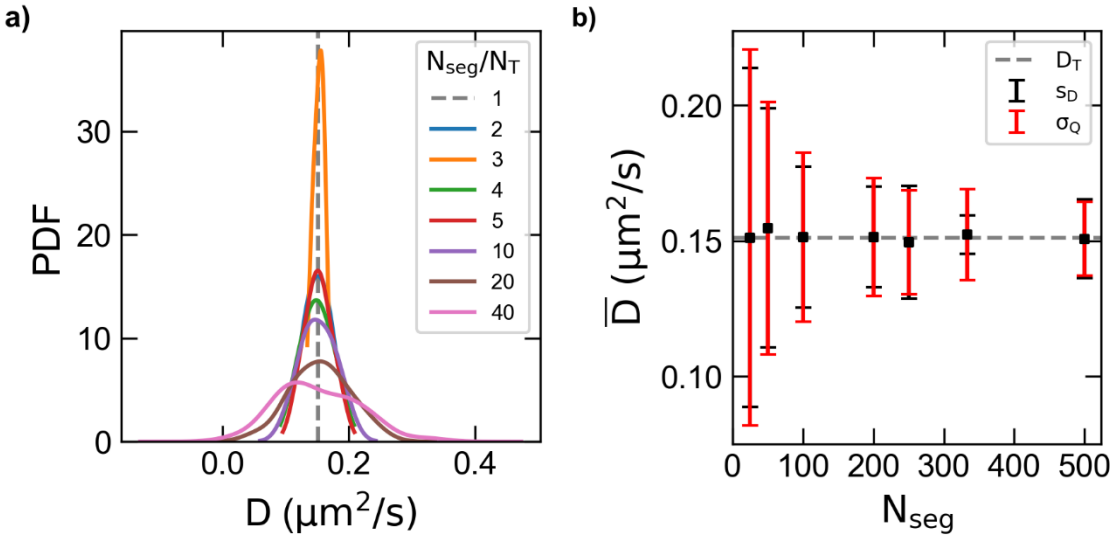

Figure 5.6 a) Probability density function distributions of diffusion coefficients (D) in relation to the number of the segmented trajectories with equal length (N_{seg}/N_T). Values for D were obtained by unweighted linear fitting to the MSD – τ curves ($D = D^*/4$) using the first n = 6 data points. The dashed grey line (N_{seg}/N_T = 1) represents the diffusion coefficient for the time-averaged MSD of the full trajectory with N_T = 1000 and is used as reference for the symmetry of the segmented trajectories. **b)** Mean values of the diffusion coefficients ($\bar{D}$, black squares) and standard deviations (s_D, black error bars) taken from the distributions' peak and half-width at half-maximum (HWHM) shown in a) as a function of the segmented trajectories length (N_{seg}). Analytical values for the standard deviations (σ_Q, red error bars) were calculated based on Qian et al. (1991) [80] from $\sigma_Q = \pm\bar{D}\left[2n/3\left(N_{seg} - n\right)\right]^{1/2}$ for n = 6 to assess the accuracy of the measured s_D. The dashed grey line (D_T) represents the diffusion coefficient for the time-averaged MSD of the full trajectory with N_T = 1000 and is used as a guide for the eye to highlight the close agreement with $\bar{D}$.

For each of these distributions, the peak and half-width at half-maximum (HWHM) correspond to the mean value ($\overline{D}$) and standard deviation (s_D) of D. To further assess the diffusion coefficient dependency on the trajectory length, $\overline{D} \pm s_D$ were plotted as a function of N_{seg} (Figure 5.6b). Although there is no significant difference between the $\overline{D}$ values (black squares), the larger N_{seg} becomes the smaller s_D is (black error bars) which indicates increase in the measurement accuracy. In particular, for $N_{seg} \geq 100$, the mean diffusion coefficient of the bead is in good agreement with the one measured from the full trajectory (D_T, dashed grey line). Furthermore, each standard deviation was compared to an analytical value (red error bars), $\sigma_Q = \pm\overline{D}\left[2n/3\left(N_{seg} - n\right)\right]^{1/2}$, which was derived from Qian et al. (1991) [80] for such distributions. By observing the black and red error bars over N_{seg} in Figure 5.6b, the empirical and analytical standard deviations are very close, except the minor discrepancy at N_{seg} = 333. Finally, the observations made from the data presented in Figures 5.6 agree again with Ernst's and Köhler's findings [165]. It is worth noting that $\overline{D}$ can be calculated only when the distribution of D for each trajectory length is known since this provides the measurement accuracy.

5.4 Measuring the effective dynamic viscosity of the solution surrounding an individual bead

So far, I have provided a detailed description for the steps required to measure the diffusion coefficient (D_T) of individual latex beads by 2D single particle tracking when diffusing on top of a cover glass in H_2O, as well as statistically assess the accuracy of this value ($\overline{D} \pm s_D$). I previously mentioned that throughout this work, no-slip boundary conditions are assumed for the interface between a solid (glass slide) and a viscous fluid (H_2O). Based on this, no relative motion is considered at this interface which means the fluid is stationary [166]. When a colloidal particle approaches a flat solid surface (Figure 5.2b), hydrodynamic interactions occur between the two which affect the drag force experienced by the particle. Its diffusive motion becomes anisotropic with the diffusion constants in the parallel ($D_{\parallel}$) and perpendicular ($D_{\perp}$) direction to the wall being hindered [162]. In this case, the correction factor γ (either $\gamma_{\parallel}$ or $\gamma_{\perp}$ or combination of both) from Equation 5.12 will be greater than 1. This topic is discussed to a greater extent in the next section (Section 5.5) where the distance between a latex bead and the glass substrate is estimated.

Here, I will analyse how the measured diffusion coefficient of a latex bead can be utilised to determine the effective viscosity (η_{eff}) of its surrounding solution. Once the two-dimensional plane (xy) where most sedimented beads was identified, following the method explained in Section 5.10.7, the trajectory of multiple individual beads was recorded to acquire statistically significant data sets. In total, 6 sets of 20 trajectories were collected over 6 consecutive days by applying the same experimental conditions. For each set, the first 10 measurements were collected from two individual beads at every location (areas I – IV within dotted lines) shown in Figure 5.7a while the remaining 10 were recorded 30 minutes after the first acquisition by repeating the same sequence.

Comparisons between these two distinct populations could eventually promote the investigation of effects in the diffusion coefficient D caused by changes in the solution temperature over time. The dotted lines (Figure 5.7a) represent area boundaries where beads were detected, and the numbering order represents the pattern of data collection (10 trajectories). Different locations on the glass slide were chosen to probe any inhomogeneity at the surface properties that could arise after the cleaning process. Here, it is worth clarifying that most beads were diffusing on the same two-dimensional (xy) plane close to the glass slide but small changes in the focal length were applied to improve focusing on the start of each recording. In addition, when looping through the

locations pattern, it is unclear whether the same beads were tracked between the first and second iteration.

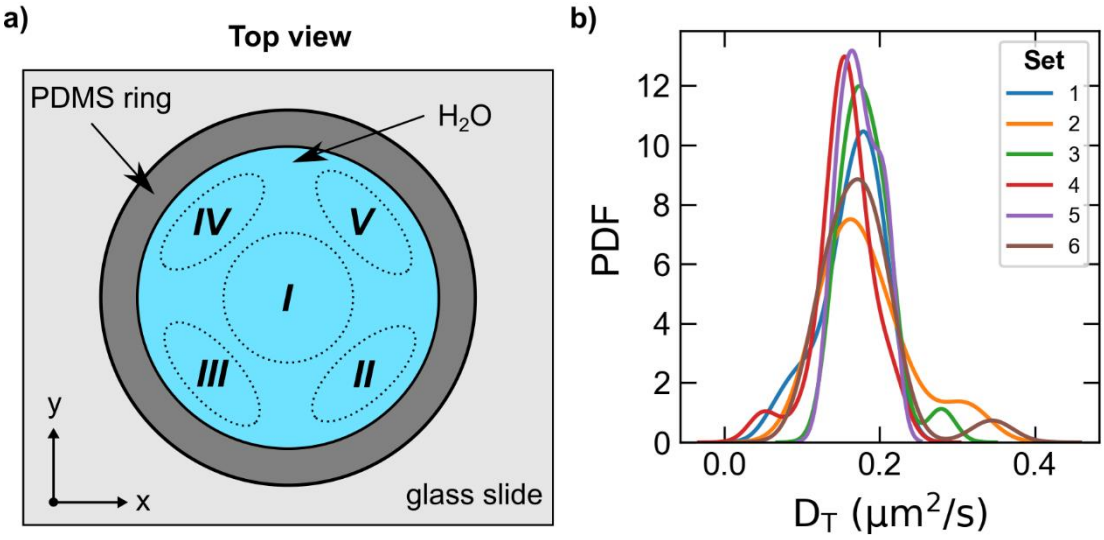

Figure 5.7 a) Schematic for the top view (xy-plane) of a glass slide (light grey) with a PDMS ring (darker grey) attached, containing 400 µL of the sample (latex beads in H_2O (cyan)). Labels *I* – *IV* indicate locations transition pattern where trajectories of 4 individual beads (20 in total) diffusing close to the glass surface were recorded. For each set of measurements, the acquisition of the first and last 2 trajectories had a gap of 30 min. The dotted lines represent the areas boundaries where latex beads were optically detected. Note that dimensions are not on scale. **b)** Probability density function distributions of diffusion coefficients (D_T) for individual beads as a function of sets of 20 measurements. Each set was acquired on a different day by applying the same experimental conditions. Values D_T were obtained by unweighted linear fitting to the MSD – τ curves ($D_T = D^*/4$) of the full trajectories using the optimum number n of data points.

The extensive analysis on measuring the diffusion coefficient of an individual bead by single particle tracking was applied this time to multiple recordings. Results from all measurements for the 6 sets are presented in Figure 5.7b. Each curve can be interpreted as the probability density function to quantify a distinct range of values for the diffusion coefficient (D_T) which were obtained by unweighted linear fitting to the MSD – τ curve of the full trajectory (N_T = 1000) using an optimum number of points n. The reason of using the value D_T here is based on the earlier conclusion that no significant difference exists between D_T and $\overline{D}$ for large N_{seg}, once n is identified. In general, the distributions indicate a relatively good agreement between the 6 sets of measurements and their peaks suggest an average diffusion coefficient smaller than 0.2 µm²/s.

Table 5.2 Mean values and standard deviations for the diffusion coefficient of individual beads for the first (D_T^i) and last (D_T^f) 10 measurements of sets obtained over 6 consecutive days. $\overline{D}_T^i, \overline{D}_T^f$ and $\delta\overline{D}_T^i, \delta\overline{D}_T^f$ were calculated from the peak and HWHM of each PDF distribution, respectively.

Set	***1***	***2***	***3***	***4***	***5***	***6***
$\boldsymbol{\overline{D}_T^i\ (\mu m^2/s)}$	**0.15**	**0.17**	**0.18**	**0.16**	**0.17**	**0.16**
$\delta\overline{D}_T^i\ (\mu m^2/s)$	0.04	0.04	0.02	0.03	0.03	0.03
$\boldsymbol{\overline{D}_T^f\ (\mu m^2/s)}$	**0.17**	**0.21**	**0.19**	**0.16**	**0.18**	**0.19**
$\delta\overline{D}_T^f\ (\mu m^2/s)$	0.03	0.06	0.04	0.03	0.02	0.06

As mentioned above, to investigate whether changes in the solution's temperature affected the diffusion coefficient of beads, the values D_T derived from the first 10 recordings of every set were compared to the values from the last 10. Between the first acquisition of each subset, 30 minutes of constant illumination of the sample were allowed as this duration was considered long enough to cause potential increase in the temperature. Table 5.2 lists the mean value and standard deviation ($\overline{D}_T^{i,f} \pm \delta\overline{D}_T^{i,f}$) for the diffusion coefficients of both groups of the 6 sets. Then, by averaging each subset I found $\overline{D_T^i} \pm \delta\overline{D_T^i}$ = 0.16 ± 0.03 μm²/s and $\overline{D_T^f} \pm \delta\overline{D_T^f}$ = 0.18 ± 0.04 μm²/s, respectively. Based on these, it can be concluded that any potential changes in the temperature of the solution between the acquisition of the two subsets does not significantly affect the diffusion coefficient of a bead.

Then, I checked whether hydrodynamic interactions between a bead and the glass surface existed. The beads used in these experiments were negatively charged to reduce the possibility of accidental clustering. At the same time, the glass substrate exposed to the solution was also negatively charged which means that when the two surfaces came close electrostatic repulsion occurred. This force was cancelled by the combination of other forces experienced by the beads, leading to diffusion along the xy-plane (Section 5.3). Vertical displacements of a bead along the z-axis were observed via fluorescent imaging. However, they were not taken into consideration due to lack of accurate determination and being considerably smaller than the ones across the xy plane. As a result, the calculated correction factor for the dynamic viscosity demonstrated hindered diffusion only in parallel to the glass wall ($\gamma_{\parallel}$).

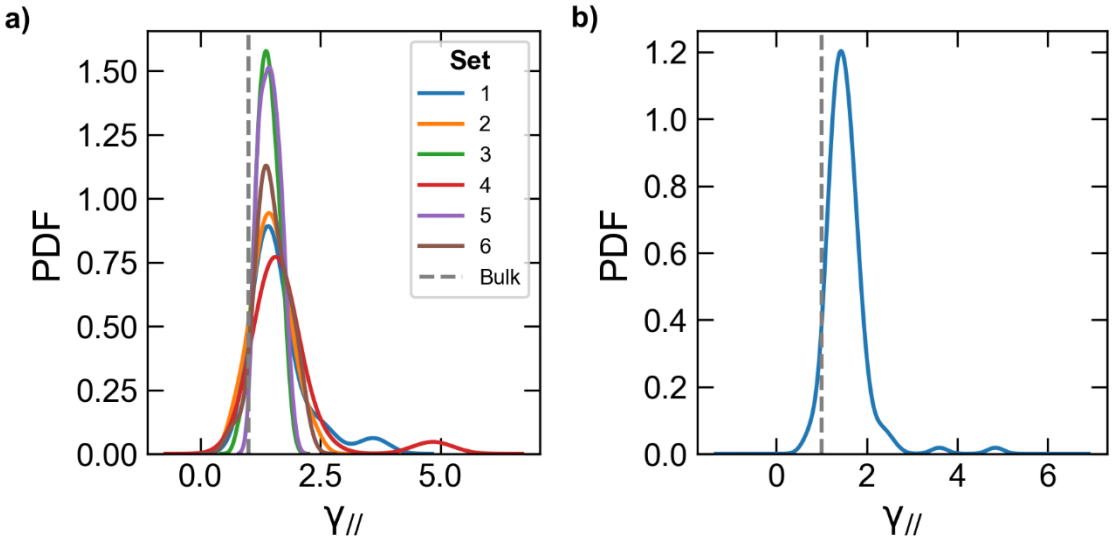

Figure 5.8 a) Probability density function distributions of the correction factor $(\gamma_{\parallel})$ for the dynamic viscosity of solution (η_0) as a function of 6 sets with 20 measurements. Each set was calculated by inputting the respective D_T distribution from Figure 5.7b into the Stokes-Einstein equation (Equation 5.12) for $T = 25$ ℃. The cyan dashed line represents unhindered free diffusion $(\gamma_{\parallel} = 1)$. Since the recorded trajectory of diffusing beads was 2D (xy plane), the correction factor for perpendicular diffusion to the glass surface $(\gamma_{\perp})$ was ignored. **b)** Probability density function distribution of the correction factor $(\gamma_{\parallel})$ for the dynamic viscosity of solution (η_0) as a function of all 120 measurements from a). The mean value and standard deviation of $\gamma_{\parallel}$ were calculated from the peak and HWHM of the PDF distribution, respectively, and found equal to 1.5 ± 0.5. Since $\gamma_{\parallel} > 1$, the diffusion of latex beads in H_2O was hindered due to hydrodynamic interactions with the glass surface.

By combining the distributions for the diffusion coefficient displayed in Figure 5.7b and the rearranged Stokes-Einstein equation $\left(\gamma_{\parallel} = k_B T / 6\pi\eta_0 r_p D_T\right)$ at T = 25 ℃, I obtained the PDFs for the correction factor $\gamma_{\parallel}$. Figure 5.8a shows the distribution for 6 sets with 20 measurements each, while Figure 5.8b depicts the probability density function distribution as a function of all 120 measurements shown in Figure 5.8a. It is evident that the symmetry axis (peak) of every distribution in both figures is higher than 1 $(\gamma_{\parallel} > 1)$ which proves that beads in H_2O interacted hydrodynamically with the glass surface and hence experienced a larger Stokes's drag force opposite to the direction of their movement when diffusing. The mean value and standard deviation of $\gamma_{\parallel}$ were calculated from the peak and HWHM of the PDF distribution in Figure 5.8b, respectively, and found equal to 1.5 ± 0.5.

The high relative error of this measurement, $\delta\gamma_{\parallel}/\bar{\gamma}_{\parallel} = 33.3\%$, could be attributed to differences in the surface properties of the glass substrate related to the cleaning

process or the stochastic nature of this motion type (Brownian motion). Nevertheless, this value will be used to estimate the mean distance between the surface of a latex bead and the glass surface in H_2O, as presented in the following section (Section 5.5). Moreover, it will be applied to rectify the magnitude of the dielectrophoretic force experienced by individual latex beads during single-molecule trapping with the nanotweezers. Note that all acquired data in this section were analysed and plotted via the Python script (https://github.com/dsoulias/depNanotweezers).

5.5 Estimating the distance between individual latex beads and the glass surface in water

In the previous section, I demonstrated that the diffusion of individual beads in H_2O along the two-dimensional plane (xy plane) was hindered due to hydrodynamic interactions with the charged surface of the glass surface. The magnitude of this effect depends on the distance between the surface of a bead and the glass [162], [167]. Based on the measured value for the correction factor $(\gamma_{\parallel})$ of the bulk dynamic viscosity of the aqueous solution (η_0), this distance (s) can be analytically estimated. However, different approximations have been derived depending on the relation between the radius of the particle and distance s [162]. In this section, I will assess which approximation is valid in the system under investigation and estimate the mean distance separating the surface of individual beads and the glass substrate.

For low Reynolds number $(Re \ll 1)$, the first two terms on the left side of the incompressible Navier-Stokes equation below are considered significantly small compared to the viscous term $\eta_0 \nabla^2 \vec{v}$ [162].

$$\rho \left[\frac{\partial \vec{v}}{\partial t} + (\vec{v} \cdot \nabla)\vec{v} \right] + \nabla p = \eta_0 \nabla^2 \vec{v} \qquad (5.16),$$

where $\vec{v}$ and p are the velocity and pressure, respectively, ρ the density of the solution and $\nabla \cdot \vec{v} = 0$. Consequently, Equation 5.16 simplifies to $\nabla p = \eta_0 \nabla^2 \vec{v}$. The method of reflections provides accurate solutions to this equation for short distances s [162]. Following this method, Faxén derived an expression to approximate the Stokes drag experienced by a spherical particle that moves in parallel to a close boundary. This equation is valid when $s \gg 0$ and is written as [162], [167], [168]:

$$\gamma_{\parallel}^{F} = \left(1 - \frac{9}{16} * \left(\frac{r_p}{s + r_p} \right) + \frac{1}{8} * \left(\frac{r_p}{s + r_p} \right)^3 - \frac{45}{256} * \left(\frac{r_p}{s + r_p} \right)^4 - \frac{1}{16} * \left(\frac{r_p}{s + r_p} \right)^5 \right)^{-1} \qquad (5.17).$$

Later, Goldman et al. (1967) [169] derived an asymptotic solution for the parallel correction factor when $s \approx 0$, known as Brenner's correction, and is expressed by the following equation:

$$\gamma_{\parallel}^{B} = 0.9588 - \left(\frac{8}{15} * ln\left(\frac{s}{r_p} \right) \right) \qquad (5.18).$$

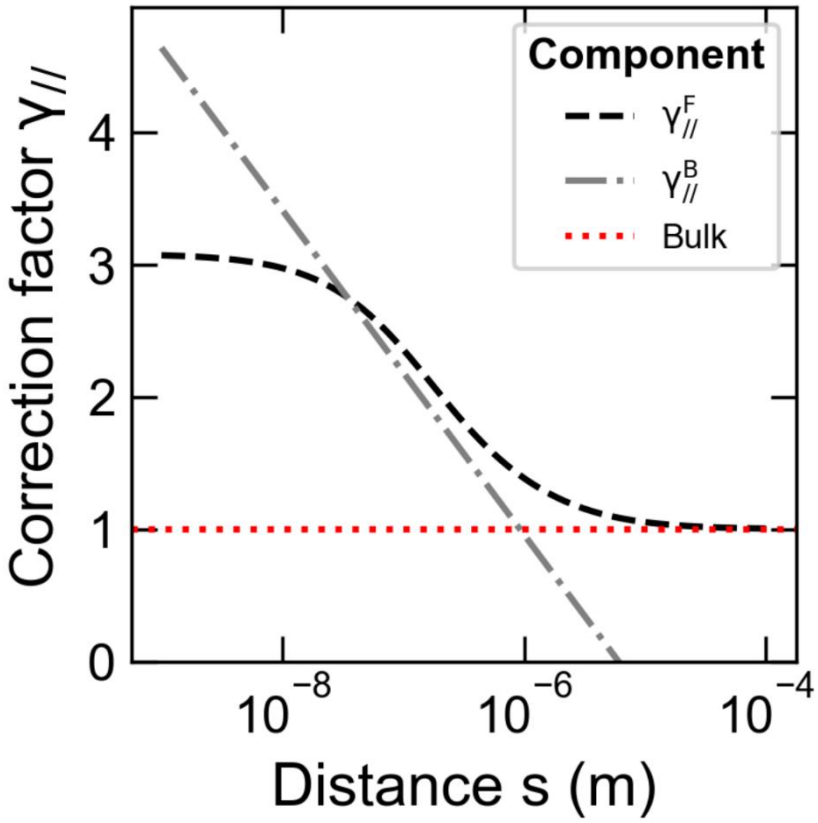

Figure 5.9 Dynamic bulk viscosity correction factors for a spherical particle $(r_p = 2\ \mu m)$ diffusing in parallel to a solid boundary at a distance s between the two surfaces. The red dotted line represents no hindered diffusion $(\gamma_0 = 1)$. The grey dashed-dotted line represents Brenner's parallel correction factor which is valid when $s \approx 0$, while the black dashed line represents Faxén's parallel correction factor which is valid when $s \gg 0$. The distance s_t where $|\gamma_{\parallel}^{F} - \gamma_{\parallel}^{B}|$ became minimum was considered the transition point, so when $\gamma_{\parallel} > 2.76$, $\gamma_{\parallel}^{B}$ was applied and when $\gamma_{\parallel} \leq 2.76$, $\gamma_{\parallel}^{F}$. The horizontal axis is set in logarithmic scale.

It is worth mentioning that both approximations have correction factors for movement perpendicular to a solid surface ($\gamma_{\perp}^{F}$ and $\gamma_{\perp}^{B}$) but will not be used for this analysis. In addition, both $\gamma_{\parallel}^{B}$ and $\gamma_{\parallel}^{F}$ can lead to slightly inaccurate results close to the solid surface due to not considering possible molecular interactions, such as overlap of the electric double layer or van der Waals interactions with the wall. Nevertheless, experimental studies have verified the accuracy of both Faxén's [170] and Brenner's [171] approximations. Since the distance s between the surface of a latex bead and the glass substrate was not defined from previous measurements, I attempted to find the value s_t for which the difference between $\gamma_{\parallel}^{B}$ and $\gamma_{\parallel}^{F}$ became minimum. This distance was then

considered as the transition point between the application of Faxén's and Brenner's correction factors. From Figure 5.9, the difference $\left|\gamma_{\parallel}^{\mathrm{F}} - \gamma_{\parallel}^{\mathrm{B}}\right|$ became minimum for $s_t = 34.5\,nm$ at $\gamma_{\parallel} = 2.76$. As a result, when $\gamma_{\parallel} > 2.76$, $\gamma_{\parallel}^{B}$ was applied and when $\gamma_{\parallel} \leq 2.76$, $\gamma_{\parallel}^{F}$ was selected.

In the previous section (Section 5.4), the calculated mean parallel correction factor $\bar{\gamma}_{\parallel} \pm \delta\gamma_{\parallel}$ was measured from 120 measurements of individual 2 μm latex beads diffusing in H_2O on top of a glass surface and was found equal to 1.5 ± 0.5. This value is significantly smaller than 2.76, hence the mean distance $\bar{s}$ between the two surfaces could be obtained by rearranging the equation describing Faxén's correction factor (Equation 5.17). If $w = r_p/(s + r_p)$, then the fifth-order polynomial below is derived:

$$\frac{1}{16}w^5 + \frac{45}{256}w^4 - \frac{1}{8}w^3 + \frac{9}{16}w + \left(\frac{1}{\gamma_{\parallel}^{F}} - 1\right) = 0 \qquad (5.19).$$

By keeping only the real and positive solution of this polynomial $(Re[w] > 0)$, the mean distance between the surface of a latex bead and the glass surface was $\bar{s} \pm \delta s = 700 \pm 200$ nm. This value broadly agrees with the distance observed, when focusing with the microscope, between diffusing latex beads and the top surface of the cover glass. Although any contribution from perpendicular movement to the glass surface was considered negligible and the error of the measurement was large (relative error of ~29%), $\bar{s}$ could then be used to position the nanotweezers tip as close as possible to the plane where most beads diffused freely. This finding together with the ones discussed in the two last sections prove how much information could be extracted from the two-dimensional trajectory of individual latex beads undergoing Brownian motion in water. Now that the motion of these dielectric beads has been fully characterised, their response under the application of AC signals needs to be determined.

5.6 Polarisability of latex beads in water under the application of AC signals

So far, I have analysed the motion of individual latex beads in water on top of a glass surface when no external field is applied in the system. However, once the nanotweezers are integrated, highly non-uniform electric fields are generated and experienced by both the dielectric particles and aqueous solution. As explained in Section 2.4.1, dielectrophoresis relies on polarisation. This is expressed in the definition of the dielectrophoretic force $\vec{F}_{DEP}$ (Equation 2.3) through the frequency dependent Clausius-Mossotti factor, $f_{CM}(\omega)$. Based on Equation 2.4 and the applied frequency, the particle-medium system is dominated by either the conductivities or permittivities of the two [158]. The frequency at which one phenomenon switches to the other is called the crossover frequency $f_{CM,0}(\omega)$, determines the direction of the dielectrophoretic force and is calculated by assuming $Re[f_{CM}(\omega)] = 0$, as follows [158]:

$$f_{CM,0}(\omega) = \frac{1}{2\pi\varepsilon_0} * \sqrt{\frac{(\sigma_m - \sigma_p)(\sigma_p + 2\sigma_m)}{(\varepsilon_p - \varepsilon_m)(\varepsilon_p + 2\varepsilon_m)}} \quad (5.20),$$

where ε_0 is the vacuum permittivity (F/m), $\varepsilon_p, \varepsilon_m$ and σ_p, σ_m are the relative electrical permittivity and conductivity of the particle and medium, respectively. In this section, I will investigate how the applied frequencies affect the polarisability of latex beads in H_2O by analytically deriving the real part of the Clausius-Mossotti factor ($Re[f_{CM}(\omega)]$) versus frequency. The Python script for performing these calculations can be found at https://github.com/dsoulias/depNanotweezers.

In Section 5.2, the conductivity of 2 μm carboxylate-modified polystyrene latex beads was measured by zeta potential measurements in aqueous medium (97.5% H_2O + 2.5% 10x PBS). Here, it is worth recalling that this small volume of PBS was added to aid data acquisition since no ζ value could be obtained at lower concentrations. Following this, it was assumed that this aqueous suspension influenced the conductivity of latex beads in the same way as pure H_2O would do. The measured conductivity of a spherical latex bead was found σ_p = 6.24 ± 0.05 mS/m. The conductivity of H_2O was measured by the resistivity value displayed on the Milli-Q system which was $\sigma_m = \frac{1}{18.2*10^4}$ = 5.5 μS/m. This means that latex beads were more conductive than the aqueous solution they were suspended in $(\sigma_p > \sigma_m)$. The electrical permittivity of the beads and H_2O were found in literature [152], [158] with ε_p = 2.56 and ε_m = 79. By inputting these four values in Equation 5.20, the crossover frequency was $f_{CM,0}$ = 1.01 ± 0.01 MHz.

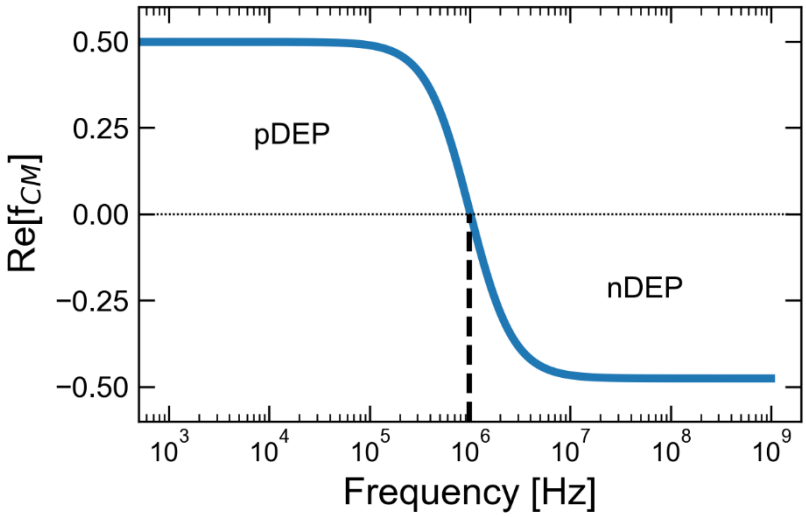

Figure 5.10 Real part of the Clausius-Mossotti factor $Re[f_{CM}]$ over a range of applied frequencies (0 – 1 GHz) for 2 μm carboxylate-modified polystyrene latex beads suspended in water. The crossover frequency $f_{CM,0}$ is the point where the black dashed line meets the blue curve and was calculated equal to 1.01 ± 0.01 MHz. For frequencies lower than $f_{CM,0}$, pDEP occurred with latex beads being attracted towards high electric field regions (values at the left side between dotted black line and blue curve). For frequencies higher than $f_{CM,0}$, nDEP occurred with latex beads being attracted towards low electric field regions (values at the right side between black dotted line and blue curve). The absolute magnitude of $Re[f_{CM}]$ for both pDEP and nDEP reached up to 0.5. Note that the horizontal axis is displayed in logarithmic scale.

Figure 5.10 presents the real part of the Clausius-Mossotti factor as a function of applied frequencies (from 0 to 1 GHz). Since the electrical conductivity of latex beads is larger than the one for H_2O $(\sigma_p > \sigma_m)$, positive dielectrophoresis (pDEP) occurs at lower frequencies $(f_{app} < f_{CM,0})$ with beads being attracted towards the high electric field regions. In contrast, the electrical permittivities dominate when $f_{app} > f_{CM,0}$, and since $\varepsilon_p < \varepsilon_m$ negative dielectrophoresis (nDEP) takes place with beads being attracted towards the low electric field regions. These findings are in full agreement with the reported behaviour of this system in the available literature [158]. Furthermore, they offer valuable information regarding what frequencies should be selected to either trap (pDEP) or repel (nDEP) individual latex beads towards/away from the nanotweezers tip, as well as how the magnitude of the generated dielectrophoretic force is affected. Comparisons with experimental results for single-molecule dielectrophoretic trapping are presented and discussed over the two following sections (Sections 5.7 and 5.8).

5.7 Determining the magnitude of dielectrophoretic forces acting on individual latex beads via single particle tracking

Once the nanotweezers were integrated on the fluorescence microscope setup, as described in Section 5.10.9, their tip was positioned approximately 1 μm above the 2D plane where most latex beads diffused in water under no external applied field. The surface of the tip was considered to be in parallel to the glass slide. In Chapter 4, I demonstrated that upon the application of an electrical potential in the hundreds of millivolts range between the closely spaced carbon nanoelectrodes, highly non-uniform electric fields are expected to be generated at the tip region. Depending on the frequency of this sinusoidal waveform, latex beads would either be attracted towards the nanotweezers tip where the highest gradients of the electric field occurred or be repelled away from this region towards the lowest ones. In this section, I will show that the magnitude of the dielectrophoretic force experienced by individual latex beads can be quantified by analysing their recorded trajectories under trapping conditions.

To start with, the nanotweezers tip was positioned at a ~5 – 15 μm distance from an isolated freely diffusing 2 μm polystyrene latex bead (Figure 5.23, Section 5.10.9). Following the simulation results from Chapter 4, this spatial range was considered as the maximum extent of the trapping area, depending on the applied electrical potential, frequency and the distance between the nanoelectrodes. The dielectrophoretic nanotweezers were then activated by applying a sinusoidal AC waveform, $\phi(t) = V_{rms} * \sin(2\pi f_{app} t)$, between the two closely spaced carbon nanoelectrodes. A highly non-uniform electric field was generated close to the nanotweezers tip, as illustrated in Section 4.3. To aid with demonstrating the developed force probing technique, this section presented only the case of $V_{rms} = 600$ mV and $f_{app} = 10$ kHz. Results from different sub-volt electrical potentials and frequencies ranging from tens of kHz to MHz are provided and analysed in Section 5.8. This particular frequency value was selected to achieve positive dielectrophoresis and eventually lead to trapping of individual latex beads at the nanotweezers tip (Figure 5.15, Section 5.7).

Figure 5.11a displays the initial position $(t = 0\ s)$ of a 2 μm fluorescent latex bead before getting attracted via dielectrophoresis towards the tip of the nanotweezers, upon the application of 600 mV at 10 kHz. The radial distance between the tip and the bead was approximately 14 μm. After $t = 2.6\ s$, the bead was captured by the nanotweezers with its final position on the xy-plane shown in Figure 5.11b. The purple curve represents the

bead's trajectory under trapping conditions and was acquired by applying the single particle tracking plugin in Fiji (ImageJ), Trackmate. More details on this technique and the chosen parameters are provided in Section 5.10.8. As expected from the simulated electric field distribution shown in Section 4.3, the trajectory of a bead was described by a non-linear curve.

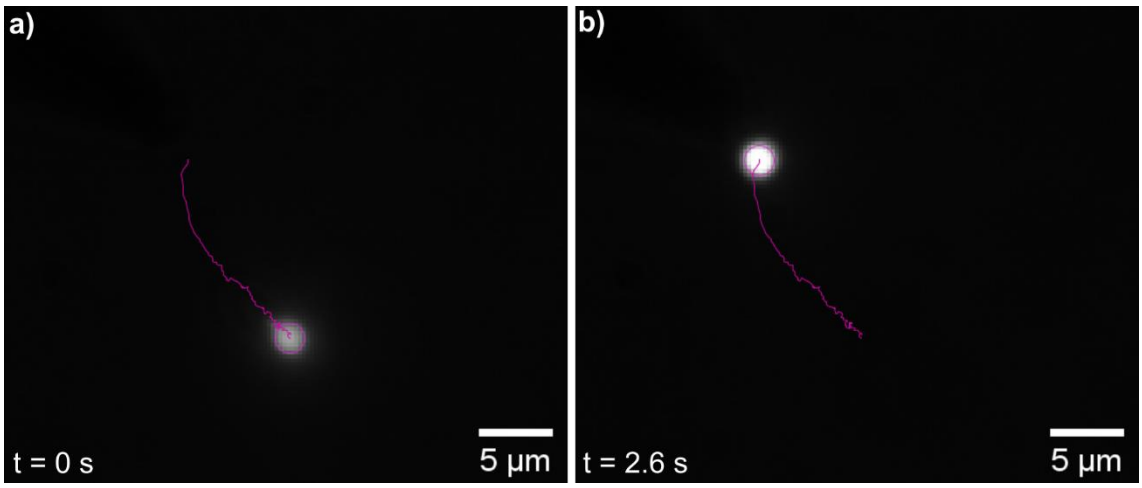

Figure 5.11 a) First $(t = 0\,s)$ and **b)** last $(t = 2.6\,s)$ frame from a recording of a fluorescent latex bead (2 µm) in water on top of a cover glass being trapped towards the tip of the dielectrophoretic nanotweezers. The purple curve represents the trajectory of the bead under trapping conditions and the purple circle around the bright spots the estimated diameter (2 µm) of the detected particle. Positive dielectrophoresis was achieved by applying a sinusoidal waveform of $V_{rms} = 600$ mV and $f_{app} = 10$ kHz between the pair of carbon nanoelectrodes at the nanopipette tip. Small differences in the intensity of the fluorescent bead were observed which proved that any displacement along the z-axis could be considered negligible. Note that the nanotweezers tip and bead were considered in the same focal plane. The nanotweezers used for this measurement were modified with FIB milling and had a 55 nm separation gap.

The nanotweezers used in this measurement had a 55 nm separation distance between the two nanoelectrodes and were treated with FIB milling prior to the experiment. The major axis of each semi-elliptical nanoelectrode was 160 nm and 150 nm, respectively, with a 60 nm glass wall thickness. Their minor axes were 70 nm long. Depending on the angle between the bead and this separation gap, the bead would move across the electric field lines where its gradient was gradually increasing (Figure 5.12a). The highest electric field gradient was predicted close to the separation gap of the nanotweezers. That was the most likely point the surfaces of the bead and nanotweezers would come in contact, preventing any further movement of the former.

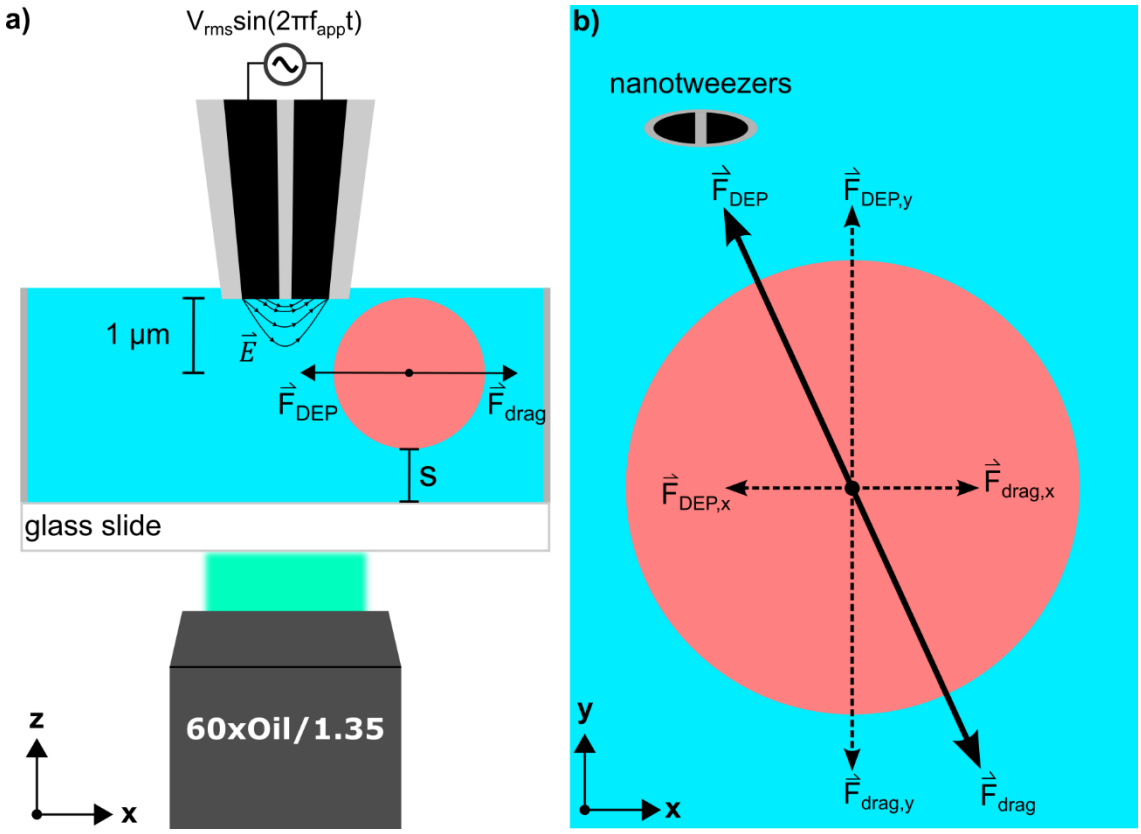

Figure 5. 12 Schematic illustrations for the two-dimensional projections (xz- and xy-planes) of the dielectrophoretic force probing system **a)** A sinusoidal waveform with V_{rms} = 600 mV and f_{app} = 10 kHz was applied to a pair of nanotweezers (double-barrel nanopipette-based carbon nanoelectrodes). When immersed in 400 µL of water, including 2 µm carboxylate-modified polystyrene latex beads, a highly-non uniform electric field $\vec{E}$ was generated at the tip region. The bead's centre of mass was considered to be 1 µm away the nanotweezers tip along the z-axis, while the distance between its surface and the glass slide (s) was found approximately equal to 700 nm. Once the nanotweezers approached an individual diffusing bead, positive dielectrophoresis occurred and the bead was attracted towards their tip centre. During its motion under trapping conditions, two forces were applied to the bead at opposite directions, $\vec{F}_{DEP}$ and $\vec{F}_{drag}$. Note that dimensions are not to scale. **b)** Focusing on the xy-plane where the bead surface and nanotweezers tip were aligned, these two forces were analysed in their x- and y-components depending on the angle between the two bodies. Based on $\vec{F} = m\vec{a}$, and due to $m = 4.4 * 10^{-15}$ kg, it is assumed that $\vec{F}_{DEP} \approx \vec{F}_{drag} = 6\pi\eta_{eff}r_p\vec{v}$. The magnitude of the dielectrophoretic force was determined by measuring the bead's velocity $(\vec{v})$ along its trajectory via single particle tracking. Note that dimensions are to scale for this panel. The bead's position was recorded over time in epifluorescence mode through a 60x oil-immersion objective with a sCMOS camera.

Unwanted permanent attachment of a bead on the nanotweezers surface was frequently observed. This phenomenon has been widely reported in literature [158] and it is related to the surface properties of polystyrene latex beads. However, I managed to detach them

with two methods, so that the nanotweezers could be used for more force probing measurements. The first one was based on bringing the nanotweezers extremely close to the glass surface and moving them in parallel until the bead attached to the glass, while the second one relied on removing the nanotweezers from water and immersing them in 100% ethanol solution to chemically dissolve the bead. However, after the latter method was applied pieces of dissolved polystyrene were detected on the nanotweezers surface which could potentially affect their performance. As a result, the first approach was adopted for detaching beads bound on the nanotweezers tip.

Figure 5.12 includes two two-dimensional illustrations for the experimental configuration of the dielectrophoretic force probing technique mentioned above. During an individual bead's motion towards the nanotweezers tip, two forces were acting on this spherical particle at opposite directions, $\vec{F}_{DEP}$ and $\vec{F}_{drag}$ (Figure 5.12a). The dielectrophoretic force was responsible for pushing the bead towards the nanotweezers, while Stokes drag force was acting against its motion due to the viscous solution. It is worth recalling that the nanotweezers tip and the bead's centre of mass were 1 μm away along the z-axis while the bottom surface of the bead was approximately 700 nm above the glass wall. Movement of any individual bead was assumed only along the xy-plane, as contributions in the z-direction were considered negligible. Focusing on the xy-plane where the bead surface and nanotweezers tip were aligned, these two forces could be analysed in their x- and y-components depending on the angle between the two bodies, as presented in Figure 5.12b. It has to be noted that the dielectrophoretic force needs to overcome forces related to thermal energy (Brownian motion) to induce directed motion of the particle. Although not included in Figure 5.12, they existed throughout the entire process but at a significantly smaller magnitude, hence they can be ignored in the force analysis.

By applying Newton's second law of motion $\vec{F} = m\vec{a}$ on an individual trapped bead with mass $m = 4.4 * 10^{-15}$ kg and an acceleration $\vec{a}$, the dielectrophoretic force experienced by the particle can be defined by:

$$\left|\vec{F}_{DEP}\right| = \vec{F} - \left|\vec{F}_{drag}\right| = m|\vec{a}| - 6\pi\eta_{eff}r_p|\vec{v}| \qquad (5.21),$$

where $|\vec{v}|$ is the magnitude of the velocity of the moving bead. However, an individual bead moving through a highly non-uniform electric field, experiences a different force at every position [95]. The total force acts on the particle and accelerates it up to a final velocity $\vec{v}$ where the Stokes drag force on the particle is equal to the dielectrophoretic force. This acceleration is very fast (order of μm/s^2) and given the mass of the particle being very small, the bead reaches its final velocity on a timescale much shorter than the exposure times in the experiment (typically 10 ms). Hence, the particle can be considered at equilibrium at each point, experiencing no acceleration ($\vec{a} = 0\ \mu m/s^2$) [95].

However, as it is then transitioning to an area of even stronger field gradient, it immediately assumes a new final velocity, reaching again equilibrium with undetectable acceleration. Consequently, the product $m\vec{a}$ is considered always zero, even though the observed velocity changes in space and Equation 5.21 becomes [95]:

$$\left|\vec{F}_{DEP}\right| = -\left|\vec{F}_{drag}\right| = -6\pi\eta_{eff}r_p|\vec{v}| \qquad (5.22).$$

According to this equation, the magnitude of the dielectrophoretic force can be determined by measuring the velocity of an individual latex bead for every time point while under trapping conditions [95]. Equation 5.22 has been adopted in several studies to measure the dielectrophoretic force acting on single particles [73], [172], [173]. Here, the velocity of an individual bead was measured from its recorded trajectory as a function of time. The x- and y-coordinates were extracted from the purple curve in Figure 5.11 over time. To simplify data analysis, I calculated the radial displacement of the bead $r(t) = \sqrt{\left[x(t) - x(t_f)\right]^2 + \left[y(t) - y(t_f)\right]^2}$ with $\left[x(t_f),\ y(t_f)\right]$ being the final coordinates of the bead when trapped on the nanotweezers tip surface. The velocity of the bead was determined by taking the time derivative of $r(t)$. However, each trajectory consisted of $n-1$ linear segments linking the n recorded frames. So, when plotting the time derivative of $r(t)$ as a function of time, sharp transitions would arise at every data point. This could be considered as artificial noise in the data which affects the accuracy in presenting and determining the dielectrophoretic force.

Across multiple scientific communities, the most widely used method for smoothing noisy data are the Savitzky-Golay filtering [174]. It is based on local least-squares polynomial approximation and acts as a low-pass filter to reduce noise in the acquired data while preserving the shape and height of peaks in any curve [175]. To smooth experimental data acquired from single particle tracking measurements, which are presented throughout this chapter, two Python scripts were developed (https://github.com/dsoulias/depNanotweezers). In a nutshell, noise generated from the spatial displacement time derivatives of individual beads during attraction towards the nanotweezers tip was filtered out in real time. This method provided smooth curves to describe the dielectrophoretic force as a function of distance from the tip. A guide for selecting the optimal parameters to achieve accurate data smoothing as well as detailed explanations for all available options are included in Section 5.10.10.

Figure 5.13a presents both the raw (black data points) and smoothed (green curve) radial displacement $r(t)$ of the individual 2 μm latex bead shown in Figure 5.11 as a function of time. Initially, the distance between the particle and the nanotweezers tip surface was approximately 14 μm (Figure 5.11a). After ~2.6 s, the bead was trapped by the nanotweezers (Figure 5.11b) following the above curve. It is worth noting that the developed data smoothing filter was capable of fitting data sets with inconsistent time intervals. To obtain the green curve above, a window size (total number of fitting points) equal to 7, second order polynomial and "interp" mode were selected. For every time point t from the $[t, r(t)]$ raw data set, a smoothed radial distance $r_{SG}(t)$ was extracted leading to $[t, r_{SG}(t)]$. Then, by taking the derivative $dr_{SG}(t)/dt$, the bead's velocity was calculated as a function of time. These values were inputted in Equation 5.22, which for a bead radius of $r_p = 1$ μm and $\eta_{eff} = 1.35$ mPa*s at 25 ℃, provided the dielectrophoretic force experienced by the bead along its trajectory.

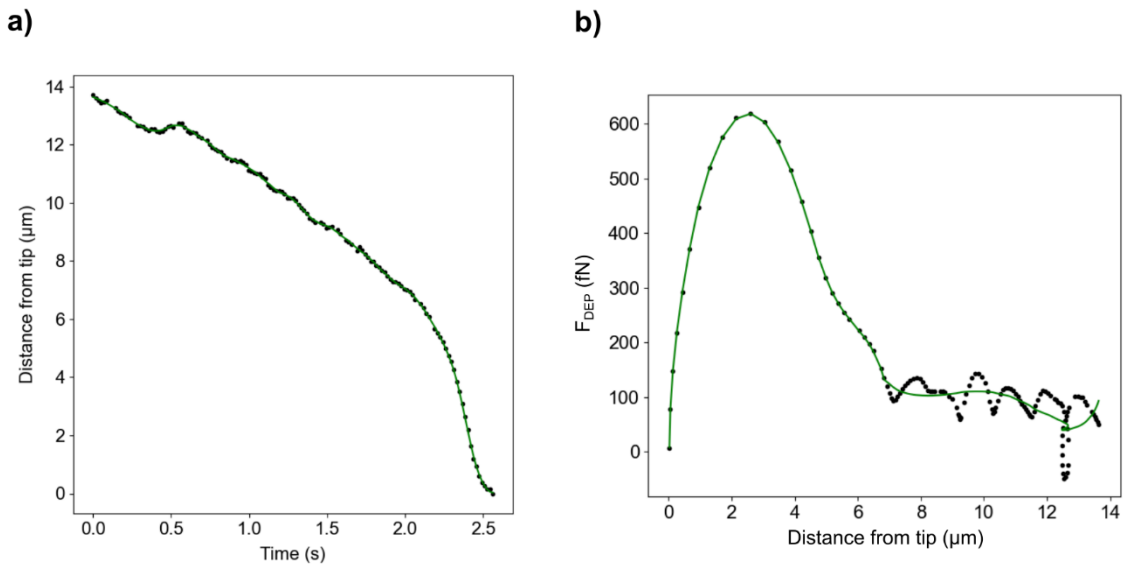

Figure 5.13 a) Radial distance $r(t) = \sqrt{[x(t) - x(t_f)]^2 + [y(t) - y(t_f)]^2}$ between an individual 2 μm latex bead and the nanotweezers tip surface as a function of time. The data points were acquired from the bead's two-dimensional trajectory while the fitted green curve was obtained by data smoothing based on a Savitzky-Golay filter. A window size of 7, polynomial order of 2 and "interp" mode were selected for fitting these data points. **b)** Measured dielectrophoretic force magnitude experienced by an individual 2 μm latex bead over the smoothed distance from the nanotweezers tip. Black data points represent F_{DEP} calculated from the time derivative of the smooth radial distance $r_{SG}(t)$ while the green curve is the fitting obtained by further smoothing of the already smoothed $r_{SG}(t)$. Note that a window size of 101, fourth order polynomial and "interp" mode were selected for smoothing the already smoothed $r_{SG}(t)$ from 7 to 14 μm.

The magnitude of the measured dielectrophoretic force (F_{DEP}) as a function of the smoothed radial distance between the individual latex bead and the nanotweezers tip surface $\left(r_{SG}(t)\right)$ is depicted by the data points in Figure 5.13b. Although a smooth curve was obtained for the first 7 μm away the nanotweezers, noise reduction was not sufficient for the remaining range from 7 to 14 μm. As a consequence, further data smoothing was applied to $r_{SG}(t)$ and hence to F_{DEP}. The final magnitude of the dielectrophoretic force over the distance from the tip was expressed by the green curve in Figure 5.13b. As the particle started approaching the nanotweezers from 13 μm away, the measured F_{DEP} increased from approximately 70 fN to 100 fN at 7 μm. Then, the particle entered an area of much stronger electric field gradients and the resulting force increased significantly, reaching a maximum magnitude of 600 fN at approximately 2.5 μm away the nanotweezers.

However, opposite to what was expected, F_{DEP} decreased over the final distance. Careful observation of the recording suggested that when the bead achieved its maximum velocity, it landed on the edge of the nanotweezers tip. This last displacement of ~2.5 μm, which is almost equal to the diameter of the bead, was attributed to a delayed reorientation of the particle towards the centre of the nanotweezers. This means that the dielectrophoretic force did not decrease over the last distance covered by the bead, and the measurement could have ended once the maximum value was measured. In the following section, these findings are analysed to a greater extent by applying a range of voltages and frequencies. This allowed to investigate how the magnitude of the dielectrophoretic force acting on individual latex beads was affected. Additionally, comparisons with simulated values reported in Section 4.4 are demonstrated.

5.8 Effect of applied electrical potential and frequency on the dielectrophoretic force magnitude

In the previous section, I explained the developed technique for measuring the magnitude of the dielectrophoretic force that acted on an individual latex bead from its two-dimensional trajectory while being attracted towards the nanotweezers tip. In this final section, the effect of the applied electrical potential and frequency on the dielectrophoretic force magnitude was investigated. This parametric study was conducted for a range of V_{rms} from 100 mV to 600 mV and f_{app} from 10 kHz to 20 MHz. Such low voltages (< 1 V) had never been reported before for single-molecule force probing with similar configurations. As points of reference, in their studies, Nadappuram et al. (2019) [10] went as low as V_{rms} = 1 V with a similar nanotweezers system while Barik et al. (2016) [69] used a minimum voltage of 200 mV on a slightly different configuration for trapping nanometre-sized entities. This sub-volt range allowed also the nanotweezers to operate safely without leading to unwanted heating effects that could affect measurements.

Following the analysis on the polarisability of the beads-H_2O system in Section 5.6, the frequency range of the applied AC signal was selected to achieve maximum values for pDEP and nDEP. Higher or lower frequencies than 20 MHz and 10 kHz, respectively, would result in the same force magnitude. It is important to note that $f_{app} <$ 10 kHz could lead to electrostatic phenomena since the induced dipole across a dielectric particle would have more time to respond to changes in the polarity of the field, affecting eventually dielectrophoresis. For the experimental measurements discussed in this section, 10 individual pairs of nanotweezers were used. Seven of them gave similar electrochemical current response to the carbon nanoelectrodes with a separation gap of 55 nm (SEM images in Figure 3.4). This distance was considered constant for these nanotweezers, but not for the remaining three which after SEM imaging were found to have a separation gap of 150 nm. Carbon recession could be present in the former ones, as it could not be visually checked, but not for the latter. Comparisons between the experimental results and simulated values from Section 4.4 are demonstrated to assess the separation gap between the two carbon nanoelectrodes and possible carbon recession inside the nanopipette tip.

5.8.1 Effect of the applied electrical potential on $\left|\vec{F}_{DEP}\right|$

Individual 2 μm latex beads were trapped with 5 different pairs of nanotweezers immersed in water. By analysing their trajectory as discussed in Section 5.7, the dielectrophoretic force magnitude experienced by the particle was measured as a function of the radial distance from the tip. Figure 5.15 displays examples for the position of a latex bead at two time-frames (start and end of trajectory) for four applied potentials (600 mV, 400 mV, 200 mV and 100 mV) and a 10 kHz frequency. The smoothed force-distance curves from 5 independent measurements (1 bead per set of nanotweezers) for each applied voltage are depicted in Figure 5.14.

When V_{rms} = 600 mV and f_{app} = 10 kHz, individual beads were trapped as far as 10 μm away from the nanotweezers tip (cyan and green curves, Figure 5.14a). The dielectrophoretic force magnitude increased non-linearly as the beads approached the tip and peaked between 0 and 2.5 μm. Maximum values ranged from approximately 400 to 600 fN between the five nanotweezers used. A window size equal to 45, third order polynomial and "fit" mode were selected for data fitting and smoothing. Interestingly, the force – distance curves showed different trends between the nanotweezers. This could potentially be attributed to deviations in the geometry of the nanopipette tip or even carbon being recessed further inside the pores, as previously discussed in Chapters 3 and 4. Another factor that could have impacted these trends is the initial position of each bead. In Section 4.4.1, simulations suggested a change in the dielectrophoretic force magnitude when the particle's initial position prior to getting trapped was at 45° rather than 0° relative to the long axis of the nanotweezers tip (x-axis).

Force – distance curves acquired for V_{rms} = 400 mV showed a decrease in the maximum force value at ~3 μm away from the tip, ranging approximately between 80 and 180 fN, while furthest trapping was achieved 8 μm away. In this case, a window size of 163, second order polynomial and "interp" mode were chosen for data fitting and smoothing. Here, the first 4 nanotweezers (NT1, NT2, NT3 and NT4) produced similar curves while NT5 (cyan curve) deviated the most, as in the case of V_{rms} = 600 mV. The trapping region in Figures 5.14c and 5.14d is reduced even further, slightly exceeding 4 μm. The force magnitude was found between 50 and 200 fN for V_{rms} = 200 mV, and 40 and 120 fN for V_{rms} = 100 mV. From these curves in Figure 5.14c and 5.14d, where maximum dielectrophoretic force was significantly smaller than the previous two (Figure 5.14a and 5.14b), it can be assumed that forces due to thermal energy had a higher impact and the overall measurement precision decreased.

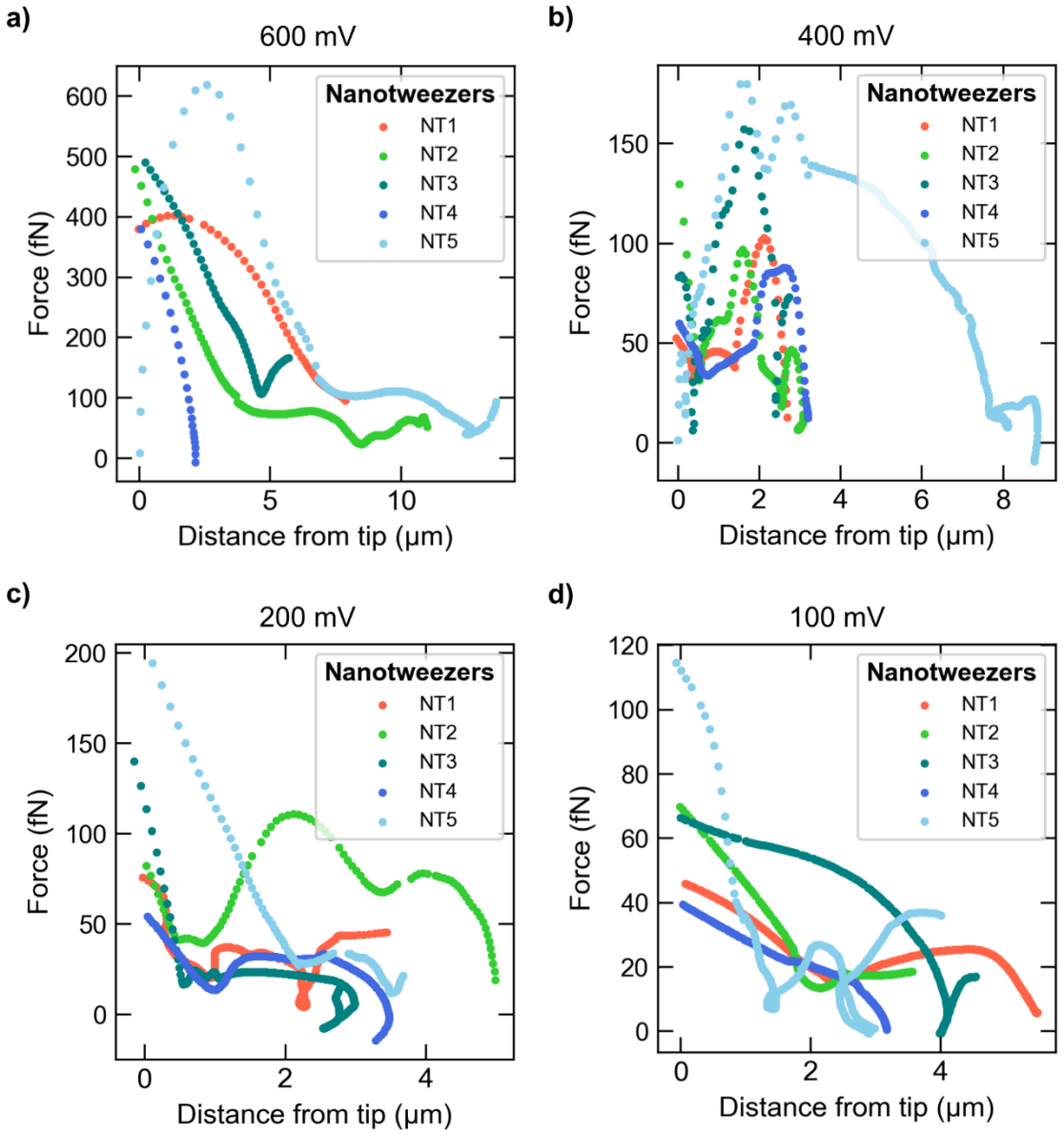

Figure 5.14 Measured dielectrophoretic force magnitude with 5 nanotweezers (NT1, NT2, NT3, NT4 and NT5) experienced by an individual 2 μm latex bead over the smoothed distance from the nanotweezers tip for a range of applied electrical potentials, **a)** 600 mV, **b)** 400 mV, **c)** 200 mV and **d)** 100 mV at 10 kHz. Data smoothing was applied to each set of measurements from separate nanotweezers. The resulting trends suggest that for the first few μm away from the nanotweezers tip the force acting on the bead increases non-linearly. Then, it enters a region of stronger electric field gradients, reaching the maximum value.

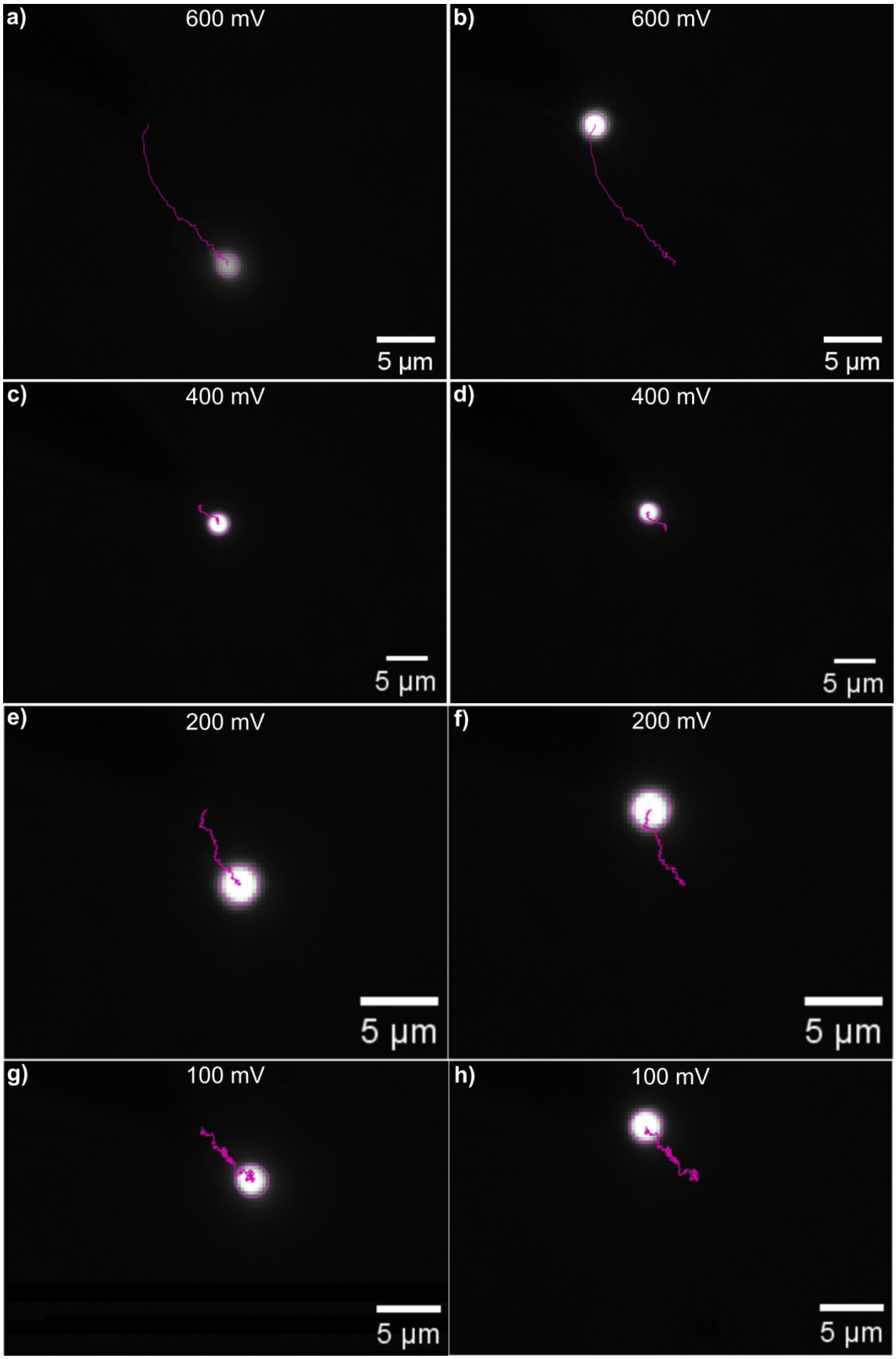

Figure 5.15 First (left column) and last (right column) frames of an individual bead attracted towards the nanotweezers tip for 10 kHz and **a, b)** 600 mV, **c, d)** 400 mV, **e, f)** 200 mV and **g, h)** 100 mV. The purple curve represents the bead's trajectory.

Another interesting phenomenon observed in Figures 5.14a and 5.14b was the decrease in the force magnitude after reaching its maximum value close to the nanotweezers tip. Individual beads trapped by NT1 (red curve) and NT5 (cyan curve) at 600 mV and 10 kHz, as well as all nanotweezers at 400 mV and 10 kHz, behaved in this way. However, when keeping the applied frequency constant and reducing the voltage (100 and 200 mV), this drop in the dielectrophoretic force disappeared. Based on the discussion in Section 2.4.4 and the fact that this phenomenon became evident when the lowest frequency (< $f_{CM,0}$) and highest voltages were applied on the nanotweezers, it is possible to assume that electroosmotic effects could occur near the tip. Bulk movement of the fluid that surrounds the nanoelectrodes' charged surfaces could act against the attractive dielectrophoretic force. Another demonstration of electroosmosis taking place at 600 mV and 10 kHz, but this time when using nanotweezers modified by FIB milling, is presented in Figure 5.16 below. The oscillating bead displacement between frames 300 and 600 suggests that electroosmotic flow prevented the bead of being trapped at the nanotweezers tip. This specific case occurred only for a pair of nanotweezers whose tip was heavily etched by FIB milling.

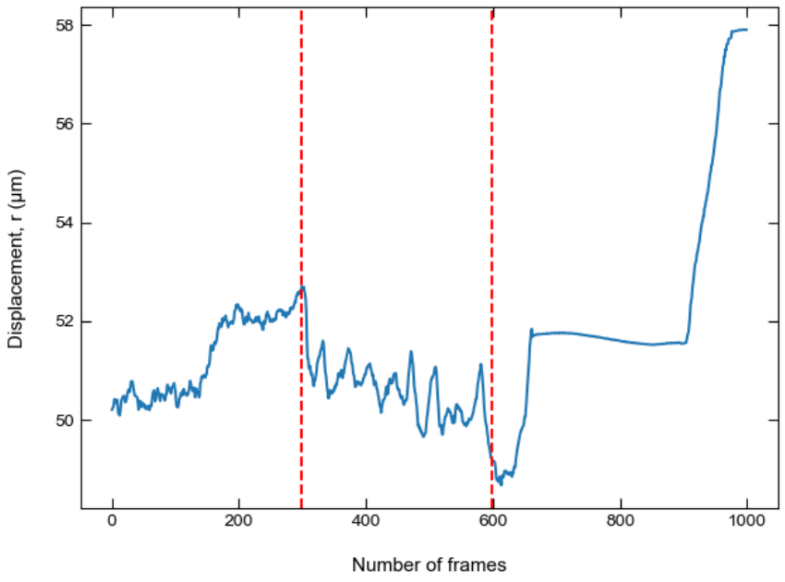

Figure 5.16 Radial displacement (r) of an individual 2 μm latex bead when attracted (600 mV, 10 kHz) towards the nanotweezers tip surface (FIB milled) as a function of the recorded number of frames. The vertical dashed red lines represent the edges of the frame range that electroosmosis occurred.

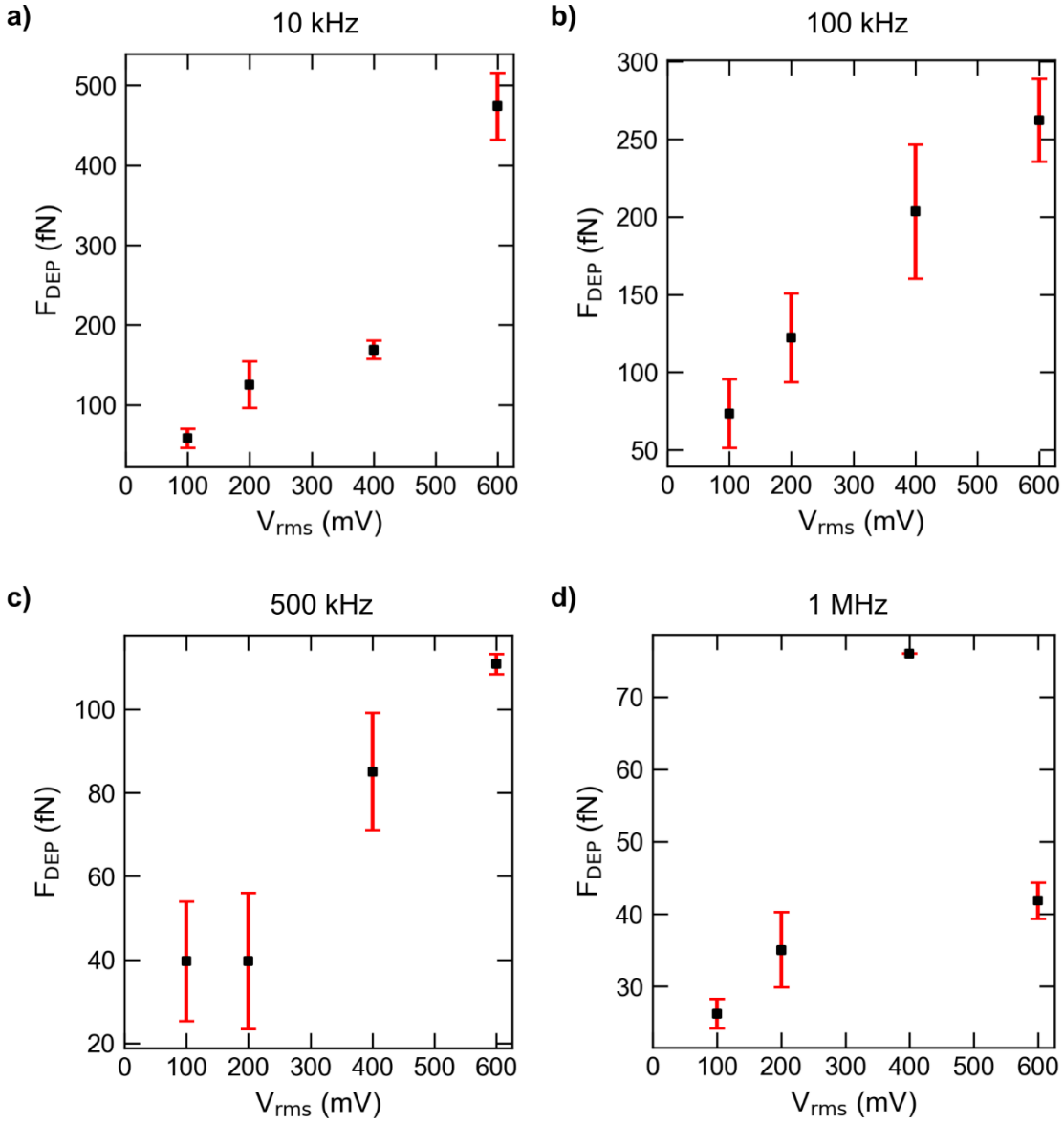

Figure 5.17 Mean maximum measured value (black squares) and standard error of the mean (red bars) of the dielectrophoretic force extracted from the trajectory of individual 2 µm latex beads in H_2O over a range of applied electrical potentials (V_{rms}) with a frequency of **a)** 10 kHz, **b)** 100 kHz **c)** 500 kHz and **d)** 1 MHz. All data were individually smoothed before calculating the mean and error.

Furthermore, the same study was performed over a range of applied frequencies as shown in Figure 5.17. The effect of the frequency on the dielectrophoretic force magnitude is analysed in the next section (Section 5.8.2). Black square points represent the mean dielectrophoretic force magnitude from 5 individual curves, as presented in Figure 5.14, and red error bars represent the standard error of the mean from these 5 measurements. Starting with Figure 5.22a, the measured mean dielectrophoretic force increased proportionally to the applied electrical potential squared, as expected from

$\left|\vec{F}_{DEP}\right| \sim V_{rms}^2$. These experimental results were not in good agreement with the ones obtained from simulations in Section 4.4. The maximum experimental mean value was equal to 474 ± 42 fN at 600 mV while the simulated one was equal to 516 fN, when the 600 mV were applied, and a 100 nm deep carbon recession was considered for a separation gap of 55 nm. Nevertheless, the model could be used for estimating the dielectrophoretic force since it provided results in the same order of magnitude to the experimental ones. At 400 mV, the experimental force magnitude was equal to 169 ± 11 fN while the simulated 230 fN for the recessed case. The maximum values for the remaining voltages did not agree with the simulated ones. This happened because as the force magnitude decreased, the precision of the measurement dropped as well due to contributions from the particle's diffusion.

Overall, results based on both experiments and simulations suggested that the average nanotweezers geometry used throughout these measurements could be described by a 55 nm separation gap between the carbon nanoelectrodes and a 100 nm carbon recession inside the nanopipette pores. The trend reported in Figure 5.17a was not reproduced for the remaining frequencies in Figure 5.17. In Figure 5.17b, an ascending trend was noticed with a maximum value of 262 ± 27 fN at 600 mV. However, the measurement errors do not allow drawing conclusions on whether it was linear or quadratic. At 500 kHz, the maximum dielectrophoretic force was 111 ± 2 nm when V_{rms} = 600 mV (Figure 5.17c). Finally, based on Figure 5.10, the crossover frequency was anticipated at 1 MHz, where the force magnitude would drop to 0. Figure 5.17d indicated significantly low force magnitudes, with a mean value of 42 ± 3 fN at 600 mV, suggesting that $f_{CM,0}(\omega)$ was close to this frequency, but could not be determined with greater precision. The crossover frequency is better visualized in Figure 5.20 in the following section.

5.8.2 Effect of the applied frequency on $\left|\vec{F}_{DEP}\right|$

Figures 5.18a, 5.18b show an individual 2 μm latex bead being attracted towards the nanotweezers tip upon the application of an AC signal of 600 mV and 10 kHz. The dielectrophoretic force magnitude as a function of the distance from the tip was measured from the bead's trajectory, after applying the smoothing technique from Section 5.10.10. This recording proved that at low frequencies (< 1 MHz) positive dielectrophoresis occurred and the beads were attracted towards the regions of strongest electric field gradients. In contrast, Figures 5.18e and 5.18f present an individual bead being repelled from the nanotweezers tip only by switching the frequency

of the AC signal to 20 MHz. The dielectrophoretic force magnitude was measured again through the same technique as shown in Figure 5.19a and 5.19b. After smoothing the experimental data (green curve in Figure 5.19a), the dielectrophoretic force magnitude was plotted over the distance from the tip. Here, a maximum force of approximately -80 fN was applied to the latex bead which decreased as it moved further than 500 nm from the tip. This recording validated that at high frequencies (> 1 MHz) negative dielectrophoresis took place and the beads were attracted towards the regions of weakest electric field gradients. For an applied frequency equal to the expected crossover frequency for this system (1 MHz), the bead did not experience attraction or repulsion by the nanotweezers and was freely diffusing in water (Figures 5.18c, 5.18d).

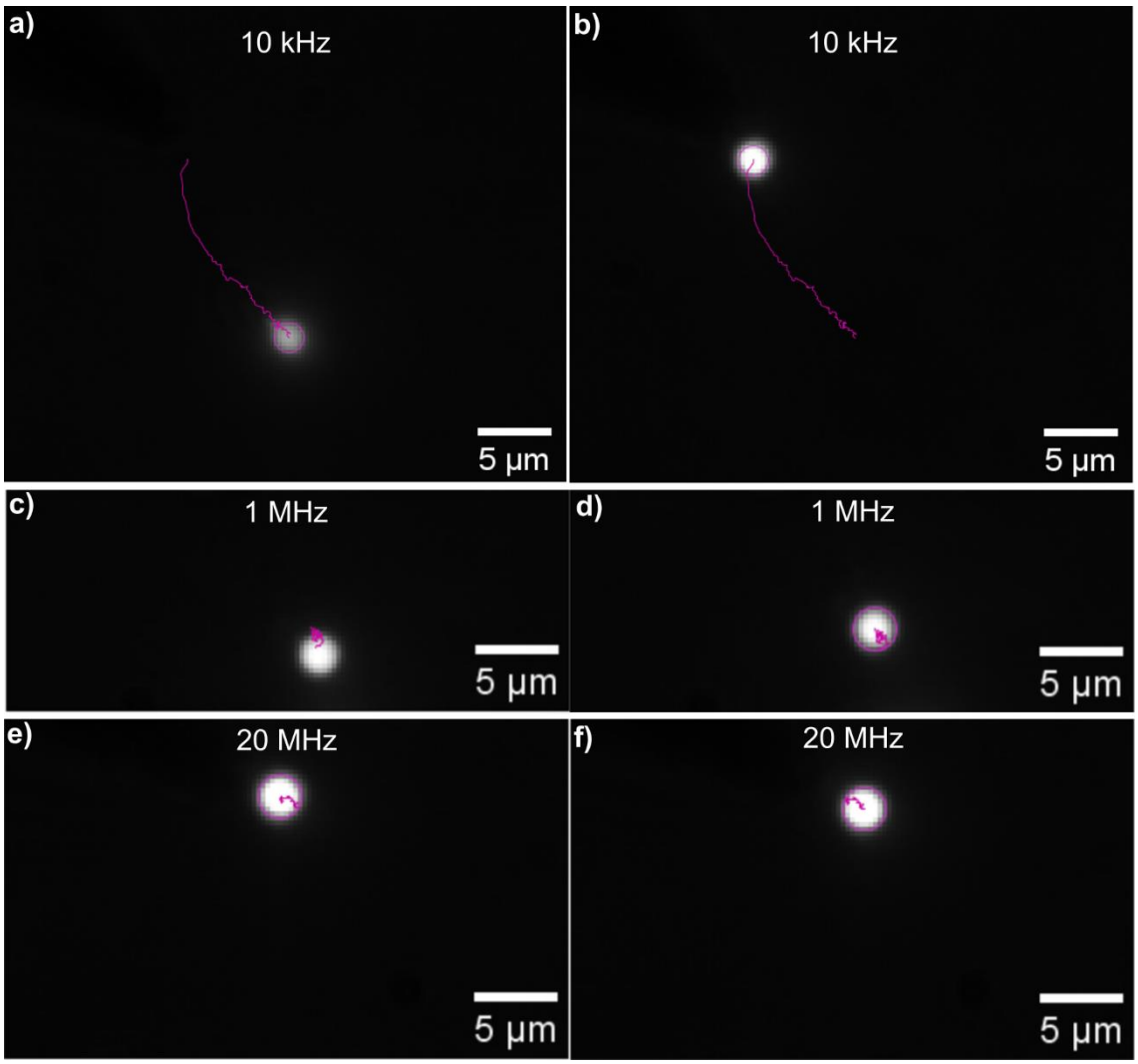

Figure 5.18 First (left column) and last (right column) frames of an individual bead being **a, b)** attracted at 10 kHz, **e, f)** repelled at 20 MHz from the nanotweezers tip or **c, d)** freely diffusing at 1 MHz for an applied electrical potential of 600 mV. The purple curves represent the beads' trajectories.

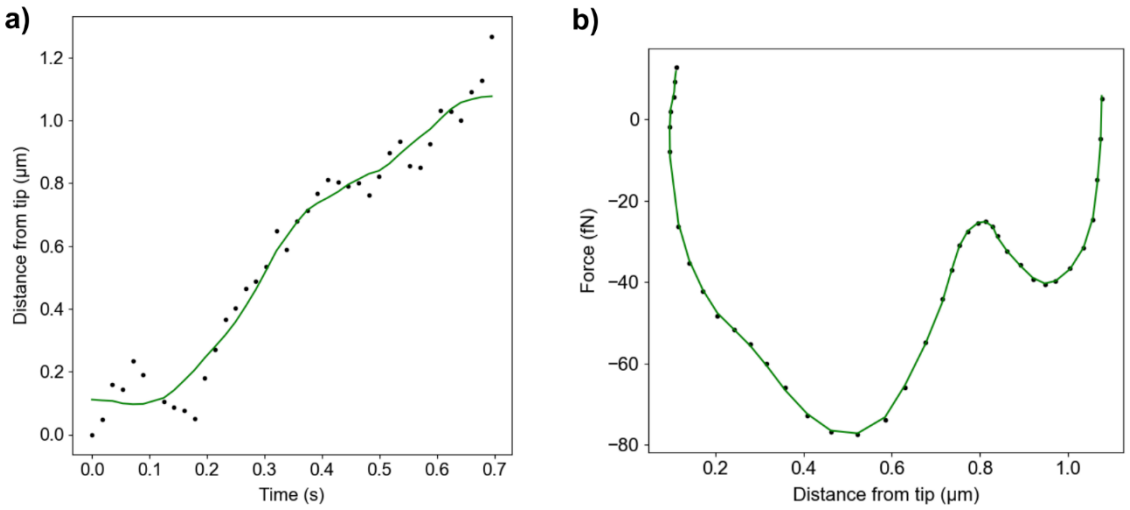

Figure 5.19 a) Radial distance $r(t)$ between an individual 2 µm latex bead and the nanotweezers tip surface as a function of time. Data points were acquired from its 2D trajectory while the fitted green curve was obtained by data smoothing. A window size of 23, polynomial order of 2 and "mirror" mode were selected. **b)** Dielectrophoretic force magnitude over the smoothed distance from a). Black data points represent F_{DEP} calculated from the time derivative of $r_{SG}(t)$ in a) while the green curve is the fitting obtained by further smoothing. The resulting trend suggests that for the first ~500 nm away the nanotweezers tip the force acting on the bead increases from ~0 fN to -80 fN. Note that a window size of 7, second order polynomial and "interp" mode were selected.

For a range of applied sub-volt potentials (V_{rms}), the dielectrophoretic force was plotted as a function of the applied frequencies and is presented in Figure 5.20. The dashed orange line represents weighted non-linear squares fitting of the data following Equation 2.3 where $\left|\vec{F}_{DEP}\right| \sim Re[f_{CM}(\omega)]$. Since the relative electric permittivity ($\varepsilon_p, \varepsilon_m$) and conductivity ($\sigma_p, \sigma_m$) of the particle and medium were defined, the only free fitting parameter was the gradient of the electric field magnitude squared $\nabla\left|\vec{E}_{rms}\right|^2$. Following the fitting curve in Figure 5.20a, the force magnitude reached a plateau value of 474 ± 42 fN at frequencies between 10 kHz and 100 kHz when 600 mV were applied. Then, it gradually decreased between 250 kHz to 750 kHz until it reached 0 magnitude at 1 MHz. At 20 MHz, the polarity of the dielectrophoretic force shifted to negative leading to the repulsion of the particle. This trend was in good agreement only at maximum pDEP (10 – 100 kHz) and at the crossover frequency (1 MHz). For the remaining frequencies the experimental values were much lower than expected. The fitting parameter $\nabla\left|\vec{E}_{rms}\right|^2$ = (2.3 ± 0.6) * 10^{14} V^2/m^3. A similar trend was noticed when 400 mV were applied, where a maximum $\left|\vec{F}_{DEP}\right|$ of 203 ± 29 fN was acquired at 100 kHz. The value at 10 kHz could be considered within the plateau region set at 100 kHz, besides the large error found for

the latter. For the remaining frequencies, except at 750 kHz which agrees with the fit value, the fitting predicted larger absolute forces than the experimental ones. The fitting parameter $\nabla\left|\vec{E}_{rms}\right|^2$ = (0.8 ± 0.2) * 10^{14} V^2/m^3.

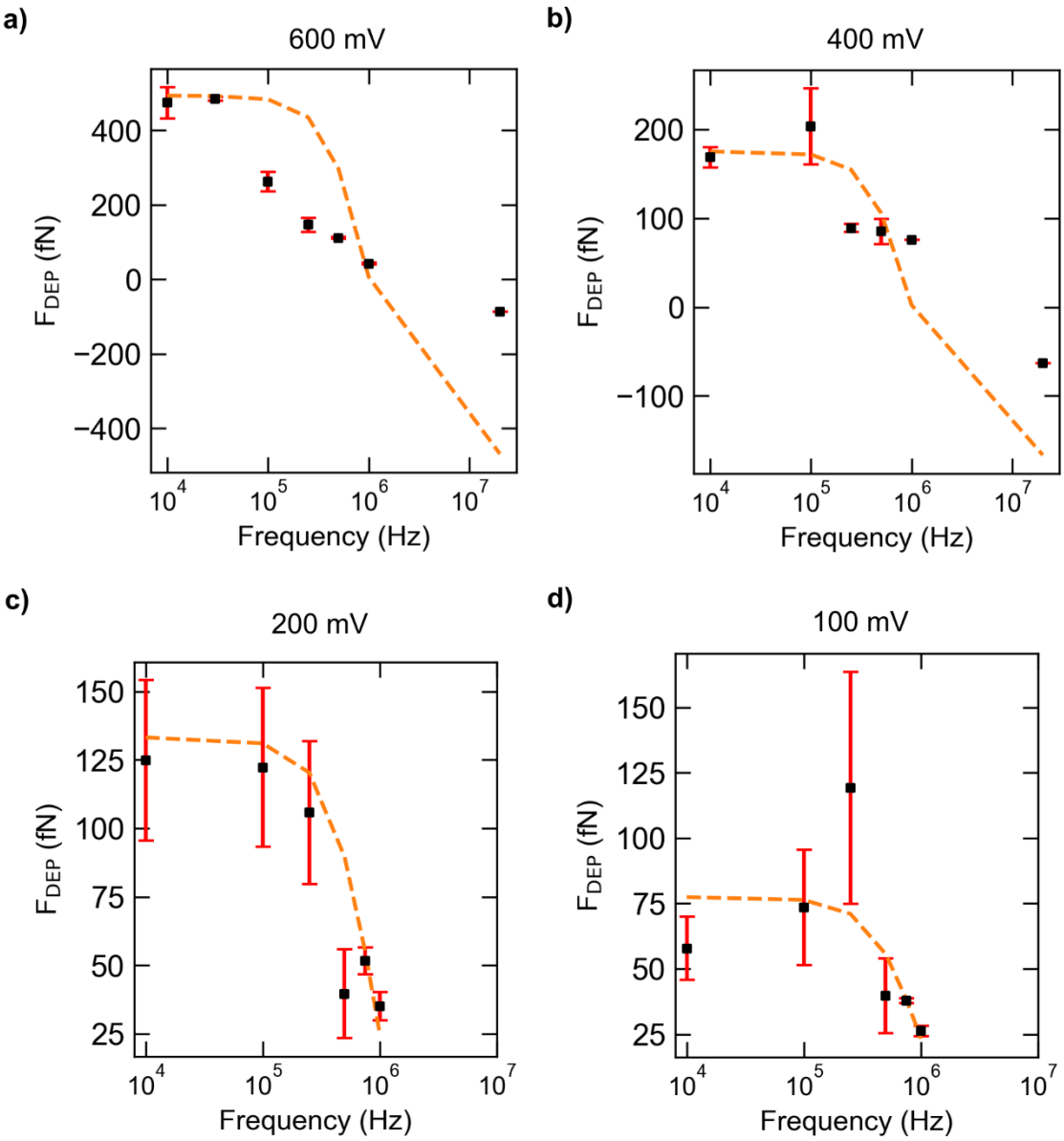

Figure 5.20 Mean maximum measured value (black squares) and standard error of the mean (red bars) of the dielectrophoretic force extracted from the trajectory of individual 2 µm latex beads in H_2O over a range of applied frequencies (f_{app}) with a voltage of **a)** 600 mV, **b)** 400 mV **c)** 200 mV and **d)** 100 mV. No data could be recorded at 20 MHz for V_{rms} = 100, 200 mV. All sets of 5 measurements per condition were individually smoothed before calculating the mean and standard error of the mean. Weighted non-linear least squares fitting was applied to the data based on Equation 2.3.

In Figure 5.20c (200 mV), although the errors in the force magnitude increased compared to the two previous cases, the data points fall close to the fitting curve. At 125 ± 29 fN between 10 and 100 kHz, the force reaches a plateau that gradually drops to approximately 30 fN at 1 MHz. In this case, the fitting parameter became (0.5 ± 0.2) * 10^{14} V^2/m^3. Finally, at 100 mV, there is no evident plateau region for low frequencies as the data points deviate significantly from the fit, whereas good agreement is observed between experimental and fit values at 750 kHz and 1 MHz, where the force magnitude fell to approximately 30 fN. This magnitude approaches reported values associated with the thermal motion of the beads in water (~2 fN [69]). Besides the reduced precision in the measurement of the dielectrophoretic force, the force probing resolution of the nanotweezers reaches a limit that has not been reported so far. The fitting parameter for this last case was (0.25 ± 0.09) * 10^{14} V^2/m^3.

Overall, the experimental results presented in this chapter showed the capability of the nanotweezers to probe dielectrophoretic forces with a resolution from tens to hundreds femtonewtons. Just by changing the electrical potential and frequency of the applied AC signal, different orders of magnitude in the femtonewtons range were established. These measurements are in the same order of magnitude with the values extracted from finite element simulations when an average separation gap of 55 nm existed between the two nanoelectrodes while recessed carbon was deposited 100 nm inside the nanopipette tip. This showed that the geometry of the nanotweezers was an additional parameter that could eventually be modulated to probe the desired force ranges. It was also demonstrated that the nanotweezers could be tuned to trap individual entities as close as the threshold value set by thermal energy in the system. This gentle force probing mechanism could potentially allow the measurement of processes that other single-molecule techniques could not accommodate. Of course, further optimisation of this configuration is required to reach the stage of comparing it with well-established single-molecule techniques. However, this work has demonstrated that dielectrophoretic nanotweezers could be an additional tool to the currently available options or be used in combination with them due to its flexibility in positioning and control in three dimensions.

5.9 Conclusions

To summarise, the findings reported in this chapter proved that quartz glass double-barrel nanopipette-based carbon electrodes can be utilised as dielectrophoretic nanotweezers for single-molecule manipulation and force probing. Individual 2 μm carboxylate-modified polystyrene latex beads, suspended in water, were successfully trapped with voltages lower than 1 V (V_{rms}). The generated dielectrophoretic force could be controllably tuned in the femtonewton range, from few tens to several hundred fN, by adjusting either the applied electrical potential or frequency. Low frequencies led to the attraction of individual particles towards the nanotweezers tip, while high frequencies repelled them further away, exactly as analytically predicted from the real part of the Clausius-Mossotti factor. As previously mentioned, this gentle force probing mechanism could potentially allow the measurement of processes that other single-molecule techniques could not accommodate (most techniques operate in > 1 pN values). Of course, further optimisation of this configuration is required to improve accuracy and reproducibility in data acquisition in order to be compared with other well-established single-molecule techniques. However, this work has also demonstrated that dielectrophoretic nanotweezers could be used in combination with them due to its flexibility in positioning and control in three dimensions.

The first step towards achieving dielectrophoretic force probing with the nanotweezers involved electrophoretic light scattering measurements to determine the zeta potential of carboxylate-modified polystyrene beads in H_2O. The obtained zeta potential value was used to analytically estimate the electrical conductivity of the particle. This value was found equal to 6.24 ± 0.05 mS/m and was then used in determining the polarisability of this suspension under the application of an AC signal. Then, the two-dimensional trajectory of individual freely diffusing beads in H_2O on top of a glass slide was recorded on an inverted fluorescence microscope by using single particle tracking. The x- and y-coordinates were used to calculate their time averaged mean squared displacement as a function of lag time for all available displacements. By applying linear fitting between these two variables, the optimum number of fitting points and trajectory length were statistically evaluated. Based on that, the mean diffusion coefficient of individual beads was measured from a trajectory including 1000 data points.

Following the analysis for the diffusion coefficient of latex beads in water, these values were used to assess whether their diffusion was hindered due to hydrodynamic interactions with the top surface of the cover glass, where most beads were found at equilibrium. From this, a correction factor of 1.5 for the bulk viscosity of the solution was

calculated and applied to measure the effective viscosity of water surrounding individual beads when diffusing close to a glass surface. The effect of temperature in the beads' diffusion coefficients was also studied by recording their trajectories while in Brownian motion both at the start of sample illumination and 30 minutes afterwards. It was concluded that temperature did not affect their diffusion at such time intervals. Then, from the measured effective viscosity of H_2O, the distance between the bottom surface of an individual bead and the top surface of the glass slide was found equal to 700 ± 200 nm. This distance was estimated by applying Faxen's and Brenner's approximations, for particle motion only parallel to the glass wall top surface.

Moreover, the polarisability of the beads-H_2O suspension under the application of an AC signal was analytically obtained. By using the electrical conductivity of latex beads (6.24 mS/m) and the one for the aqueous solution together with their known relative electrical permittivities, the real part of the Clausius-Mossotti factor was analytically measured as a function to the applied frequency. This value reached a plateau of 0.5 at frequencies lower than 100 kHz, and -0.5 for frequencies higher than 10 MHz. The crossover frequency was equal to 1.01 ± 0.01 MHz. After all these, I explained the developed technique to measure dielectrophoretic forces experienced by individual latex beads under trapping conditions based on single particle tracking. After integrating the nanotweezers on the inverted fluorescent microscope and placing their tip 1 μm above the 2D plane where most beads diffused, AC signals of sub-volt voltages and tenths of kHz frequencies were applied to achieve pDEP. From the individual trajectories of trapped beads, their spatial coordinates were extracted for a range of time frames. By taking their time derivative, their velocity was defined as a function of the distance from the nanotweezers tip. Since, the dielectrophoretic force was equal to the Stokes drag force at every time point, their velocity was used to measure the magnitude of the dielectrophoretic force. A data smoothing algorithm was developed to filter noise created from the time derivatives.

Finally, the effect on the dielectrophoretic force magnitude by the electrical potential and frequency of the applied AC signal between the nanotweezers were investigated. A range of voltages (100 mV, 200 mV, 400 mV and 600 mV) and frequencies (10 kHz, 100 kHz, 250 kHz, 500 kHz, 750 kHz, 1 MHz and 20 MHz) were applied to assess changes in the dielectrophoretic force. This frequency range was selected to verify whether pDEP and nDEP occurred at low and high values, respectively. Maximum $\left|\vec{F}_{DEP}\right|$ of 474 ± 42 fN at 600 mV and 10 kHz was measured from 5 trapping events with separate nanotweezers. Interestingly, minimum $\left|\vec{F}_{DEP}\right|$ = 40 ± 14 fN at 100 mV and 500 kHz was also measured from 5 trapping events with separate nanotweezers. Comparisons to simulated results were found in the same order of magnitude for $V_{pk,rms}$ = 600 mV and

suggested that the average nanotweezers used throughout these experiments had a carbon recession towards inside the tip opening equal to 100 nm and the separation distance between the two carbon nanoelectrodes at 55 nm. Finally, at low frequencies (10 kHz) and high voltages (600 mV), the drop in the dielectrophoretic force could potentially be linked to electroosmotic flow which was suggested to act opposite to the dielectrophoretic force that attracted the beads to the nanotweezers tip.

5.10 Experimental materials, methods and setups

This section contains information related to the materials used in this chapter, as well as the experimental configurations and methods applied to acquire and analyse data.

5.10.1 Latex beads sample preparation

Carboxylate-modified polystyrene latex beads with a 2 μm mean diameter (1 mL aqueous suspension with 2.5% solids content, containing 0.1% NaN_3) functionalised with red fluorescent dye ($\lambda_{ex}/\lambda_{em}$ ≈ 553/635 nm) were purchased from Sigma-Aldrich (L3030-1ML, Saint Louis, MO, USA). The number of beads in 1 mL stock solution was ~ 5.7 x 10^9. For every fluorescence imaging experiment, the stock solution was diluted 10^5 times in Milli-Q type 1 water (18.2 MΩ*cm at 25 °C, Milli-Q EQ7000, Merck, Darmstadt, Germany), and from this diluted suspension a volume of 400 μL, which contained approximately 23,000 beads, was used as the sample.

5.10.2 Zeta potential measurements

The zeta potential of the latex beads (L3030-1ML) was determined by electrophoretic light scattering (ELS) experiments using the Zetasizer Nano system equipped with a He-Ne laser and scattered light detected at 173° (Malvern Panalytical Ltd., Worcestershire, UK). A disposable folded capillary zeta cell (Malvern Panalytical Ltd., Worcestershire, UK) was loaded with 1 mL of sample used in these experiments, which consisted of 25 μL of 10x PBS (phosphate-buffered saline) solution (pH 7.4, composed of 1.37 M NaCl, 27 mM KCl, 100 mM Na_2HPO_4 and 18 mM KH_2PO_4) mixed with 975 μL of 10^4 times diluted latex beads stock solution (L3030-1ML) in Milli-Q type 1 water. The sample was run 3 times with 92 recordings per run at 25 °C and the measurements were reported as the mean ± standard deviation (see Figure 5.1 and Table 5.1). Note that the Zetasizer Nano system was operated by Dr George Newham (School of Physics and Astronomy, University of Leeds).

5.10.3 Viscosity measurements

Viscosity measurements of Milli-Q water were carried out using the Kinexus Ultra+

Rheometer (Nexus Analytics Sdn Bhd, Selangor, Malaysia) at 25 °C by recording data every 30 s over 5 min in total. The geometry used was a cone CP4/40 (4° angle, 40 mm diameter) and a plate (60 mm diameter). Note that the instrument was operated by Dr Nataricha Phisarnchananan (University of Leeds), while Dr Chalmers Chau (University of Leeds) prepared the sample. The results from three repetitions are listed in Table 5.3 together with their average value at every time interval.

Table 5.3 Average measured shear viscosity of Milli-Q H_2O at 25 ℃ recorded every 30 s [30, 300 s] after 3 repetitions.

	Shear Viscosity (mPa*s)			
Time (s)	Milli-Q H_2O (25 ℃)			
	Repetition 1	*Repetition 2*	*Repetition 3*	*Average*
30	0.9025	0.93947	0.86535	0.90244
60	0.84396	0.88768	0.92033	0.88399
90	0.89908	0.87321	0.83284	0.868377
120	0.86748	0.92694	0.89092	0.895113
150	0.86842	0.83476	0.88735	0.86351
180	0.91106	0.9061	0.81868	0.878613
210	0.83305	0.89769	0.92841	0.886383
240	0.91792	0.8394	0.85365	0.870323
270	0.86555	0.90952	0.87123	0.8821
300	0.85634	0.85031	0.89459	0.86708

By calculating the mean viscosity and its standard deviation from the 10 average values listed above, it was found that the measured viscosity of water is $\eta_{0,exp}$ = 0.88 ± 0.01 mPa*s which agrees with its expected theoretical value $\eta_{0,th}$ = 0.89 mPa*s at 25 °C [152].

5.10.4 Microscope cover glasses preparation

Rectangular cover glasses (24x36 mm, #1.5, Menzel-Gläser) were purchased from Epredia to hold the latex beads solution in place during fluorescence microscopy imaging. Prior to the solution loading, each cover glass was cleaned by immersion in absolute ethanol (for HPLC, ≥ 99.8%, 34852-2.5L-M, Sigma-Aldrich) for 1 minute. The cover glass was then washed twice in Milli-Q H_2O for 1 minute each time and finally dried with N_2 gas.

5.10.5 Attachment of PDMS ring on cover glass

A 10:1 polydimethylsiloxane (PDMS) pre-polymer – curing agent mixture was prepared, poured on a custom-designed mould, degassed in a desiccator for 20 minutes and stored in an oven at 60 – 70 ℃ for 3 hours. The mould was constructed by milling a transparent cast acrylic cubic block (Perspex, Rapid Electronics) based on a three-dimensional computer aided design (3D CAD) prepared on Fusion 360 (Autodesk). The resulting PDMS structure, which had a ring-shaped design with internal and external diameters of 15 and 20 mm respectively and a height of 2.5 mm, was then detached from the mould with a scalpel blade and attached on a clean rectangular cover glass (Section 5.10.4) by applying manually a low stress. This assembly was then used to hold 400 μL of stationary solution in place during fluorescence microscopy imaging.

5.10.6 Fluorescence imaging configuration

Figure 5.21a labels the key components of the motorised inverted microscope (Olympus IX81) used for single particle tracking, while Figure 5.21b focuses on the microscope's stage where a glass slide with a PDMS ring attached on its top surface contains 400 μL of fluorescent latex beads solution. A Mercury light source (100 W U-L100HG, Olympus) was used due to its broad emission spectrum (typical wavelength range of strongest peaks is 185 – 578 nm). In epifluorescence mode, its output passes first from an excitation filter (BP 510-550 nm) of a fluorescence filter cube (U-MWG2, Olympus), is reflected by a dichroic mirror (DM 570 nm), collected by a super apochromat oil-immersion objective (UPlanSApo 60x / 1.35 Oil, ∞ / 0.17 / FN 26.5) and eventually gets absorbed by latex beads in H_2O solution. Then, the beads' fluorescence (~635 nm) is collected by the same objective, passes through the dichroic mirror and a barrier filter (LP 590 nm) of the fluorescence filter cube and is finally focused on the chip of a back illuminated sCMOS camera (Photometrics Prime).

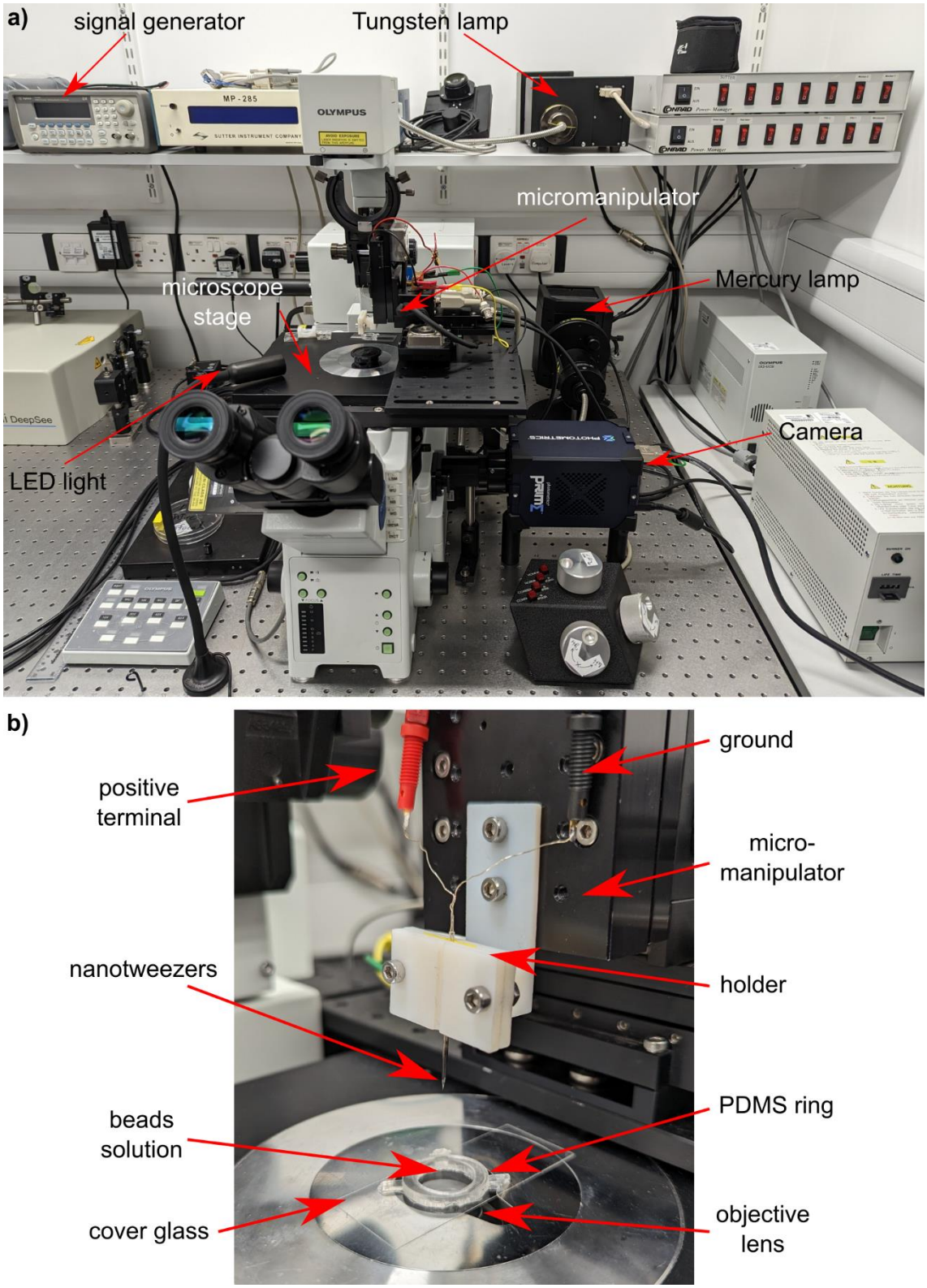

Figure 5.21 a) Picture of the imaging configuration built around an inverted fluorescence microscope (Olympus IX81). The labelled microscope stage, micromanipulator, sCMOS camera, Tungsten lamp, Mercury lamp, LED light and signal generator are the key components of this experimental setup. **b)** Zoomed picture on the microscope stage showing a PDMS ring attached to a cover glass on top of the objective lens. The PDMS well was filled with 400 µL latex beads solution. A set of nanotweezers was clamped on the designed holder mounted on the micromanipulator stage. The positive terminal and ground of the circuit were connected via copper wires to the deposited carbon via the back of the double-barrel nanopipette.

5.10.7 Focusing on latex beads

The transmitted light (Tungsten lamp) is turned on and adjusted via the microscope's software (Olympus FLUOVIEW FV1000). As explained above, the PDMS ring attached on the glass slide is filled with 400 µL of latex beads solution and centred above the microscope objective (UPlanSApo 10x / 0.40, ∞ / 0.17 / FN 26.5). On the top side of the cover glass but outside the PDMS ring area, a black line is drawn to aid with focusing precisely on the top glass surface. At this point, the sample was left for 10 minutes to equilibrate at room temperature (~22 °C). After this time, the beads have sedimented at a close distance to the top surface of the glass due to their density being greater than H_2O (see Section 5.3). Then, by imaging with the sCMOS camera, the edge of the black drawn line is focused with the 10x objective. To increase the focus accuracy on this sample the 20x and 40x objectives (UPlanSApo 20x / 0.75, ∞ / 0.17 / FN 26.5 and UPlanSApo 40x / 0.99, ∞ / 0.11 – 0.23 / FN 26.5) were used in sequence. By switching to epifluorescence mode (Hg lamp intensity set to ~ 50%) and to the 60x oil-immersion objective, the focal length obtained with the 40x objective (value is taken from FV1000 software) is slightly adjusted, due to different working distances between the two objectives, to focus on the plane where most sedimented beads diffused. Figure 5.22a displays a snapshot of a fluorescent bead diffusing in H_2O on top of the cover glass.

5.10.8 Single particle tracking technique

The sCMOS camera was controlled via µManager, a plugin for ImageJ which is an open-source software for image processing and analysis [176]. The selected imaging settings were 10 ms as the exposure time and 2x2 binning mode (1024 x 1024 px window size, 16-bit). During live imaging, the area around an individual diffusing bead, which was several µm away from other diffusing beads, was chosen as the region of interest. Then, a multi-dimensional acquisition was used to record 1000 time points (frames) of the individual diffusing bead within the region of interest with a 0 ms time interval. This acquisition was saved as an image stack file which was imported to Fiji, an ImageJ distribution equipped with Trackmate, the most suitable plugin for single particle tracking [83].

Based on the metadata of this file, two Python scripts (https://github.com/dsoulias/depNanotweezers) were written to convert the length units from pixels to µm and the time units from frames to seconds. After loading TrackMate

and checking that the calibration settings matched the inputted parameters, the LoG (Laplacian of Gaussian) detector was selected with an estimated object diameter of 2 μm (equal to beads' diameter) and a quality threshold of 80 (higher than 0 to reduce detection noise). Once the detection process was completed yielding 1000 positions, the Simple LAP tracker was chosen to connect these points and build the bead's trajectory, with a 5 μm linking and gap-closing maximum distance and 30 frames as the gap-closing maximum gap [83]. Figure 5.22b shows the bead's trajectory in purple, when the tracking process is completed. Finally, the two-dimensional coordinates (x, y) over time (t) were extracted in a .csv file.

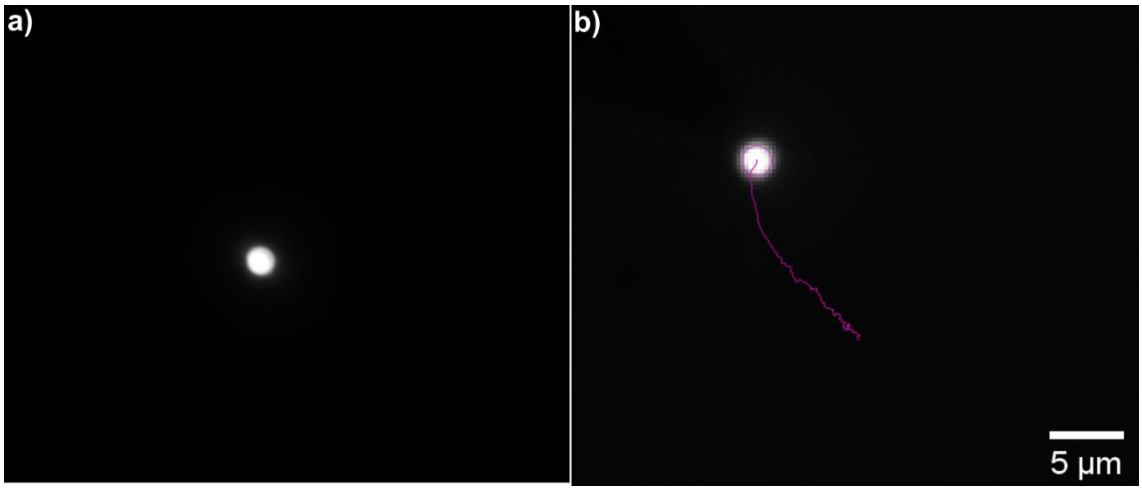

Figure 5.22 a) Snapshot of a fluorescent latex bead (2 μm) diffusing in H_2O on top of a cover glass. **b)** Trajectory (purple curve) of a freely diffusing latex bead (2 μm) in H_2O on top of a cover glass. Single particle tracking was performed with Fiji's plugin, Trackmate. Both images were recorded by a sCMOS camera at 2x2 binning mode with a 60x oil-immersion objective lens.

5.10.9 Positioning the nanotweezers tip at the same plane with diffusing latex beads in H_2O on top of a cover glass

In Section 5.10.7, I described the procedure of focusing on the two-dimensional plane where most sedimented latex beads diffused in H_2O on top of a cover glass. The next step was to integrate a pair of quartz glass nanopipette-based carbon nanoelectrodes, the so-called nanotweezers, on the microscope stage and position their tip on the same plane with the diffusing beads as accurately as possible. Initially, the micromanipulator device (MP-285, Sutter Instrument Co.) was mounted on a stainless-steel stage in parallel to the microscope stage, as shown in Figure 5.21a. This device was controlled via a rotary optical encoder (Sutter Instrument Co.) in three dimensions (xyz plane) with

a maximum displacement of 12.5 mm. The ROE step size per turn was set to 200 nm in coarse mode and 40 nm in fine mode.

A polylactic acid (PLA) 3D-printed holder for mounting nanopipettes was designed in Fusion 360 (Autodesk) by me and manufactured by Rhys Moore (School of Mechanical Engineering workshop, University of Leeds). The holder (white holder, Figure 5.21b) consisted of two parts, its base which was fixed on the vertical stage of the micromanipulator and the nanopipette clamp which secured the nanopipette between two parallel surfaces that were tightened by two bolts at the sides. The nanopipette was oriented as carefully as possible so that its tip was parallel to the cover glass. A Pt wire (250 μm in diameter) was inserted at each barrel (two in total) from the backside of a nanopipette until it made physical contact with the deposited carbon surface. The other end, sticking outside the nanopipette body was soldered on a 2 mm banana socket which was connected to the output of a signal generator (Agilent 33220A, 20 MHz Waveform Generator, Agilent Technologies). In this configuration, one nanoelectrode acted as the positive terminal and the other as the ground of the electrical circuit.

After switching back to the 10x objective and not changing the focus of the microscope, its stage was moved so that the cover glass translated away from the objective lens. While in epifluorescence mode but without enabling the Hg lamp's output, the bright field filter was selected. An additional LED lamp, positioned in parallel to the microscope stage and close to the objective (Figure 5.21a) was used for illuminating the sample. By lowering the nanopipette along the z-axis, its tip was brought in focus by the formed shadow from the side-illumination. Then, by switching to the 20x and 40x objective the optimal z-displacement for the tip to reach focus was recorded. This value was used as the maximum vertical displacement to prevent the tip from crashing on the glass surface and destroying its geometry.

Next, the nanopipette was raised above the stage so that the cover glass was brought again on top of the 60x oil objective lens. As in Section 5.10.7, the output of the Hg lamp was adjusted to 50% and the wide-green filter was selected again. Once I verified that beads continued diffusing on the same focal plane as before, the nanopipette tip was lowered following the displacement value recorded outside the aqueous suspension. The LED light was left on throughout the entire imaging session to monitor the position of the nanotweezers tip. Small adjustments in the z-position of the tip were needed so that it was eventually positioned as accurately as possible 1 μm above the sedimented beads. In this case, dielectrophoretic trapping and force probing could be maintained within two dimensions, the xy plane. Figure 5.23 displays the projection of a nanopipette tip close to a latex bead during fluorescence imaging. The actual orientation of the tip is perpendicular to the plane shown in the image, with its tip surface being located at the

smallest end of the conical shadow. The contrast of the original image was adjusted to highlight these features and aid with visualisation.

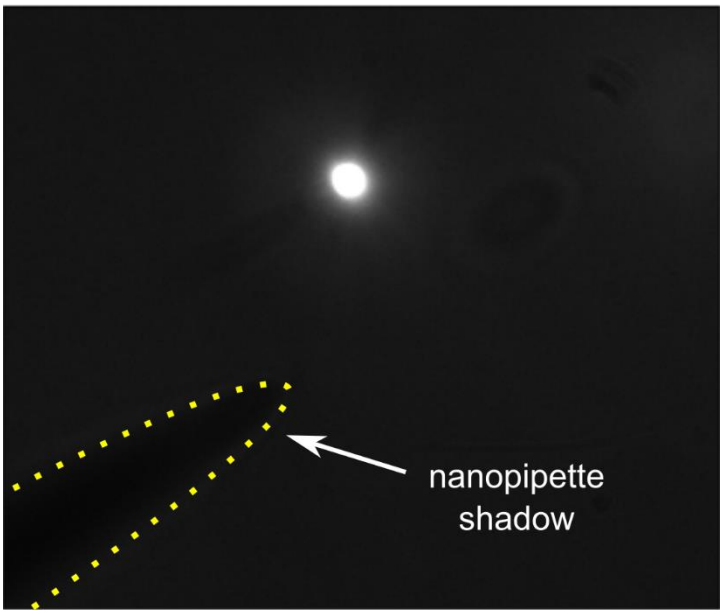

Figure 5.23 Snapshot of a fluorescent latex bead (2 μm) diffusing in H_2O on top of a cover glass close to quartz glass double-barrel nanopipette-based carbon nanoelectrodes, the so-called nanotweezers. The nanotweezers tip and bead were considered in the same focal plane. Note that the geometry of the nanopipette shown (yellow dotted line) is its projection after illumination via a LED light on the side. The contrast of the originally recorded image was adjusted to aid with visualisation.

5.10.10 Data smoothing/filtering algorithm

An algorithm based on least-squares polynomial approximation was developed for smoothing experimental data acquired from single particle tracking measurements. In particular, a function was created in Python (https://github.com/dsoulias/depNanotweezers) based on the Savitzky-Golay filtering method [174] which acted as a low-pass filter to reduce noise in the acquired data while preserving the shape and height of peaks in a curve [175]. Noise generated from the spatial displacement time derivatives of individual beads moving towards the nanotweezers tip was filtered out. This method provided smooth curves to describe the dielectrophoretic force as a function of distance from the tip. In contrast to a typical Savitzky-Golay filter, this function allowed fitting of unequally spaced data points. By

tuning some or all of its 8 possible arguments, data smoothing was optimised based on the user's needs. These were the following:

- "arr": 1 or 2-dimensional array to input to the function. If "arr" is 1D, it contains the data to be smoothed, and the x-axis is considered to be equally spaced with spaces of delta.
- "window_size": this has to be an odd number, so that half_window = (window_size - 1)/2 is an integer. For all data points other than the ones at the ends, a polynomial is now fitted to half_window points to the left, the point itself, and half_window points to the right. The value of this polynomial at the point is now taken as the smoothed data point.
- "order": the order of the polynomial to be used to fit the data. This cannot be equal or greater than the "window_size".
- "deriv": returns the smoothed derivative order selected. The default is to return the smoothed version of the data.
- "delta": spacing if an equally-spaced x-axis is used (see "arr").
- "axis": if "arr" is 2D, "axis" defines which one is the x-axis. If axis=-1, then the x-axis is equally spaced with delta and all others are smoothed.
- "mode": the mode parameter defines how the data at the beginning and the end are handled. It is possible to use different modes at the leading and the tail end of the data. The allowed modes were:
    - "mirror": the data array is extended at the beginning and the end by half_window points and then all real data points can be fitted as normal.
    - "constant": the data array is extended at the beginning and the end with half_window constant value points. The value is "cval" which is the last argument of the function.
    - "nearest": like constant, but instead of a "cval" the value of the first and last point, respectively, is used.
    - "wrap": the last half_window data points are added to the beginning and the first half_window data points to the end (the data are now circular).
    - "skip": the data array is not extended and the first and last half_window data points are not fitted but are left as are.
    - "interp": the data array is not extended, and the first and last half_window data points are not fitted but interpolated, using the last full fit at the beginning and the end, respectively.
    - "fit": the data array is not extended, and the first and last half_window data points are fitted with reduced number of points.

- “cval”: it can be set to give more weight to points towards the beginning and the end, respectively.

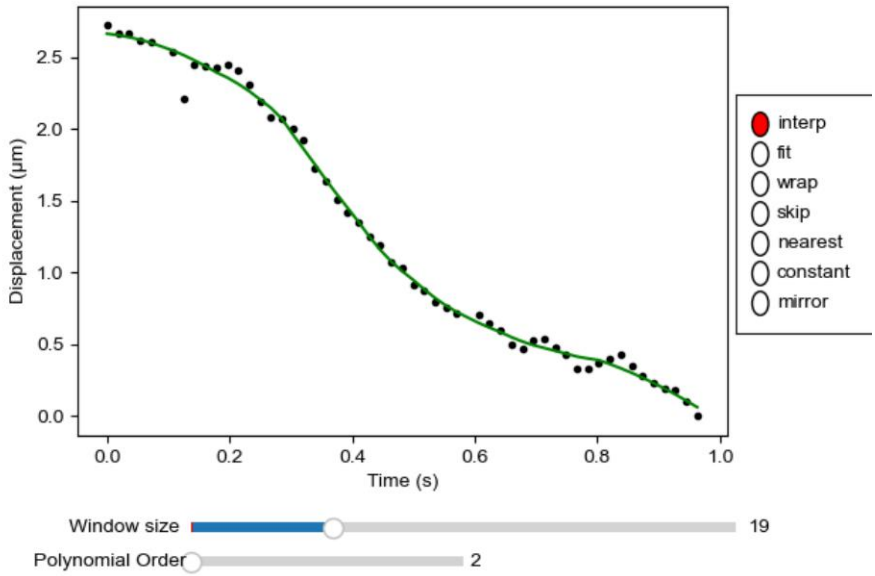

Figure 5.24 Radial distance from the nanotweezers tip (displacement) as a function of time when a bead moves towards the tip under DEP trapping. Coordinates (0, 0) represent the starting position of the bead away from the tip. The black points represent experimental data acquired from single particle tracking measurements while the green curve is the trend of smoothed data based on the algorithm in Section 5.10.10. Two sliding bars at the bottom indicate the values for the window size and polynomial order selected, while the box on the right allows selection of the mode that would give the optimum fitting results.

To smooth either the bead’s radial distance from the nanotweezers tip as a function of time or the dielectrophoretic force over this radial distance, three of the above options were selected; the “window_size”, “order” and “mode”. Regarding the size of the sampling window, its value should be adjusted to obtain a filtered signal which preserves all the meaningful information contained in the original one but with as little noise as possible. The order of the polynomial fitting should be kept as low as possible to introduce as little distortion of the original signal as possible. Finally, the mode can be visually checked in real-time and the one offering the optimum fitting should be selected. Figure 5.4 presents an example of the distance from the nanotweezers tip over time when a bead moves towards the tip under DEP trapping. The black points represent experimental data acquired from single particle tracking measurements while the green curve is the trend of smoothed data based on this algorithm. Two sliding bars at the bottom indicate the values for the window size (19) and polynomial order (2) selected, while the box on the right allows selection of the mode (interp) that would give the optimum fitting results.

Chapter 6

Conclusions and future outlook

This thesis concerns the development and validation of dielectrophoretic nanotweezers, based on two closely-spaced carbon nanoelectrodes at the tip of a glass nanopipette, for single-molecule manipulation and force probing. The following section (Section 6.1) summarises the key achievements presented in the previous chapters alongside with a critical discussion. Additionally, preliminary results are reported regarding possible future directions for the work in this thesis (Section 6.2).

6.1 Summary of key thesis achievements

6.1.1 Chapter 3 summary

- Dual-barrel quartz glass nanopipettes were fabricated with average pore openings of approximately 120 nm and 400 nm for different pulling parameters. Although, SEM imaging and electrochemical characterisation did not show good agreement between them, when combined they provide a valid characterisation of the nanopipette tip (Section 3.2).
- A new setup based on an Arduino PID-controller was developed to deposit pyrolytically carbon inside the quartz nanopipettes and turn them into dual-carbon nanoelectrodes (Section 3.3). This technique achieved greater fabrication yield (~33%) compared to others in literature.
- SEM imaging and electrochemical cyclic voltammetry with a redox mediator were applied to characterise the diameter of the formed carbon nanoelectrodes at the nanopipette tip (Section 3.4). The average geometry had a separation gap of 55 nm between the two nanoelectrodes at the tip, each with a disk-shaped diameter of ~150 nm.
- FIB milling was also performed to tackle carbon not being deposited until the nanopipette pore openings. Smooth co-planar disk-shaped carbon nanoelectrodes with defined dimensions were achieved through this technique (Figure 6.1 and Section 3.4).

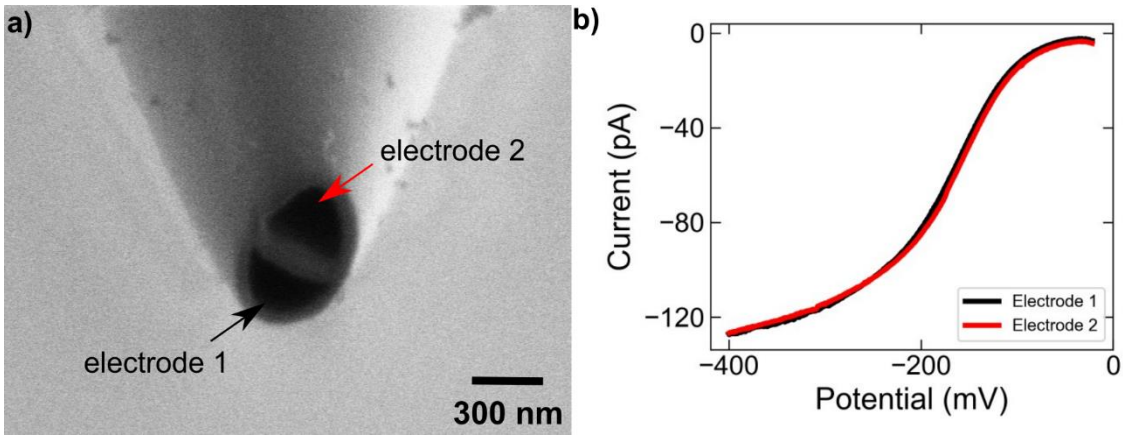

Figure 6.1 Characterisation of quartz glass double-barrel nanopipette-based carbon electrodes based on **a)** SEM imaging and **b)** cyclic voltammetry with hexaammineruthenium(III) chloride ($[Ru(NH_3)_6]Cl_3$) as the electrochemical reduction-oxidation mediator in 0.1 M potassium chloride (KCl) solution.

6.1.2 Chapter 4 summary

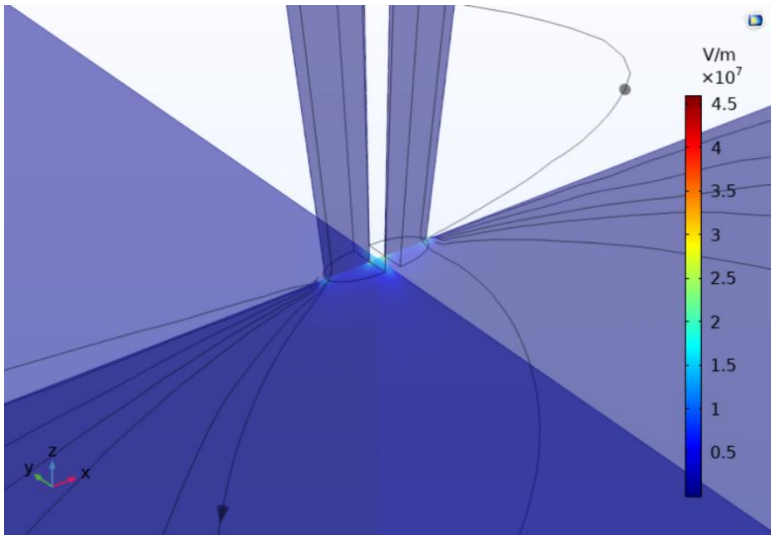

Figure 6.2 3D view of the electric field distribution around the nanotweezers tip for an applied voltage V_{pk} = 600 mV and an electrode separation gap of 55 nm. Lines show the direction of the electric field vector, while the colour map illustrates the magnitude of the electric field magnitude.

- A finite element method model was developed for the dielectrophoretic tweezers system. A simplified geometry for the nanotweezers was designed based on a truncated cone consisting of two semi-elliptical channels filled with carbon, immersed in a cubical domain that represented water (Section 4.2.1). The simulation was built on the “Electric currents” package of the “AC/DC Module”

from COMSOL Multiphysics software. The main initial boundary conditions applied to the geometry of the model were a positive and negative electrical potential at the top surface of the carbon nanoelectrodes (Section 4.2.2). Finally, the geometry was meshed into smaller 3D elements where the software solved the equations (Section 4.2.3).

- The electrical potential distribution (V_{pk}) was simulated across all 2D planes (xy, xz and yz) of the model geometry (Section 4.3.1). The same technique was used to determine the electric field magnitude and visualise its lines distribution in three dimensions (Figure 6.2 and Section 4.3.2). Both variables were determined as a function of the distance from the nanotweezers tip and for a range of applied voltages. For $V_{pk} = \pm$600 mV, the simulated electric field modulus was found $\left|\vec{E}\right|_{xz}^{max}$ = 7.7 kV/m and $\left|\vec{E}\right|_{yz}^{max}$ = 7.5 kV/m, demonstrating small differences between the xz- and yz- planes when crossing the symmetry axis (x = y = 0 nm).
- The dielectrophoretic force magnitude close to the nanotweezers tip was simulated for different geometrical parameters and applied voltages. By calculating the spatial derivative of the squared variable $\left|\vec{E}\right|$ across the z-axis, the magnitude of $\vec{F}_{DEP}$ was probed along 1D lines drawn on 2D planes (xz- and yz-planes) for a range of applied voltages and as a function of the distance from the nanotweezers tip (Section 4.4.1). For $V_{pk} = \pm$600 mV, $\left|\vec{F}_{DEP}\right|_{xz}^{max}$ = 773 fN and $\left|\vec{F}_{DEP}\right|_{yz}^{max}$ = 711 fN, demonstrating small differences between the peak force magnitudes on the xz- and yz-planes when crossing the symmetry axis (x = y = 0 nm). The dielectrophoretic force distribution was probed also at an angle of ±45° between the xz- and yz-planes (Section 4.4.1). Moreover, the effect of the widths separating the two carbon nanoelectrodes at the nanotweezers tip was studied (Section 4.4.2). Finally, the effect of carbon recession, further inside the nanopipette tip, on the dielectrophoretic force magnitude was assessed for a set of recession depths and applied voltages (Section 4.4.3).
- A revised FEM simulation was developed based on the one described in Chapter 4.2 (Section 4.5). The main differences were the addition of the previously removed glass domains and the use of a frequency dependent solver instead of a stationary. In this section, the nanotweezers impedance magnitude and phase were simulated for three cases. Firstly, for when left in air (Section 4.5.1), secondly when immersed in water (Section 4.5.2) and finally when a 2 μm spherical particle (latex bead) was trapped at their tip while immersed in water (4.5.3). In a nutshell, the simulated impedance magnitude decreased when going

from air (3.65 kΩ) to water (2.09 kΩ) to the trapped bead (1.62 kΩ) while the phase became lower only in the last case from -1.57 rad to -1.53 rad.

6.1.3 Chapter 5 summary

- Electrophoretic light scattering measurements were performed to determine the zeta potential of carboxylate-modified polystyrene beads in water (Section 5.2). The obtained zeta potential (-2.38 ± 0.5 mV) was used to estimate the electrical conductivity of the particle (6.24 ± 0.05 mS/m) which could then be utilised in determining the polarisability of this suspension under the application of an AC signal.
- The two-dimensional trajectory of individual freely diffusing beads in H_2O on top of a glass slide was recorded on an inverted fluorescence microscope by using single particle tracking (Section 5.3). The x- and y-coordinates were used to calculate their time averaged mean squared displacement as a function of lag time for all available displacements. By applying linear fitting between these two variables, the optimum number of fitting points and trajectory length were statistically evaluated. Based on that, the mean diffusion coefficient of individual beads was measured from a trajectory including 1000 data points.
- A correction factor for the bulk viscosity of the solution (1.5) was calculated and applied to measure the effective viscosity of water surrounding individual beads when diffusing close to the glass slide's surface (Section 5.4).
- The distance between the bottom surface of an individual bead and the top surface of the glass wall (Section 5.5) was found equal to 700 ± 200 nm based on Faxen's and Brenner's approximations, for particle motion only parallel to the glass wall top surface.
- The polarisability of the beads-H_2O suspension under the application of an AC signal was analytically obtained (Section 5.6). The real part of the Clausius-Mossotti factor was analytically measured as a function to the applied frequency. This could predict the frequency ranges at which positive and negative dielectrophoresis would occur.
- Dielectrophoretic forces experienced by individual latex beads under trapping conditions were measured based on single particle tracking (Section 5.7). AC signals of sub-volt voltages and tens of kHz frequencies were applied to achieve pDEP. From the individual trajectories of trapped beads, their spatial coordinates were extracted for a range of time frames. By taking their time derivative, their

velocity was defined as a function of the distance from the nanotweezers tip. Since, the dielectrophoretic force was equal to the Stokes drag force at every time point, their velocity was used to measure the magnitude of the dielectrophoretic force. A data smoothing algorithm was developed to filter noise created from the time derivatives.

- The effect on the dielectrophoretic force magnitude by changing the electrical potential and frequency of the applied AC signal between the nanotweezers were investigated. A range of voltages (100 mV, 200 mV, 400 mV and 600 mV) and frequencies (10 kHz, 100 kHz, 250 kHz, 500 kHz, 750 kHz, 1 MHz and 20 MHz) were applied to assess such changes. This frequency range verified pDEP and nDEP at low and high values, respectively. Comparisons to simulated results from Section 4.4 concluded that the average nanotweezers used throughout these experiments had a carbon recession towards inside the tip opening and the separation distance between the two carbon nanoelectrodes was close to 55 nm.

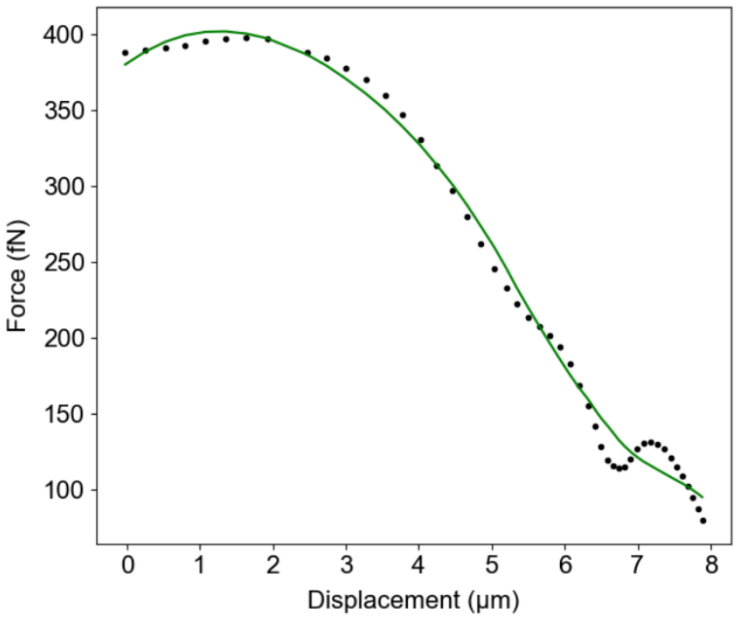

Figure 6.3 Measured dielectrophoretic force over the distance from the nanotweezers tip covered by a 2 μm latex bead when under trapping conditions $\left(V_{pk,rms} = 600\ mV, f_{app} = 10\ kHz\right)$. The black data points were extracted from its 2D trajectory while the green curve was obtained by applying a data smoothing algorithm.

6.1.4 Discussion of key findings

In Chapter 3, a new instrument based on an Arduino-PID controller was developed to deposit pyrolytic carbon inside quartz nanopipettes and turn them into dual-carbon nanoelectrodes. This technique achieved greater fabrication yield (~33%) compared to the most common configuration in literature (~10% {Takahashi et al., 2011}) because the heating cycle applied to the nanopipette tip was applied in a more controlled manner. Although, SEM imaging and cyclic voltammetry verified successful fabrication of disk-shaped carbon nanoelectrodes at the tip of dual-barrel nanopipettes, considerable deviations from this geometry occurred regularly. Besides the successfully fabricated ones, carbon nanoelectrodes were also found to form further inside the nanopipette pores (recessed carbon deposition) which led to an increase in their size and the gap separating them. FIB milling was performed on such carbon nanoelectrodes to modify their tip structure until reaching the desired geometry. However, this process is expensive, time consuming, and leads to an increase in the nanoelectrodes dimensions due to the removal of excess material. For the DEP force probing measurements on latex beads, only carbon nanoelectrodes with similar dimensions were kept.

Then, in Chapter 4, a finite element method (FEM) model was developed for the dielectrophoretic nanotweezers system. A simplified 3D geometry of a dual-barrel nanopipette filled with carbon and immersed into water was designed. After applying the boundary conditions ($\pm V_{pk}$ at the top electrode boundaries), a stationary solver provided the simulated electric potential and field distributions. Based on these, the electric field gradient, and hence the dielectrophoretic force experienced by a 2 μm latex bead, were simulated. For V_{pk} = 600 mV, the maximum F_{DEP} across the xz- and yz-planes was equal to 773 fN and 711 fN, respectively. However, changes in the dielectrophoretic force magnitude were found when the particle's initial position was located at a 45° angle between the xz- and yz-planes or when carbon recession occurred at the nanopipette tip.

The model used so far excluded glass wall domains and assumed them as ideal insulators. A revised model that included the glass walls was developed to estimate the impedance across the nanoelectrodes pair. It was found that the impedance amplitude decreased when transitioning from air to water and to a trapped bead at the tip, while the phase did not show a significant shift. Although the simulations provided results for specific scenarios, they provide a broader understanding of, firstly, how the electric field gradient is distributed around the nanopipette tip, secondly, what order of magnitude to expect for the dielectrophoretic force experienced by a trapped particle and how the impedance of the circuit is affected under different conditions. So far, such an extensive

FEM model for a DEP-based platform was not available in the current literature, so this work adds an additional tool in the DEP simulations field which could eventually be tuned to any possible configuration.

Finally, in Chapter 5, the fabricated nanopipette-based carbon nanoelectrodes were used as dielectrophoretic nanotweezers for trapping individual 2 μm polystyrene latex beads and quantifying the experienced force magnitude. Prior to the trapping measurements, the conductivity of the particles (6.24 ± 0.05 mS/m) was measured by electrophoretic light scattering. This value was then used to analytically find the $Re[f_{CM}(\omega)]$ for the beads-water system which was equal to 1.01 ± 0.01 MHz. Moreover, the mean diffusion coefficient of individual beads was defined via single particle tracking which was used to estimate a correction factor for the bulk viscosity of water and the mean distance between a freely diffusing bead and the top surface of the glass slide. By applying an AC signal to the nanoelectrodes where the voltage (V_{rms}) was between 100 and 600 mV and the frequency (f_{app}) between 10 and 750 kHz, pDEP led to entrapment of individual beads. Then, by monitoring their trajectories and applying a smoothing filter, the DEP force was quantified.

Results showed different force magnitudes between nanotweezers which could be due to either small variations in the electrodes' geometry or the particle's initial position, as discussed in Chapter 4. Maximum forces of ~500 fN were reported for 600 mV and 10 kHz with most results showing a decreasing non-linear force-voltage trend when lowering the voltage. In some cases, the measurement accuracy did not allow valid conclusions. Interestingly, when low frequencies (10 – 100 kHz) and high voltages (400 – 600 mV) were applied, the force-distance curves decreased after reaching peak values at ~3 μm away from the tip. This phenomenon in addition to cases where the beads would continuously rotate around the nanotweezers tip were an indication that electroosmotic effects occur and act against the attractive dielectrophoretic force. These findings could be a possible explanation for this decrease in the dielectrophoretic force when approaching the tip.

Furthermore, the DEP force decreased as the frequency became larger, approached minimum values at 1 MHz and became negative (repulsion) at 20 MHz. Non-linear weighted least squares fitting showed that in most cases the fit followed a similar trend to that of the real part of the Clausius-Mossotti factor. From the fitting curves, it was found that the gradient of the electric field magnitude squared was in the order of 10^{14} V^2/m^3. Overall, this type of dielectrophoretic nanotweezers verified the successful quantification of femtonewton forces on individual 2 μm latex beads, probing forces as low as tens of fN. From the currently developed platforms that were discussed in Chapter 2.2, there is no report of measuring such low forces. Although the measurement precision was not

significant in some cases, future improvements in the carbon nanoelectrodes design and configuration could improve it.

6.2 Future outlook

After validating the dielectrophoretic nanotweezers developed in this work as a tool for single-entity manipulation and force probing measurements, they could potentially find other applications. One example could be to expand their current use for studying more challenging and interesting biological molecules, such as DNA origamis or lipid vesicles. In addition, these nanotweezers could be implemented as single-molecule detectors though impedance-based measurements. Preliminary experimental data for these two suggested applications are briefly presented in the following sections.

6.2.1 Dielectrophoretic force probing on single lipid vesicles

Following the same setup as in Chapter 5, the nanotweezers were used to trap individual fluorescent giant unilamellar vesicles (GUVs). GUVs are a powerful model system for cell membrane with promising biomedical delivery platforms and applications in artificial cell technologies [177]. Individual trapping of GUVs has been reported in the past by optical tweezers [178]. However, GUVs follow the single-shell model because the dielectric properties of its core differ from the ones on its outer layer. This behaviour is similar to cells and their Clausius-Mossotti factor as a function of the applied frequency has a different trend from the one for homogeneous spherical particles (i.e., latex beads).

Dielectrophoretic tweezers could be used to distinguish lipid vesicles with different properties either in their core or on their layer by tuning the applied frequency [179]. Figure 6.4a shows the 2D trajectory of a trapped GUV at the nanotweezers tip under an applied AC signal of 600 mV and 10 MHz. Positive dielectrophoresis was observed at much higher frequencies for lipid vesicles compared to latex beads. The measured dielectrophoretic force experienced by the GUV reached a maximum value of approximately 120 fN at the nanotweezers tip (Figure 6.4b). This is a highly optimisable particle in terms of its dielectric properties, so multiple parametric studies could be performed to study its response under DEP fields generated by the nanotweezers. Besides this particular analyte, the dielectrophoretic nanotweezers could be combined with other single-molecule force probing techniques, such as the optical and magnetic tweezers, to study and probe small forces on more sophisticated systems.

An interesting case would be to stretch a DNA molecule with either optical or magnetic tweezers and use the dielectrophoretic nanotweezers to manipulate single proteins hybridised on the DNA molecule. Since the DEP nanotweezers have the capacity to

operate in the low force regime (tens of fN), the structure of proteins could be minimally affected by the external field and it is likely that valuable information about their dielectric properties to be obtained. Another potential application, but far more complicated, would be to repeat the study reported by Nadappuram et al. (2019) [10], insert the DEP nanotweezers inside living cells and probe the force experienced by fluorescently labelled molecules. The difficulty, however, lies to the highly sophisticated intracellular environment where unwanted binding or trapping would most likely occur at the nanopipette tip. Finally, the integration of the DEP nanotweezers with a spinning confocal microscope would allow 3D tracking of the fluorescently labelled molecule which would increase dramatically the precision of the dielectrophoretic force magnitude measurement.

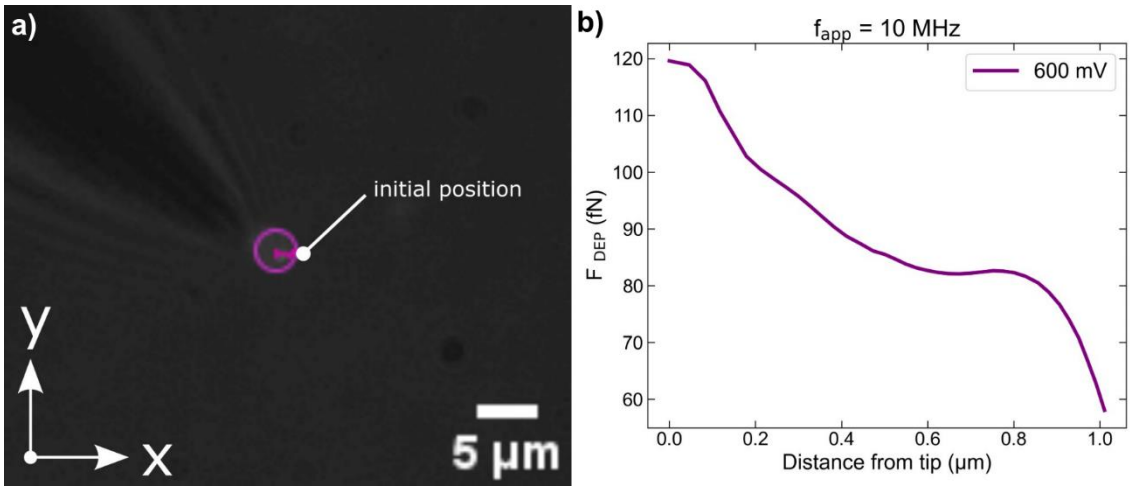

Figure 6.4 a) 2D (xy-plane) trajectory (pink curve) of a ~3 µm trapped GUV at the nanotweezers tip when 600 mV and 10 MHz were applied. The white spot represents its initial position before getting attracted towards the tip. b) Measured smoothed dielectrophoretic force (purple curve) as a function of the distance from the nanotweezers tip with a maximum value of 120 fN for 600 mV and 10 MHz.

6.2.2 Impedance-based detection with the DEP nanotweezers

Furthermore, the DEP nanotweezers could be potentially used also for single-particle label-free detection based on impedance spectroscopy techniques. The presence of a dielectric particle between the two nanoelectrodes at the tip is expected to distort the electric field gradients formed initially. By integrating a lock-in amplifier and probing the impedance of a component of this circuit, particle trapping should be accompanied by a change either in the impedance or phase of this component. Although successful single-particle detection was not achieved in early measurements, the nanotweezers were able to distinguish differences in the electrical permittivity of the solution they were immersed in. Figures 6.5a and 6.5b show how the impedance amplitude (R) and phase (θ)

changed, respectively, when the nanotweezers were switched between different solutions. In this system, a 470 Ω resistor, connected in series to one of the two carbon nanoelectrodes, was used to probe the impedance.

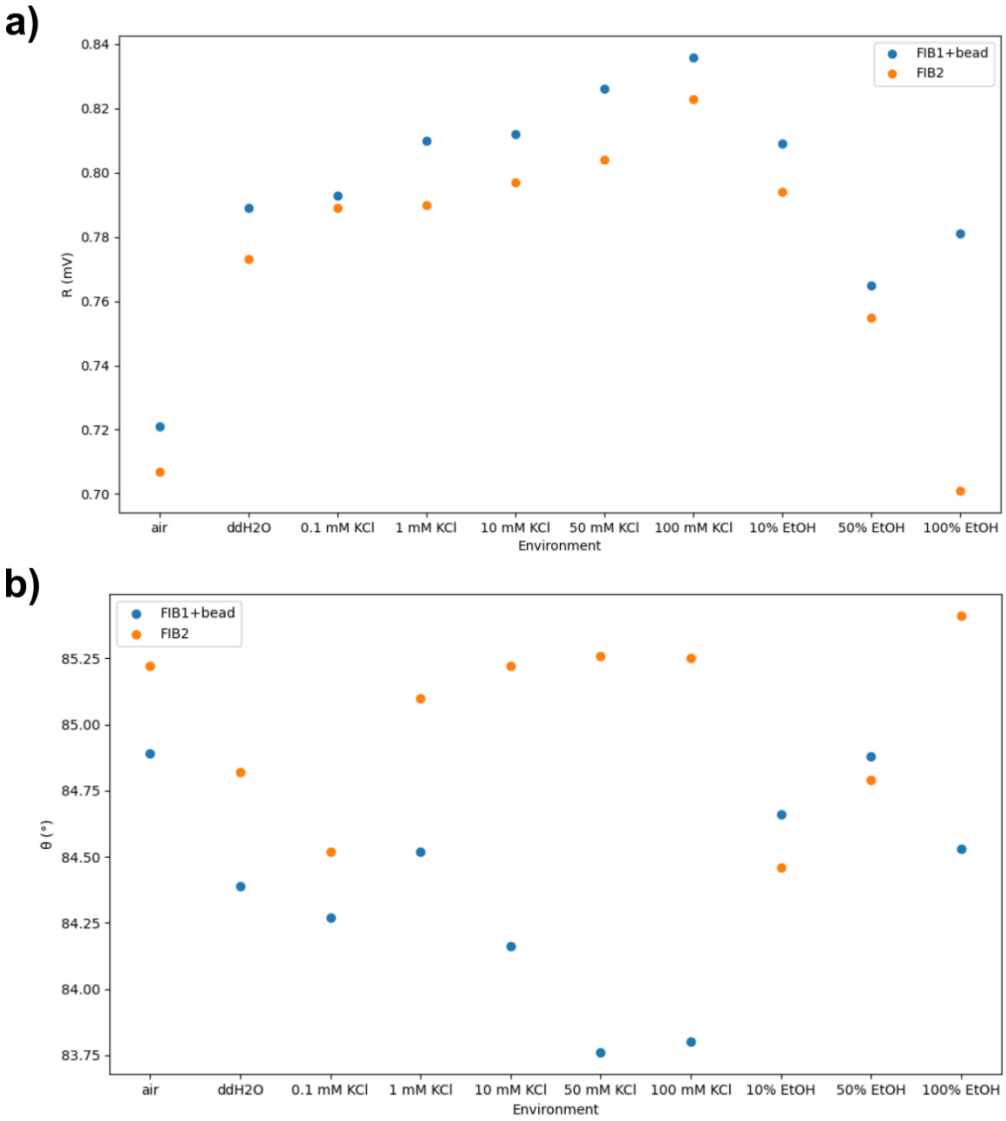

Figure 6.5 Measured impedance **a)** magnitude (R) and **b)** phase (θ) of a 470 Ω resistor connected in series to one of the two carbon nanoelectrodes after the application of a 600 mV and 100 kHz AC signal. The nanotweezers were immersed in different aqueous solutions for each measurement (solutions are labelled on the horizontal axis). Blue data points represent values obtained with a pair of FIB milled nanotweezers having a 2 μm latex attached to its tip surface. The orange ones represent data obtained from another FIB milled pair of nanotweezers without beads attached.

From Figure 6.5a, the impedance magnitude R increased when going from air to Milli-Q H_2O and also as the concentration of KCl became higher (from 10 to 100 mM). When switching to 10% ethanol, a small decrease was reported with lower values recorded as

the concentration of ethanol became larger (50% and 100%). There was no evident trend in the measurements regarding the probed phase (Figure 6.5b). It is worth noting blue and orange data points represent measurements with two different FIB milled nanotweezers. One of them (blue), after imaging under the fluorescence microscope, was found to have a latex bead permanently attached to its tip surface. The presence of the bead could be the reason why the blue data points have a fixed difference with the orange ones. These findings could be an early indication that the nanotweezers are capable of single-molecule detection but more advanced equipment needs to be introduced to the current setup to achieve this. Nevertheless, it is a very interesting application as the system could then be used for label-free single-molecule manipulation and force probing.

Finally, the DEP nanotweezers could be used to detect changes in the impedance between the cytoplasm and a cell's membrane. Recently, Hughes (2023) [180] reported that the model followed so far for the dielectrophoretic analysis of the electrical properties of a cell was giving a higher value than that acquired by patch clamp techniques. In this study, the author introduces the "electrome model" to describe the cell's electrical characteristics and suggests that the cell membrane acts as a capacitor with a membrane potential (V_m). This potential can be monitored by changes to the zeta potential or the conductivity of the cytoplasm and the medium. By placing the DEP nanotweezers close or at the membrane of a cell, the total impedance of the system could be monitored to quantify this membrane potential. In addition, variations in the Clausius-Mossotti factor response of the system could also be detected by the DEP nanotweezers.

References

[1] H. Miller, Z. Zhou, J. Shepherd, A. J. M. Wollman, and M. C. Leake, 'Single-molecule techniques in biophysics: a review of the progress in methods and applications', *Rep. Prog. Phys.*, vol. 81, no. 2, p. 024601, Dec. 2017, doi: 10.1088/1361-6633/aa8a02.

[2] K. C. Neuman and A. Nagy, 'Single-molecule force spectroscopy: optical tweezers, magnetic tweezers and atomic force microscopy', *Nat Methods*, vol. 5, no. 6, Art. no. 6, Jun. 2008, doi: 10.1038/nmeth.1218.

[3] S. S. Mandal, 'Force Spectroscopy on Single Molecules of Life', *ACS Omega*, vol. 5, no. 20, pp. 11271–11278, 2020, doi: 10.1021/acsomega.0c00814.

[4] K. Norregaard, R. Metzler, C. M. Ritter, K. Berg-Sørensen, and L. B. Oddershede, 'Manipulation and Motion of Organelles and Single Molecules in Living Cells', *Chem. Rev.*, vol. 117, no. 5, pp. 4342–4375, Mar. 2017, doi: 10.1021/acs.chemrev.6b00638.

[5] A. Ozcelik *et al.*, 'Acoustic tweezers for the life sciences', *Nat Methods*, vol. 15, no. 12, Art. no. 12, Dec. 2018, doi: 10.1038/s41592-018-0222-9.

[6] D. Kim, M. Sonker, and A. Ros, 'Dielectrophoresis: From Molecular to Micrometer-Scale Analytes', *Anal. Chem.*, vol. 91, no. 1, pp. 277–295, Jan. 2019, doi: 10.1021/acs.analchem.8b05454.

[7] P. Modarres and M. Tabrizian, 'Alternating current dielectrophoresis of biomacromolecules: The interplay of electrokinetic effects', *Sensors and Actuators B: Chemical*, vol. 252, pp. 391–408, Nov. 2017, doi: 10.1016/j.snb.2017.05.144.

[8] R.-J. Yu, Y.-L. Ying, R. Gao, and Y.-T. Long, 'Confined Nanopipette Sensing: From Single Molecules, Single Nanoparticles, to Single Cells', *Angewandte Chemie International Edition*, vol. 58, no. 12, pp. 3706–3714, 2019, doi: 10.1002/anie.201803229.

[9] C. A. Morris, A. K. Friedman, and L. A. Baker, 'Applications of nanopipettes in the analytical sciences', *Analyst*, vol. 135, no. 9, pp. 2190–2202, Aug. 2010, doi: 10.1039/C0AN00156B.

[10] B. P. Nadappuram *et al.*, 'Nanoscale tweezers for single-cell biopsies', *Nature Nanotechnology*, vol. 14, no. 1, pp. 80–88, 2019, doi: 10.1038/s41565-018-0315-8.

[11] F. Marcuccio *et al.*, 'Mechanistic Study of the Conductance and Enhanced Single-Molecule Detection in a Polymer–Electrolyte Nanopore', *ACS Nanosci. Au*, vol. 3, no. 2, pp. 172–181, Apr. 2023, doi: 10.1021/acsnanoscienceau.2c00050.

[12] C. J. Bustamante, Y. R. Chemla, S. Liu, and M. D. Wang, 'Optical tweezers in single-molecule biophysics', *Nat Rev Methods Primers*, vol. 1, no. 1, Art. no. 1, Mar. 2021, doi: 10.1038/s43586-021-00021-6.

[13] A. Ashkin, 'Acceleration and Trapping of Particles by Radiation Pressure', *Phys. Rev. Lett.*, vol. 24, no. 4, pp. 156–159, Jan. 1970, doi: 10.1103/PhysRevLett.24.156.

[14] A. Ashkin, J. M. Dziedzic, J. E. Bjorkholm, and S. Chu, 'Observation of a single-beam gradient force optical trap for dielectric particles', *Opt. Lett., OL*, vol. 11, no. 5, pp. 288–290, May 1986, doi: 10.1364/OL.11.000288.

[15] A. Ashkin, J. M. Dziedzic, and T. Yamane, ‘Optical trapping and manipulation of single cells using infrared laser beams’, *Nature*, vol. 330, no. 6150, Art. no. 6150, Dec. 1987, doi: 10.1038/330769a0.
[16] K. Svoboda, C. F. Schmidt, B. J. Schnapp, and S. M. Block, ‘Direct observation of kinesin stepping by optical trapping interferometry’, *Nature*, vol. 365, no. 6448, Art. no. 6448, Oct. 1993, doi: 10.1038/365721a0.
[17] C. L. Asbury, A. N. Fehr, and S. M. Block, ‘Kinesin Moves by an Asymmetric Hand-Over-Hand Mechanism’, *Science*, vol. 302, no. 5653, pp. 2130–2134, Dec. 2003, doi: 10.1126/science.1092985.
[18] A. Ramaiya, B. Roy, M. Bugiel, and E. Schäffer, ‘Kinesin rotates unidirectionally and generates torque while walking on microtubules’, *Proceedings of the National Academy of Sciences*, vol. 114, no. 41, pp. 10894–10899, Oct. 2017, doi: 10.1073/pnas.1706985114.
[19] I. Heller, T. P. Hoekstra, G. A. King, E. J. G. Peterman, and G. J. L. Wuite, ‘Optical Tweezers Analysis of DNA–Protein Complexes’, *Chem. Rev.*, vol. 114, no. 6, pp. 3087–3119, Mar. 2014, doi: 10.1021/cr4003006.
[20] S. Mohapatra, C.-T. Lin, X. A. Feng, A. Basu, and T. Ha, ‘Single-Molecule Analysis and Engineering of DNA Motors’, *Chem. Rev.*, vol. 120, no. 1, pp. 36–78, Jan. 2020, doi: 10.1021/acs.chemrev.9b00361.
[21] S. B. Smith, Y. Cui, and C. Bustamante, ‘Overstretching B-DNA: The Elastic Response of Individual Double-Stranded and Single-Stranded DNA Molecules’, *Science*, vol. 271, no. 5250, pp. 795–799, Feb. 1996, doi: 10.1126/science.271.5250.795.
[22] P. Gross, N. Laurens, L. B. Oddershede, U. Bockelmann, E. J. G. Peterman, and G. J. L. Wuite, ‘Quantifying how DNA stretches, melts and changes twist under tension’, *Nature Phys*, vol. 7, no. 9, Art. no. 9, Sep. 2011, doi: 10.1038/nphys2002.
[23] G. A. King, F. Burla, E. J. G. Peterman, and G. J. L. Wuite, ‘Supercoiling DNA optically’, *Proceedings of the National Academy of Sciences*, vol. 116, no. 52, pp. 26534–26539, Dec. 2019, doi: 10.1073/pnas.1908826116.
[24] J. W. Shaevitz, E. A. Abbondanzieri, R. Landick, and S. M. Block, ‘Backtracking by single RNA polymerase molecules observed at near-base-pair resolution’, *Nature*, vol. 426, no. 6967, Art. no. 6967, Dec. 2003, doi: 10.1038/nature02191.
[25] C. Hodges, L. Bintu, L. Lubkowska, M. Kashlev, and C. Bustamante, ‘Nucleosomal Fluctuations Govern the Transcription Dynamics of RNA Polymerase II’, *Science*, vol. 325, no. 5940, pp. 626–628, Jul. 2009, doi: 10.1126/science.1172926.
[26] F. M. Fazal, C. A. Meng, K. Murakami, R. D. Kornberg, and S. M. Block, ‘Real-time observation of the initiation of RNA polymerase II transcription’, *Nature*, vol. 525, no. 7568, Art. no. 7568, Sep. 2015, doi: 10.1038/nature14882.
[27] B. J. Roxworthy *et al.*, ‘Application of Plasmonic Bowtie Nanoantenna Arrays for Optical Trapping, Stacking, and Sorting’, *Nano Lett.*, vol. 12, no. 2, pp. 796–801, Feb. 2012, doi: 10.1021/nl203811q.
[28] Y. Pang and R. Gordon, ‘Optical Trapping of a Single Protein’, *Nano Lett.*, vol. 12, no. 1, pp. 402–406, Jan. 2012, doi: 10.1021/nl203719v.
[29] L. Lin *et al.*, ‘Opto-thermoelectric nanotweezers’, *Nature Photonics*, vol. 12, no. 4, pp. 195–201, 2018, doi: 10.1038/s41566-018-0134-3.
[30] B. H. Blehm, T. A. Schroer, K. M. Trybus, Y. R. Chemla, and P. R. Selvin, ‘In vivo optical trapping indicates kinesin’s stall force is reduced by dynein during

intracellular transport', *Proceedings of the National Academy of Sciences*, vol. 110, no. 9, pp. 3381–3386, Feb. 2013, doi: 10.1073/pnas.1219961110.
[31] D. H. Goldman, C. M. Kaiser, A. Milin, M. Righini, I. Tinoco, and C. Bustamante, 'Mechanical force releases nascent chain–mediated ribosome arrest in vitro and in vivo', *Science*, vol. 348, no. 6233, pp. 457–460, Apr. 2015, doi: 10.1126/science.1261909.
[32] I. De Vlaminck and C. Dekker, 'Recent Advances in Magnetic Tweezers', *Annual Review of Biophysics*, vol. 41, no. 1, pp. 453–472, 2012, doi: 10.1146/annurev-biophys-122311-100544.
[33] F. H. C. Crick and A. F. W. Hughes, 'The physical properties of cytoplasm: A study by means of the magnetic particle method Part I. Experimental', *Experimental Cell Research*, vol. 1, no. 1, pp. 37–80, Jan. 1950, doi: 10.1016/0014-4827(50)90048-6.
[34] S. B. Smith, L. Finzi, and C. Bustamante, 'Direct Mechanical Measurements of the Elasticity of Single DNA Molecules by Using Magnetic Beads', *Science*, vol. 258, no. 5085, pp. 1122–1126, Nov. 1992, doi: 10.1126/science.1439819.
[35] T. R. Strick, J.-F. Allemand, D. Bensimon, A. Bensimon, and V. Croquette, 'The Elasticity of a Single Supercoiled DNA Molecule', *Science*, vol. 271, no. 5257, pp. 1835–1837, Mar. 1996, doi: 10.1126/science.271.5257.1835.
[36] Y. Harada, O. Ohara, A. Takatsuki, H. Itoh, N. Shimamoto, and K. Kinosita, 'Direct observation of DNA rotation during transcription by Escherichia coli RNA polymerase', *Nature*, vol. 409, no. 6816, Art. no. 6816, Jan. 2001, doi: 10.1038/35051126.
[37] J. Gore, Z. Bryant, M. Nöllmann, M. U. Le, N. R. Cozzarelli, and C. Bustamante, 'DNA overwinds when stretched', *Nature*, vol. 442, no. 7104, Art. no. 7104, Aug. 2006, doi: 10.1038/nature04974.
[38] J. Lipfert, J. W. J. Kerssemakers, T. Jager, and N. H. Dekker, 'Magnetic torque tweezers: measuring torsional stiffness in DNA and RecA-DNA filaments', *Nat Methods*, vol. 7, no. 12, Art. no. 12, Dec. 2010, doi: 10.1038/nmeth.1520.
[39] M. T. J. van Loenhout, M. V. de Grunt, and C. Dekker, 'Dynamics of DNA Supercoils', *Science*, vol. 338, no. 6103, pp. 94–97, Oct. 2012, doi: 10.1126/science.1225810.
[40] E. Ostrofet, F. S. Papini, and D. Dulin, 'Correction-free force calibration for magnetic tweezers experiments', *Sci Rep*, vol. 8, no. 1, Art. no. 1, Oct. 2018, doi: 10.1038/s41598-018-34360-4.
[41] M. T. J. van Loenhout *et al.*, 'Scanning a DNA Molecule for Bound Proteins Using Hybrid Magnetic and Optical Tweezers', *PLOS ONE*, vol. 8, no. 6, p. e65329, Jun. 2013, doi: 10.1371/journal.pone.0065329.
[42] Z. Zhou, H. Miller, A. J. M. Wollman, and M. C. Leake, 'Developing a New Biophysical Tool to Combine Magneto-Optical Tweezers with Super-Resolution Fluorescence Microscopy', *Photonics*, vol. 2, no. 3, Art. no. 3, Sep. 2015, doi: 10.3390/photonics2030758.
[43] C. Gosse and V. Croquette, 'Magnetic Tweezers: Micromanipulation and Force Measurement at the Molecular Level', *Biophysical Journal*, vol. 82, no. 6, pp. 3314–3329, Jun. 2002, doi: 10.1016/S0006-3495(02)75672-5.
[44] C.-H. Chiou, Y.-Y. Huang, M.-H. Chiang, H.-H. Lee, and G.-B. Lee, 'New magnetic tweezers for investigation of the mechanical properties of single DNA molecules', *Nanotechnology*, vol. 17, no. 5, p. 1217, Feb. 2006, doi: 10.1088/0957-4484/17/5/009.

[45] S. Schuerle, S. Erni, M. Flink, B. E. Kratochvil, and B. J. Nelson, ‘Three-Dimensional Magnetic Manipulation of Micro- and Nanostructures for Applications in Life Sciences’, *IEEE Transactions on Magnetics*, vol. 49, no. 1, pp. 321–330, Jan. 2013, doi: 10.1109/TMAG.2012.2224693.
[46] L. M. González, W. C. Ruder, P. R. Leduc, and W. C. Messner, ‘Controlling Magnetotactic Bacteria through an Integrated Nanofabricated Metallic Island and Optical Microscope Approach’, *Sci Rep*, vol. 4, no. 1, Art. no. 1, Feb. 2014, doi: 10.1038/srep04104.
[47] M. Krieg *et al.*, ‘Atomic force microscopy-based mechanobiology’, *Nat Rev Phys*, vol. 1, no. 1, Art. no. 1, Jan. 2019, doi: 10.1038/s42254-018-0001-7.
[48] M. L. Hughes and L. Dougan, ‘The physics of pulling polyproteins: a review of single molecule force spectroscopy using the AFM to study protein unfolding’, *Rep. Prog. Phys.*, vol. 79, no. 7, p. 076601, Jun. 2016, doi: 10.1088/0034-4885/79/7/076601.
[49] M. Rief, F. Oesterhelt, B. Heymann, and H. E. Gaub, ‘Single Molecule Force Spectroscopy on Polysaccharides by Atomic Force Microscopy’, *Science*, vol. 275, no. 5304, pp. 1295–1297, Feb. 1997, doi: 10.1126/science.275.5304.1295.
[50] B. T. Marshall, M. Long, J. W. Piper, T. Yago, R. P. McEver, and C. Zhu, ‘Direct observation of catch bonds involving cell-adhesion molecules’, *Nature*, vol. 423, no. 6936, Art. no. 6936, May 2003, doi: 10.1038/nature01605.
[51] J. M. Fernandez and H. Li, ‘Force-Clamp Spectroscopy Monitors the Folding Trajectory of a Single Protein’, *Science*, vol. 303, no. 5664, pp. 1674–1678, Mar. 2004, doi: 10.1126/science.1092497.
[52] M. Dong, S. Husale, and O. Sahin, ‘Determination of protein structural flexibility by microsecond force spectroscopy’, *Nature Nanotech*, vol. 4, no. 8, Art. no. 8, Aug. 2009, doi: 10.1038/nnano.2009.156.
[53] F. Rico, C. Su, and S. Scheuring, ‘Mechanical Mapping of Single Membrane Proteins at Submolecular Resolution’, *Nano Lett.*, vol. 11, no. 9, pp. 3983–3986, Sep. 2011, doi: 10.1021/nl202351t.
[54] D. Martinez-Martin, E. T. Herruzo, C. Dietz, J. Gomez-Herrero, and R. Garcia, ‘Noninvasive Protein Structural Flexibility Mapping by Bimodal Dynamic Force Microscopy’, *Phys. Rev. Lett.*, vol. 106, no. 19, p. 198101, May 2011, doi: 10.1103/PhysRevLett.106.198101.
[55] P. J. de Pablo, I. A. T. Schaap, F. C. MacKintosh, and C. F. Schmidt, ‘Deformation and Collapse of Microtubules on the Nanometer Scale’, *Phys. Rev. Lett.*, vol. 91, no. 9, p. 098101, Aug. 2003, doi: 10.1103/PhysRevLett.91.098101.
[56] R. P. Goodman *et al.*, ‘Rapid Chiral Assembly of Rigid DNA Building Blocks for Molecular Nanofabrication’, *Science*, vol. 310, no. 5754, pp. 1661–1665, Dec. 2005, doi: 10.1126/science.1120367.
[57] D. Vorselen, M. Marchetti, C. López-Iglesias, P. J. Peters, W. H. Roos, and G. J. L. Wuite, ‘Multilamellar nanovesicles show distinct mechanical properties depending on their degree of lamellarity’, *Nanoscale*, vol. 10, no. 11, pp. 5318–5324, 2018, doi: 10.1039/C7NR09224E.
[58] F. Guo *et al.*, ‘Three-dimensional manipulation of single cells using surface acoustic waves’, *Proceedings of the National Academy of Sciences*, vol. 113, no. 6, pp. 1522–1527, Feb. 2016, doi: 10.1073/pnas.1524813113.
[59] D. Baresch, J.-L. Thomas, and R. Marchiano, ‘Observation of a Single-Beam Gradient Force Acoustical Trap for Elastic Particles: Acoustical Tweezers’, *Phys. Rev. Lett.*, vol. 116, no. 2, p. 024301, Jan. 2016, doi: 10.1103/PhysRevLett.116.024301.

[60] X. Chen *et al.*, ‘An adjustable multi-scale single beam acoustic tweezers based on ultrahigh frequency ultrasonic transducer’, *Biotechnology and Bioengineering*, vol. 114, no. 11, pp. 2637–2647, 2017, doi: 10.1002/bit.26365.
[61] J. Y. Hwang *et al.*, ‘Acoustic tweezers for studying intracellular calcium signaling in SKBR-3 human breast cancer cells’, *Ultrasonics*, vol. 63, pp. 94–101, Dec. 2015, doi: 10.1016/j.ultras.2015.06.017.
[62] G. Sitters, D. Kamsma, G. Thalhammer, M. Ritsch-Marte, E. J. G. Peterman, and G. J. L. Wuite, ‘Acoustic force spectroscopy’, *Nat Methods*, vol. 12, no. 1, Art. no. 1, Jan. 2015, doi: 10.1038/nmeth.3183.
[63] D. Kamsma, R. Creyghton, G. Sitters, G. J. L. Wuite, and E. J. G. Peterman, ‘Tuning the Music: Acoustic Force Spectroscopy (AFS) 2.0’, *Methods*, vol. 105, pp. 26–33, Aug. 2016, doi: 10.1016/j.ymeth.2016.05.002.
[64] A. Marzo and B. W. Drinkwater, ‘Holographic acoustic tweezers’, *Proceedings of the National Academy of Sciences*, vol. 116, no. 1, pp. 84–89, Jan. 2019, doi: 10.1073/pnas.1813047115.
[65] V. Bogatyr, A. S. Biebricher, G. Bergamaschi, E. J. G. Peterman, and G. J. L. Wuite, ‘Quantitative Acoustophoresis’, *ACS Nanosci. Au*, vol. 2, no. 4, pp. 341–354, Aug. 2022, doi: 10.1021/acsnanoscienceau.2c00002.
[66] R. Hölzel, N. Calander, Z. Chiragwandi, M. Willander, and F. F. Bier, ‘Trapping Single Molecules by Dielectrophoresis’, *Phys. Rev. Lett.*, vol. 95, no. 12, p. 128102, Sep. 2005, doi: 10.1103/PhysRevLett.95.128102.
[67] A. E. Cohen and W. E. Moerner, ‘Suppressing Brownian motion of individual biomolecules in solution’, *Proceedings of the National Academy of Sciences*, vol. 103, no. 12, pp. 4362–4365, Mar. 2006, doi: 10.1073/pnas.0509976103.
[68] G. Giraud *et al.*, ‘Dielectrophoretic manipulation of ribosomal RNA’, *Biomicrofluidics*, vol. 5, no. 2, p. 024116, Jun. 2011, doi: 10.1063/1.3604395.
[69] A. Barik, X. Chen, and S.-H. Oh, ‘Ultralow-Power Electronic Trapping of Nanoparticles with Sub-10 nm Gold Nanogap Electrodes’, *Nano Lett.*, vol. 16, no. 10, pp. 6317–6324, Oct. 2016, doi: 10.1021/acs.nanolett.6b02690.
[70] A. Barik *et al.*, ‘Graphene-edge dielectrophoretic tweezers for trapping of biomolecules’, *Nature Communications*, vol. 8, no. 1, 2017, doi: 10.1038/s41467-017-01635-9.
[71] L. Xue, H. Yamazaki, R. Ren, M. Wanunu, A. P. Ivanov, and J. B. Edel, ‘Solid-state nanopore sensors’, *Nat Rev Mater*, vol. 5, no. 12, Art. no. 12, Dec. 2020, doi: 10.1038/s41578-020-0229-6.
[72] P. Cadinu *et al.*, ‘Double Barrel Nanopores as a New Tool for Controlling Single-Molecule Transport’, *Nano Lett.*, vol. 18, no. 4, pp. 2738–2745, Apr. 2018, doi: 10.1021/acs.nanolett.8b00860.
[73] K. J. Freedman, L. M. Otto, A. P. Ivanov, A. Barik, S. H. Oh, and J. B. Edel, ‘Nanopore sensing at ultra-low concentrations using single-molecule dielectrophoretic trapping’, *Nature Communications*, vol. 7, 2016, doi: 10.1038/ncomms10217.
[74] K. J. Freedman *et al.*, ‘On-Demand Surface- and Tip-Enhanced Raman Spectroscopy Using Dielectrophoretic Trapping and Nanopore Sensing’, *ACS Photonics*, vol. 3, no. 6, pp. 1036–1044, Jun. 2016, doi: 10.1021/acsphotonics.6b00119.
[75] L. Tang *et al.*, ‘Combined quantum tunnelling and dielectrophoretic trapping for molecular analysis at ultra-low analyte concentrations’, *Nat Commun*, vol. 12, no. 1, Art. no. 1, Feb. 2021, doi: 10.1038/s41467-021-21101-x.

[76] S. Schmid, P. Stömmer, H. Dietz, and C. Dekker, ‘Nanopore electro-osmotic trap for the label-free study of single proteins and their conformations’, *Nat. Nanotechnol.*, vol. 16, no. 11, Art. no. 11, Nov. 2021, doi: 10.1038/s41565-021-00958-5.
[77] M. Krishnan, N. Mojarad, P. Kukura, and V. Sandoghdar, ‘Geometry-induced electrostatic trapping of nanometric objects in a fluid’, *Nature*, vol. 467, no. 7316, Art. no. 7316, Oct. 2010, doi: 10.1038/nature09404.
[78] F. Ruggeri *et al.*, ‘Single-molecule electrometry’, *Nature Nanotech*, vol. 12, no. 5, Art. no. 5, May 2017, doi: 10.1038/nnano.2017.26.
[79] L. von Diezmann, Y. Shechtman, and W. E. Moerner, ‘Three-Dimensional Localization of Single Molecules for Super-Resolution Imaging and Single-Particle Tracking’, *Chem. Rev.*, vol. 117, no. 11, pp. 7244–7275, Jun. 2017, doi: 10.1021/acs.chemrev.6b00629.
[80] H. Qian, M. P. Sheetz, and E. L. Elson, ‘Single particle tracking. Analysis of diffusion and flow in two-dimensional systems’, *Biophysical Journal*, vol. 60, no. 4, pp. 910–921, Oct. 1991, doi: 10.1016/S0006-3495(91)82125-7.
[81] W. E. Moerner and D. P. Fromm, ‘Methods of single-molecule fluorescence spectroscopy and microscopy’, *Review of Scientific Instruments*, vol. 74, no. 8, pp. 3597–3619, Aug. 2003, doi: 10.1063/1.1589587.
[82] J. Chao, S. Ram, E. S. Ward, and R. J. Ober, ‘Ultrahigh accuracy imaging modality for super-localization microscopy’, *Nat Methods*, vol. 10, no. 4, Art. no. 4, Apr. 2013, doi: 10.1038/nmeth.2396.
[83] J.-Y. Tinevez *et al.*, ‘TrackMate: An open and extensible platform for single-particle tracking’, *Methods*, vol. 115, pp. 80–90, Feb. 2017, doi: 10.1016/j.ymeth.2016.09.016.
[84] T. C. Rösch, L. M. Oviedo-Bocanegra, G. Fritz, and P. L. Graumann, ‘SMTracker: a tool for quantitative analysis, exploration and visualization of single-molecule tracking data reveals highly dynamic binding of B. subtilis global repressor AbrB throughout the genome’, *Scientific Reports*, vol. 8, no. 1, p. 15747, Oct. 2018, doi: 10.1038/s41598-018-33842-9.
[85] N. Granik *et al.*, ‘Single-Particle Diffusion Characterization by Deep Learning’, *Biophysical Journal*, vol. 117, no. 2, pp. 185–192, Jul. 2019, doi: 10.1016/j.bpj.2019.06.015.
[86] S. Hou, J. Exell, and K. Welsher, ‘Real-time 3D single molecule tracking’, *Nat Commun*, vol. 11, no. 1, Art. no. 1, Jul. 2020, doi: 10.1038/s41467-020-17444-6.
[87] T. Kuhn, J. Hettich, R. Davtyan, and J. C. M. Gebhardt, ‘Single molecule tracking and analysis framework including theory-predicted parameter settings’, *Scientific Reports*, vol. 11, no. 1, p. 9465, May 2021, doi: 10.1038/s41598-021-88802-7.
[88] H. A. Pohl, ‘The Motion and Precipitation of Suspensoids in Divergent Electric Fields’, *Journal of Applied Physics*, vol. 22, no. 7, pp. 869–871, Jul. 1951, doi: 10.1063/1.1700065.
[89] H. A. Pohl and I. Hawk, ‘Separation of Living and Dead Cells by Dielectrophoresis’, *Science*, vol. 152, no. 3722, pp. 647–649, Apr. 1966, doi: 10.1126/science.152.3722.647.b.
[90] H. A. Pohl and J. S. Crane, ‘Dielectrophoresis of Cells’, *Biophysical Journal*, vol. 11, no. 9, pp. 711–727, Sep. 1971, doi: 10.1016/S0006-3495(71)86249-5.
[91] R. Pethig, ‘Review Article—Dielectrophoresis: Status of the theory, technology, and applications’, *Biomicrofluidics*, vol. 4, no. 2, p. 022811, Jun. 2010, doi: 10.1063/1.3456626.

[92] S. Dash and S. Mohanty, ‘Dielectrophoretic separation of micron and submicron particles: A review’, *ELECTROPHORESIS*, vol. 35, no. 18, pp. 2656–2672, 2014, doi: 10.1002/elps.201400084.
[93] B. M. Kim, T. Murray, and H. H. Bau, ‘The fabrication of integrated carbon pipes with sub-micron diameters’, *Nanotechnology*, vol. 16, no. 8, pp. 1317–1320, Jun. 2005, doi: 10.1088/0957-4484/16/8/056.
[94] Y.-T. Li *et al.*, ‘Nanoelectrode for Amperometric Monitoring of Individual Vesicular Exocytosis Inside Single Synapses’, *Angewandte Chemie International Edition*, vol. 53, no. 46, pp. 12456–12460, 2014, doi: 10.1002/anie.201404744.
[95] H. Morgan and N. G. Green, *AC Electrokinetics: Colloids and Nanoparticles*. Research Studies Press, 2003.
[96] R. Pethig, ‘The Clausius–Mossotti Factor’, in *Dielectrophoresis*, John Wiley & Sons, Ltd, 2017, pp. 119–144. doi: 10.1002/9781118671443.ch6.
[97] E. A. Kwizera, M. Sun, A. M. White, J. Li, and X. He, ‘Methods of Generating Dielectrophoretic Force for Microfluidic Manipulation of Bioparticles’, *ACS Biomater. Sci. Eng.*, vol. 7, no. 6, pp. 2043–2063, Jun. 2021, doi: 10.1021/acsbiomaterials.1c00083.
[98] Z. R. Gagnon, ‘Cellular dielectrophoresis: Applications to the characterization, manipulation, separation and patterning of cells’, *ELECTROPHORESIS*, vol. 32, no. 18, pp. 2466–2487, 2011, doi: 10.1002/elps.201100060.
[99] H. Morgan and N. G. Green, ‘Dielectrophoretic manipulation of rod-shaped viral particles’, *Journal of Electrostatics*, vol. 42, no. 3, pp. 279–293, Dec. 1997, doi: 10.1016/S0304-3886(97)00159-9.
[100] A. Kuzyk, ‘Dielectrophoresis at the nanoscale’, *ELECTROPHORESIS*, vol. 32, no. 17, pp. 2307–2313, 2011, doi: 10.1002/elps.201100038.
[101] A. Nakano and A. Ros, ‘Protein dielectrophoresis: Advances, challenges, and applications’, *ELECTROPHORESIS*, vol. 34, no. 7, pp. 1085–1096, 2013, doi: 10.1002/elps.201200482.
[102] S. S. Seyedi and D. V. Matyushov, ‘Protein Dielectrophoresis in Solution’, *J. Phys. Chem. B*, vol. 122, no. 39, pp. 9119–9127, Oct. 2018, doi: 10.1021/acs.jpcb.8b06864.
[103] R. Pethig, ‘Limitations of the Clausius-Mossotti function used in dielectrophoresis and electrical impedance studies of biomacromolecules’, *ELECTROPHORESIS*, vol. 40, no. 18–19, pp. 2575–2583, 2019, doi: 10.1002/elps.201900057.
[104] A. Ramos, H. Morgan, N. G. Green, and A. Castellanos, ‘The role of electrohydrodynamic forces in the dielectrophoretic manipulation and separation of particles’, *Journal of Electrostatics*, vol. 47, no. 1–2, pp. 71–81, 1999, doi: 10.1016/S0304-3886(99)00031-5.
[105] B. G. Hawkins and B. J. Kirby, ‘Electrothermal flow effects in insulating (electrodeless) dielectrophoresis systems’, *ELECTROPHORESIS*, vol. 31, no. 22, pp. 3622–3633, 2010, doi: 10.1002/elps.201000429.
[106] S. Sridharan, J. Zhu, G. Hu, and X. Xuan, ‘Joule heating effects on electroosmotic flow in insulator-based dielectrophoresis’, *ELECTROPHORESIS*, vol. 32, no. 17, pp. 2274–2281, 2011, doi: 10.1002/elps.201100011.
[107] A. Kale, S. Patel, G. Hu, and X. Xuan, ‘Numerical modeling of Joule heating effects in insulator-based dielectrophoresis microdevices’, *ELECTROPHORESIS*, vol. 34, no. 5, pp. 674–683, 2013, doi: 10.1002/elps.201200501.
[108] R. Pethig, ‘Review—Where Is Dielectrophoresis (DEP) Going?’, *J. Electrochem. Soc.*, vol. 164, no. 5, p. B3049, Dec. 2016, doi: 10.1149/2.0071705jes.

[109] Z. Zou, S. Lee, and C. H. Ahn, ‘A Polymer Microfluidic Chip With Interdigitated Electrodes Arrays for Simultaneous Dielectrophoretic Manipulation and Impedimetric Detection of Microparticles’, *IEEE Sensors Journal*, vol. 8, no. 5, pp. 527–535, May 2008, doi: 10.1109/JSEN.2008.918907.
[110] N. Mureau, E. Mendoza, S. R. P. Silva, K. F. Hoettges, and M. P. Hughes, ‘In situ and real time determination of metallic and semiconducting single-walled carbon nanotubes in suspension via dielectrophoresis’, *Applied Physics Letters*, vol. 88, no. 24, p. 243109, Jun. 2006, doi: 10.1063/1.2207501.
[111] R. Hamada, H. Takayama, Y. Shonishi, L. Mao, M. Nakano, and J. Suehiro, ‘A rapid bacteria detection technique utilizing impedance measurement combined with positive and negative dielectrophoresis’, *Sensors and Actuators B: Chemical*, vol. 181, pp. 439–445, May 2013, doi: 10.1016/j.snb.2013.02.030.
[112] A. Koklu, A. C. Sabuncu, and A. Beskok, ‘Enhancement of dielectrophoresis using fractal gold nanostructured electrodes’, *ELECTROPHORESIS*, vol. 38, no. 11, pp. 1458–1465, 2017, doi: 10.1002/elps.201600456.
[113] G. Bhatt, K. Mishra, G. Ramanathan, and S. Bhattacharya, ‘Dielectrophoresis assisted impedance spectroscopy for detection of gold-conjugated amplified DNA samples’, *Sensors and Actuators B: Chemical*, vol. 288, pp. 442–453, Jun. 2019, doi: 10.1016/j.snb.2019.02.081.
[114] G. Mao, M. Kilani, and M. Ahmed, ‘Review—Micro/Nanoelectrodes and Their Use in Electrocrystallization: Historical Perspective and Current Trends’, *J. Electrochem. Soc.*, vol. 169, no. 2, p. 022505, Feb. 2022, doi: 10.1149/1945-7111/ac51a0.
[115] Y.-L. Ying, Z. Ding, D. Zhan, and Y.-T. Long, ‘Advanced electroanalytical chemistry at nanoelectrodes’, *Chemical Science*, vol. 8, no. 5, pp. 3338–3348, 2017, doi: 10.1039/C7SC00433H.
[116] C. J. Slevin, N. J. Gray, J. V. Macpherson, M. A. Webb, and P. R. Unwin, ‘Fabrication and characterisation of nanometre-sized platinum electrodes for voltammetric analysis and imaging’, *Electrochemistry Communications*, vol. 1, no. 7, pp. 282–288, Jul. 1999, doi: 10.1016/S1388-2481(99)00059-4.
[117] P. Sun, Z. Zhang, J. Guo, and Y. Shao, ‘Fabrication of Nanometer-Sized Electrodes and Tips for Scanning Electrochemical Microscopy’, *Anal. Chem.*, vol. 73, no. 21, pp. 5346–5351, Nov. 2001, doi: 10.1021/ac010474w.
[118] J. J. Watkins, J. Chen, H. S. White, H. D. Abruña, E. Maisonhaute, and C. Amatore, ‘Zeptomole Voltammetric Detection and Electron-Transfer Rate Measurements Using Platinum Electrodes of Nanometer Dimensions’, *Anal. Chem.*, vol. 75, no. 16, pp. 3962–3971, Aug. 2003, doi: 10.1021/ac0342931.
[119] T. G. Strein and A. G. Ewing, ‘Characterization of submicron-sized carbon electrodes insulated with a phenol-allylphenol copolymer’, *Anal. Chem.*, vol. 64, no. 13, pp. 1368–1373, Jul. 1992, doi: 10.1021/ac00037a012.
[120] B. B. Katemann and W. Schuhmann, ‘Fabrication and Characterization of Needle-Type’, *Electroanalysis*, vol. 14, no. 1, pp. 22–28, 2002, doi: 10.1002/1521-4109(200201)14:1<22::AID-ELAN22>3.0.CO;2-F.
[121] W. J. Blaedel and G. A. Mabbott, ‘A pyrolytic carbon film electrode’, *Anal. Chem.*, vol. 50, no. 7, pp. 933–936, Jun. 1978, doi: 10.1021/ac50029a027.
[122] D. K. Y. Wong and L. Y. F. Xu, ‘Voltammetric studies of carbon disk electrodes with submicrometer-sized structural diameters’, *Anal. Chem.*, vol. 67, no. 22, pp. 4086–4090, Nov. 1995, doi: 10.1021/ac00118a009.

[123] M. McNally and D. K. Y. Wong, ‘An in Vivo Probe Based on Mechanically Strong but Structurally Small Carbon Electrodes with an Appreciable Surface Area’, *Anal. Chem.*, vol. 73, no. 20, pp. 4793–4800, Oct. 2001, doi: 10.1021/ac0104532.
[124] M. G. Schrlau, E. M. Falls, B. L. Ziober, and H. H. Bau, ‘Carbon nanopipettes for cell probes and intracellular injection’, *Nanotechnology*, vol. 19, no. 1, p. 015101, Nov. 2007, doi: 10.1088/0957-4484/19/01/015101.
[125] R. Singhal, S. Bhattacharyya, Z. Orynbayeva, E. Vitol, G. Friedman, and Y. Gogotsi, ‘Small diameter carbon nanopipettes’, *Nanotechnology*, vol. 21, no. 1, p. 015304, Nov. 2009, doi: 10.1088/0957-4484/21/1/015304.
[126] R. Chen, K. Hu, Y. Yu, M. V. Mirkin, and S. Amemiya, ‘Focused-Ion-Beam-Milled Carbon Nanoelectrodes for Scanning Electrochemical Microscopy’, *Journal of The Electrochemical Society*, vol. 163, no. 4, pp. H3032–H3037, 2016, doi: 10.1149/2.0071604jes.
[127] K. Hu *et al.*, ‘Open Carbon Nanopipettes as Resistive-Pulse Sensors, Rectification Sensors, and Electrochemical Nanoprobes’, *Anal. Chem.*, vol. 86, no. 18, pp. 8897–8901, Sep. 2014, doi: 10.1021/ac5022908.
[128] Y. Yu *et al.*, ‘Carbon Pipette-Based Electrochemical Nanosampler’, *Anal. Chem.*, vol. 86, no. 7, pp. 3365–3372, Apr. 2014, doi: 10.1021/ac403547b.
[129] C. Yang *et al.*, ‘Cavity Carbon-Nanopipette Electrodes for Dopamine Detection’, *Anal. Chem.*, vol. 91, no. 7, pp. 4618–4624, Apr. 2019, doi: 10.1021/acs.analchem.8b05885.
[130] Y. Takahashi *et al.*, ‘Multifunctional Nanoprobes for Nanoscale Chemical Imaging and Localized Chemical Delivery at Surfaces and Interfaces’, *Angewandte Chemie International Edition*, vol. 50, no. 41, pp. 9638–9642, 2011, doi: 10.1002/anie.201102796.
[131] K. McKelvey *et al.*, ‘Fabrication, Characterization, and Functionalization of Dual Carbon Electrodes as Probes for Scanning Electrochemical Microscopy (SECM)’, *Anal. Chem.*, vol. 85, no. 15, pp. 7519–7526, Aug. 2013, doi: 10.1021/ac401476z.
[132] J. Clausmeyer, P. Wilde, T. Löffler, E. Ventosa, K. Tschulik, and W. Schuhmann, ‘Detection of individual nanoparticle impacts using etched carbon nanoelectrodes’, *Electrochemistry Communications*, vol. 73, pp. 67–70, Dec. 2016, doi: 10.1016/j.elecom.2016.11.003.
[133] P. Wilde *et al.*, ‘Towards Reproducible Fabrication of Nanometre-Sized Carbon Electrodes: Optimisation of Automated Nanoelectrode Fabrication by Means of Transmission Electron Microscopy’, *ChemElectroChem*, vol. 5, no. 20, pp. 3083–3088, 2018, doi: 10.1002/celc.201800600.
[134] H. Gao *et al.*, ‘Precise Polishing and Electrochemical Applications of Quartz Nanopipette-Based Carbon Nanoelectrodes’, *Anal. Chem.*, vol. 94, no. 41, pp. 14092–14098, Oct. 2022, doi: 10.1021/acs.analchem.2c02296.
[135] R. Hao and B. Zhang, ‘Nanopipette-Based Electroplated Nanoelectrodes’, *Anal. Chem.*, vol. 88, no. 1, pp. 614–620, Jan. 2016, doi: 10.1021/acs.analchem.5b03548.
[136] J. T. Cox and B. Zhang, ‘Nanoelectrodes: Recent Advances and New Directions’, *Annual Review of Analytical Chemistry*, vol. 5, no. 1, pp. 253–272, 2012, doi: 10.1146/annurev-anchem-062011-143124.
[137] J. Heinze, ‘Ultramicroelectrodes in Electrochemistry’, *Angewandte Chemie International Edition in English*, vol. 32, no. 9, pp. 1268–1288, 1993, doi: 10.1002/anie.199312681.
[138] H. B. Aiyappa *et al.*, ‘Oxygen Evolution Electrocatalysis of a Single MOF-Derived Composite Nanoparticle on the Tip of a Nanoelectrode’, *Angewandte Chemie*

International Edition, vol. 58, no. 26, pp. 8927–8931, 2019, doi: 10.1002/anie.201903283.
[139] M. A. G. Zevenbergen, P. S. Singh, E. D. Goluch, B. L. Wolfrum, and S. G. Lemay, 'Stochastic Sensing of Single Molecules in a Nanofluidic Electrochemical Device', *Nano Lett.*, vol. 11, no. 7, pp. 2881–2886, Jul. 2011, doi: 10.1021/nl2013423.
[140] P. Actis *et al.*, 'Electrochemical Nanoprobes for Single-Cell Analysis', *ACS Nano*, vol. 8, no. 1, pp. 875–884, Jan. 2014, doi: 10.1021/nn405612q.
[141] M. Marquitan *et al.*, 'Intracellular Hydrogen Peroxide Detection with Functionalised Nanoelectrodes', *ChemElectroChem*, vol. 3, no. 12, pp. 2125–2129, 2016, doi: 10.1002/celc.201600390.
[142] B. Zhang, and Y. Zhang, and H. S. White*, 'The Nanopore Electrode', *Analytical Chemistry*, vol. 76, no. 21, pp. 6229–6238, Nov. 2004, doi: 10.1021/AC049288R.
[143] R. Ren *et al.*, 'Nanopore extended field-effect transistor for selective single-molecule biosensing', *Nat Commun*, vol. 8, no. 1, Art. no. 1, Sep. 2017, doi: 10.1038/s41467-017-00549-w.
[144] D. Perry, D. Momotenko, R. A. Lazenby, M. Kang, and P. R. Unwin, 'Characterization of Nanopipettes', *Analytical Chemistry*, vol. 88, no. 10, pp. 5523–5530, 2016, doi: 10.1021/acs.analchem.6b01095.
[145] H. S. White and A. Bund, 'Ion Current Rectification at Nanopores in Glass Membranes', *Langmuir*, vol. 24, no. 5, pp. 2212–2218, Mar. 2008, doi: 10.1021/la702955k.
[146] P. Actis, A. C. Mak, and N. Pourmand, 'Functionalized nanopipettes: toward label-free, single cell biosensors', *Bioanal Rev*, vol. 1, no. 2, pp. 177–185, Aug. 2010, doi: 10.1007/s12566-010-0013-y.
[147] J. Stanley and N. Pourmand, 'Nanopipettes—The past and the present', *APL Materials*, vol. 8, no. 10, p. 100902, Oct. 2020, doi: 10.1063/5.0020011.
[148] N. McEvoy *et al.*, 'Synthesis and analysis of thin conducting pyrolytic carbon films', *Carbon*, vol. 50, no. 3, pp. 1216–1226, Mar. 2012, doi: 10.1016/j.carbon.2011.10.036.
[149] L. A. Giannuzzi and F. A. Stevie, 'A review of focused ion beam milling techniques for TEM specimen preparation', *Micron*, vol. 30, no. 3, pp. 197–204, Jun. 1999, doi: 10.1016/S0968-4328(99)00005-0.
[150] A. W. Colburn, K. J. Levey, D. O'Hare, and J. V. Macpherson, 'Lifting the Lid on the Potentiostat: A Beginners Guide to Understanding Electrochemical Circuitry and Practical Operation', *Physical Chemistry Chemical Physics*, 2021, doi: 10.1039/d1cp00661d.
[151] S. Ching, R. Dudek, and E. Tabet, 'Cyclic Voltammetry with Ultramicroelectrodes', *J. Chem. Educ.*, vol. 71, no. 7, p. 602, Jul. 1994, doi: 10.1021/ed071p602.
[152] W. M. Haynes, Ed., *CRC Handbook of Chemistry and Physics, 97th Edition*, 97th edition. CRC Press, 2016.
[153] C. A. Schneider, W. S. Rasband, and K. W. Eliceiri, 'NIH Image to ImageJ: 25 years of image analysis', *Nat Methods*, vol. 9, no. 7, Art. no. 7, Jul. 2012, doi: 10.1038/nmeth.2089.
[154] G. R. Liu and S. S. Quek, 'Chapter 3 - Fundamentals for Finite Element Method', in *The Finite Element Method (Second Edition)*, G. R. Liu and S. S. Quek, Eds., Second Edition.Oxford: Butterworth-Heinemann, 2014, pp. 43–79. doi: https://doi.org/10.1016/B978-0-08-098356-1.00003-5.
[155] O. C. Zienkiewicz, *The finite element method its basis and fundamentals*, 6th ed. Amsterdam ; Elsevier Butterworth-Heinemann, 2005.

[156] G. I. Dovbeshko *et al.*, ‘Optical Properties of Pyrolytic Carbon Films Versus Graphite and Graphene’, *Nanoscale Res Lett*, vol. 10, no. 1, p. 234, May 2015, doi: 10.1186/s11671-015-0946-8.
[157] M. P. Hughes, H. Morgan, and M. F. Flynn, ‘The Dielectrophoretic Behavior of Submicron Latex Spheres: Influence of Surface Conductance’, *Journal of Colloid and Interface Science*, vol. 220, no. 2, pp. 454–457, Dec. 1999, doi: 10.1006/jcis.1999.6542.
[158] Q. Chen and Y. J. Yuan, ‘A review of polystyrene bead manipulation by dielectrophoresis’, *RSC Advances*, vol. 9, no. 9, pp. 4963–4981, 2019, doi: 10.1039/C8RA09017C.
[159] C. M. White, L. A. Holland, and P. Famouri, ‘Application of capillary electrophoresis to predict crossover frequency of polystyrene particles in dielectrophoresis’, *Electrophoresis*, vol. 31, no. 15, pp. 2664–2671, Aug. 2010, doi: 10.1002/elps.201000086.
[160] M. P. Hughes and N. G. Green, ‘The Influence of Stern Layer Conductance on the Dielectrophoretic Behavior of Latex Nanospheres’, *Journal of Colloid and Interface Science*, vol. 250, no. 1, pp. 266–268, Jun. 2002, doi: 10.1006/jcis.2002.8324.
[161] E. Morganti *et al.*, ‘A dielectrophoresis-based microdevice coated with nanostructured TiO2 for separation of particles and cells’, *Microfluid Nanofluid*, vol. 10, no. 6, pp. 1211–1221, Jun. 2011, doi: 10.1007/s10404-010-0751-8.
[162] C. C. Chio and Y.-L. S. Tse, ‘Hindered Diffusion near Fluid–Solid Interfaces: Comparison of Molecular Dynamics to Continuum Hydrodynamics’, *Langmuir*, vol. 36, no. 32, pp. 9412–9423, Aug. 2020, doi: 10.1021/acs.langmuir.0c01228.
[163] X. Michalet, ‘Mean square displacement analysis of single-particle trajectories with localization error: Brownian motion in an isotropic medium’, *Phys Rev E Stat Nonlin Soft Matter Phys*, vol. 82, no. 4 Pt 1, pp. 041914–041914, Oct. 2010, doi: 10.1103/PhysRevE.82.041914.
[164] A. Einstein, ‘On the Electrodynamics of Moving Bodies’, in *The Principle of Relativity*, Dover Publications, 1905, pp. 35–65.
[165] D. Ernst and J. Köhler, ‘Measuring a diffusion coefficient by single-particle tracking: statistical analysis of experimental mean squared displacement curves’, *Phys. Chem. Chem. Phys.*, vol. 15, no. 3, pp. 845–849, Dec. 2012, doi: 10.1039/C2CP43433D.
[166] S. Richardson, ‘On the no-slip boundary condition’, *Journal of Fluid Mechanics*, vol. 59, no. 4, pp. 707–719, Aug. 1973, doi: 10.1017/S0022112073001801.
[167] J. Leach *et al.*, ‘Comparison of Faxen’s correction for a microsphere translating or rotating near a surface’, *Phys. Rev. E*, vol. 79, no. 2, p. 026301, Feb. 2009, doi: 10.1103/PhysRevE.79.026301.
[168] A. L. Nord *et al.*, ‘Dynamic stiffening of the flagellar hook’, *Nat Commun*, vol. 13, no. 1, Art. no. 1, May 2022, doi: 10.1038/s41467-022-30295-7.
[169] A. J. Goldman, R. G. Cox, and H. Brenner, ‘Slow viscous motion of a sphere parallel to a plane wall—I Motion through a quiescent fluid’, *Chemical Engineering Science*, vol. 22, no. 4, pp. 637–651, Apr. 1967, doi: 10.1016/0009-2509(67)80047-2.
[170] P. Sharma, S. Ghosh, and S. Bhattacharya, ‘A high-precision study of hindered diffusion near a wall’, *Appl. Phys. Lett.*, vol. 97, no. 10, p. 104101, Sep. 2010, doi: 10.1063/1.3486123.

[171] M. D. Carbajal-Tinoco, R. Lopez-Fernandez, and J. L. Arauz-Lara, ‘Asymmetry in Colloidal Diffusion near a Rigid Wall’, *Phys. Rev. Lett.*, vol. 99, no. 13, p. 138303, Sep. 2007, doi: 10.1103/PhysRevLett.99.138303.
[172] Y. Huang, R. Holzel, R. Pethig, and X.-B. Wang, ‘Differences in the AC electrodynamics of viable and non-viable yeast cells determined through combined dielectrophoresis and electrorotation studies’, *Phys. Med. Biol.*, vol. 37, no. 7, p. 1499, Jul. 1992, doi: 10.1088/0031-9155/37/7/003.
[173] T. L. Mahaworasilpa, H. G. L. Coster, and E. P. George, ‘Forces on biological cells due to applied alternating (AC) electric fields. I. Dielectrophoresis’, *Biochimica et Biophysica Acta (BBA) - Biomembranes*, vol. 1193, no. 1, pp. 118–126, Jul. 1994, doi: 10.1016/0005-2736(94)90340-9.
[174] R. W. Schafer, ‘What Is a Savitzky-Golay Filter? [Lecture Notes]’, *IEEE Signal Processing Magazine*, vol. 28, no. 4, pp. 111–117, Jul. 2011, doi: 10.1109/MSP.2011.941097.
[175] Abraham. Savitzky and M. J. E. Golay, ‘Smoothing and Differentiation of Data by Simplified Least Squares Procedures.’, *Anal. Chem.*, vol. 36, no. 8, pp. 1627–1639, Jul. 1964, doi: 10.1021/ac60214a047.
[176] A. D. Edelstein, M. A. Tsuchida, N. Amodaj, H. Pinkard, R. D. Vale, and N. Stuurman, ‘Advanced methods of microscope control using μManager software’, *J Biol Methods*, vol. 1, no. 2, p. e10, 2014, doi: 10.14440/jbm.2014.36.
[177] H. A. Faizi, R. Dimova, and P. M. Vlahovska, ‘A vesicle microrheometer for high-throughput viscosity measurements of lipid and polymer membranes’, *Biophysical Journal*, vol. 121, no. 6, pp. 910–918, Mar. 2022, doi: 10.1016/j.bpj.2022.02.015.
[178] G. Bolognesi *et al.*, ‘Sculpting and fusing biomimetic vesicle networks using optical tweezers’, *Nat Commun*, vol. 9, no. 1, Art. no. 1, May 2018, doi: 10.1038/s41467-018-04282-w.
[179] L. Shi and L. Esfandiari, ‘An Electrokinetically-Driven Microchip for Rapid Entrapment and Detection of Nanovesicles’, *Micromachines*, vol. 12, no. 1, Art. no. 1, Jan. 2021, doi: 10.3390/mi12010011.
[180] M. P. Hughes, ‘The surface conductance of red blood cells and platelets is modulated by the cell membrane potential’, *ELECTROPHORESIS*, vol. 44, no. 9–10, pp. 845–853, 2023, doi: 10.1002/elps.202200289.
[181] Z.-L. Hu, M.-Z. Huo, Y.-L. Ying, and Y.-T. Long, ‘Biological Nanopore Approach for Single-Molecule Protein Sequencing’, *Angewandte Chemie*, vol. 133, no. 27, pp. 14862–14873, 2021, doi: 10.1002/ange.202013462.
[182] Y. Wang, Y. Zhao, A. Bollas, Y. Wang, and K. F. Au, ‘Nanopore sequencing technology, bioinformatics and applications’, *Nat Biotechnol*, vol. 39, no. 11, Art. no. 11, Nov. 2021, doi: 10.1038/s41587-021-01108-x.
[183] V. Wang, N. Ermann, and U. F. Keyser, ‘Current Enhancement in Solid-State Nanopores Depends on Three-Dimensional DNA Structure’, *Nano Lett.*, vol. 19, no. 8, pp. 5661–5666, Aug. 2019, doi: 10.1021/acs.nanolett.9b02219.
[184] Y. Zhang *et al.*, ‘Ionic current modulation from DNA translocation through nanopores under high ionic strength and concentration gradients’, *Nanoscale*, vol. 9, no. 2, pp. 930–939, Jan. 2017, doi: 10.1039/C6NR08123A.
[185] J. Houghtaling *et al.*, ‘Estimation of Shape, Volume, and Dipole Moment of Individual Proteins Freely Transiting a Synthetic Nanopore’, *ACS Nano*, vol. 13, no. 5, pp. 5231–5242, May 2019, doi: 10.1021/acsnano.8b09555.
[186] E. C. Yusko *et al.*, ‘Real-time shape approximation and fingerprinting of single proteins using a nanopore’, *Nature Nanotech*, vol. 12, no. 4, Art. no. 4, Apr. 2017, doi: 10.1038/nnano.2016.267.

[187] L. Restrepo-Pérez, C. Joo, and C. Dekker, ‘Paving the way to single-molecule protein sequencing’, *Nature Nanotech*, vol. 13, no. 9, Art. no. 9, Sep. 2018, doi: 10.1038/s41565-018-0236-6.
[188] J. P. Thiruraman, P. Masih Das, and M. Drndić, ‘Stochastic Ionic Transport in Single Atomic Zero-Dimensional Pores’, *ACS Nano*, vol. 14, no. 9, pp. 11831–11845, Sep. 2020, doi: 10.1021/acsnano.0c04716.
[189] A. Fragasso, S. Schmid, and C. Dekker, ‘Comparing Current Noise in Biological and Solid-State Nanopores’, *ACS Nano*, vol. 14, no. 2, pp. 1338–1349, Feb. 2020, doi: 10.1021/acsnano.9b09353.
[190] J. K. Rosenstein, M. Wanunu, C. A. Merchant, M. Drndic, and K. L. Shepard, ‘Integrated nanopore sensing platform with sub-microsecond temporal resolution’, *Nat Methods*, vol. 9, no. 5, Art. no. 5, May 2012, doi: 10.1038/nmeth.1932.
[191] J. Rabinowitz, M. A. Edwards, E. Whittier, K. Jayant, and K. L. Shepard, ‘Nanoscale Fluid Vortices and Nonlinear Electroosmotic Flow Drive Ion Current Rectification in the Presence of Concentration Gradients’, *J. Phys. Chem. A*, vol. 123, no. 38, pp. 8285–8293, Sep. 2019, doi: 10.1021/acs.jpca.9b04075.
[192] W. J. Lan *et al.*, ‘Voltage-Rectified Current and Fluid Flow in Conical Nanopores’, *Accounts of Chemical Research*, vol. 49, no. 11, pp. 2605–2613, Nov. 2016, doi: 10.1021/acs.accounts.6b00395.
[193] R. T. Perera, R. P. Johnson, M. A. Edwards, and H. S. White, ‘Effect of the Electric Double Layer on the Activation Energy of Ion Transport in Conical Nanopores’, *J. Phys. Chem. C*, vol. 119, no. 43, pp. 24299–24306, Oct. 2015, doi: 10.1021/acs.jpcc.5b08194.
[194] L. Luo, D. A. Holden, W.-J. Lan, and H. S. White, ‘Tunable Negative Differential Electrolyte Resistance in a Conical Nanopore in Glass’, *ACS Nano*, vol. 6, no. 7, pp. 6507–6514, Jul. 2012, doi: 10.1021/nn3023409.
[195] L. S. Lastra, Y. M. N. D. Y. Bandara, M. Nguyen, N. Farajpour, and K. J. Freedman, ‘On the origins of conductive pulse sensing inside a nanopore’, *Nat Commun*, vol. 13, no. 1, Art. no. 1, May 2022, doi: 10.1038/s41467-022-29758-8.
[196] C. Wei, A. J. Bard, and S. W. Feldberg, ‘Current Rectification at Quartz Nanopipet Electrodes’, *Anal. Chem.*, vol. 69, no. 22, pp. 4627–4633, Nov. 1997, doi: 10.1021/ac970551g.
[197] C. C. Chau, S. E. Radford, E. W. Hewitt, and P. Actis, ‘Macromolecular Crowding Enhances the Detection of DNA and Proteins by a Solid-State Nanopore’, *Nano Lett.*, vol. 20, no. 7, pp. 5553–5561, Jul. 2020, doi: 10.1021/acs.nanolett.0c02246.
[198] Z. Zhang *et al.*, ‘Dynamics of Water Associated with Lithium Ions Distributed in Polyethylene Oxide’, *Phys. Rev. Lett.*, vol. 115, no. 19, p. 198301, Nov. 2015, doi: 10.1103/PhysRevLett.115.198301.
[199] C. Ren, W. Tian, I. Szleifer, and Y. Ma, ‘Specific Salt Effects on Poly(ethylene oxide) Electrolyte Solutions’, *Macromolecules*, vol. 44, no. 6, pp. 1719–1727, Mar. 2011, doi: 10.1021/ma1027752.
[200] L. Poudel, R. Podgornik, and W.-Y. Ching, ‘The Hydration Effect and Selectivity of Alkali Metal Ions on Poly(ethylene glycol) Models in Cyclic and Linear Topology’, *J. Phys. Chem. A*, vol. 121, no. 24, pp. 4721–4731, Jun. 2017, doi: 10.1021/acs.jpca.7b04061.
[201] Z. Tao and P. T. Cummings, ‘Molecular dynamics simulation of inorganic ions in PEO aqueous solution’, *Molecular Simulation*, vol. 33, no. 15, pp. 1255–1260, Dec. 2007, doi: 10.1080/08927020701697691.
[202] M. Giesecke, F. Hallberg, Y. Fang, P. Stilbs, and I. Furó, ‘Binding of Monovalent and Multivalent Metal Cations to Polyethylene Oxide in Methanol Probed by

Electrophoretic and Diffusion NMR', *J. Phys. Chem. B*, vol. 120, no. 39, pp. 10358–10366, Oct. 2016, doi: 10.1021/acs.jpcb.6b08923.
[203] Z. S. Siwy, 'Ion-Current Rectification in Nanopores and Nanotubes with Broken Symmetry', *Advanced Functional Materials*, vol. 16, no. 6, pp. 735–746, 2006, doi: 10.1002/adfm.200500471.
[204] D. Momotenko, F. Cortés-Salazar, J. Josserand, S. Liu, Y. Shao, and H. H. Girault, 'Ion current rectification and rectification inversion in conical nanopores: a perm-selective view', *Phys. Chem. Chem. Phys.*, vol. 13, no. 12, pp. 5430–5440, Mar. 2011, doi: 10.1039/C0CP02595J.
[205] C. Wen, S. Zeng, S. Li, Z. Zhang, and S.-L. Zhang, 'On Rectification of Ionic Current in Nanopores', *Anal. Chem.*, vol. 91, no. 22, pp. 14597–14604, Nov. 2019, doi: 10.1021/acs.analchem.9b03685.
[206] A. P. Ivanov, P. Actis, P. Jönsson, D. Klenerman, Y. Korchev, and J. B. Edel, 'On-Demand Delivery of Single DNA Molecules Using Nanopipets', *ACS Nano*, vol. 9, no. 4, pp. 3587–3595, Apr. 2015, doi: 10.1021/acsnano.5b00911.
[207] L. J. Steinbock, A. Lucas, O. Otto, and U. F. Keyser, 'Voltage-driven transport of ions and DNA through nanocapillaries', *ELECTROPHORESIS*, vol. 33, no. 23, pp. 3480–3487, 2012, doi: 10.1002/elps.201100663.
[208] J. E. Reiner, J. J. Kasianowicz, B. J. Nablo, and J. W. F. Robertson, 'Theory for polymer analysis using nanopore-based single-molecule mass spectrometry', *Proc. Natl. Acad. Sci. U.S.A.*, vol. 107, no. 27, pp. 12080–12085, Jul. 2010, doi: 10.1073/pnas.1002194107.
[209] C. C. Chau *et al.*, 'Cooperative electrolyte-PEG interactions drive the signal amplification in a solid-state nanopore'. bioRxiv, p. 2021.11.01.466478, Nov. 03, 2021. doi: 10.1101/2021.11.01.466478.
[210] R. Karnik, C. Duan, K. Castelino, H. Daiguji, and A. Majumdar, 'Rectification of Ionic Current in a Nanofluidic Diode', *Nano Lett.*, vol. 7, no. 3, pp. 547–551, Mar. 2007, doi: 10.1021/nl062806o.
[211] I. Vlassiouk, S. Smimov, and Z. Siwy, 'Nanofluidic ionic diodes. Comparison of analytical and numerical solutions', *ACS Nano*, vol. 2, no. 8, pp. 1589–1602, Aug. 2008, doi: 10.1021/nn800306u.
[212] B. Vilozny, A. L. Wollenberg, P. Actis, D. Hwang, B. Singaram, and N. Pourmand, 'Carbohydrate -actuated nanofluidic diode: switchable current rectification in a nanopipette', *Nanoscale*, vol. 5, no. 19, pp. 9214–9221, 2013, doi: 10.1039/C3NR02105J.
[213] T. S. Plett, W. Cai, M. Le Thai, I. V. Vlassiouk, R. M. Penner, and Z. S. Siwy, 'Solid-State Ionic Diodes Demonstrated in Conical Nanopores', *J. Phys. Chem. C*, vol. 121, no. 11, pp. 6170–6176, Mar. 2017, doi: 10.1021/acs.jpcc.7b00258.
[214] L. Ma, Z. Li, Z. Yuan, C. Huang, Z. S. Siwy, and Y. Qiu, 'Modulation of Ionic Current Rectification in Ultrashort Conical Nanopores', *Analytical Chemistry*, vol. 92, no. 24, pp. 16188–16196, Dec. 2020, doi: 10.1021/acs.analchem.0c03989.
[215] E. R. Scott, H. S. White, and J. Bradley. Phipps, 'Iontophoretic transport through porous membranes using scanning electrochemical microscopy: application to in vitro studies of ion fluxes through skin', *Anal. Chem.*, vol. 65, no. 11, pp. 1537–1545, Jun. 1993, doi: 10.1021/ac00059a010.
[216] S. W. Kowalczyk, D. B. Wells, A. Aksimentiev, and C. Dekker, 'Slowing down DNA Translocation through a Nanopore in Lithium Chloride', *Nano Lett.*, vol. 12, no. 2, pp. 1038–1044, Feb. 2012, doi: 10.1021/nl204273h.

[217] S. Confederat, I. Sandei, G. Mohanan, C. Wälti, and P. Actis, ‘Nanopore fingerprinting of supramolecular DNA nanostructures’, *Biophysical Journal*, Aug. 2022, doi: 10.1016/j.bpj.2022.08.020.

Appendix A

Mechanistic Study of the Enhanced Single-Molecule Detection in a Polymer Electrolyte Nanopore

Fabio Marcuccio[1,2,‡], Dimitrios Soulias[1,2,‡], Chalmers C. Chau[1,2,3], Sheena E. Radford[3], Eric W. Hewitt[3], Paolo Actis[1,2,], Martin A. Edwards[4,*]*

[1]School of Electronic and Electrical Engineering, University of Leeds, Leeds LS2 9JT, UK

[2]Bragg Centre for Materials Research, University of Leeds, Leeds, UK

[3]School of Molecular and Cellular Biology and Astbury Centre for Structural Molecular Biology, University of Leeds, Leeds LS2 9JT, UK

[4]Department of Chemistry and Biochemistry, University of Arkansas, Fayetteville, AR 72701, USA

‡ *These authors contributed equally to this work.*

* *Corresponding authors: P.Actis@leeds.ac.uk , maedw@uark.edu*

KEYWORDS

Nanopipette, nanopore, finite-element modelling, nanofluidic diode, ion-current rectification, DNA, polyethylene-glycol, PEG

SUPPORTING INFORMATION

The Supporting Information is available free of charge at https://pubs.acs.org/doi/10.1021/acsnanoscienceau.2c00050.

ABSTRACT

Solid-state nanopores have been widely employed in the detection of biomolecules, but low signal-to-noise ratios still represent a major obstacle to enable the discrimination of nucleic acid and protein sequences substantially smaller than the nanopore diameter. The addition of 50% polyethylene glycol (PEG) to the external solution was recently demonstrated as a simple way to enhance the detection of such biomolecules translocating through a model solid-state nanopore. Here, we provide a comprehensive description of the physics describing a nanopore measurement carried out in 50% PEG that is supported by finite-element modelling and experiments. We demonstrate that the addition of PEG to the external solution introduces a strong imbalance in the transport properties of cations and anions, drastically affecting the characteristic current response of the nanopore. We further show that the strong asymmetric current response is due to a polarity-dependent ion distribution and transport at the nanopipette tip region, leading to either ion depletion or enrichment for few tens of nanometers across its aperture. We then provide evidence that a combination of the decreased/increased diffusion coefficients of cations/anions in the bath outside the nanopore and the mechanical interaction between a translocating molecule and the nanopore-bath interface is responsible for the increase in the translocation signals. We expect this new mechanism to contribute to further developments in nanopore sensing by suggesting that tuning the diffusion coefficients of ions could enhance the sensitivity of the system.

INTRODUCTION

Nanopore sensing is one of the leading label-free techniques for the analysis and manipulation of single molecules due to its high throughput and sensitivity[71], [181], [182]. In nanopore measurements, an ionic current is generated by applying a potential between two electrodes situated in two reservoirs separated by a small orifice. In general, the translocation of an analyte through a nanopore causes a decrease in magnitude of the ionic current due to temporary restricted transport of ions across the orifice [71]. However, under low electrolyte concentrations, charged molecules, such as double-stranded DNA (dsDNA), carry a counterion cloud which leads to a local ion enrichment, inducing a current enhancement[71], [183], [184]. The amplitude, duration and shape of the translocation event provide important information about the physicochemical properties of the molecule, such as size, charge, and shape [71], [185], [186].

Despite the developments in the field over the past decades[187], using solid-state nanopores to detect proteins and short nucleic acids still remains challenging, requiring nanopores of comparable size to the molecules (< 10 nm diameter), which are difficult to fabricate reproducibly[188]. Furthermore, the nanopore system needs to have a high signal-to-noise ratio[189] to detect small perturbations to the ion current caused by the translocation of molecules, and high bandwidth electronics to characterize rapid translocations with sufficient temporal resolution[190]. So far, finite element modelling has been extensively used to examine electrokinetic phenomena in nanopores[184], [191]–[194]. In such systems, the ion current is due to the transport of ionic species under the influence of an electric field and its physics can be considerably more complex than the one regulating simple ohmic conductors[195]. For example, the charge on the nanopore wall induces an electric double layer leading to non-uniform ion concentration distributions and the interacting physics of ion transport, electric fields and fluid flows result in a wide range of non-linear behavior[145], [192], [196].

We have recently reported the enhanced single molecule detection by a nanopore when 50% poly(ethylene) glycol (PEG) is added to the external solution, which leads to a ~ 6x increase in the amplitude of the translocation signal[197]. Here, we describe the mechanism explaining this enhancement by using a combination of experiments and multi-physics modelling[197]. We developed a finite element model by coupling Nernst-Planck and Poisson equations to describe the physics of ion transport under an applied electric field when a nanopore sensing experiment is carried out in the presence of 50% PEG. Based on the cation-binding properties of PEG that have been previously reported in literature, our model assumes a decrease/increase in the diffusion coefficients of cations/anions in the external solution, respectively[198]–[202]. The model reproduces

the experimental current-voltage responses in the presence and absence of PEG and provides insight into the ion concentrations and transport rates responsible for the observed behavior. We then prove that the increase in the translocation signal is a combination of the decreased/increased diffusion coefficients of cations/anions, respectively, in the bath outside the nanopore and the mechanical interaction between a translocating molecule and the nanopore-PEG interface. We expect this new mechanism to inform further developments in nanopore sensing by suggesting that approaches that affect the diffusion coefficients of ions in the external bath could be used to enhance the sensitivity of the system.

RESULTS AND DISCUSSION

Figure D.1a shows the experimental setup used throughout this work in which a model solid-state nanopore based on a quartz nanopipette (aperture 25 nm in diameter) filled with a 0.1 M KCl solution is immersed into a bath containing 0.1 M KCl with or without 50% (w/v) PEG. In nanopore measurements, the current-voltage (*i-V*) response characterizes the ion transport, indirectly providing information about the physical properties of the nanopore (size, shape, surface charge). The gray line in Figure D.1b shows the current-voltage response of a nanopipette filled with a 0.1M KCl solution and immersed in a bath containing 0.1 M KCl (no PEG). The slightly higher conductivity observed at a negative bias applied versus a positive bias is termed ion-current rectification (ICR) and arises from the negatively charged glass wall of the nanopipette, which makes the aperture region permselective to cations and this effect has been extensively described in literature[196], [203]–[205].

When the same nanopipette is immersed in a bath of 0.1 M KCl with 50% PEG, a dramatic reversal in the rectification is observed in the *i-V* curve (orange line). The PEG solution is ~ 9 times less conductive than 0.1 M KCl (Table ST1.2, Supporting Information 1) and, counterintuitively, the ion current observed at +500 mV is greater than the one measured in a PEG-free bath (above-bulk conductivity). Also, under negative bias, the ion current is ~ 4 times lower than observed without PEG in the external solution. This response cannot be explained only considering the difference in conductivity between the two solutions, or as a rectification effect induced by surface charge on the nanopore wall, indicating that a different mechanism is responsible for the observed *i-V* response. We also demonstrated that the viscosity of the solution is not responsible for this observed phenomenon, as the *i-V* response obtained with PEG cannot be reproduced with other viscous solutions such as 50% (v/v) glycerol (Section S3, Supporting Information 1). In the following section, we describe a numerical model we developed to calculate ionic currents (points in Figure D.1b) in the PEG system and to explain this anomalous current-voltage behavior.

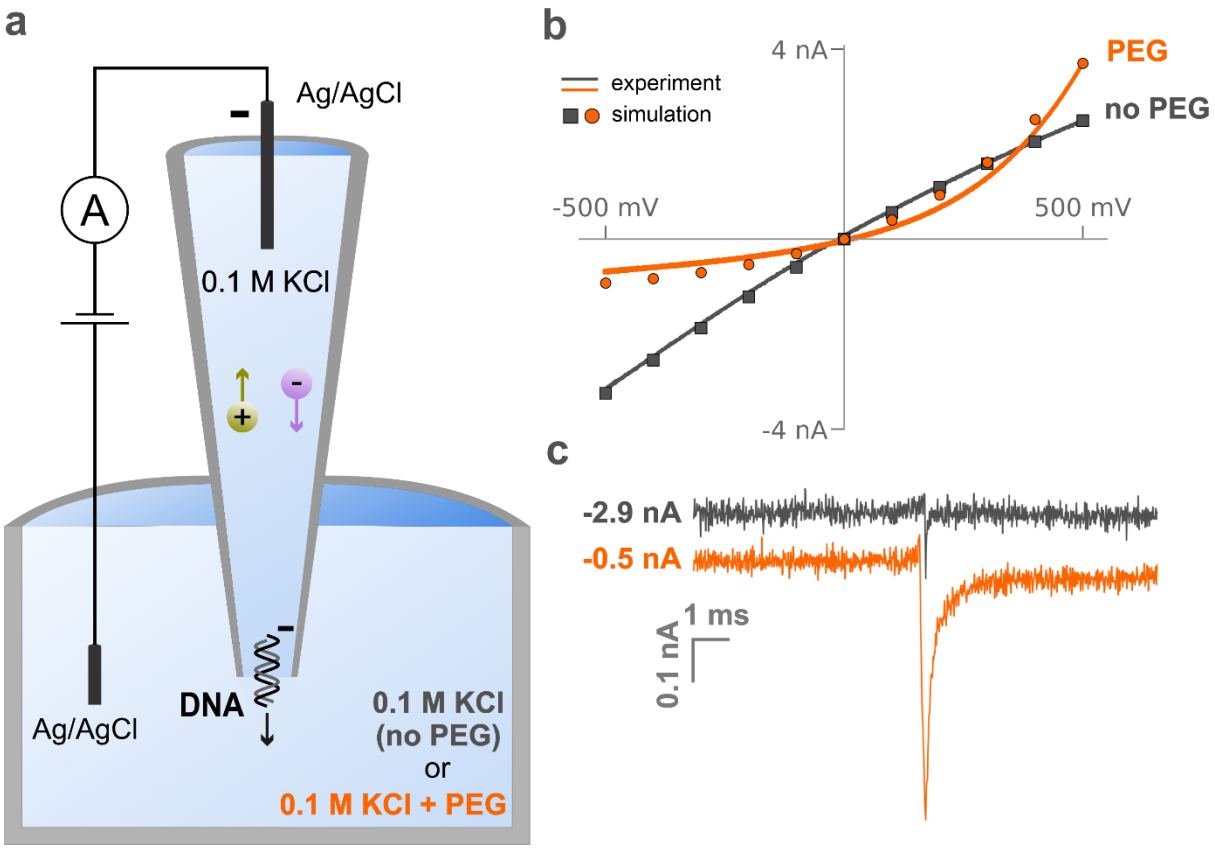

Figure A.1 Schematic and representative data for conductive-pulse measurements of double-stranded DNA translocation through a nanopipette. (a) A nanopipette (12.5 nm pore radius), filled with a 0.3 nM solution of 4.8kbp dsDNA in 0.1 M KCl, is immersed in a solution of the same electrolyte with and without the presence of 50% (w/v) PEG 35K. The application of a negative potential to an Ag/AgCl quasi-reference electrode inside the nanopipette with respect to a ground electrode in the external solution causes outbound migration of DNA molecules, initially present in the nanopipette solution. (b) Experimental (curves) and simulated (points) voltammograms of the nanopipette in the presence (orange) and absence (gray) of PEG in the outside solution. Current trace recorded upon translocation of a dsDNA molecule through the nanopipette aperture with (orange trace) and without (gray trace) the presence of PEG in the external solution.

As we have previously reported[197], the presence of PEG in the external solution leads to a 4 fold enhancement of the ion current observed when a single molecule translocates through the nanopore (Figure D.1c). It is worth noting that as the two current traces displayed in Figure D.1c were both recorded using the same nanopipette tip aperture (r = 12.5 nm), applied voltage (-500 mV), and composition of the inner solution (0.1 M KCl and 0.3 nM 4.8 kbp dsDNA), the observed enhancement is only driven by the presence of PEG in the external solution. During a conventional dsDNA translocation measurement through a nanopore where the solution is identical in both reservoirs, the current increase is attributed to the presence of the counter-ion cloud carried by the dsDNA molecule, which results in a temporary increase in the ions concentration in this region[183], [184], [206], [207]. The final section presents a new mechanism in nanopore

systems that not only explains the anomalous *i-V* response related to PEG, but also the enhanced single molecule sensitivity.

Finite Element Simulations

We developed a finite element model that coupled ion transport (diffusion, electromigration) and electrostatics at different applied potentials. A detailed description of the model is given in the Supporting Information 1 (Sections S1, S2) and 2 (COMSOL report). Briefly, a 2D axisymmetric model simulates the geometry of a nanopipette as a simplified truncated hollow cone immersed in a circular bath (Figure SF1.1, Supporting Information 1). The model was informed by experimental measurements (scanning electron microscopy graphs of the nanopipette tip geometry in Figure SF2.1 bulk conductivities and viscosities of the solutions in Table ST1.2, Supporting Information 1), with only the inner half-cone angle (θ), the surface charge of the quartz glass (σ) and the diffusion coefficients of the ions in the bath containing 50% PEG 35K (D_{K^+}, D_{Cl^-}) could not be experimentally measured. The inner-half cone angle ($\theta = 7°$) was determined parametrically by solving analytically the resistance of the nanopipette immersed in a 0.1 M KCl solution (Section S2.2, Supporting Information 1 for more details). Similarly, the surface charge at the nanopipette quartz wall $\left(\sigma = -12\,\frac{\mathrm{mC}}{\mathrm{m}^2}\right)$ was estimated using the closest fit to the experimental data (Section S2.4, Supporting Information 1).

In our system, charge is carried by ions migration due to the presence of an electric field (electromigration) and concentration gradient (diffusion)[145]. In 0.1 M KCl, the ion flux generated by electromigration $\left(\vec{J}_i^m\right)$ depends on the sum of the diffusion coefficients of ions in solution (Section S2.3, Supporting Information 1) which defines the solution conductivity according to the following equation:

$$\vec{J}_i^m = \vec{J}_{K^+}^m + \vec{J}_{Cl^-}^m = \frac{(D_{K^+} + D_{Cl^-})}{RT} F^2 c_b \vec{E} = \kappa \vec{E} \qquad \text{(D.1)},$$

where D_{K^+} and D_{Cl^-} are the diffusion coefficients of potassium and chloride, respectively, c_b the bulk concentration, F the Faraday constant, R the natural gas constant, T the temperature, κ the solution conductivity, and $\vec{E}$ the electric field. For KCl, in normal conditions (no PEG), the ratio between the diffusion coefficients of the two species is very close to unity $\left(\frac{D_{K^+}}{D_{Cl^-}} \sim 1\right)$, meaning that the contribution of potassium and chloride to the total conductivity κ is approximately the same.

Evidence in literature has shown that poly(ethylene) glycol associates with cations in solution[199]–[202], [208]. Zhang et al.[198] developed a molecular dynamics model and

proved the interaction between cations and poly(ethylene) glycol, finding that the trapping time of the ion in the polymer chain is highly dependent on the ion radius with longer trapping time for larger radii. These findings clearly indicate that the diffusion properties of cations in solution are affected in the presence of PEG. In the simulations, we considered this effect by assuming a change in the diffusion coefficients of the two ion species in the external solution. The properties of the 0.1 M KCl electrolyte inside the nanopipette were kept constant as described above.

We performed a parametric study to determine the ratio of the diffusion coefficients by decreasing the contribution of the potassium ion and increasing that of chloride $\left(\frac{D_{K^+}}{D_{Cl^-}} < 1\right)$ to the total conductivity κ_{PEG} (Section S2.3, Supporting Information 1) to describe the experimental *i-V* of the nanopipette in the presence of PEG shown in Figure D.1b (orange curve). This study revealed that the lower the ratio of diffusion coefficients, the more asymmetric the *i-V* response will be (Figure SF2.3, Supporting Information 1), which supports our hypothesis that the polymer-cation interactions are responsible for the distinctive current response in presence of PEG[197], [209]. We obtained the closest fit to the experimental data (orange square points, Figure D.1b) by selecting a diffusion coefficient ratio of $\frac{D_{K^+}}{D_{Cl^-}}$ = 0.54, meaning a 35% contribution from the cations and 65% from the anions to the total conductivity of the PEG solution. The simulated currents shown in Figure D.1b (orange data points) quantitatively reproduce the experimentally observed *i-V* response (orange curve).

It is worth clarifying that all inputted parameters, with or without PEG in the external solution, were either measured experimentally (electrical conductivity, fluid viscosity and electrolyte concentration) (Table ST1.2, Supporting Information 1) or found in literature (S1.1, Supporting Information 2). In addition, we found that the nanopipette surface charge and any fluid flow in the system minimally influence the simulated *i-V* response in the presence of PEG in the external solution (Section 2.5 and Table ST2.1, Supporting Information 1), thus all modelling results related to PEG presented below were obtained without considering these factors.

Average ion concentration at the tip region

Figure D.2 shows the average ion concentration $c_{avg} = \frac{[\boldsymbol{K^+}]+[\boldsymbol{Cl^-}]}{\mathbf{2}}$ obtained with finite element modelling under two opposite voltages applied ($V = \pm 500\ \mathrm{mV}$) in presence (Figure D.2a, D.2b) and absence (Figure D.2c, D.2d) of PEG in the external solution (Section S5, Supporting Information 1). In the presence of PEG, a pronounced ion depletion is observed for $V = -500\ \mathrm{mV}$ (Figure D.2a) while ion enrichment is noticeable when $V = +500\ \mathrm{mV}$ (Figure D.2b) with a 20-fold increase in ion concentration compared

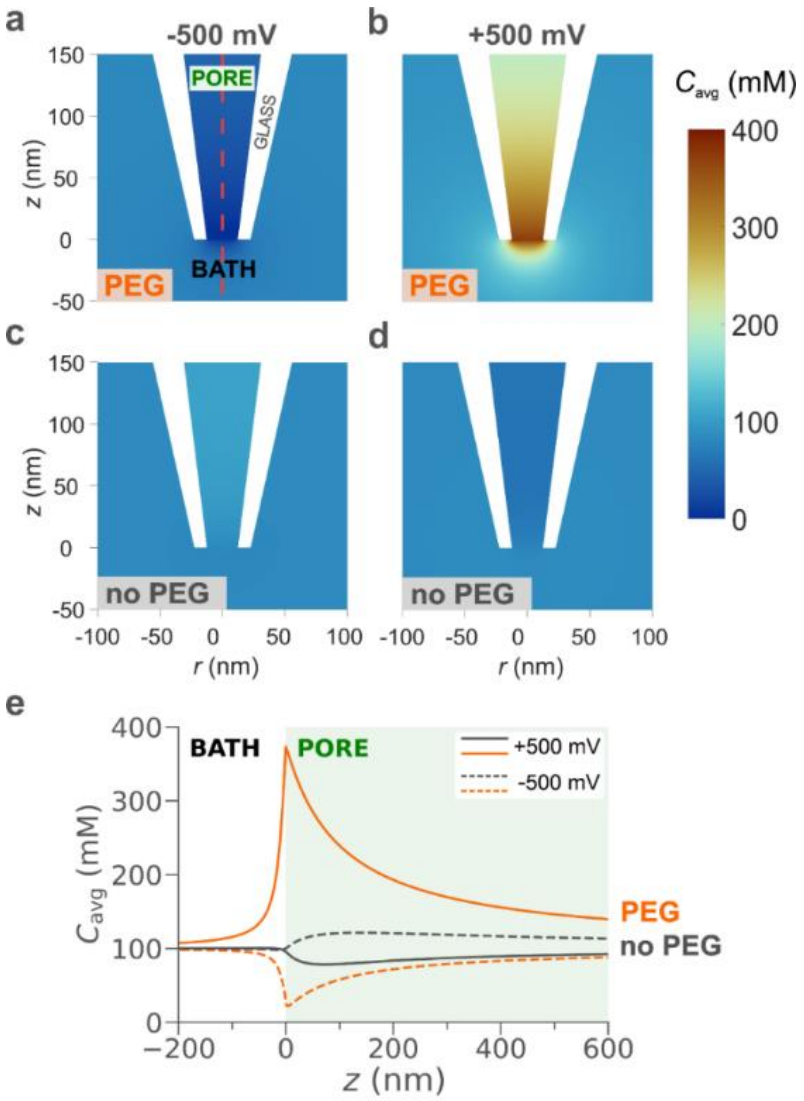

Figure A.2 Simulated ion distributions close to the nanopipette tip at ±500 mV in the presence and absence of PEG in the external solution. Average concentration $\left(C_{avg} = ½([K^+] + [Cl^-])\right)$ with (a, b) and without (c, d) PEG in the external solution for an applied voltage of (a, c) -500mV and (b, d) 500 mV. (e) Average ion concentrations along the nanopipette axis of symmetry (red dashed line in a) in presence (orange) and absence (gray) of PEG for negative (dashed curves) and positive (solid curves) bias applied. The diameter of the nanopipette is 25 nm and the internal and external solution is 0.1 M KCl for both PEG and no PEG but in the PEG case, the external solution also contains PEG 35K.

to when a negative bias is applied. This observation is the origin of the asymmetric current response observed in the presence of PEG (Figure D.1b**).** In the absence of PEG in the external solution, a slightly higher ion concentration can be observed within the pore region under $V = -500\ \mathrm{mV}$ (Figure D.2c) compared to the case with $V = +500\ \mathrm{mV}$ (Figure D.2d). This explains the slightly asymmetric curve (ICR) for the no PEG case (gray curve) shown in Figure D.1b[196]. Figure D.2e plots the average ion concentration along the symmetry axis of the nanopipette (dashed red line, Figure D.2a), allowing for quantitative comparison of the simulations. The average concentration for the PEG

(orange curve) and no PEG (gray curve) case is plotted for $V = -500\ \mathrm{mV}$ (dashed line) and $V = +500\ \mathrm{mV}$ (solid line). In our reference system, the interface between nanopipette and external solution is positioned at $z = 0\ \mathrm{nm}$, while $z > 0\ \mathrm{nm}$ correspond to the axis of symmetry inside the nanopipette and $z < 0\ \mathrm{nm}$ to the external solution (Figure SF1.1, Supporting Information 1). Interestingly, the maximum ion concentration for $V = +500\ \mathrm{mV}$ in the presence of PEG (orange solid line) is approximately 4 times higher than the corresponding case with no PEG (gray solid line). This observation indicates that the above-bulk conductivity arises from a dramatic increase in the ion concentration at the tip region of the nanopipette, despite the external solution in the presence of PEG being 9 times less conductive (Table ST1.2, Supporting Information 1).

Experimentally, a similar increase in conductivity is observed upon the translocation of a single dsDNA molecule in presence of PEG in the external solution, as shown in Figure D.1c, suggesting that the signal amplification is related to the number of ions in the sensing region of the nanopipette. The vast difference in ion concentration between positive and negative bias is similar to the behavior of nanofluidic diodes[210]–[214] for ultrashort conical nanopores. In these studies, nanofluidic diodes were developed by introducing a surface charge discontinuity on a nanochannel which forms a junction similar to bipolar semiconductors. In our case, we achieve a similar behavior by introducing an interface between a region where the value for the diffusion coefficient for cations and anions is approximately the same (i.e. the inner solution) to a region where the diffusion coefficient for the cations is much smaller than the one for anions due to the presence of PEG (i.e. the external solution). This discontinuity not only affects ions distribution but also ions transport, as we describe in the next section.

Ions transport at the tip region

The origin of the significant differences in ion concentration (c_{avg}) in the presence of PEG can be understood by a careful analysis of the ion transport (N_{K^+}, N_{Cl^-}) across the interface close to the nanopipette tip aperture, which represents the most sensitive region of our system[215] (Section S6, Supporting Information 1).

We define “sensing region” as the region between two equipotential lines where a 50% drop of the applied voltage is observed. In case of -500 mV applied, the voltage drop across the sensing region (ΔV_{sens}) is equal to 250 mV. In the presence of PEG and under -500 mV, we found that this region is about 40 nm in length along the z-axis (from z = -20 nm to z = 20 nm with the interface between inner and external solution set at z = 0) (Figure SF6.3 and SF6.4, Supporting Information 1). This clearly indicates a highly resistive region positioned at the nanopipette tip which leads to a significant drop in the

measured current magnitude (baseline current), as shown in Figure D.1b (orange curves and square points).

In any enclosed volume, the flux of ions through the surface surrounding the volume is equal to the rate of change in the ions number (mass and charge conservation)[95]. The transport rate for each ion species (N_i) was calculated by integrating the total flux of K^+ and Cl^- separately, along the equipotential lines (dashed gray lines, Figure D.3) selected around the nanopipette tip. An extensive description of these calculations is provided in section S6 of Supporting Information 1. In a nutshell, for 0.1 M KCl, where both ion species have a valence of $z_i = 1$, the difference between the number of charges (ions) entering and exiting each dashed line over time is proportional to the current.

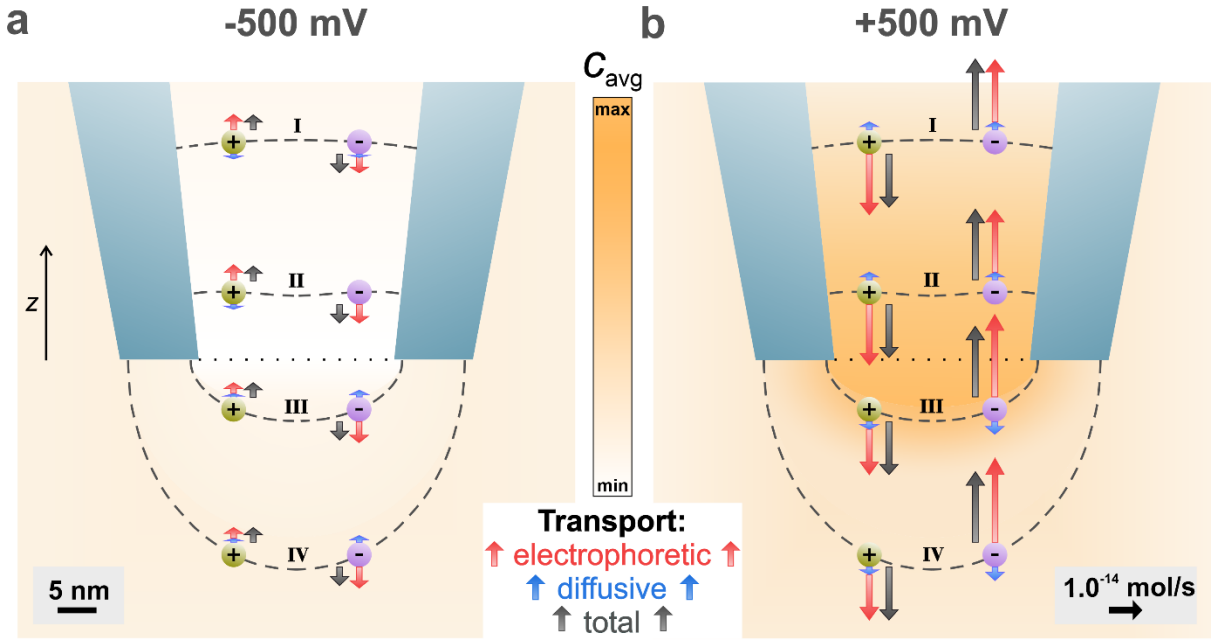

Figure A.3 Visualization of the relative contributions of different physical processes to the transport rates of K^+ and Cl^- at ± 500 mV with PEG in the outer solution. The lengths of the arrows represent the magnitude of the total transport rate (black) across the respective equipotential line (dashed gray), which is the sum of electrophoretic (red) and diffusive (blue) contributions. In addition, the arrows being parallel to the z-axis and the ions positions were selected for illustration purposes only. Arrows for negligible diffusive contributions are not shown in the plot for ease of representation. The colour map in the background represents the average ion concentration and the dotted line at the nanopipette aperture the interface between the inner and the external solution.

Since no convection was considered for this simulation, the total ion transport rate (black arrow, Figure D.3) can be broken down to two components, the electrophoretic (N_i^m) and diffusive (N_i^d) (red and blue arrow, respectively, Figure D.3). Figure D.3 illustrates all these three components, for both cations (green sphere) and anions (purple sphere), at 4 equipotential lines to highlight the marked difference in ion transport between the inner and outer solution for V = ± 500 mV. The total ion transport rate (black arrows) of each ion species for each applied potential remains constant across the designed

dashed lines, verifying that mass and charge is conserved in the system and that the sum of the electrophoretic and diffusive components will always be the same. Based on the polarity of the applied voltage, cations/anions will get attracted/repelled resulting in electrophoretic ion transport either in or out of the nanopipette tip (dotted black line, Figure D.3). Additionally, any gradients in the ion concentration (color map in background of Figure D.3) give rise to diffusive ion transport with both species moving towards (with V = -500 mV) or away the tip interface (with V = 500 mV).

Figure D.3 shows that the total ion transport rate at -500 mV is lower than the rate at 500 mV by 75% which is in agreement with the experimental and simulated *i-V* responses presented in Figure D.1b. It is important to note that the electrophoretic transport dominates diffusion in all cases. To summarize, when V = 500 mV, there is a larger number of ions flowing across the nanopipette tip aperture over time which results in a higher current magnitude (Table ST6.2, Supporting Information 1) demonstrating that an asymmetric ion mobility is responsible for the observed above-bulk conductivity. In contrast, when V = -500 mV, there is a low number of ions flowing across the nanopipette tip aperture over time resulting in a much lower current magnitude (Table ST6.1, Supporting Information 1), which again is consistent with the experimental data.

Mechanism of current enhancement upon dsDNA translocation

DNA molecules carry a negative surface charge and form counter-ion clouds when immersed in electrolyte solutions (0.1 M KCl)[183], [216]. In standard conditions (no PEG) and under negative potentials (-500 mV), the temporary increase in the current magnitude recorded during dsDNA translocation is due to the additional ions carried by the molecule to the sensing region of the nanopipette which results in a temporary higher ion concentration[183].

In the presence of PEG, the physics related to the generated current upon dsDNA translocation through the nanopipette aperture is considerably more complex. As previously explained, the nanopipette shows a remarkable ion depletion at the tip region with very few ions transporting through the interface when -500 mV is applied (see ion concentrations in Figure D.2a and transport in Figure D.3a), while the external solution is mainly populated by anions with cations transport hindered by intercalation in the PEG molecules[198]. In these conditions, the counter-ion cloud carried by the dsDNA molecule certainly contributes to the temporal increase of the ion concentration, thus the conductivity, of the system. However, this is not sufficient to explain the drastic current enhancement recorded experimentally. In fact, the charge carried by the translocating dsDNA molecule is the same regardless the presence or absence of PEG in the external solution, thus the increased conductivity should be approximately equal in both cases (see Section S7.1, Supporting Information 1).

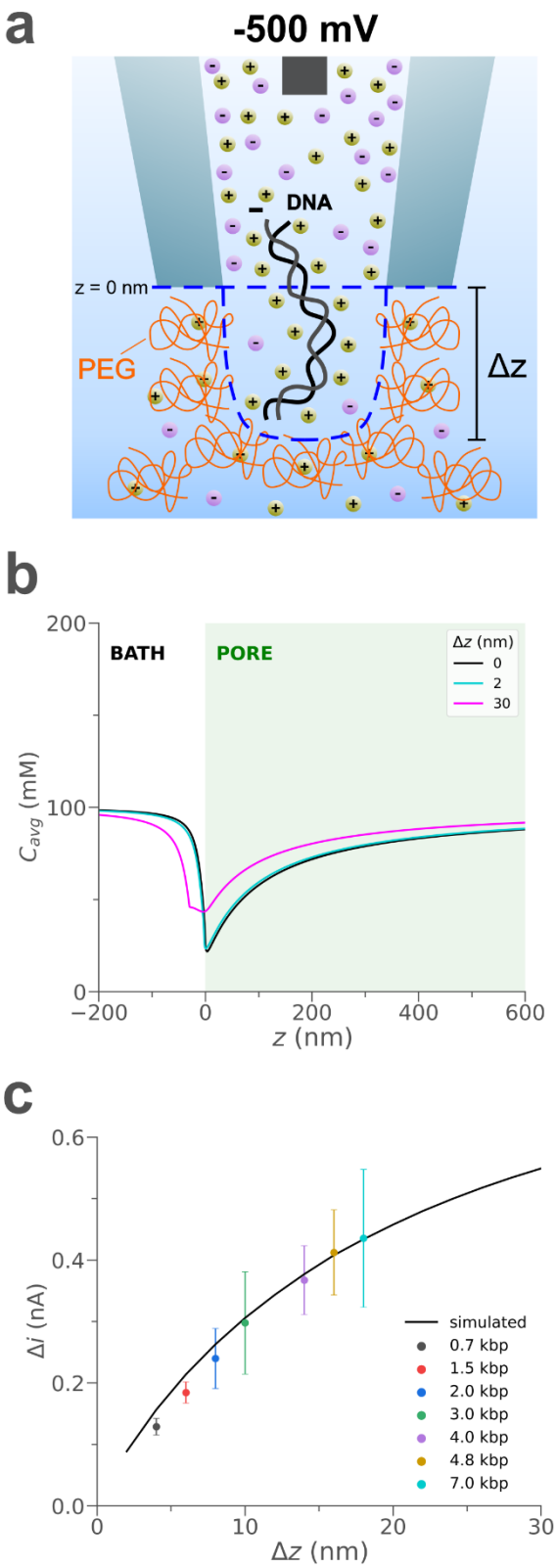

Figure A.4 Proposed mechanism of current enhancement upon a dsDNA molecule translocation. (a) The translocation of a dsDNA molecule through the nanopipette causes a temporary displacement of the interface (*Δz*) between the pore and external solution (blue dashed line) which results in a temporary ion enrichment in the nanopipette tip region (note: the illustrations are not in scale and geometries were chosen for illustration purposes only). (b) Simulated average ion concentration along the axis of symmetry (r = 0 nm) for 0 nm (black), 2 nm (cyan) and 30 nm (magenta) interface displacement. (c) Simulated (black curve) and experimental (coloured points) current peak maxima (Δ*i*) for different interface displacements towards the external solution and sizes of dsDNA molecules translocating through the nanopipette tip aperture towards the bath, respectively. The error bars represent the standard deviation of the experimental current peak maxima values. The horizontal coordinate of experimental data points was chosen according to the expected *Δz* (Table ST7.1, Supporting Information 1).

We explored if the mechanical interactions between a dsDNA and PEG molecules at the interface of the internal and the external solutions could temporarily alter the ion concentrations at the tip region. Briefly, we considered a rectangular protrusion of the domain inside the nanopipette (i.e. inner solution) towards the bath domain (i.e. external solution) to get a simplistic model of the interface shift caused by the arrival of dsDNA, as shown in Figure D.4a. We performed a parametric study by varying the size of this protrusion (Δz) from $z = 0$ nm to $z = -30$ nm with 2 nm steps. Figure D.4b presents the simulated average ion concentration along the symmetry axis for three different interface displacements (0, 2 and 30 nm). As the interface moves further away from the nanopipette tip opening (z = 0 nm), the number of ions in the nanopipette's sensing region increases, resulting in an enhanced current value. We found that an interface displacement of 16 nm towards the external solution is sufficient to cause an increase in the ion current to match the current peak maxima measured experimentally for the translocation of a single 4.8 kbp dsDNA molecule (Section S7.2 and S7.3, Supporting Information 1). This current enhancement is due to a 33% increase in ion concentration in the nanopipette sensing region (0 < z < 20 nm) caused by this shift in the interface.

To summarize, we found that the translocation of dsDNA molecules through the pore causes a temporary displacement of the interface, which results in a shift of the ion depleted region towards the bath. The consequence is ion enrichment in the sensing region inside the nanopipette, which results in higher conductivity, thus higher measured currents (Figure D.4a). Note that in our simulations, we simplistically assume that the interface between pore and external solution without DNA is a straight line at $z = 0$ nm (no mixing, blue dashed line in Figure D.4). Using a more sophisticated model for the interface would certainly improve the accuracy of our calculations, but not the level of our understanding of the system.

Based on this mechanism, we expect various dsDNA molecule sizes to have different effects on the translocation current, as recently reported by Confederat et al.[217] for DNA origamis. For instance, longer dsDNA molecules would displace the interface further towards the external solution. To prove this hypothesis, we repeated the same experiment as the one illustrated in Figure D.1 using a range of sizes of dsDNA as the analyte (0.7 – 7 kbp) with and without PEG in the outside bath (Figure D.4c and Section S7.3, S7.4, Supporting Information 1). In PEG, experimental current peak maxima for the translocation of dsDNA molecules with sizes from 0.7 kbp up to 7 kbp are in close agreement with the trend obtained from the simulated current values due to interface displacements, as shown in Figure D.4c and Table ST7.1 in Supporting Information 1. In the no PEG case, not only there is no evident correlation, but the detection is limited to molecules with a minimum size of 4.8 kbp (Figure SF7.2c, Supporting Information 1).

These findings confirm our initial hypothesis that the current enhancement in the presence of PEG 35K upon dsDNA translocation cannot be explained only in terms of additional ions carried by the analyte, as recently reported by Lastra et al[195] for a system based on a pore's flux imbalance, but a mechanical interaction between the analyte and PEG molecules at the nanopipette tip opening must be taken into account.

To further support this, we experimentally verified that the voltametric responses and current enhancement caused by PEG disappear when a positive pressure is applied at the back of the nanopipette to mechanically push PEG molecules away from the tip opening (Section S7.5, Supporting Information 1). This result shows that the PEG effect is completely cancelled by disrupting the interface, underpinning the importance of the latter to the experienced current enhancement.

CONCLUSION

To summarize, we developed a finite element model to improve our understanding of the dramatic current enhancement upon dsDNA molecule translocation through a nanopipette to an external solution containing 50% (w/v) PEG 35K. This system was successfully simulated by assuming a decrease/increase in the diffusion coefficients of cations/anions, respectively, due to the cation binding properties of PEG. We observed that the characteristic *i-V* response in the presence of PEG is due to voltage-dependent ion concentrations at the tip region with ion enrichment at positive and ion depletion at negative potentials. A similar behaviour was noticed in the asymmetric transport rates for each ion species across the tip orifice, resulting in higher currents at positive applied bias compared to negative. Furthermore, we demonstrated that conventional mechanisms of current enhancement based on additional ions carried by the analyte are not sufficient to fully explain our system. Hence, we proposed a novel mechanism supported by experimental evidence which relies on mechanical interaction between the translocating analyte and the solutions interface. We proved that such interactions could lead to alteration of the ion distribution at the tip orifice which can result into temporary current increases. We expect that this work can provide a new paradigm in nanopore sensing, where the alteration of the ion transport properties of the external solution can be harnessed to provide enhanced signal-to-noise ratios allowing for the biochemical and structural analysis of proteins and other biomolecules.

MATERIALS AND METHODS

Nanopipette fabrication

Quartz capillaries of 1.0 mm outer diameter and 0.5 mm inner diameter (QF100-50-7.5; Sutter Instrument) were used to fabricate the nanopipette using the SU-P2000 laser puller (World Precision Instruments). A two-line protocol was used, line 1: HEAT 750/FIL

4/VEL 30/DEL 150/PUL 80, followed by line 2: HEAT 625/FIL 3/VEL 40/DEL 135/PUL 150. The pulling protocol is instrument specific and there is variation between different SU-P2000 pullers.

External bath preparation

To generate 10 ml of the 50% (w/v) poly(ethylene) glycol (PEG 35K) (Sigma Aldrich; 94646) 0.1 M KCl solution, 1 ml of 1 M KCl solution, 4 ml of ddH_2O and 5 g of PEG 35K were mixed inside a tube. The tube was then left inside a 70°C incubator for 2 hours followed by overnight incubation at 37°C. The tubes were then left on bench for 4 hours to reach the room temperature prior to use. All electrolytes were stored at room temperature.

Double-stranded DNA preparation

To prepare the individual dsDNA samples, the GeneRuler 1 kbp plus DNA Ladder (SM1331: Thermo Fisher) was separated via a 0.8% agarose gel. The individual bands (0.7 kbp, 1.5 kbp, 2 kbp, 3 kbp, 4kbp, 4.8 kbp, 7 kbp) were physically isolated with a blade and the dsDNA was extracted using the Monarch® DNA Gel Extraction Kit according to the manufacturer specifications (T1020; New England Biolabs Inc.). The extracted dsDNA was further purified using the Genomic Clean and Concentrator Kit (D4010; Zymo Research). All dsDNA was eluted in the Monarch® DNA Elution Buffer (T1016L; New England BioLabs Inc.) and stored at -20°C. All the dsDNA was then diluted from stock to 0.3 nM with 0.1 M KCl.

Ion current trace recording

The nanopipettes were all filled with 0.3 nM dsDNA diluted in 0.1 M KCl (P/4240/60; Fisher Scientific) and fitted with a Ag/AgCl working electrode. The nanopipettes were immersed into the electrolyte bath containing or not containing poly(ethylene) glycol 35K with a Ag/AgCl reference electrode. The ionic current trace was recorded using a MultiClamp 700B patch-clamp amplifier (Molecular Devices) in voltage-clamp mode. The signal was filtered using low-pass filter at 20 kHz and digitized with a Digidata 1550B at a 100 kHz sampling rate and recorded using the software pClamp 10 (Molecular Devices).

Finite Element Modelling

Finite element simulations were performed with COMSOL Multiphysics 5.6 (COMSOL Inc.).

Appendix B

Supplementary information for Chapter 3

This Appendix includes additional information for experimental results discussed in Chapter 3.

B.1 SEM images of carbon nanoelectrodes

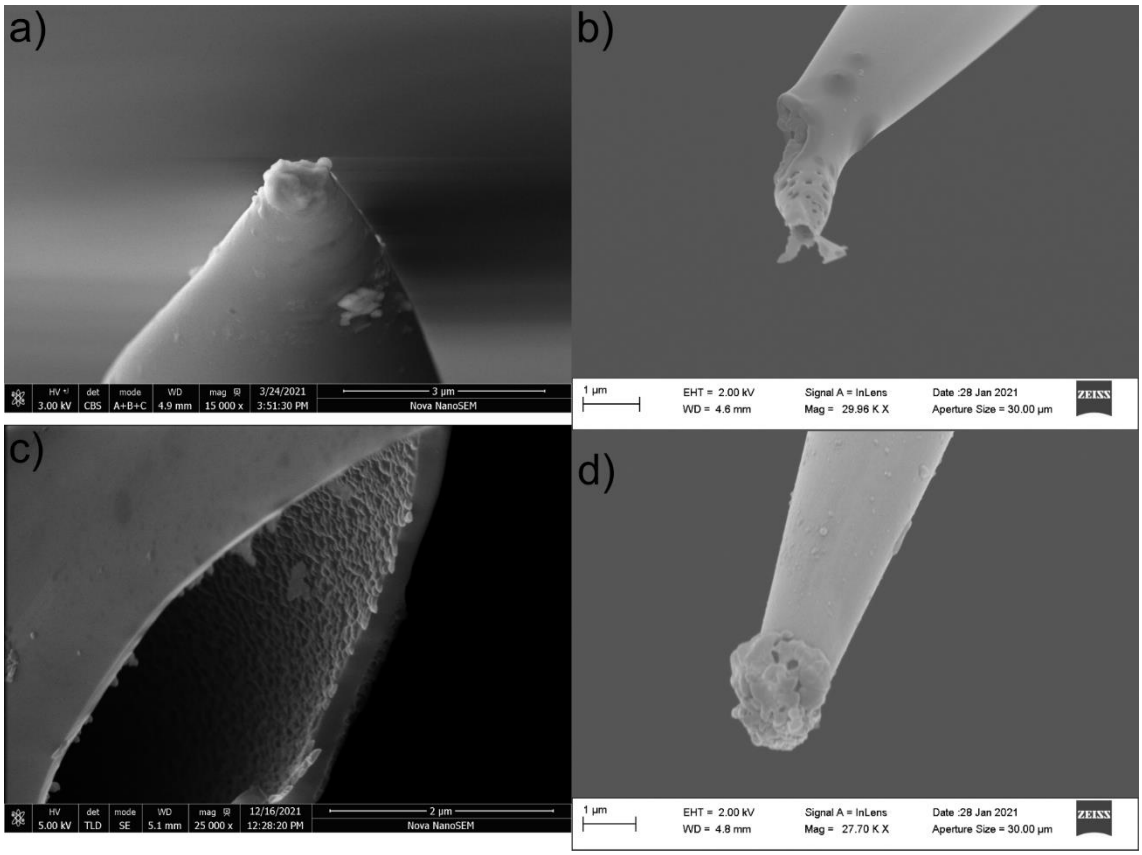

Figure B.1 SEM micrographs of unsuccessful pyrolytic carbon deposition inside quartz glass single-barrel nanopipettes. **a)** Fully sealed nanopipette tip with melted glass after extreme heating. **b)** Melted nanopipette tip after extreme heating with a large carbon surface being exposed by the side. **c)** Broken nanopipette tip. Pyrolytic carbon deposition is observed at the inner glass wall (rough surface). **d)** Fully sealed nanopipette tip with melted glass after extreme heating.

Figure A.1 shows examples of unsuccessful carbon deposition inside quartz glass nanopipettes due to material melting after the pyrolysis procedure. In contrast, Figure A.2 illustrates two additional nanopipette tips with semi-elliptical carbon nanoelectrodes before and after FIB milling was performed.

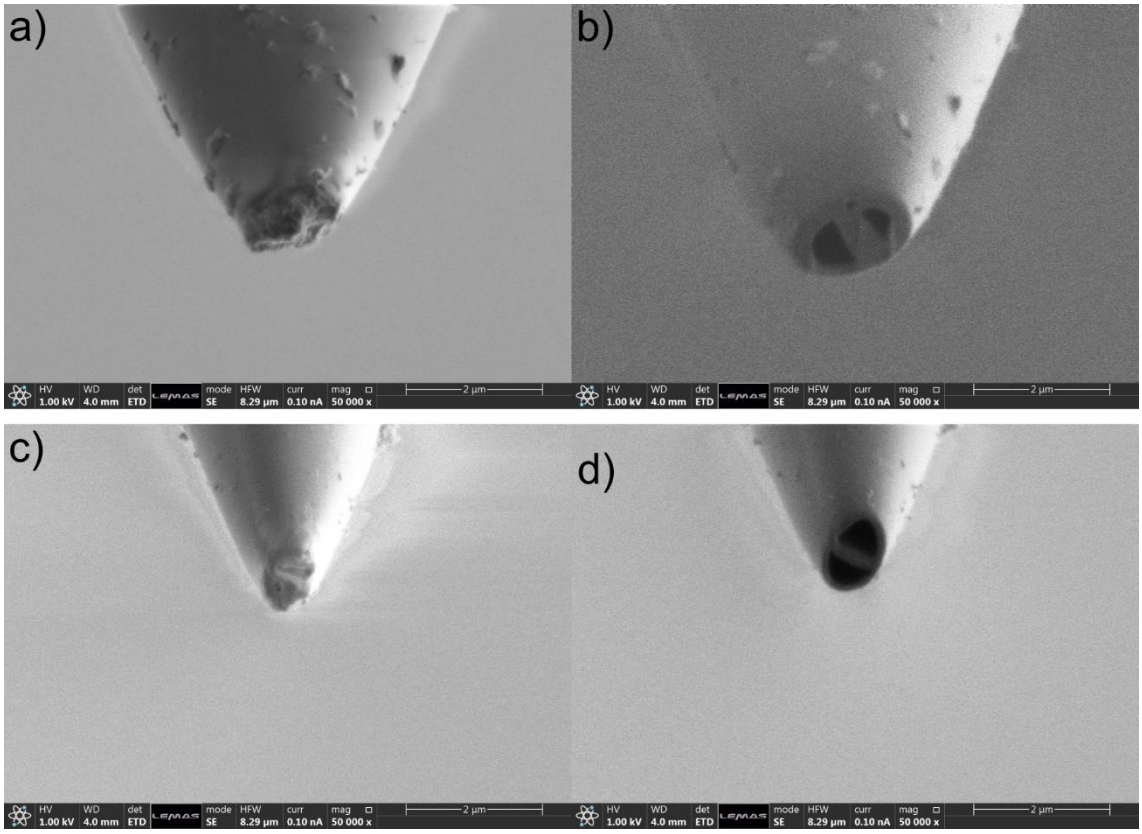

Figure B.2 Scanning electron microscope (SEM) images of quartz glass double-barrel nanopipette-based carbon electrodes **a)**, **c)** before and **b)**, **d)** after the application of focused ion beam (FIB) milling at the tip surface. At the left column, carbon was covered by melted glass inside the semi-elliptical pores. At the right column, excessive glass wall was removed by a focused beam of accelerated Ga^{+} ions perpendicular to the tip surface, resulting in a smooth and flat surface where semi-elliptical carbon nanoelectrodes (black domain) are considered co-planar. Note that quartz glass theta capillaries were laser pulled with Programme 2 and the nanopipettes external wall was not sputtered with a conductive layer so that the carbon nanoelectrodes could be used as dielectrophoretic nanotweezers. Any protrusions in the geometry of the outer glass walls were due to salt contamination during electrochemical measurements that was not removed after cleaning. Dr Stuart Micklethwaite (LEMAS, University of Leeds) acquired the SEM micrographs and performed FIB milling at the regions of interest I selected.

B.2 Cyclic voltammograms

Figure A.3 presents peak-shaped voltammograms for a conventional macroelectrode (1 mm in diameter) where the oxidation and reduction curves do not overlap as for nanoelectrodes. Furthermore, Figure B.4 depicts additional sigmoid cyclic voltammograms for a pair of nanoelectrodes before and after FIB milling.

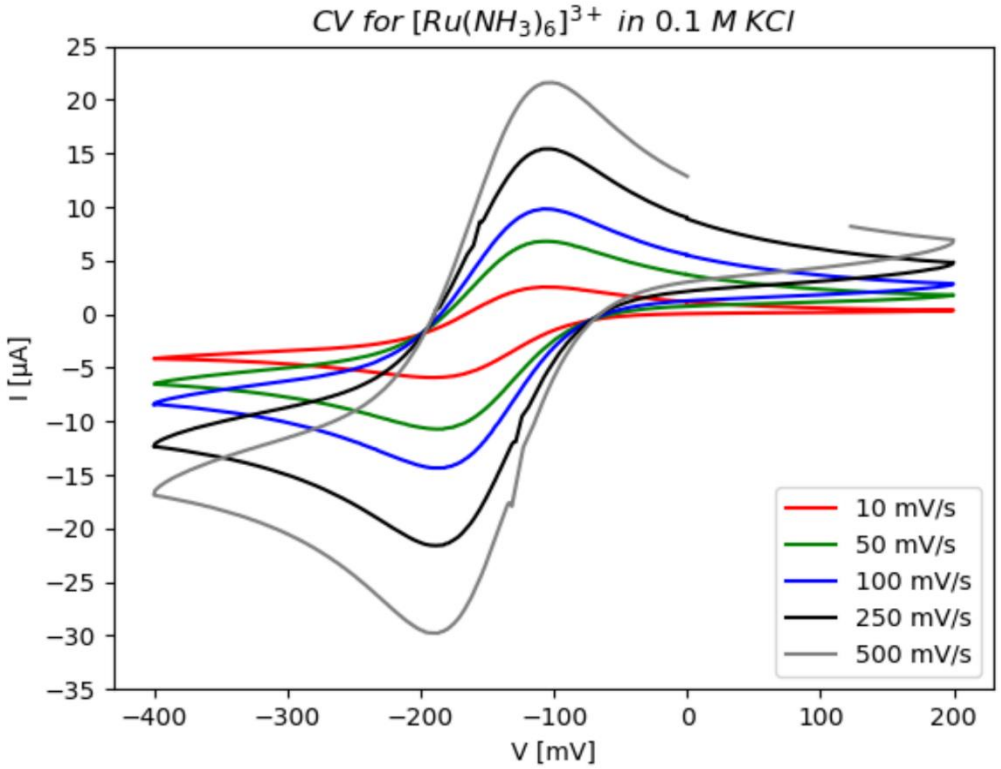

Figure B.3 Cyclic voltammograms at different scan rates (10, 50, 100, 200 and 500 mV/s) for a conventional planar macroelectrode (1 mm in diameter) when immersed in 10 mM RuHex and 0.1 M KCl. A three-electrode configuration was used for these measurements.

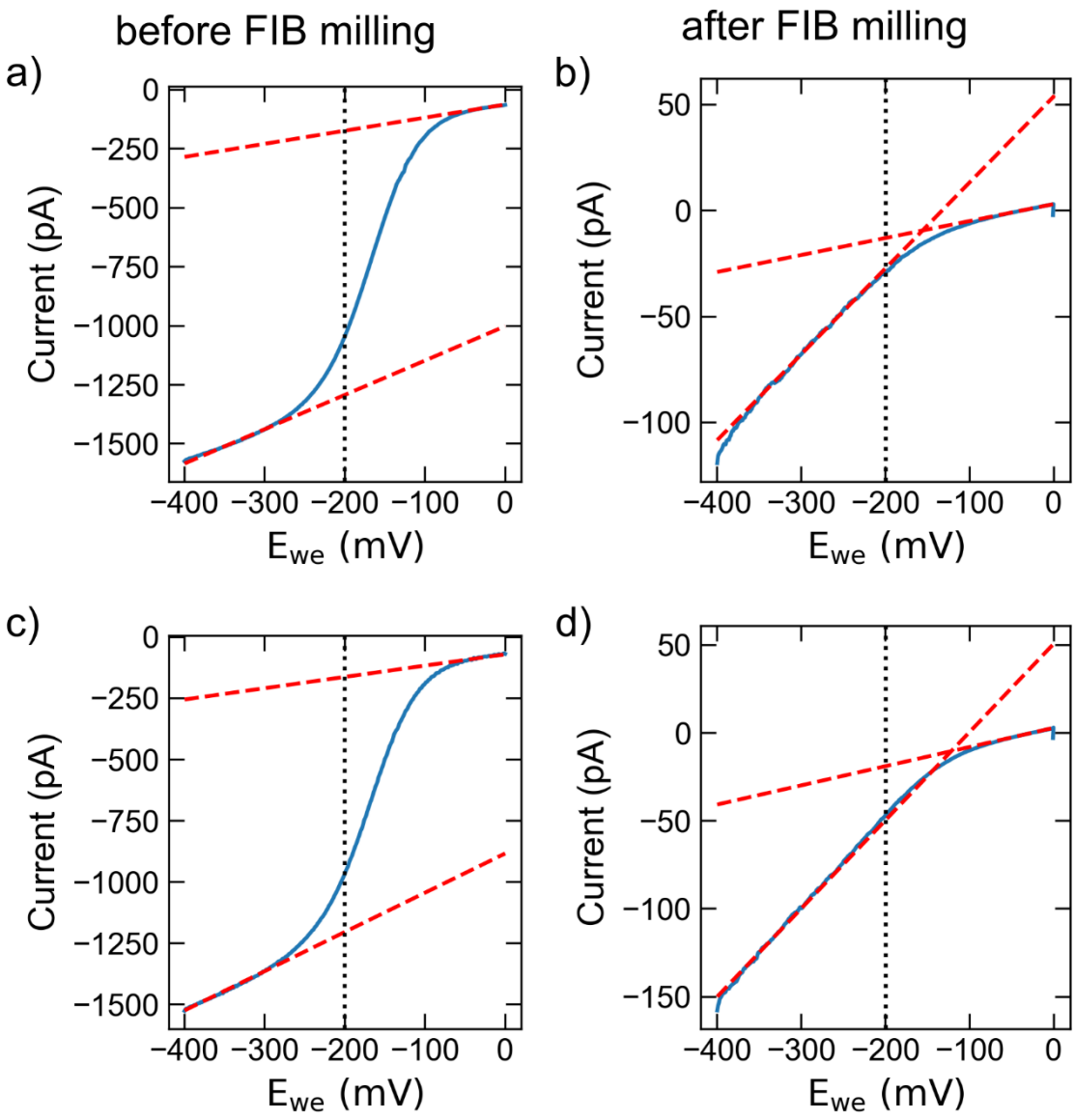

Figure B.4 Sigmoid cyclic voltammograms (cyan curve) for a pair of semi-elliptical carbon nanoelectrodes **a), c)** before and **b), d)** after FIB milling of the quartz glass double-barrel nanopipette tip. The carbon nanoelectrodes are presented in Figure 3.4d. A potential sweep from 0 to -400 mV was repeated 3 times with a 50 mV/s scan rate. The curves represent the last reduction process. A three-electrode system, where the carbon nanoelectrode acted as the working electrode, was used for these measurements. Linear fitting (red dashed lines) between two points at the baseline and plateau was applied to estimate the mass transport limiting current (i_{ss}) at the standard redox potential (black dotted line at -200 mV). The presence of capacitive currents in the system is responsible for the plateau region not being stationary.

Appendix C

A detailed description for the geometry, initial boundary conditions and mesh of the finite element method model developed in Chapter 4 is provided below in the form of a COMSOL model report.

Global Definitions

Parameters

Parameters 1

Name	Expression	Value	Description
VApp	0.6 [V]	0.6 V	Applied voltage
fApp	100[kHz]	1E5 Hz	Applied frequency
T	21[degC]	294.15 K	Room temperature
ParticleDiameter	2[um]	2E−6 m	Diameter of polystyrene latex beads
ParticleDensity	1055[kg/m^3]	1055 kg/m³	Density of polystyrene latex beads
epsilon_m	79	79	Permittivity of medium
ParticleRelativePermittivity	2.56	2.56	Relative permittivity of polystyrene latex beads
ParticleConductivity	6[mS/m]	0.006 S/m	Conductivity of polystyrene latex beads
SemiAxisCH1a	75[nm]	7.5E−8 m	
SemiAxisCH1b	160[nm]	1.6E−7 m	
SemiAxisCH2a	75[nm]	7.5E−8 m	
SemiAxisCH2b	150[nm]	1.5E−7 m	
SeptumHeight	150[nm]	1.5E−7 m	
SeptumWidth	55[nm]	5.5E−8 m	
WallThickness	60[nm]	6E−8 m	
PoreHeight	5[um]	5E−6 m	
PoreAngle	8[deg]	0.13963 rad	
RatioX	(2*PoreHeight*tan(PoreAngle) + SemiAxisCH1b + SemiAxisCH2b +	4.8504	

Name	Expression	Value	Description
	SeptumWidth)/(SemiAxisCH1b + SemiAxisCH2b + SeptumWidth)		
RatioY	(2*PoreHeight*tan(PoreAngle) + SemiAxisCH1a + SemiAxisCH2a + SeptumHeight)/(SemiAxisCH1a + SemiAxisCH2a + SeptumHeight)	5.6847	
CarbonOffset	0[nm]	0 m	
BathWidth	30[um]	3E−5 m	
BathHeight	3[um]	3E−6 m	
BathDepth	30[um]	3E−5 m	
RatioXOffset	(2*CarbonOffset*tan(PoreAngle) + SemiAxisCH1b + SemiAxisCH2b + SeptumWidth)/(SemiAxisCH1b + SemiAxisCH2b + SeptumWidth)	1	
RatioYOffset	(2*CarbonOffset*tan(PoreAngle) + SemiAxisCH1a + SemiAxisCH2a + SeptumHeight)/(SemiAxisCH1a + SemiAxisCH2a + SeptumHeight)	1	

Component 1

Settings

Description	Value
Unit system	Same as global system (SI)

Definitions

Coordinate Systems

Boundary System 1

Coordinate system type	Boundary system
Tag	sys1

Coordinate names

First	Second	Third
t1	t2	n

Geometry 1

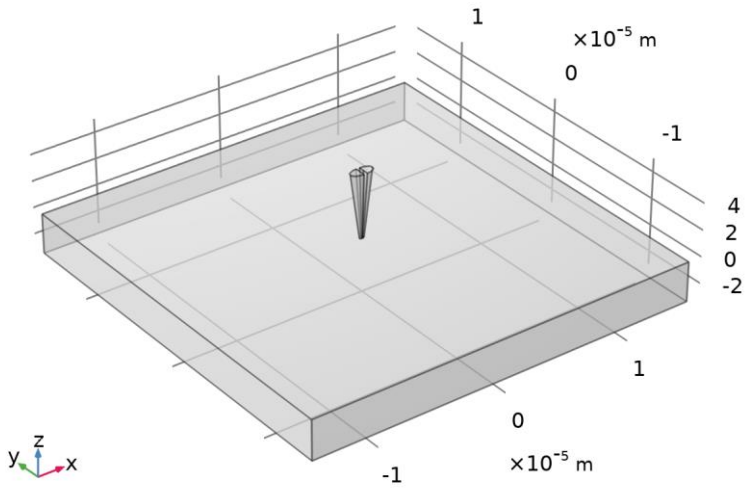

Geometry 1

Units

Length unit	m
Angular unit	deg

Geometry statistics

Description	Value
Space dimension	3
Number of domains	3
Number of boundaries	18
Number of edges	36
Number of vertices	24

Bath (blk1)

Position

Description	Value
Position	{0, 0, -(CarbonOffset + BathHeight)/2}
Base	Center

Axis

Description	Value
Axis type	z - axis

Size and shape

Description	Value
Width	BathWidth
Depth	BathDepth
Height	BathHeight + CarbonOffset

Tip Plane (Bath) (wp1)

Unite objects

Description	Value
Unite objects	On

Tip Geometry (Bath) (sequence2D)

Tip Channel 1 (e1)

Position

Description	Value
Position	{-SeptumWidth/2, 0}

Rotation angle

Description	Value
Rotation	90

Size and shape

Description	Value
a-semiaxis	SemiAxisCH1a
b-semiaxis	SemiAxisCH1b
Sector angle	180

Tip Channel 2 (e2)

Position

Description	Value
Position	{SeptumWidth/2, 0}

Rotation angle

Description	Value
Rotation	-90

Size and shape

Description	Value
a-semiaxis	SemiAxisCH2a
b-semiaxis	SemiAxisCH2b
Sector angle	180

Tip Glass wall (e3)

Position

Description	Value
Position	{0, 0}

Rotation angle

Description	Value
Rotation	90

Size and shape

Description	Value
a-semiaxis	(SemiAxisCH1a + SemiAxisCH2a + SeptumWidth)/2
b-semiaxis	(SemiAxisCH1b + SemiAxisCH2b + SeptumHeight)/2

Tip Plane (Carbon) (wp2)

Unite objects

Description	Value
Unite objects	On

Tip Geometry (Carbon) (sequence2D)

Tip Channel 1 (e1)

Position

Description	Value
Position	{(-SeptumWidth/2)*RatioXOffset, 0}

Rotation angle

Description	Value
Rotation	90

Size and shape

Description	Value
a-semiaxis	SemiAxisCH1a*RatioYOffset
b-semiaxis	SemiAxisCH1b*RatioXOffset
Sector angle	180

Tip Channel 2 (e2)

Position

Description	Value
Position	{(SeptumWidth/2)*RatioXOffset, 0}

Rotation angle

Description	Value
Rotation	-90

Size and shape

Description	Value
a-semiaxis	SemiAxisCH2a*RatioYOffset
b-semiaxis	SemiAxisCH2b*RatioXOffset
Sector angle	180

Tip Glass wall (e3)

Position

Description	Value
Position	{0, 0}

Rotation angle

Description	Value
Rotation	90

Size and shape

Description	Value
a-semiaxis	RatioYOffset*(SemiAxisCH1a + SemiAxisCH2a + SeptumWidth)/2
b-semiaxis	RatioXOffset*(SemiAxisCH1b + SemiAxisCH2b + SeptumHeight)/2

Extrude (Carbon) (ext4)

Settings

Description	Value
Work plane	Tip Plane (Carbon)
Input object handling	Keep

Distances

Distances (m)
PoreHeight

Scales

Scales xw	Scales yw
RatioX	RatioY

Displacements

Displacements xw (m)	Displacements yw (m)
0	0

Twist angles

Twist angles (deg)
0

Materials

Pyrolytic Carbon (Graphite)

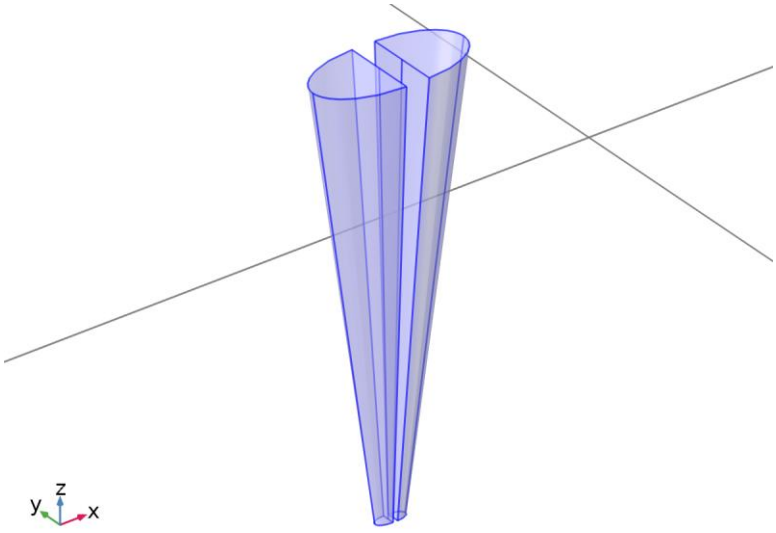

Pyrolytic Carbon (Graphite)

Selection

Geometric entity level	Domain
Selection	Geometry geom1: Dimension 3: Domains 2–3

Material parameters

Name	Value	Unit
Electrical conductivity	5e4	S/m
Relative permittivity	5	1

Water, liquid

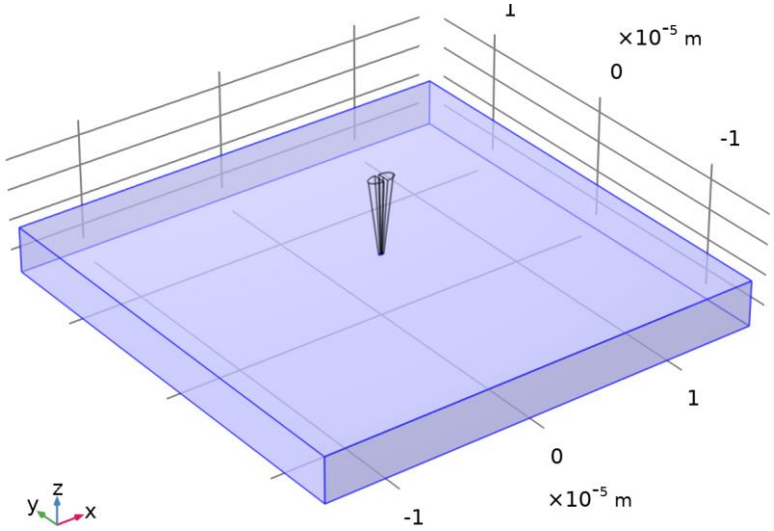

Water, liquid

Selection

Geometric entity level	Domain
Selection	Geometry geom1: Dimension 3: Domain 1

Material parameters

Name	Value	Unit
Electrical conductivity	5.5e-6[S/m]	S/m
Relative permittivity	79	1

Electric Currents

Used products

COMSOL Multiphysics

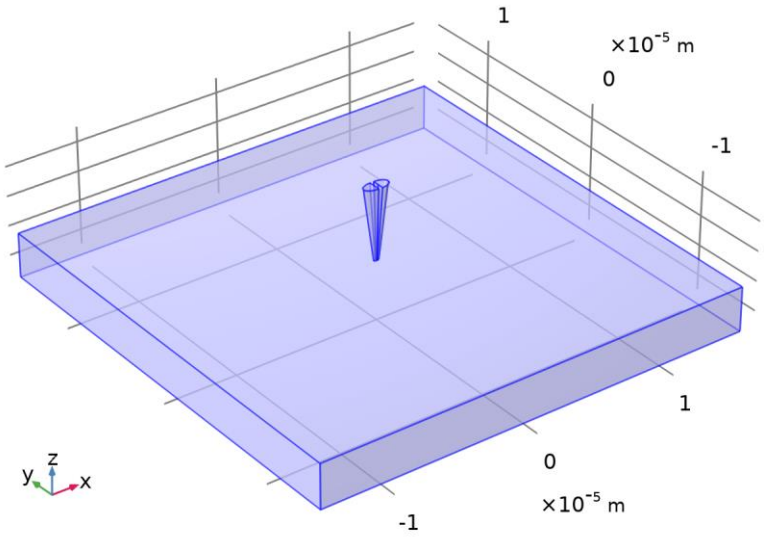

Electric Currents

Selection

Geometric entity level	Domain
Selection	Geometry geom1: Dimension 3: All domains

Equations

$$\nabla \cdot \mathbf{J} = Q_{j,v}$$
$$\mathbf{J} = \sigma \mathbf{E} + \mathbf{J}_e$$
$$\mathbf{E} = -\nabla V$$

Interface Settings

Discretization

Settings

Description	Value
Electric potential	Quadratic

Manual Terminal Sweep Settings

Settings

Description	Value
Use manual terminal sweep	Off
Reference impedance	50[ohm]

Current Conservation 1

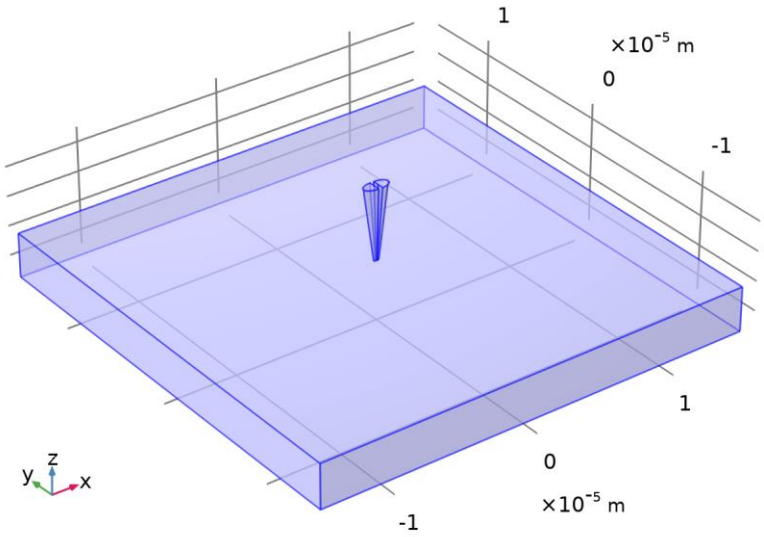

Current Conservation 1

Selection

Geometric entity level	Domain
Selection	Geometry geom1: Dimension 3: All domains

Equations

$$\nabla \cdot \mathbf{J} = Q_{j,v}$$
$$\mathbf{J} = \sigma \mathbf{E} + \mathbf{J}_e$$
$$\mathbf{E} = -\nabla V$$

Constitutive Relation Jc-E

Settings

Description	Value
Conduction model	Electrical conductivity
Electrical conductivity	From material

Constitutive Relation D-E

Settings

Description	Value
Dielectric model	Relative permittivity
Relative permittivity	From material

Coordinate System Selection

Settings

Description	Value
Coordinate system	Global coordinate system

Properties from material

Property	Material	Property group
Electrical conductivity	Pyrolytic Carbon (Graphite)	Basic
Relative permittivity	Pyrolytic Carbon (Graphite)	Basic
Electrical conductivity	Water, liquid	Basic

Property	Material	Property group
Relative permittivity	Water, liquid	Basic

Electric Insulation 1

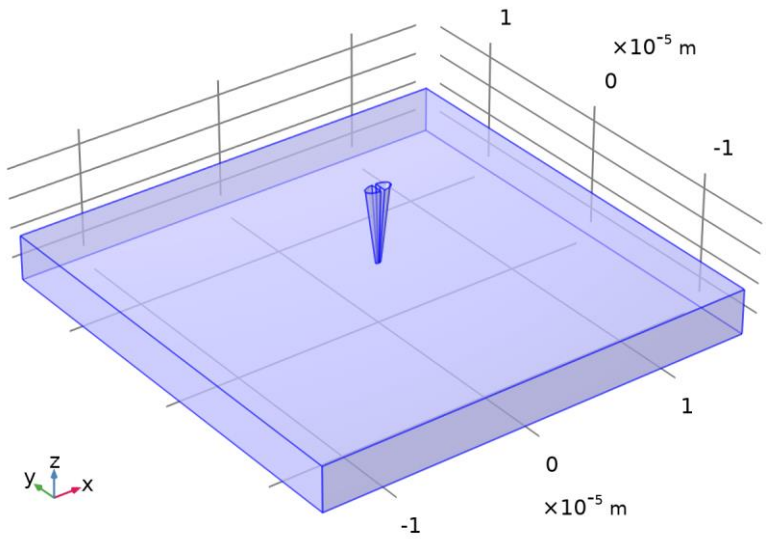

Electric Insulation 1

Selection

Geometric entity level	Boundary
Selection	Geometry geom1: Dimension 2: All boundaries

Equations

$$\mathbf{n} \cdot \mathbf{J} = 0$$

Variables

Name	Expression	Unit	Description	Selection	Details
ec.nJ	0	A/m²	Normal current density	Boundaries 1–7, 10–12, 14–16, 18	+ operation

Initial Values 1

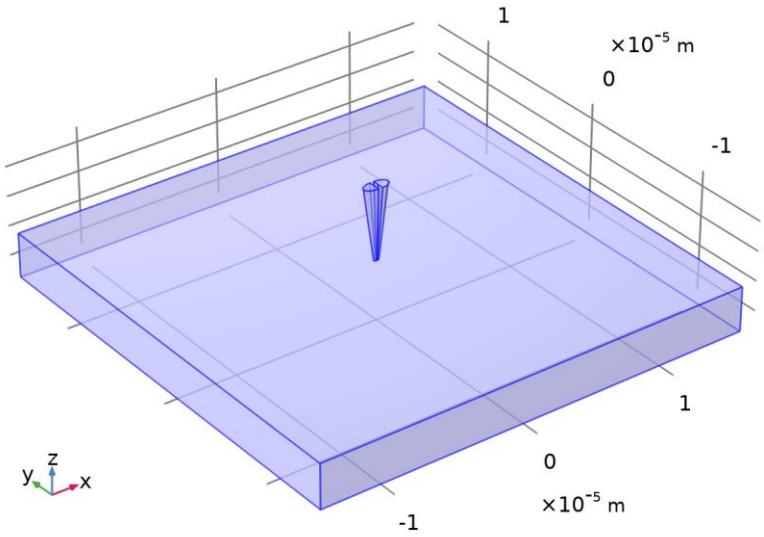

Initial Values 1

Selection

Geometric entity level	Domain
Selection	Geometry geom1: Dimension 3: All domains

Settings

Description	Value
Electric potential	0

Electric Potential +

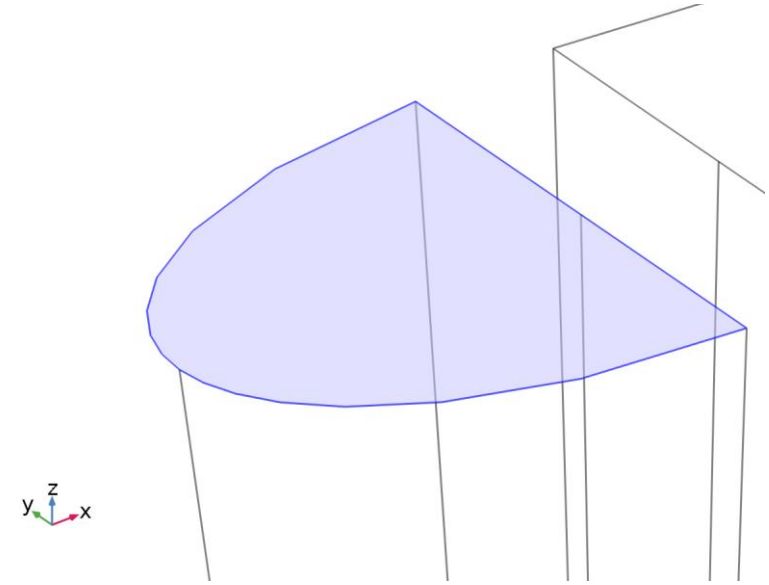

Electric Potential +

Selection

Geometric entity level	Boundary
Selection	Geometry geom1: Dimension 2: Boundary 8

Equations

$V = V_0$

Electric Potential

Settings

Description	Value
Electric potential	VApp

Electric Potential -

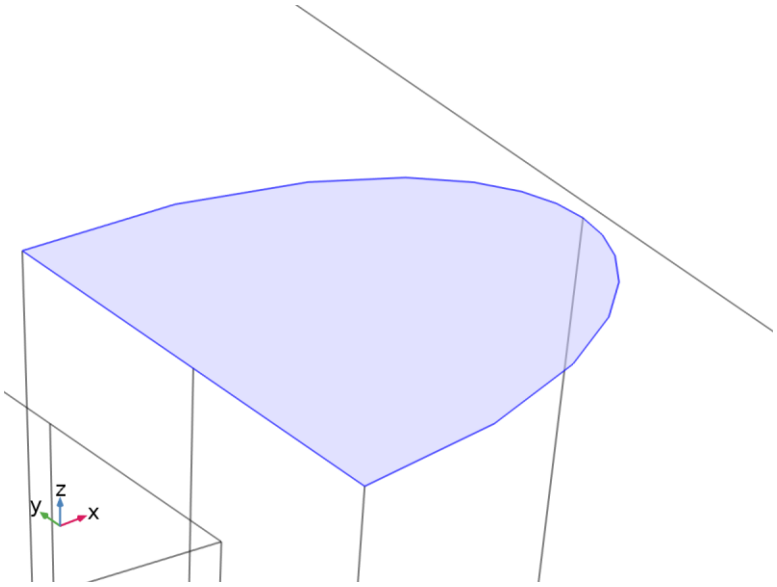

Electric Potential -

Selection

Geometric entity level	Boundary
Selection	Geometry geom1: Dimension 2: Boundary 17

Equations

$V = V_0$

Electric Potential

Settings

Description	Value
Electric potential	-VApp

Mesh 1

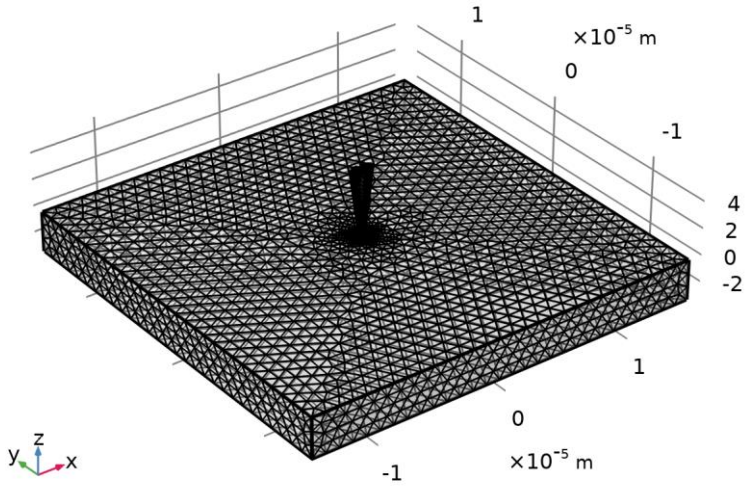

Mesh 1

Size (size)

Settings

Description	Value
Maximum element size	1.05E-6
Minimum element size	4.5E-8
Curvature factor	0.3
Resolution of narrow regions	0.85
Maximum element growth rate	1.35
Predefined size	Extra fine

Edge 1 (edg1)

Selection

Geometric entity level	Edge
Selection	Geometry geom1: Dimension 1: Edges 19–21, 24

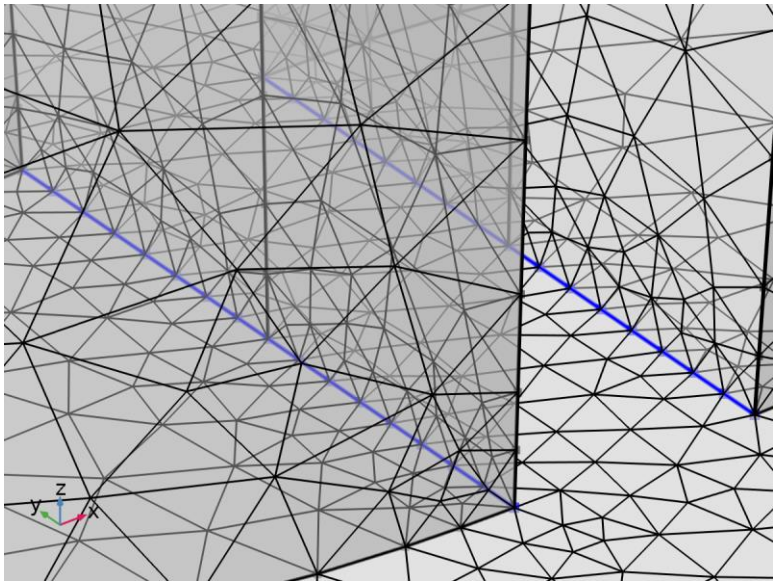

Edge 1

Size 1 (size1)

Selection

Geometric entity level	Edge
Selection	Geometry geom1: Dimension 1: Edges 19–21, 24

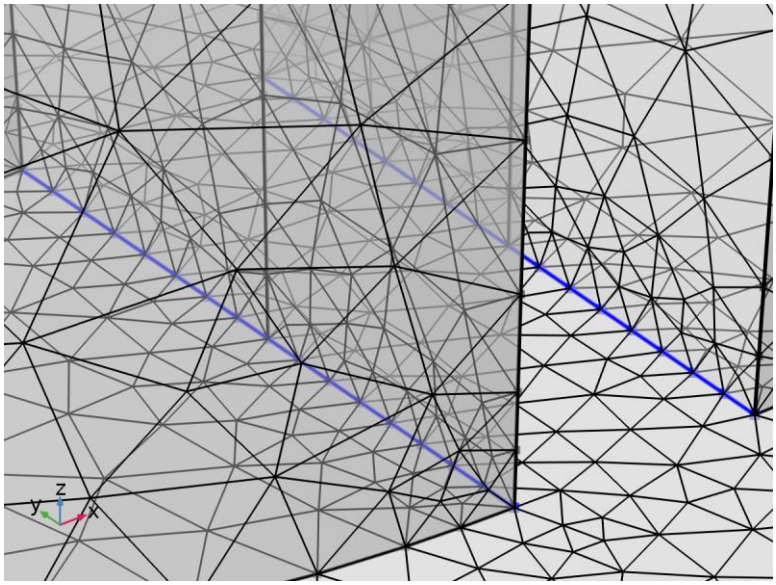

Size 1

Settings

Description	Value
Maximum element size	1e-8
Minimum element size	1e-8
Curvature factor	0.6
Curvature factor	Off
Resolution of narrow regions	0.5
Resolution of narrow regions	Off
Maximum element growth rate	1.5
Maximum element growth rate	Off
Custom element size	Custom

Boundary Layers 1 (bl1)

Selection

Geometric entity level	Domain
Selection	Geometry geom1

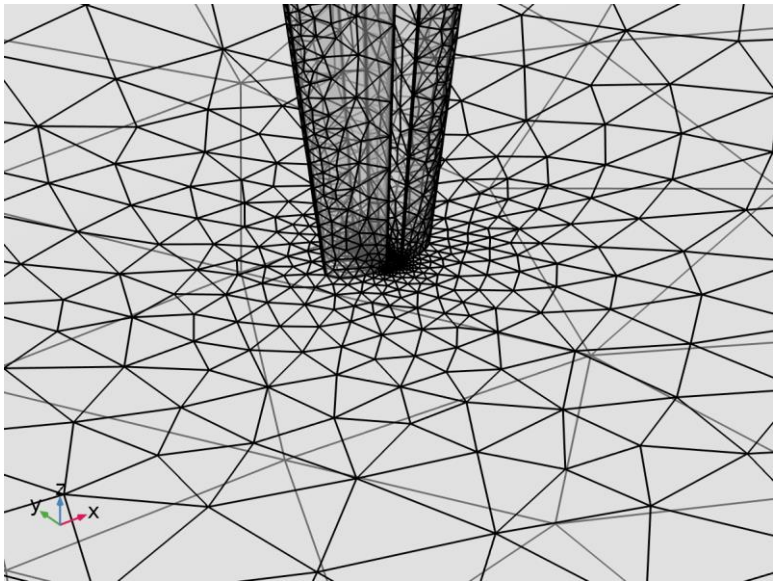

Boundary Layers 1

Boundary Layer Properties (blp)

Selection

Geometric entity level	Boundary
Selection	Geometry geom1: Dimension 2: No boundaries